

Electronic Theses and Dissertations, 2004-2019

2012

Influence Of Topographic Elevation Error On Modeled Storm Surge

Matthew Bilskie
University of Central Florida

 Part of the [Engineering Commons](#), and the [Water Resource Management Commons](#)
Find similar works at: <https://stars.library.ucf.edu/etd>
University of Central Florida Libraries <http://library.ucf.edu>

This Masters Thesis (Open Access) is brought to you for free and open access by STARS. It has been accepted for inclusion in Electronic Theses and Dissertations, 2004-2019 by an authorized administrator of STARS. For more information, please contact STARS@ucf.edu.

STARS Citation

Bilskie, Matthew, "Influence Of Topographic Elevation Error On Modeled Storm Surge" (2012). *Electronic Theses and Dissertations, 2004-2019*. 2260.
<https://stars.library.ucf.edu/etd/2260>

**INFLUENCE OF TOPOGRAPHIC ELEVATION ERROR
ON MODELED STORM SURGE**

by

MATTHEW BILSKIE
B.S. University of Central Florida, 2009

A thesis submitted in partial fulfillment of the requirements
for the degree of Master of Science
in the Department of Civil, Environmental, and Construction Engineering
in the College of Engineering and Computer Science
at the University of Central Florida
Orlando, Florida

Spring Term
2012

Major Professor: Scott C. Hagen

© 2012 Matthew Vernon Bilskie

ABSTRACT

The following presents a method for determining topographic elevation error for overland unstructured finite element meshes derived from bare earth LiDAR for use in a shallow water equations model. This thesis investigates the development of an optimal interpolation method to produce minimal error for a given element size. In hydrodynamic studies, it is vital to represent the floodplain as accurately as possible since terrain is a critical factor that influences water flow. An essential step in the development of a coastal inundation model is processing and resampling dense bare earth LiDAR to a DEM and ultimately to the mesh nodes; however, it is crucial that the correct DEM grid size and interpolation method be employed for an accurate representation of the terrain. The following research serves two purposes: 1) to assess the resolution and interpolation scheme of bare earth LiDAR data points in terms of its ability to describe the bare earth topography and its subsequent performance during relevant tide and storm surge simulations.

To my grandparents

ACKNOWLEDGMENTS

The following thesis is a culmination of not only my individual efforts, but also the aid and guidance of several friends and colleagues. First, I would like to express gratitude towards Dr. Scott Hagen for his enduring support and guidance as well as providing the opportunity to work in the CHAMPS Lab. I would also like to thank Dr. Manoj Chopra and Dr. Dingbao Wang for serving on my thesis committee.

The collaboration and learning experience among students in the CHAMPS Lab, past and present, is world class. I would like to express gratitude to Michael Salisbury, David Coggin, Derek Giardino, Alfredo Ruiz, Lillie Thomas, Peter Bacopoulos, Ammarin Daranpob, Hitoshi Tamura, Daina Smar, Davina Passeri, Karim Alizad, Amanda Tritinger, and especially Stephen Medeiros, for his mentorship, a hard to come by relationship nowadays. It will be paid forward. Additional thanks to Peter Bacopoulos, Stephen Medeiros, Davina Passeri, and Daina Smar for editing this thesis.

Much thanks to professional colleagues John Atkinson, Hugh Roberts, Zachary Cobell, and Shan Zou from Arcadis; Casey Dietrich from the University of Texas; Alan Zundel from Brigham Young University; Jason Fleming from Seahorse Coastal Consulting; and Crystal Fulcher from the UNC-Ch Institute of Marine Sciences.

Last and certainly not least, I am blessed to have such a supportive and loving family. This thesis would not have been possible without their guidance, understanding, and encouragement. With this, I thank you.

This study is funded in part under Contract No. NFWWMD-08-073 from the Northwest Florida Water Management District (NFWWMD). The statements, findings, conclusions, and recommendations expressed herein are those of the authors and do not necessarily reflect the views of the NFWWMD or their affiliates.

TABLE OF CONTENTS

LIST OF TABLES	xi
LIST OF FIGURES	xiv
LIST OF ABBREVIATIONS.....	xxvi
CHAPTER 1: INTRODUCTION	1
CHAPTER 2: LITERATURE REVIEW	6
2.1 Large Domain Storm Surge Modeling.....	6
2.2 Digital Elevation Models	9
2.2.1 Interpolation Error	11
2.2.2 DEM Grid Size	14
2.3 LiDAR in Coastal Hydrodynamic Finite Element Models	21
2.4 Introduction to Storm Surge.....	29
CHAPTER 3: INTERPOLATION METHODS	34
3.1 Linear Interpolation.....	34
3.2 Inverse Distance Weighed Interpolation	36
3.3 Natural Neighbor Interpolation	37
3.4 Area Averaging	39

CHAPTER 4: DESCRIPTION OF STUDY DOMAIN	41
CHAPTER 5: LiDAR DATA ACQUISITION	46
5.1 LiDAR Requirements for Flood Modeling	46
5.2 LiDAR Source Data	48
CHAPTER 6: TOPOGRAPHIC ERROR ASSESSMENT METHODOLOGY	53
6.1 Selection of Test Sites	53
6.2 DEM and Finite Element Mesh Generation	57
6.3 Accuracy Analysis Statistics (RMSE)	58
6.4 Test for Normality	59
6.5 Accuracy Assessment Results	65
6.6 Louisiana Test Sites	78
6.7 Preliminary Conclusions	85
CHAPTER 7: DEM DEVELOPMENT	87
7.1 Terrain Dataset	87
7.2 Test and Training Data	89
7.3 Raster DEM Generation	90
7.4 Results of LiDAR DEM Generation	90
7.5 Seamless Pascagoula Floodplain DEM Generation	95

CHAPTER 8: FINITE ELEMENT MESH DEVELOPMENT	102
8.1 In-Bank Mesh Development	103
8.1.1 Digitization of Model Boundary.....	104
8.1.2 Triangulation	108
8.1.3 Bathymetry	111
8.2 Floodplain Mesh Development	119
8.2.1 Equilateral Regions.....	119
8.2.2 Remaining Floodplain Mesh	130
8.2.3 Mesh Node Interpolation	137
CHAPTER 9: LARGE DOMAIN TOPOGRAPHIC ERROR ASSESSMENT.....	139
9.1 Equilateral Mesh Node Interpolation	139
9.2 Accuracy Assessment Results and Discussion	140
CHAPTER 10: NUMERICAL CODE DOCUMENTATION	152
10.1 Numerical Model Description.....	152
10.2 Governing Equations.....	152
10.3 ADCIRC Bottom Friction Formulation	155
CHAPTER 11: MODEL SETUP.....	158
11.1 Astronomic Tide Model Setup	158
11.2 Coupled Tide and Storm Surge Model Setup.....	159

CHAPTER 12: MODEL RESULTS.....	170
12.1 Astronomic Tide Results.....	170
12.2 Storm Surge Results	182
CHAPTER 13: CONCLUSIONS AND FUTURE WORK.....	197
REFERENCES	200

LIST OF TABLES

Table 1	Hancock & Jackson Counties LiDAR sensor parameters	51
Table 2	Harrison County LiDAR sensor parameters	52
Table 3	LiDAR point statistics for test sites	57
Table 4	Normality test results of error distribution.....	62
Table 5	RMSE for all test sites with a linear interpolation of the training dataset onto the FEMs and DEMs.....	67
Table 6	RMSE for Test Site 1 using linear, IDW, and NN interpolation from the 5-m and 10-m DEM	67
Table 7	RMSE for Test Site 2 using linear, IDW, and NN interpolation from the 5-m and 10-m DEM	68
Table 8	RMSE for Test Site 3 using linear, IDW, and NN interpolation from the 5-m and 10-m DEM	68
Table 9	95 th and 5 th percentiles of elevation errors for Test Site 1 using the 5-m DEM ...	75
Table 10	95 th and 5 th percentiles of elevation errors for Test Site 2 using the 5-m DEM ...	75
Table 11	95 th and 5 th percentiles of elevation errors for Test Site 3 using the 5-m DEM ...	76
Table 12	RMSE for all both test sites with a linear interpolation of the training dataset onto the finite element meshes and DEMs.....	82
Table 13	RMSE for the Urban Test Site using linear, IDW, and NN interpolation from the 5-m and 10-m DEM	83

Table 14	RMSE for the Marsh Test Site using linear, IDW, and NN interpolation from the 5-m and 10-m DEM.....	83
Table 15	Parameters used during generation of the Terrain (ESRI, 2011a; Medeiros <i>et al.</i> , 2011).....	89
Table 16	RMSE of each training-derived DEM when compared to the test points.....	95
Table 17	RMSE of the training data interpolated to each FEM using a linear, IDW, and NN method compared to the test dataset.....	141
Table 18	RMSE of the training-derived 5-m DEM interpolated to each FEM using a linear, IDW, and NN method compared to the test dataset.....	141
Table 19	Best performing cell averaging method for each equilateral FEM zone at each equilateral element size in terms of RMSE.....	150
Table 20	Best performing cell averaging method for each equilateral FEM zone at each equilateral element size in terms of the 95 th percentile.....	150
Table 21	Equation 9.1 applied for each element size in Table 19 with a 5-m DEM.....	150
Table 22	Best performing cell averaging method for each equilateral FEM for each Test Site near Pascagoula and New Orleans presented in Chapter 6.....	151
Table 23	Tidal constituents used to force the ADCIRC model.	159
Table 24	Breakdown of the 21.5-day astronomic tide and storm surge simulation.....	160
Table 25	Manning's <i>n</i> , surface roughness, and canopy values obtained by using the 1992 LULC database (Bunya <i>et al.</i> , 2010).	169
Table 26	23 tidal constituents applied in harmonic resynthesis - constituent names gathered from (Kojima, 2005).....	173

Table 27	37 tidal constituents gathered from the NOS tidal stations - constituent names gathered from (Kojima, 2005)	174
Table 28	RMSE for all 9 stations for both in-bank models.	181

LIST OF FIGURES

Figure 1	Large model domain approach encompassing the deep ocean, continental shelf, shoreline, and coastal floodplain.....	9
Figure 2	Raster DEM with regularly spaced grid cells in the x- and y-directions	16
Figure 3	Plot depicting a set of measured elevation points along a transect (Hengl, 2006). The red line indicates the continuous surface representation and the black circles represent the measured values (Hengl, 2006).	19
Figure 4	Plot with the continuous surface in red, measurements in black, and a 20-m DEM grid representation of the continuous surface (Hengl, 2006).....	19
Figure 5	Plot with the continuous surface in red, measurements in black, and a 5-m DEM grid representation of the continuous surface (Hengl, 2006).....	20
Figure 6	Plot with the continuous surface in red, measurements in black, and a 2.5-m DEM grid representation of the continuous surface (Hengl, 2006).....	20
Figure 7	Arc placement for mesh generation. Blue lines represent the sub mesh region and red lines represent the raised features. Black lines represent arc within SMS. Published with authors' permission. (Roberts, 2004).....	24
Figure 8	Final product of vertical features (black lines). Published with authors' permission. (Coggin, 2008).....	26
Figure 9	Aerial image with vertical features in red and finite element mesh triangulation in black. Published with authors' permission. (Coggin, 2008)	27

Figure 10	Interpolation of nodal point via polygon control area for LiDAR data. Published with authors' permission. (Coggin, 2008)	28
Figure 11	Interpolation of nodal points via rectangle control volume (Atkinson, 2007).....	29
Figure 12	Image depicting the addition of the astronomical tide (2 ft) and storm surge (15 ft) to produce a storm tide of 17 ft (NOAA, 2010) above mean sea level.....	30
Figure 13	Figure of the hurricane eye wall and a cross-section view of the winds and pressure distributed throughout the storm (Department of Atmospheric Sciences at University of Illinois at Urbana-Champaign, 2010).....	33
Figure 14	3D representation of a triangle using a linear interpolation.....	36
Figure 15	Thiessen polygon resulting from a Delaunay Triangulation. The bold lines are the Thiessen polygons and the thin lines represent the Delaunay triangulation. From (Burrough & McDonnell, 1998) page 114.....	38
Figure 16	Example of interpolation using a 1 cell average (direct lookup).....	40
Figure 17	Example of interpolation using a nine cell area averaging scheme	40
Figure 18	Pascagoula River Basin and its rivers	42
Figure 19	Land cover distribution in the Pascagoula River Basin (Mississippi Department of Environmental Quality, 2001).	43
Figure 20	2001 National LandCover Data and classification for the Pascagoula River Basin (Homer <i>et al.</i> , 2004).....	44
Figure 21	Map of the floodplain boundary (blue + red). The extent of the LiDAR coverage is represented by the red line. Elevation data within the blue boundary was obtained from a previous FEM. The counties are bounded by the black lines. The	

	background is NED (Gesch <i>et al.</i> , 2002; Gesch, 2007) elevation data over Landsat satellite imagery (Goslee, 2011).	49
Figure 22	Pascagoula River, MS with box insets representing accuracy testing sites 1, 2, and 3.....	53
Figure 23	Test Site 1	54
Figure 24	Test Site 2	54
Figure 25	Test Site 3	55
Figure 26	The boundary of the LiDAR coverage for the test sites. The blue and red points indicate the training and test datasets, respectively. The yellow points represent the transition area dataset.....	56
Figure 27	Refinement splits the element into four sub-elements and divides the edge length in half.	58
Figure 28	Error distribution in the 40-m FEM (49 cell averaging) for Test Site 3 and in the 5-m FEM (training NN) for Test Site 2.	63
Figure 29	Error distribution in the 40-m FEM (49 cell averaging) for Test Site 3 and in the 5-m FEM (training NN) for Test Site 2 with outliers removed.	64
Figure 30	5 m FEM for Test Site 2. The black line represents cross-section A.....	69
Figure 31	Plot of (top) elevation (m) and (bottom) absolute elevation error (cm) at Test Site 2 for the 5-m FEM along cross-section A. The blue boxes indicate the highest errors along the cross-section correlating with high topographic slopes.....	70
Figure 32	Plot of (top) elevation (m) and (bottom) absolute elevation error (cm) at Test Site 2 for the 80-m FEM along cross-section A.....	71

Figure 33	RMSE (cm) for Test Site 1 using area averaging from the 5-m DEM	73
Figure 34	RMSE (cm) for Test Site 2 using area averaging from the 5-m DEM	73
Figure 35	RMSE (cm) for Test Site 3 using area averaging from the 5-m DEM	74
Figure 36	95 th percentile for Test Site 1 using area averaging from the 5-m DEM.....	77
Figure 37	95 th percentile for Test Site 2 using area averaging from the 5-m DEM.....	77
Figure 38	95 th percentile for Test Site 3 using area averaging from the 5-m DEM.....	78
Figure 39	Southern Louisiana test site locations outlined in red.	79
Figure 40	Louisiana Urban Test Site with the outer and inner boundary in black.....	80
Figure 41	Louisiana Marsh Test Site with the outer and inner boundary in black	80
Figure 42	RMSE (cm) for the Urban Test Site using area averaging from the 5-m DEM ...	84
Figure 43	RMSE (cm) for the Mash Test Site using area averaging from the 5-m DEM	85
Figure 44	A) 1.25-m training dataset-derived DEM B) 2.5-m training dataset-derived DEM	91
Figure 45	A) 5-m training dataset-derived DEM B) 10 m training dataset-derived DEM ...	92
Figure 46	A) 20-m training dataset-derived DEM 40-m training dataset-derived DEM	93
Figure 47	80-m training dataset-derived DEM	94
Figure 48	Seamless 5-m DEM of study including offshore bathymetry. The blue line is the mesh boundary. Elevations beyond the mesh boundary are obtained from the NED 1-arc-second DEM (Gesch <i>et al.</i> , 2002; Gesch, 2007).....	96
Figure 49	Inset boxes for zooms of the 5-m DEM found in Figure 50 through Figure 53. ...	97
Figure 50	5-m DEM near the upper Escatawpa River	98

Figure 51	5-m DEM near the East Pascagoula Inlet and Port of Pascagoula with floodplain boundary (blue line).....	99
Figure 52	5-m DEM near the West Pascagoula Inlet and Graveline Bay with the floodplain mesh boundary (blue line).	100
Figure 53	5-m DEM near Gulfport Mississippi. The blue line is the floodplain mesh boundary. Elevation beyond the blue line is from the NED 1-arc-second DEM (Gesch <i>et al.</i> , 2002; Gesch, 2007).....	101
Figure 54	53K mesh (Hagen <i>et al.</i> , 2006).....	105
Figure 55	53K mesh bathymetry (Hagen <i>et al.</i> , 2006).....	106
Figure 56	Location of the incision on the 53K mesh	107
Figure 57	Final digitized boundary excluding islands	108
Figure 58	Three elements across the channel representing a trapezoidal cross-section	109
Figure 59	A) Localized frame of the in-bank Pascagoula River mesh with blue inset box B) relatively low-resolution in-bank FEM C) relatively high-resolution in-bank FEM.....	111
Figure 60	Pascagoula River in-bank finite element mesh. The mesh consists of 334,589 nodes and 634,210 elements. It extends from the deep Atlantic Ocean and Gulf of Mexico into Pascagoula Bay and into the Pascagoula River.....	114
Figure 61	Triangulation of the Pascagoula Bay and River. The mesh elements are outlined in red. The background imagery is LANDSAT satellite imagery and aerial photography.	115

Figure 62	Sections which utilized different bathymetry sources. The red indicates elevations taken from SL15 (Bunya <i>et al.</i> , 2010), blue from FLPH_AL (Northwest Florida Water Management District, 2011), and purple from Wang (2008).....	116
Figure 63	In-bank model bathymetry around Louisiana, Mississippi, and Alabama. Key features include the Mississippi-Alabama Shelf, Mississippi Delta, Chandeleur Sound and the shipping channels around southeastern Louisiana, Pascagoula Bay, and Mobile Bay.....	117
Figure 64	In-bank model bathymetry for the Pascagoula River.	118
Figure 65	In-bank model bathymetry around the east and west Pascagoula inlets.	119
Figure 66	Equilateral regions in red and the triangular finite elements in black	121
Figure 67	Left, center, and right zones outlined in yellow. The model floodplain boundary is in red. The background image is Landsat (Goslee, 2011).....	122
Figure 68	\mathcal{A} -ARC criteria for the area of one and two, A_1 and A_2 , respectively. The ratio shown is $A_1:A_2 = 0.5:1$	123
Figure 69	Left, center, and right zones outlined in yellow. The interior buffer regions are bounded by the blue boundary. The red line is the floodplain boundary.	125
Figure 70	Zoom in on the Pascagoula Port located in the Right Equilateral Zone. The red triangles represent the in-bank triangular elements, the blue is the transitional elements following the geometric criteria, and the black elements are the 16-m equilateral elements.	126

Figure 71	Zoom in on the Pascagoula Port located in the Right Equilateral Zone. The red triangles represent the in-bank triangular elements, the blue is the transitional elements following the geometric criteria, and the black elements are the 80-m equilateral elements.	127
Figure 72	Zoom in on the Pascagoula Port located in the Right Equilateral Zone. The red triangles represent the in-bank triangular elements, the blue is the transitional elements following the geometric criteria, and the black elements are the 40-m equilateral elements.	128
Figure 73	Zoom in on the Pascagoula Port located in the Right Equilateral Zone. The red triangles represent the in-bank triangular elements, the blue is the transitional elements following the geometric criteria, and the black elements are the 20-m equilateral elements.	129
Figure 74	The extent of the LiDAR coverage is represented by the red line. The equilateral region is the orange boundary. Nodal placement and elevation data within the blue boundary was obtained from a previous FEM. The counties are bounded by the black lines. The background is NED (Gesch <i>et al.</i> , 2002; Gesch, 2007) elevation data over Landsat satellite imagery (Goslee, 2011).	132
Figure 75	Digitized boundaries for use in floodplain mesh development (black). The background image is Landsat satellite imagery (Goslee, 2011).	133
Figure 76	Digitized boundaries for use in floodplain mesh development (black). The background is 1-arc-second (30 m) NED DEM (Gesch <i>et al.</i> , 2002; Gesch, 2007).	134

Figure 77	Digitized vertical feature arcs (purple) used as element (black triangles) edges. The background is the bare earth LiDAR-derived 5-m DEM.	135
Figure 78	Floodplain mesh in red, transition to FLPH_AL mesh (light blue), and FLPH_AL mesh (blue). The equilateral zones are bounded by the orange boundary. The background is Landsat (Goslee, 2011).....	136
Figure 79	Floodplain mesh (withholding the equilateral zones) merged to in-bank mesh number 1. The contours are elevations with respect to NAVD88.	138
Figure 80	RMSE of the training-derived 5-m DEM interpolated to each FEM for the Left Zone using a direct lookup and area averaging method from 9 to 441 neighboring cells.	144
Figure 81	RMSE of the training-derived 5-m DEM interpolated to each FEM for the Center Zone using a direct lookup and area averaging method from 9 to 441 neighboring cells.	145
Figure 82	RMSE of the training-derived 5-m DEM interpolated to each FEM for the Right Zone using a direct lookup and area averaging method from 9 to 441 neighboring cells.	146
Figure 83	95 th percentile of the training-derived 5-m DEM interpolated to each FEM for the Left Zone using a direct lookup and area averaging method from 9 to 441 neighboring cells.....	147
Figure 84	95 th percentile of the training-derived 5-m DEM interpolated to each FEM for the Center Zone using a direct lookup and area averaging method from 9 to 441 neighboring cells.....	148

Figure 85	95 th percentile of the training-derived 5-m DEM interpolated to each FEM for the Right Zone using a direct lookup and area averaging method from 9 to 441 neighboring cells.....	149
Figure 86	Hurricane Katrina storm track – courtesy of NASA.....	161
Figure 87	Extents of the wind and pressure fields	162
Figure 88	Manning's <i>n</i> for the Pascagoula River and surrounding floodplain. Values were obtained via direct lookup from Table 25 based on the 1992 NLCD landcover classification. Hotter colors represent higher resistance to flow.	165
Figure 89	Wind reduction factors (<i>Z0</i>) for the Pascagoula River and surrounding floodplain with a wind blowing from west to east. Values were obtained via direct lookup from Table 17 based on the 1992 NLCD landcover classification. Hotter colors represent higher wind reduction than the cooler colors.....	166
Figure 90	Wind reduction factors (<i>Z0</i>) for the Pascagoula River and surrounding floodplain with a wind blowing from south to north. Values were obtained via direct lookup from Table 17 based on the 1992 NLCD landcover classification. Hotter colors represent higher wind reduction than the cooler colors.....	167
Figure 91	Surface canopy coefficients for the Pascagoula River and surrounding floodplain. Values were obtained via direct lookup from Table 17 based on the 1992 NLCD landcover classification. Wind is turned off for nodes with a value of 0 and wind is enabled for nodes with a value of 1.....	168
Figure 92	Location of NOS stations located within the in-bank Pascagoula model domain.	172

Figure 93	Location of USGS stations located within the in-bank Pascagoula model domain.	172
Figure 94	A resynthesis of historical (red) and modeled (black and blue) tidal constituents for a complete spring and neap tidal cycle at tidal station NOS 8732828 – Weeks Bay, Alabama.....	176
Figure 95	A resynthesis of historical (red) and modeled (black and blue) tidal constituents for a complete spring and neap tidal cycle at tidal station NOS 8735180 – Dauphin Island, Alabama.....	176
Figure 96	A resynthesis of historical (red) and modeled (black and blue) tidal constituents for a complete spring and neap tidal cycle at tidal station NOS 8741041 – Dock E Port of Pascagoula, Mississippi.	177
Figure 97	A resynthesis of historical (red) and modeled (black and blue) tidal constituents for a complete spring and neap tidal cycle at tidal station NOS 8741196 – Pascagoula Point, Mississippi.....	177
Figure 98	A resynthesis of historical (red) and modeled (black and blue) tidal constituents for a complete spring and neap tidal cycle at tidal station NOS 8741533 – Pascagoula NOAA Lab, Mississippi.....	178
Figure 99	A resynthesis of historical (red) and modeled (black and blue) tidal constituents for a complete spring and neap tidal cycle at water level station USGS 02480212 – Pascagoula River mile 1, Pascagoula, Mississippi.	178

Figure 100	A resynthesis of historical (red) and modeled (black and blue) tidal constituents for a complete spring and neap tidal cycle at water level station USGS 02480285 – West Pascagoula River at Highway 90 at Gautier, Mississippi.....	179
Figure 101	A resynthesis of historical (red) and modeled (black and blue) tidal constituents for a complete spring and neap tidal cycle at water level station USGS 0248018020 – Escatawpa River at I-10 near Orange Grove, Mississippi.	179
Figure 102	A resynthesis of historical (red) and modeled (black and blue) tidal constituents for a complete spring and neap tidal cycle at water level station USGS 02479310 – Pascagoula River at Graham Ferry, Mississippi.	180
Figure 103	Maximum inundation area (or maximum of maximums) for the four ADCIRC meshes. The black line is the ADCIRC mesh boundary.....	183
Figure 104	The total inundation area (blue) over the inundation area from the MOM (red) for A) 160-m, B) 80-m, C) 40-m, and D) 20-m equilateral meshes. Figures in the red inset box are shown in Figure 105.....	184
Figure 105	The total inundation area (blue) over the inundation area from the MOM (red) for A) 160-m, B) 80-m, C) 40-m, and D) 20-m equilateral meshes for red inset from Figure 104.	185
Figure 106	Equilateral mesh contributing to the MOM.....	187
Figure 107	Equilateral mesh contributing to the lowest water level from the MOM.	188
Figure 108	5-m DEM with ADCIRC mesh boundary (black) and equilateral zones (orange). Elevations are referenced to NAVD88.	189

Figure 109	Difference in maximum water levels between the 160-m and 20-m equilateral mesh simulations. Hot colors represent higher water levels for the 160-m mesh and cool colors are higher water levels for the 20-m mesh.	191
Figure 110	Difference in maximum water levels between the 160-m and 40-m equilateral mesh simulations. Hot colors represent higher water levels for the 160-m mesh and cool colors are higher water levels for the 40-m mesh.	192
Figure 111	Difference in maximum water levels between the 160-m and 80-m equilateral mesh simulations. Hot colors represent higher water levels for the 160-m mesh and cool colors are higher water levels for the 80-m mesh.	193
Figure 112	Difference in maximum water levels between the 80-m and 20-m equilateral mesh simulations. Hot colors represent higher water levels for the 80-m mesh and cool colors are higher water levels for the 20-m mesh.	194
Figure 113	Difference in maximum water levels between the 80-m and 40-m equilateral mesh simulations. Hot colors represent higher water levels for the 80-m mesh and cool colors are higher water levels for the 40-m mesh.	195
Figure 114	Difference in maximum water levels between the 40-m and 20-m equilateral mesh simulations. Hot colors represent higher water levels for the 40-m mesh and cool colors are higher water levels for the 20-m mesh.	196

LIST OF ABBREVIATIONS

2D	Two-Dimensional
3D	Three-Dimensional
ADCIRC-2DDI	Advanced Circulation Model for Oceanic, Coastal, and Estuarine Waters, Two-Dimensional Depth-Integrated
Æ-ARC	Adjacent Element Area Ratio Criteria
AMT	Above Mean Terrain
ASPRS	American Society for Photogrammetry and Remote Sensing
CA	Cell Average
DEM	Digital Elevation Model
fGDB	File Geodatabase
GIWW	Gulf Intracoastal Waterway
GWCE	Generalized Wave Continuity Equation
IMU	Inertial Measuring Unit
LTEA	Localized Truncation Error Analysis
MEE	Mean Elevation Error
MOM	Maximum of Maximums
NDEP	National Digital Elevation Program
NED	National Elevation Dataset
NOAA	National Oceanic and Atmospheric Administration

NOS	National Ocean Service
NFWFMD	Northwest Florida Water Management District
NWS	National Weather Service
PDE	Partial Differential Equation
RMSE	Root Mean Square Error
SDE	Spatial Database Engine
SMS	Surface Water Modeling System
SWE	Shallow Water Equations
TB	Terrabyte
TDS	Terrain Dataset
UCF	University of Central Florida
USGS	United States Geological Survey
UTC	Coordinated Universal Time
WNAT	Western North Atlantic Tidal

CHAPTER 1: INTRODUCTION

Much of the U.S.'s population (51-percent) reside in coastal areas (within 80 km of the ocean or Great Lakes), which includes 13-percent of the total land area and 57-percent of the civilian income (Rappaport, 2003). In fact, the population in coastal regions is expected to increase by 27 million people between 1998 and 2015 (National Oceanic and Atmospheric Administration (NOAA), 1998). With more people migrating to low-lying coastal cities, much is at stake when flooding due to hurricane storm surge occurs, as witnessed in 2005 by Hurricane Katrina, and more recently in 2011, by Hurricane Irene. A better understanding of hurricanes and the accompanying surge can help mitigate human and economic loss. With this in mind, advancements in sophisticated numerical modeling techniques have considerably advanced the planning and preparation process for these natural disasters.

Given that many models focus on the floodplain rather than exclusively on the aquatic environment, river reaches, barrier islands, and other large topographic gradients are typically described with high resolution (Bunya *et al.*, 2010; Salisbury *et al.*, 2011). The physical processes of areas becoming inundated and then dried (inundation process) further complicate the model when it expands beyond the immediate shoreline. Including proper shoreline and floodplain geometry is vital in simulating the inundation process. Using high resolution in the areas that may become wet during the incoming tide (astronomic or storm) can aid in proper description of the inundation process (Medeiros & Hagen, 2011). To this end, a balance of

accuracy (topographically and hydrodynamically) and computational efficiency must be achieved (Salisbury *et al.*, 2011).

Advancements in automatic mesh generation, computing power, and high-resolution, high-accuracy topographic data have produced a new generation of large-domain unstructured meshes. Currently, state-of-the-art storm surge models regularly contain millions of nodes and are computed using high-performance computer clusters on the order of hundreds to thousands of processors (Dietrich *et al.*, 2012). Also, the spatial scale of topographic data is no longer an issue; most data collection is now composed and produced at finer scales than the mesh elements themselves (Bates *et al.*, 2003). One such source, LiDAR (Light Detection And Ranging), is now common for assigning model node elevations.

LiDAR, if processed correctly, can produce an almost exact replica of the ground surface with errors on the order of +/- 15-cm (Zandbergen, 2011) (These ground surface LiDAR points are referred to as *bare earth* points). Concurrently, the increase in computer power permits model domain size to increase along with finer discretizations in both space and time. Decreasing element size presents an opportunity to enhance the description of the topography. Combining a better image of the land surface with smaller spatial discretizations raises the need to understand how different element sizes can affect topographic and hydrodynamic accuracy. For the purpose of this thesis it is postulated that the size of the element affects the accuracy of the ground surface as represented by the model and the simulated water levels and currents, and that the method used to resample the bare earth LiDAR onto the model nodes can have an impact as well. The interpolation of bare earth LiDAR to the finite element mesh (FEM) nodes can be

just as important as mesh size. A non-sufficient interpolation scheme may increase the topographic error of the FEM, ultimately leading to inaccurate results.

Accurately representing the topography is crucial given that it's a significant contributor to flood hydraulics and inundation extent (Horrit & Bates, 2001). Improving the representation of the ground surface via bare earth LiDAR allows a better topographic representation permitting the natural inundation processes to occur. Sub-element size features such as roadbeds, levees, berms, creeks and valleys are fully described, representing the natural physics of the system. Raised features (i.e. roadbed) would naturally inhibit water flow while valleys would tend to promote it.

The source elevation data must be transformed to the FEM without losing relevant information that may alter the natural physics of water flow. Recent advancements in state-of-the-art storm surge models coupled with improvements in remote sensing techniques and processing have enabled the progression of physically based numerical models. Since LiDAR data are at higher resolution than the mesh elements, sophisticated techniques have been developed to improve topographic representation in the model. However, much remains unanswered about the effect on topographic and hydrodynamic accuracy with respect to mesh element size and interpolation routines used to resample the source LiDAR, or LiDAR-derived DEM (Digital Elevation Model), to the individual mesh nodes. This thesis uses the advancements in computer power and high-resolution LiDAR data to gain an understanding of how interpolation of elevation data to a FEM effects overall global topographic error and its affect on simulated storm tide.

While airborne LiDAR presents the opportunity to capture an image of the ground surface, applying a proper mesh element size and interpolation scheme is vital to resample the elevation from its source data to the FEM without losing any significant information that could affect flow dynamics. To investigate this further, six major research objectives are undertaken:

1. Develop and test a method for determining topographic error in coastal Mississippi. The topographic error is tested for different DEM grid sizes as well as different FEM resolution coupled with changes in the source elevation (bare earth LiDAR, 5m DEM and 10m DEM).
2. Develop a water-only (in-bank) FEM of the Pascagoula River Mississippi and incorporate the Western North Atlantic Tidal (WNAT) model domain such that astronomic tides can be accurately modeled using a large-domain approach.
3. Apply the methods from step 1 to three large-scale regions of coastal Pascagoula, Mississippi.
4. Develop a high-resolution DEM of the coastal floodplain of Mississippi based on the findings from step 3.
5. Generate a FEM with varying resolutions (160-m, 80-m, 40-m, and 20-m) of the coastal floodplain and merge it with the in-bank model.
6. Simulate astronomic tides, winds and pressures from Hurricane Katrina for all three finite element meshes using the ADCIRC-2DDI (Advanced Circulation Model for Oceanic, Coastal, and Estuarine Waters, Two-Dimensional Depth-Integrated) numerical code.

This research will result in an understanding of how interpolation methods, DEM grid size, and mesh element size influence topographic and hydrodynamic error resulting from astronomic

tides and hurricane storm surge for the Pascagoula River. The methodology and analysis presented in the following thesis is not limited to southern Mississippi and can be applied to any coastal region in the world.

CHAPTER 2: LITERATURE REVIEW

This chapter presents a literature review on five main topics: 1) large domain storm surge modeling; 2) an introduction to DEMs; 3) interpolation and grid size error in digital elevation model development; 4) LiDAR in coastal hydrodynamic finite element models; and 5) an introduction to storm surge generation.

2.1 Large Domain Storm Surge Modeling

Numerical models used for flood inundation studies solve a set of governing equations; typically a form of the Navier-Stokes equations, in many cases, the shallow water equations (SWE). The SWE are a set of non-linear partial differential equations (PDE) that include continuity (conservation of mass) and momentum. In order to solve the SWE, the PDE must be reformulated to algebraic expressions, resulting in discretization for space and time. The discretized SWE are solved iteratively via a computer code to compute unknown values, water levels and velocities, for every time step at each computational point (node) in the model domain. Improved algorithms and computer technology allow the size of the model area to span an entire meteorological event (i.e., hurricane or tropical cyclone), capturing the full extent of the dominant physics and water level responses therein.

Significant hurricane dynamics occur at great spatial scales along the hurricane track as it moves from the deep ocean onto the continental shelf and into the coastal floodplain (Roberts, 2004). Therefore it is important to understand the physical processes that occur across the area affected by the storm. Research in two-dimensional (2D) storm surge numerical modeling has

demonstrated that domain size can drastically influence numerical results, with large domains yielding more accurate physics (Blain *et al.*, 1994). Model domains that strictly encompass the continental shelf or the size of the storm itself neglect the basin-to-shelf dynamics and severely under-predict the water levels' response to storm surge (Blain *et al.*, 1994; Westerink *et al.*, 2004). With a large domain approach, boundary conditions reside in the deep ocean and are far removed from the more complex processes occurring on the continental shelf and floodplain. The storms natural propagation onto the continental shelf and other significant physics are thus captured without any boundary influence. Further, small scale dynamics in the shallow regions are important and must be captured for accurate results (Blain *et al.*, 1994; Westerink *et al.*, 2004; Dietrich *et al.*, 2011; Kennedy *et al.*, 2011). Early 2D storm surge models employed coarse structured grids wherein the model was discretized at regularly spaced intervals. This method tends to under-resolve the continental shelf and shallow waters leading to overprediction errors and overpredicted peak surge at the coast. To this end, grid resolution near the coastline is the most significant feature in the accuracy of storm surge prediction. In addition, predicted surge can be a function of the complexity of the shoreline itself (Blain *et al.*, 1998). With this in mind, another method is needed since structured grids are limited in the description of the intricate geometry of the coastline. Enabling an unstructured mesh approach (i.e. element sizes are non-uniform and vary spatially) can resolve this shortcoming (Westerink *et al.*, 2004).

Understanding the benefits of a large domain approach with spatially varying discretization (i.e., unstructured mesh) has lead to a new generation of storm surge models. The use of unstructured finite element meshes has proven superior to other techniques in capturing small scale dynamics across a large model domain, allowing mesh resolution to vary with respect

to the hydrodynamics on a spatial scale. Due to the nature of unstructured grids, the location of mesh nodes can be precisely placed allowing for a computationally efficient and robust mesh. Larger elements are placed in the deep ocean where the effects of small scale dynamics are less important and smaller elements are placed in locations where small scale dynamics must be captured to ensure accurate results (Hagen *et al.*, 2000; Hagen, 2001; Hagen *et al.*, 2001; Hagen & Parrish, 2004; Hagen *et al.*, 2006). This large domain, unstructured mesh approach permits a description of the natural physics of storm surge as it circulates from the deep ocean to the continental shelf and onto the coastal floodplain (Figure 1) (Roberts, 2004; Westerink *et al.*, 2004; Dietrich *et al.*, 2011).

Another advantage of the large domain, unstructured mesh approach is to apply finer mesh resolution in areas of interest, rather than just in the regions where high resolution is important to capture the essential physics. Many features that exhibit high topographic gradients such as river reaches, barrier islands, roadways, and levees are typically described with high resolution. These features, especially in the floodplain, can alter simulated water levels and inundation extent from hurricane storm surge. Therefore they must be properly described in the model, as they are on the natural ground surface. LiDAR and high DEMs present an opportunity to better include the natural ground surface in storm surge models.

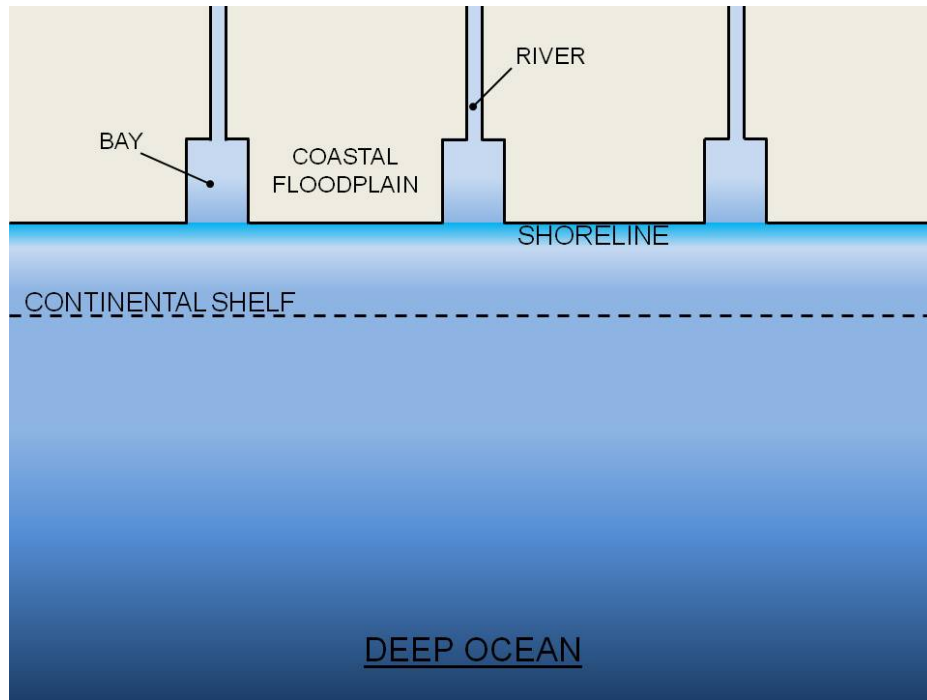


Figure 1 Large model domain approach encompassing the deep ocean, continental shelf, shoreline, and coastal floodplain.

2.2 Digital Elevation Models

Spanning the past decade, much advancement has been made in DEM development mainly due to the availability of high-resolution, high accuracy topographic data. In hydraulic models, the topography is an essential factor that can influence simulated flood hydraulics and inundation extent (Horrit & Bates, 2001). It is crucial the floodplain be accurately represented since the topographic elevation is the first feature that can promote or inhibit water flow (Coggin, 2011). Past modeling techniques have been limited by the spatial resolution of topographic data resulting in finer resolution for the mesh elements than the available topographic information (Bates *et al.*, 2003). Thanks to developments in remote sensing, high accurate, high density topographic data can be obtained using LiDAR (Samburg, 1997). LiDAR provides an approach

to incorporate high-resolution 3D point cloud data into a high-quality DEM (Lohr, 1998; Wehr & Lohr, 1999; Lefsky *et al.*, 2002; Lloyd & Atkinson, 2006; Liu *et al.*, 2007a, 2007b; Coggin, 2011; Medeiros *et al.*, 2011). For a detailed description of LiDAR acquisition systems, see Coggin (2008).

Generally speaking, a DEM is a term for digital elevation data, either topographic or bathymetric. Further, a DEM implies only the elevation of the terrain (bare earth), excluding elevation of vegetation and manmade features. A DSM (digital surface model) is a DEM including vegetation and manmade features (Maune, 2007). Several filtering techniques are well documented for removing non-bare earth points (Fritsch & Kilian, 1994; Eckstein & Munkelt, 1995; Lohmann & Hug, 1998; Axelsson, 1999; Liu, 2008). For the study presented herein, a DEM is defined as bare earth elevations (z-values) at regularly spaced intervals in x (Eastings) and y (Northings), referenced to a vertical and horizontal datum (Maune, 2007; Shi, 2010). DEMs are widely used for a variety of environmental applications including hydraulic, hydrologic and hydrodynamic modeling (Kenward *et al.*, 2000; Darboux *et al.*, 2002; Chaplot *et al.*, 2006; Hagen *et al.*, 2009; Bunya *et al.*, 2010; Bilskie *et al.*, 2011).

Since a DEM is an approximation of the natural surface of the earth, a difference exists between the surface of the earth and the surface represented by a DEM. This difference is DEM error (Shi, 2010). Many factors can affect the quality and accuracy of DEMs including source data density, terrain, and land cover type. Furthermore, the applied interpolation method and grid size (Δx and Δy), can strengthen or weaken the quality of a DEM from its original source data. This is mainly due to the discontinuous representation of a continuous surface and smoothing of the original source data (Desmet, 1997; Gong *et al.*, 2000; Schoorl *et al.*, 2000; Ali,

2004; Li *et al.*, 2005; Anderson *et al.*, 2006; Fisher & Tate, 2006; Liu, 2008; Bater & Coops, 2009).

2.2.1 Interpolation Error

Interpolation of irregularly spaced points is needed to generate DEMs to provide better representation of the land surface (Lloyd & Atkinson, 2002; Anderson *et al.*, 2005). Interpolation is the procedure to estimate values at unknown locations based on values at sampled locations (Ali, 2004). In digital terrain modeling, interpolation is used to estimate terrain elevations at a point in space by using the known elevation and location of neighboring points. This is fundamental to digital terrain modeling (Li *et al.*, 2005; Maune, 2007). Much has been published in regard to interpolation error on DEM accuracy; however, differing opinions exist in the literature for the best interpolation algorithm: spline (Kubik & Botman, 1976); kriging (Lloyd & Atkinson, 2002; Chaplot *et al.*, 2006); natural neighbor (Bater & Coops, 2009); and inverse distance schemes (Ali, 2004; Anderson *et al.*, 2005; Su & Borke, 2006). Furthermore, there is an absence in the literature on interpolation of point data to a FEM for use in shallow water hydrodynamic model.

Kubik and Botman (1976) stated that accuracy of the interpolation is largely dependent on the properties of the surface, the density and spacing of control points, and on the interpolating function itself. They constructed several DEMs based on a suite of interpolation methods from irregularly spaced sample points and evaluated their precision and shape reliability. Generally, shape reliability issues are those in which artificial troughs or peaks are present after interpolation of points to a gridded dataset. The spline interpolator produced the best results with respect to both precision and shape reliability.

Chaplot *et al.* (2006) evaluated the effect of landform types, density of observational data and interpolation techniques on DEM accuracy. The source data were contour lines and field surveys obtained by a laser theodolite. Five interpolation techniques, commonly used in geomorphological research, were studied producing a DEM in a mountainous region including inverse distance weighted (IDW), ordinary kriging (OK), universal kriging, multiquadratic radial basis function, and regularized spline with tension (RST) (Weber & Englund, 1994; Longley *et al.*, 1999; Zimmerman *et al.*, 1999; Aguilar *et al.*, 2005). When the sampling density was high, minor differences were observed between the interpolation techniques; however, when the sampling density was low, the interpolation technique had a higher impact on the resulting DEM. The kriging method produced the best results if high elevations were dominant, but when the spatial structure was weak, IDW and RST performed best.

Lloyd (2002) employed IDW, OK, and kriging with a trend model (KT) to an area of smoothly varying hillslope topography to create a digital surface model (DSM) from LiDAR data. It was found that IDW produced the largest error, but resulted in a lower standard deviation than the other interpolators. When the point densities were low, OK and KT provided the most accurate predictions compared to the other methods, but no advantage existed when the point densities were high.

Ali (2004) studied the effect of IDW, kriging, and a triangular irregular network (TIN) from picking candidate points from the VIP (very important point) algorithm using LiDAR. It was found that IDI results were comparable to the triangulation model; however, the TIN produced the most accurate results in terms of random error where only single locations were considered. Also, IDI produced more realistic and accurate cross-section profiles compared to

the other interpolation functions. Ali determined that this is due to the nature of the high-density LiDAR, which is a suboptimal input for a kriging interpolation scheme. He concludes that triangulation produces the best results at single locations; however, it does not produce the best profiles. Further, he concludes kriging should not be used to generate terrain models based on LiDAR.

Anderson *et al.* (2005) found that IDW is the most sufficient interpolating function for creating a DEM from irregularly spaced LiDAR data by way of assessing mean error and root mean square error. Not only was IDW found to produce minimal error, compared to OK, but IDW was computationally more efficient.

Su *et al.* (2006) examined the performance of three interpolation techniques (spline, IDW, and kriging) on the generation of a DEM from high-density LiDAR (~ 0.75 points/m²) in a region of rolling hills. They employed a root mean square error (RMSE) approach and found the IDW interpolation method was the simplest and most accurate for DEM creation. However, Su *et al.* (2006) also stated the accuracy of the DEM varied across the landscape with greater errors in areas of forest and lowland meadows than that of shrublands or grasslands. This was a result of LiDAR not fully penetrating the ground in areas of thick canopy and vegetation. Also, the accuracy was weakened as the slope of the terrain increased. The overall LiDAR-derived DEM had a mean error (ME) of 2 cm and RMSE of 59 cm, from that of reference points.

Bater *et al.* (2009) examined seven interpolation routines (linear, quintic, natural neighbor (NN), spline with tension, regularized spline, IDW, and ANUDEM) to determine the most accurate combination of interpolator and spatial resolution for DEM generation as well as the effects of LiDAR ground point density, slope, canopy cover, and vegetation structure on

interpolation errors. The linear, quintic, and NN techniques used a TIN as its base and the others were interpolated from the raw points themselves. The techniques were assessed by creating a DEM for each interpolator at resolutions of 0.5-m, 1-m and 1.5-m. The DEMs were produced by randomly selecting 97-percent of the LiDAR points. The remaining 3-percent were used to compute the accuracy of each DEM. Accuracies of IDW and spline were found to be sensitive to their parameterization, producing ± 6 -m outliers. IDW interpolated surfaces showed artifacts that would have serious impacts on geomorphic analysis. Ultimately, the linear and NN methods were found to have the lowest overall error and were the most conservative. Of these two, linear was too simplistic, whereas natural neighbor was preferred for its performance and characteristics, such as its ease of use, simple parameterization, and generally smooth and visually attractive surface. Also, the results indicated that the spatial resolution is just as important as the interpolation scheme.

At this point it is clear that no interpolation scheme is universally sufficient for producing a DEM from its source data, whether the source data is contour lines, field survey points, or high-density LiDAR (Fisher & Tate, 2006; Liu, 2008). However, Liu *et al.* (2007b) showed the IDW method performs well for high sampling density LiDAR, even for complex terrain. Still, this disagrees with both Lloyd *et al.* (2002) and Bater *et al.* (2009). Also, all studies presented are not focused on the application of modeling shallow water flow, in particular with the use of a FEM.

2.2.2 DEM Grid Size

“Determination of a DEM grid size is the central problem for DEM generation and spatial analysis” (p. 40) (Liu, 2008).

When interpolating irregularly spaced points, it is common to produce a DEM at regularly spaced intervals. These regularly spaced cells are called DEM grid cells, where the value of the cell represents the surface, a numeric value of elevation, across the entire cell area (Figure 2) (Maune, 2007). The resolution of the DEM is that of the regular spacing interval between the grid cells center points, or the length of the grid cell itself, Δx and Δy ; typically, $\Delta x = \Delta y$. In terrain modeling, it is important to synchronize three key concerns: 1) a DEM grid size that well represents the land surface; 2) large enough resolution to allow efficient data storage; and 3) maintain a particular level of accuracy (Gao, 1997). It is intuitive that as the DEM grid size becomes coarser, i.e., decreases in resolution, the terrain representation becomes degraded, and vice versa (Kienzle, 2004). Typically, DEM resolution should not be higher than that of the source data (Florinsky, 1998); however, using a dense terrain dataset to develop a coarse resolution DEM will reduce the integrity of the high-resolution source data (Liu, 2008). Liu (2008) states that an appropriate DEM resolution can be a function of many items including source data density, complexity of the surface, and the application. Several attempts have been made in determining the best possible DEM size from the source data.

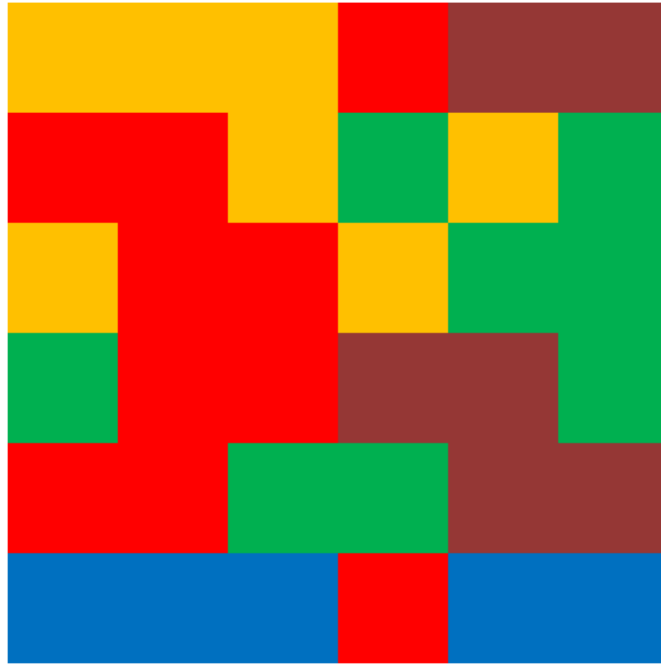


Figure 2 Raster DEM with regularly spaced grid cells in the x- and y-directions

Kienzle (2004) generated DEMs from sparse elevation points and found that terrain variables differ appreciably with DEM grid size. Depending on the parameter of interest, cell sizes varying from 5-m to 20-m should be used. However, shallow water flow was not the particular application for this study. Hengl (2006) linked terrain grid resolution with that of digital signal processing since construction of a DEM is equivalent to discretizing a 2D function of the terrain. According to the Shannon-Nyquist sampling theorem (Shannon, 1949), a continuous function can be reconstructed from a discrete function (sampled data) if the sampling rate exceeds two times the maximum frequency. In other words, if two samples per the shortest wavelength are collected, then the continuous function can be recomposed from the set of sampled data (Florinsky, 2002). Using this rule, Hengl states the cell resolution, at a minimum, along a cross-section, should be half of the average spacing between inflection points:

$$p \leq \frac{l}{2 \bullet n(\delta z)} \quad 2.1$$

Where p is the points spacing, l = length of cross-section transect, and $n(\delta z)$ = number of inflection points measured. Hengl gives an example of 20 measured points with an average spacing of 0.8-m. Equation 2.1 yields a grid size of at least 0.4-m; however, the smallest distance found between any two points, among all points, should be the smallest grid resolution used. Figure 3 shows a plot of a continuous surface and measurements taken at random distance intervals along the same surface. In this instance, the continuous surface represents the bare-earth terrain, where an infinite amount of measurements can theoretically be taken. Figure 4 demonstrates a low resolution (20-m) DEM insufficiently describing the surface. Producing a low resolution DEM from high density source data lessens the accuracy of the data (Liu *et al.*, 2008), whereas a decrease in DEM size (5-m, Figure 5) better represents the terrain. Using the rule put forth by Hengl (Eq. 2.1) a transect with average horizontal spacing of measured points equaling 5-m (Figure 6), a DEM size of 2.5-m is recommended. However, this rule does not take into account the relative size of the DEM datasets. Others have stated that DEM resolution should be no less than that of the original source data density (McCullagh, 1988; Florinsky, 1998, 2002; Liu *et al.*, 2008):

$$GS = \sqrt{\frac{A}{N}} \quad 2.2$$

where GS = grid size; A = total area containing the measured points; and N = total number of measured points. Therefore, an optimal grid size for DEM development should be a function of both computational efficiency and accuracy (Hengl, 2006).

Further exploration of this topic can lead into studies of LiDAR data density reduction and its result on DEM accuracy. Essentially, when generating a DEM from a set of mass points (i.e. bare earth LiDAR), the mass point data is being reduced, or resampled, to fit a regular grid. This research area aims to determine how LiDAR data can be reduced while still providing sufficient accuracy for DEM generation, resulting in more efficient DEM generation due to the reduction of the mass point data (Anderson *et al.*, 2005). Liu (2007a) extracted 90-percent of the bare earth LiDAR points for training data and 10-percent for check points in the region of Corangamite Catchment Management Authority in southwestern Victoria, Australia. They reduced the training data down from 100-percent to 1-percent at several intervals and generated 5-m DEMs based on the reduced datasets. It was found that reducing the training dataset from 100-percent to 50-percent resulted in an RMSE increase of 1-cm, when compared to the check points. The data density from the 50-percent reduced dataset was roughly equivalent to 5-m, the size of the DEM. Liu proved that the accuracy of the DEM can be preserved while reducing the data density by half.

It can be concluded that an optimal combination of the two main parameters in DEM generation, interpolation scheme and grid size, is not consistent in published literature or in practice.

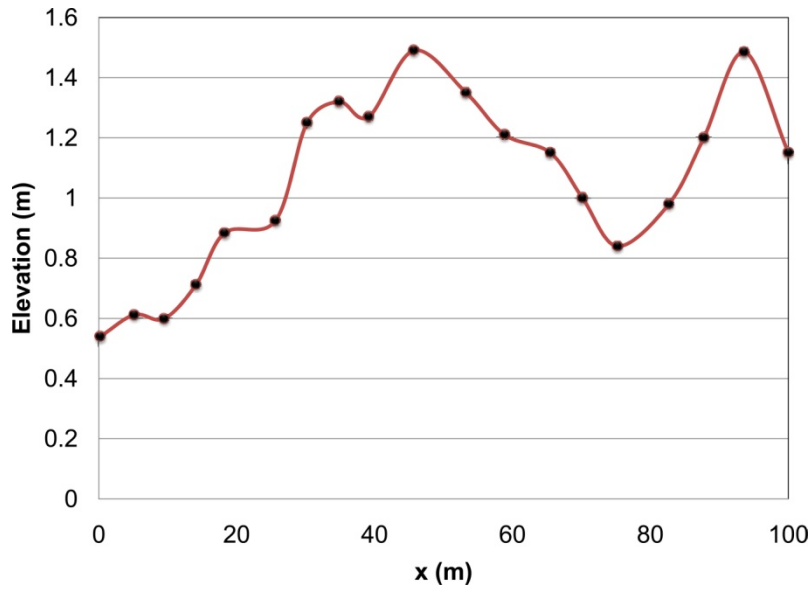


Figure 3 Plot depicting a set of measured elevation points along a transect (Hengl, 2006). The red line indicates the continuous surface representation and the black circles represent the measured values (Hengl, 2006).

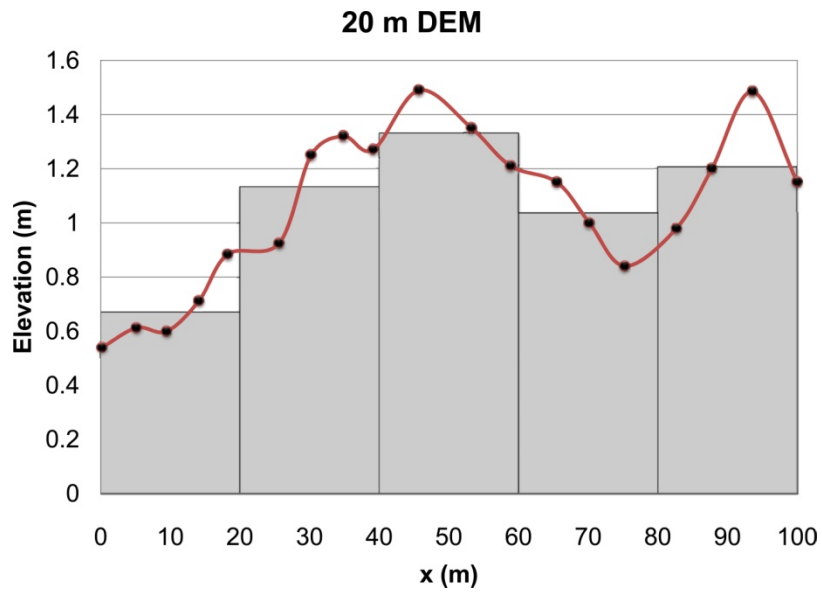


Figure 4 Plot with the continuous surface in red, measurements in black, and a 20-m DEM grid representation of the continuous surface (Hengl, 2006).

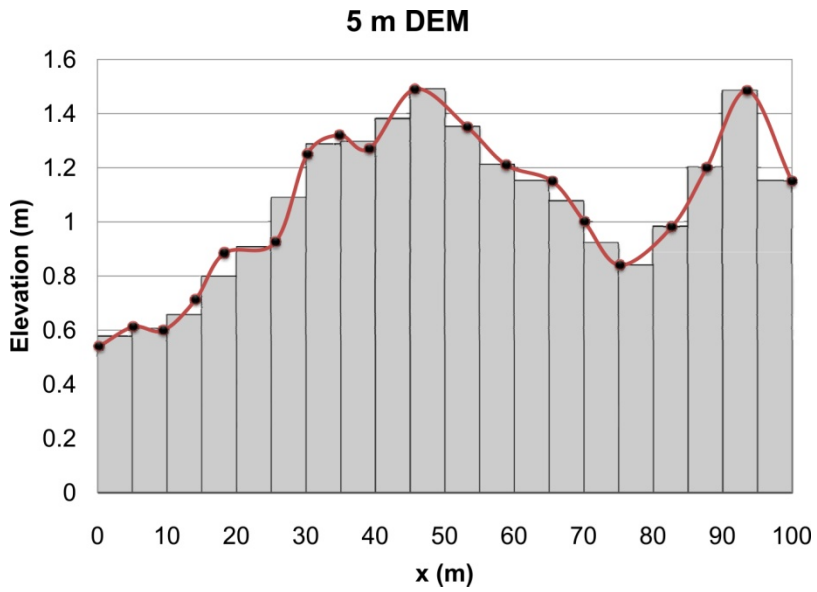


Figure 5 Plot with the continuous surface in red, measurements in black, and a 5-m DEM grid representation of the continuous surface (Hengl, 2006).

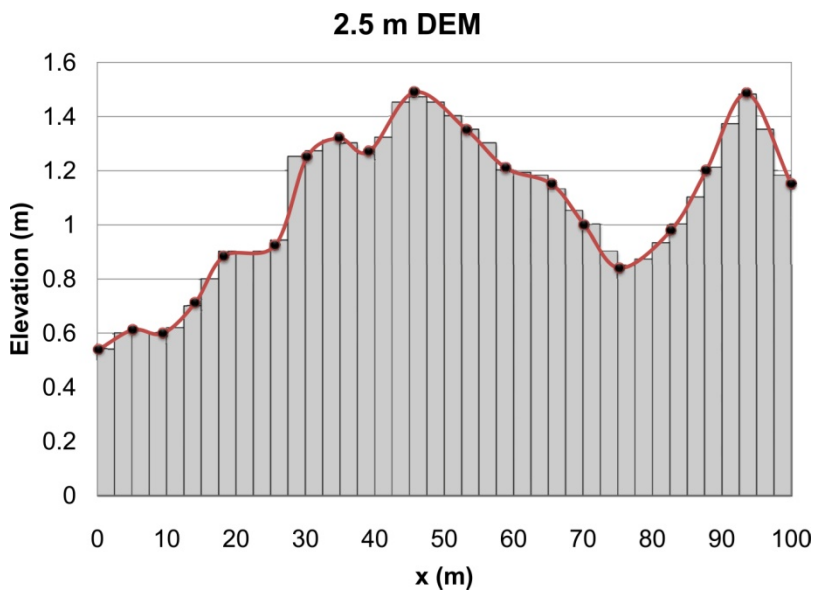


Figure 6 Plot with the continuous surface in red, measurements in black, and a 2.5-m DEM grid representation of the continuous surface (Hengl, 2006).

2.3 LiDAR in Coastal Hydrodynamic Finite Element Models

The following is a review of research that has used LiDAR in coastal finite element hydrodynamic models.

As presented, much research has been published in terms of LiDAR DEMs and the effect interpolation, DEM grid size, and LiDAR point density have on topographic accuracy. However, few studies focus on the transfer of bare earth LiDAR points or LiDAR DEMs to a FEM. The general concept of interpolation can still be applied; however, the data structures are severely different. The distinction being a DEM is at a regularly spaced interval (square cells) and an unstructured FEM is not (non-uniform triangulated network). Efficient and accurate interpolation from points, either uniform (DEM) or non-uniform (raw bare earth), to a FEM is not a trivial task. Geospatial programs such as ArcGIS (ESRI, 2011a) and Global Mapper (Blue Marble Geographics, 2011) are more suited to work with raster products. Also, the density of nodal points (directly relates to element size) in the FEM plays a role in the method chosen for a node to obtain its elevation from bare earth LiDAR points or a LiDAR-derived DEM. Recent studies have employed methods to incorporate bare earth LiDAR in a FEM for astronomic tides and storm surge simulations. They primarily focused on incorporating significant raised features (i.e. raised roadway, levee, and channel banks) found from the bare earth LiDAR into the FEM.

Roberts (2004) enhanced a FEM for use in a tide and storm surge model of southeastern Louisiana. His main focus was advancing an existing mesh of the area (S08 ADCIRC mesh) to accurately include channels, rivers, levees, and raised roadways by resolving the features in the mesh (i.e. higher resolution) and using precise elevation data from bare earth LiDAR to assign nodal elevations. He developed a method to scan a 5-m DEM generated from the bare earth

points to filter out important raised features. The points had to meet specific requirements in order to be classified as significant features that could alter the flow physics if not correctly incorporated into the model. The requirements outlined were as follows:

1. A given point must have a minimum height of 1.9-m above the elevation of the lowest point around a 60-m by 60-m area.
2. The point must be 1-m above the average elevation of the surrounding points in the area.
3. A minimum slope of 0.086-m/m between the center node and another node in the 60-m by 60 m-region.
4. A minimum slope of 0.040-m/m in the opposite direction of the maximum slope.

Requirements three and four were to limit channel banks because the topography in the channel would reduce the average topographic elevation for a region in which a data point would meet the first two requirements. In other words, elevation values in the channel would significantly alter the average elevation for an area for a given point near the channel, allowing requirements one and two to hold when the point is not a significant raised feature.

After performing labor intensive manual edits to the raised features, the floodplain was discretized (or “meshed”) using a triangular paving method with the significant features being polygon edges. Nodal density varied throughout the domain with high resolution in the adjacent floodplain. Element size was controlled to sufficiently represent high gradients in flow as surge inundates the floodplain. Paving was done via sub-meshes and additional arcs were created in order to apply a smooth transition of element sizes (Figure 7).

After the FEM was constructed, mesh nodes received elevations from the 5-m DEM via interpolation. Roberts decided against direct interpolation, seeing as it would use just over one

half of one percent of the available LiDAR available. Also, direct interpolation would result in missing gradients over element edge lengths, especially for large elements that may space up to 1 km in element edge length. Therefore he developed a grid-scale averaging scheme to incorporate data points that surround an individual mesh node, rather than using the closest data point. The total number of topographic data points for each element as well as the elevation of each point was found. The average of all points was computed and assigned to each element. Nodal elevations were determined by averaging the elevations of the surrounding elements about each node (Roberts, 2004).

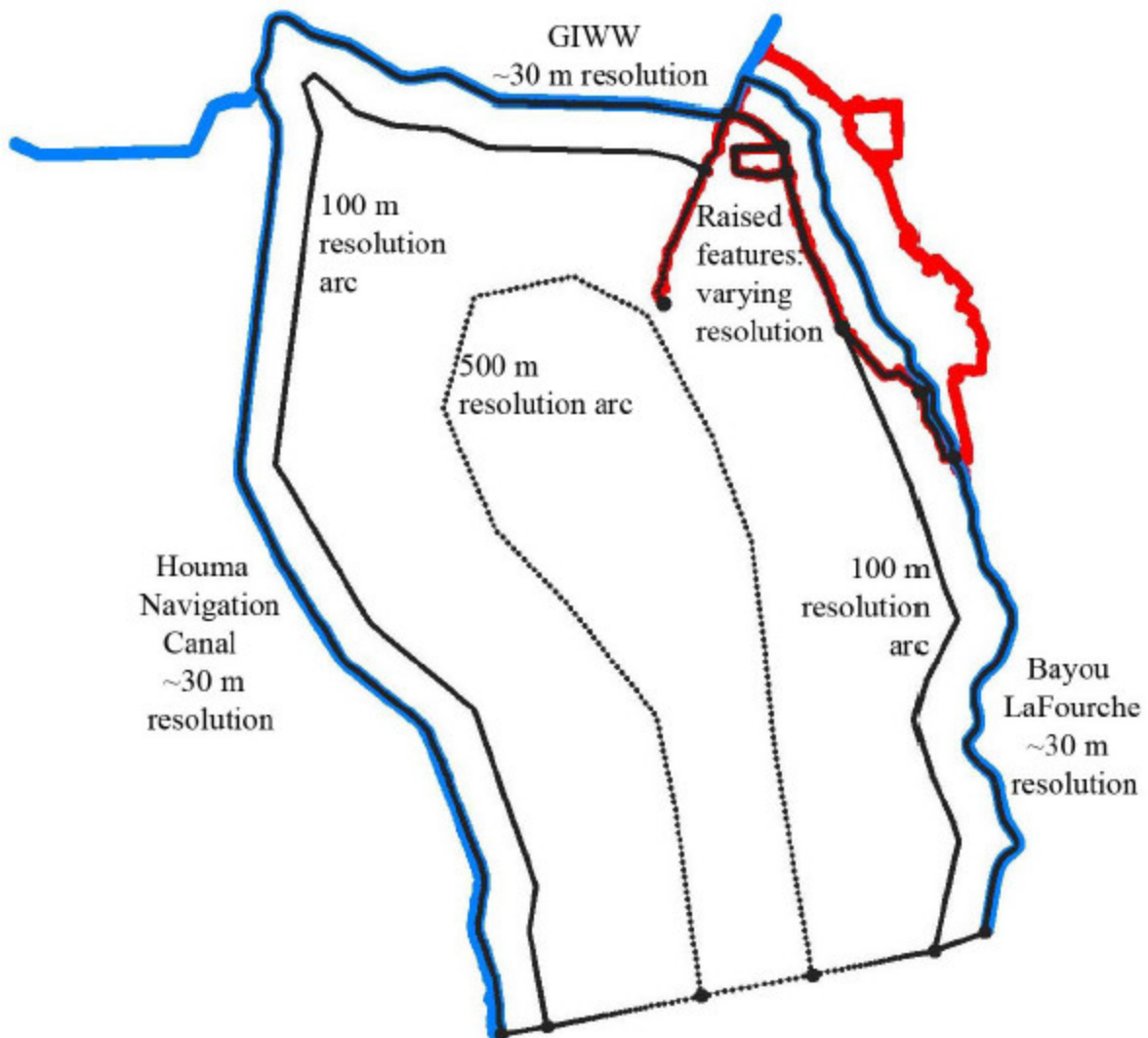


Figure 7 Arc placement for mesh generation. Blue lines represent the sub mesh region and red lines represent the raised features. Black lines represent arc within SMS. Published with authors' permission. (Roberts, 2004)

Coggin (2008) enhanced the work of Roberts (2004) by developing an automated method for extracting linear raised features from LiDAR data. He implemented a methodology to extract watershed boundaries and then analyzed those boundaries to determine which were significant to alter flow dynamics. The watershed boundaries were converted to lines and checked against the

following three criteria to determine which lines should be classified as significant topographic features (p. 72) (Coggin, 2008):

1. “High enough relative to surrounding terrain to form a hydraulically significant impediment to storm surge”
2. “Narrow enough that not purposely including the ridge as a finite element edge would risk significant mesh elevation error”
3. “Long enough to space at least one element edge”

The three requirements, performed for Manatee County, FL, resulted in a set of line segments (Figure 8).

Coggin then constructed two FEMs for use in the ADCIRC-2DDI model (Luettich *et al.*, 1992). One mesh included the vertical features as element edges (Figure 9) and the other mesh had similar triangulation, but did not include vertical features as element edges. To interpolate the source data, generally LiDAR, to a mesh node, a control area polygon was constructed. This polygon was formed by connecting all centers of the surrounding elements. All LiDAR points within this control area were averaged and assigned to the mesh node (Figure 10). When forced with a synthetic hurricane, it was found that a considerable difference in total inundation area existed between the two meshes, especially around the roadways. Coggin found it important to properly include the bare earth topography, especially significant raised features, in the model.

Coggin’s vertical feature method has since been enhanced by the addition of valley features and it’s currently used in FEM generation for coastal storm surge studies in support of development of digital flood insurance rate maps (DFIRM) for FEMA (Coggin, 2011; Salisbury *et al.*, 2011).

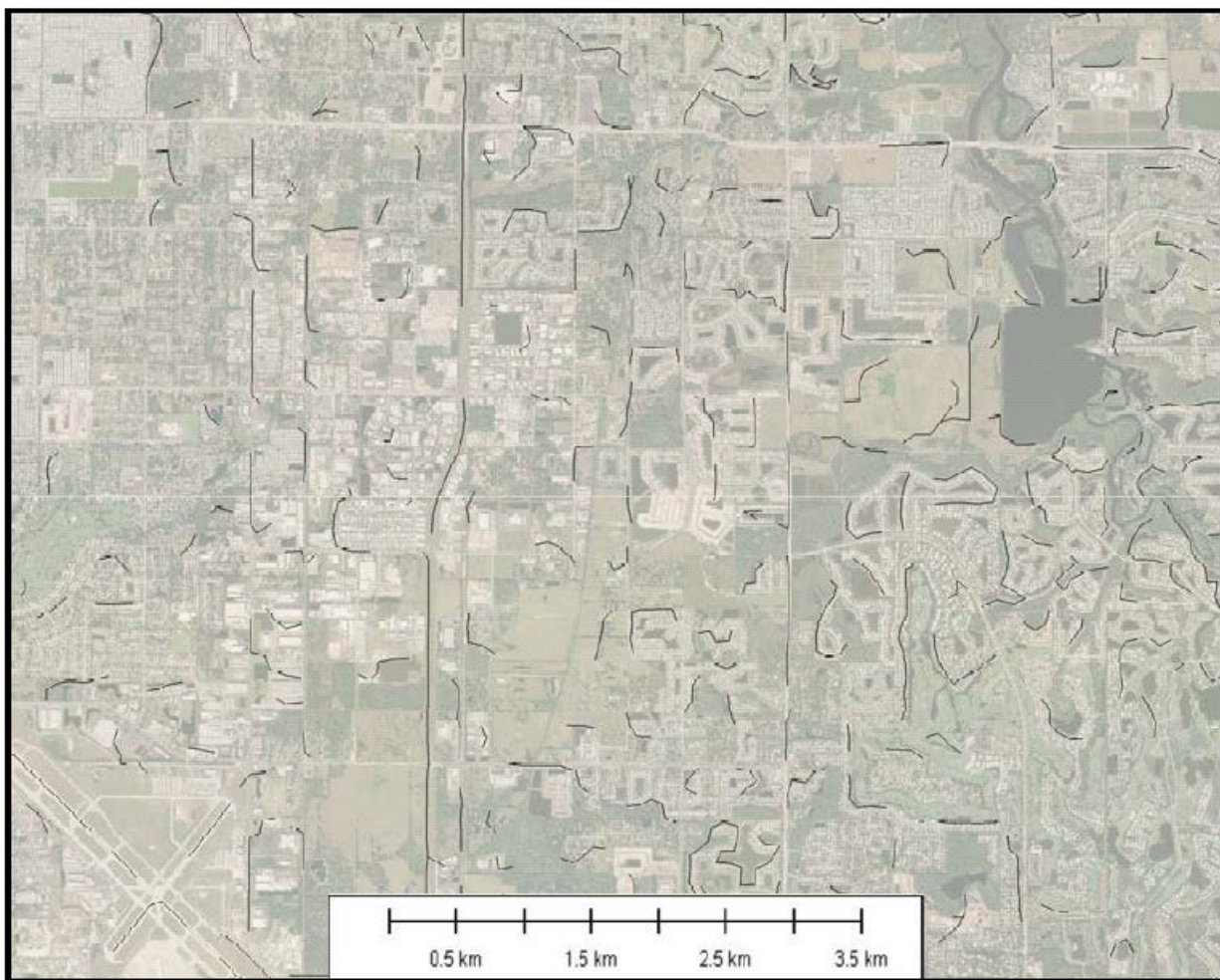


Figure 8 Final product of vertical features (black lines). Published with authors' permission. (Coggin, 2008)

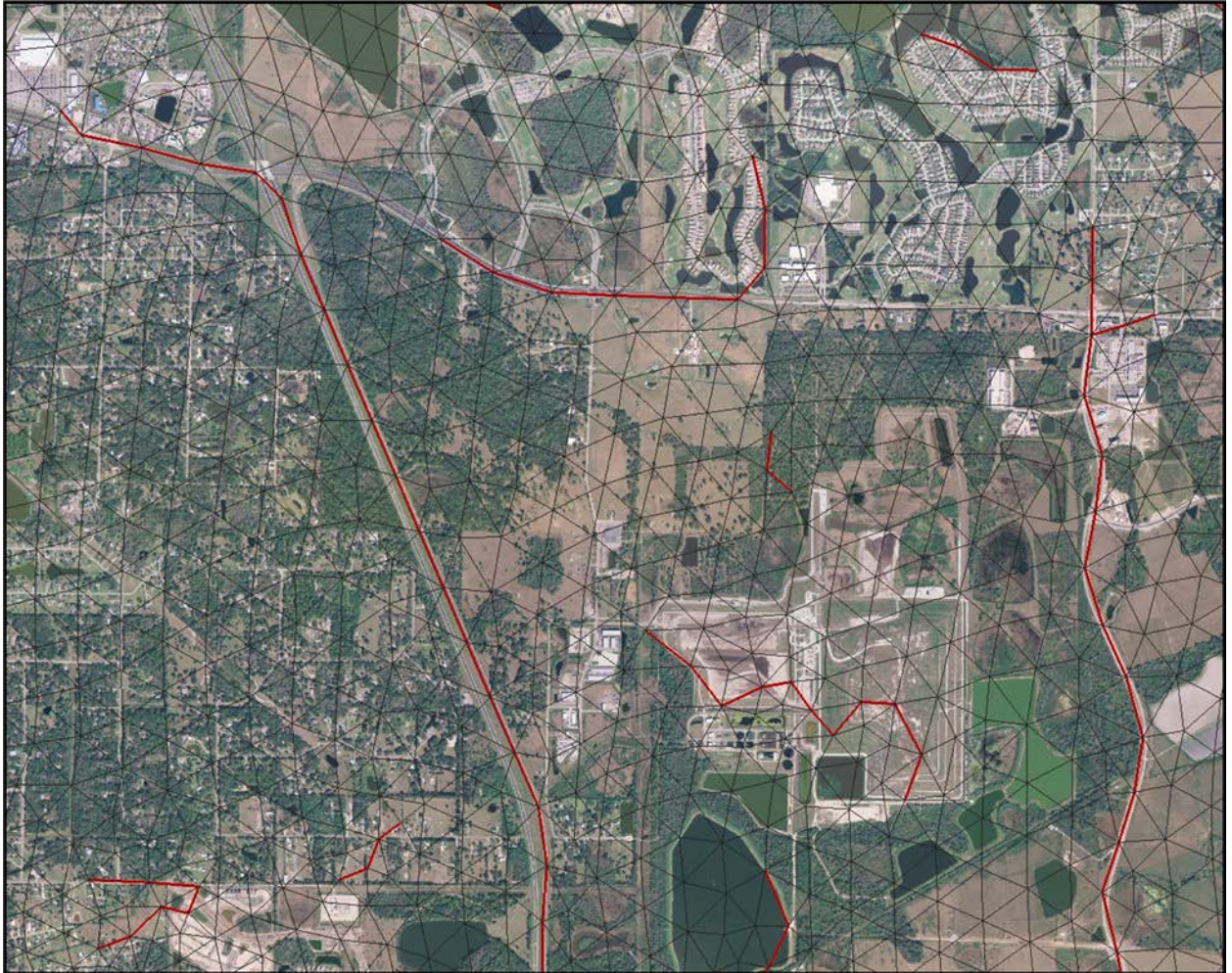


Figure 9 Aerial image with vertical features in red and finite element mesh triangulation in black. Published with authors' permission. (Coggin, 2008)

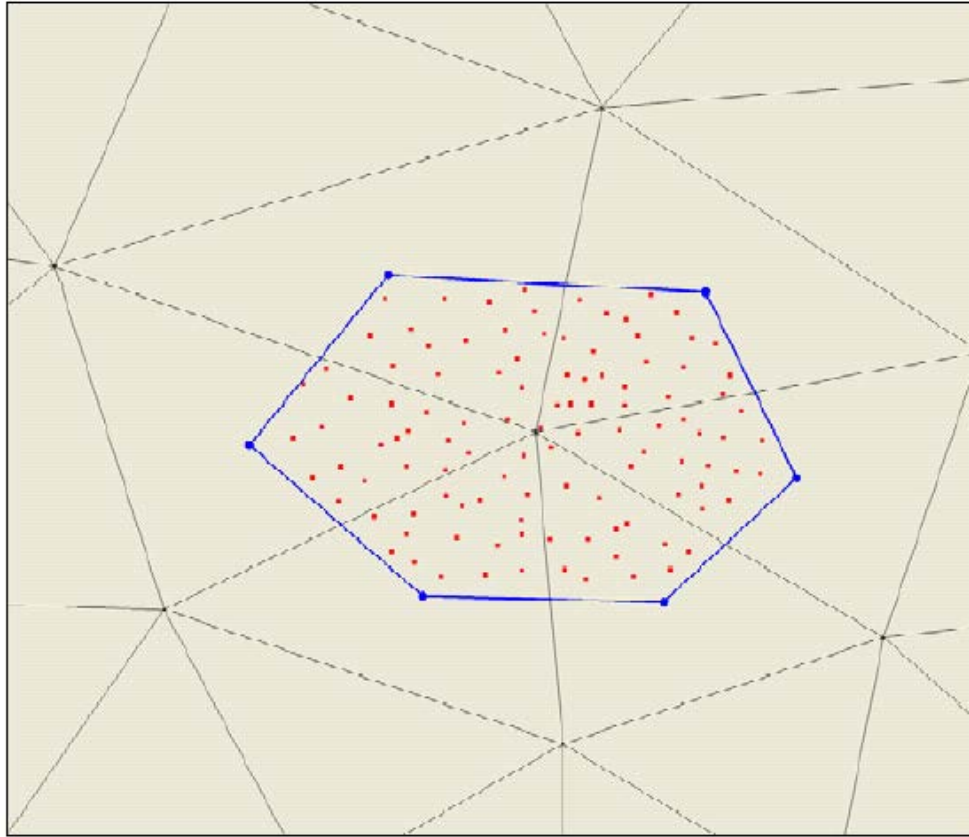


Figure 10 Interpolation of nodal point via polygon control area for LiDAR data. Published with authors' permission. (Coggin, 2008)

Atkinson (2007) developed an interpolation method similar to that of Coggin (2008) in which the centroids of the surrounding elements of a given node were used to create a control volume. As Coggin employed a control area bounded by and including all centroids of the surrounding elements (Figure 10), Atkinson used a rectangle as the control volume, with its minimum and maximum x- and y-directions found from the centroids (Figure 11). However, Atkinson's method was not constructed for elevation value interpolation from a DEM raster to a FEM, but from a raster containing frictional characteristics (i.e. manning's n) to a FEM.

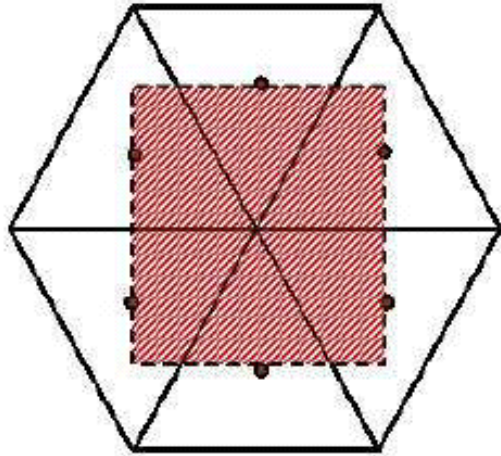


Figure 11 Interpolation of nodal points via rectangle control volume (Atkinson, 2007).

2.4 Introduction to Storm Surge

Among storm surge, wind, rain, and tornadoes, storm surge is the cause of over 90-percent of deaths due to hurricanes (Pielke, 1990). Storm surge is “an abnormal rise in sea level accompanying a hurricane or other intense storm, and whose height is the difference between the observed level of the sea surface and the level that would be occurred in the absence of the cyclone” (National Weather Service, 2009). The combined effect of storm surge and the astronomic tide results in storm tide (Figure 12).

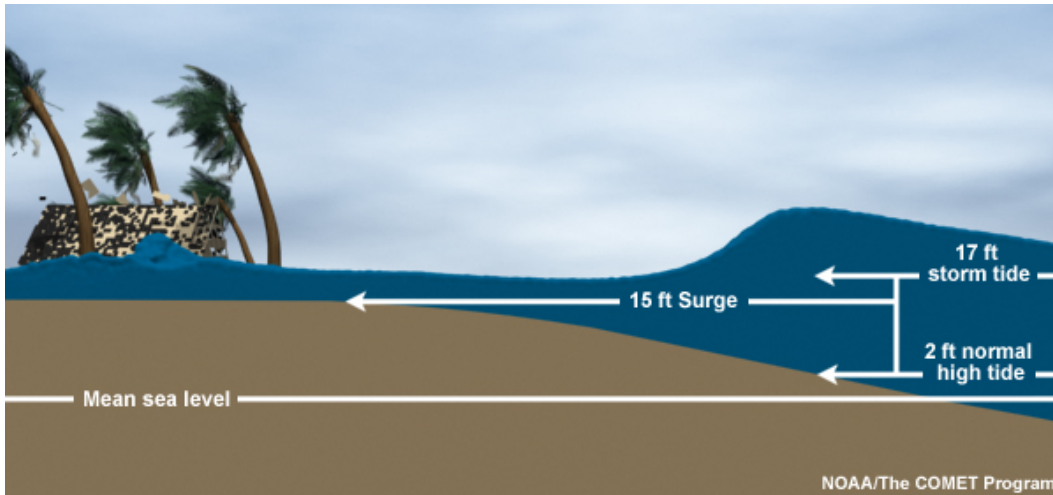


Figure 12 Image depicting the addition of the astronomical tide (2 ft) and storm surge (15 ft) to produce a storm tide of 17 ft (NOAA, 2010) above mean sea level.

Harris (1963) discussed the five main processes that accompany a storm. These include: 1) the pressure effect; 2) the direct wind effect; 3) the effect of the earth’s rotation (Coriolis force); 4) the effect of the waves; and 5) the rainfall effect. More specific to coastal flooding, Westerink *et al.* (2008) considers coastal flooding being “driven by wind, atmospheric pressure gradients, tides, river flow, short-crested wind waves, and rainfall” (p. 834). In general, storm surge is made up of the following components at or along the shoreline: 1) wind-driven surge caused by a strong onshore wind; 2) inverted barometric effect; 3) geostrophic tilt, a result of alongshore current; and 4) setup from a short (wind induced) wave (Reid, 1990).

Wind, the main force behind storm surge, blowing over the ocean creates a frictional drag on the water. The relationship between wind speed and its drag on the water surface creates a wind stress represented by the empirical formula:

$$\tau_s = \rho C_D V_{10}^2 \quad 2.3$$

where τ_s is the wind stress, ρ is the density of water, C_D is a dimensionless friction coefficient and V_{10} is the wind speed measured in meters per second at ten meters above the water surface (Dean & Dalrymple, 2002; Powell *et al.*, 2003). Again, following continuity principles, as the depth of water decreases (e.g. continental shelf) the surge increases due to the mass of water being pushed from the deep water into the shallow regions. This can be observed in the following 1D equation in which the wind stress relates to the surface slope:

$$\frac{d\eta_w}{dx} = \frac{(\tau_s - \tau_b)}{\rho g (h + \eta_w)} \quad 2.4$$

where τ_b and η_w are the bottom shear stress and the water level increase, respectively (Dean & Dalrymple, 2002). Not only does the equation show that the greater the wind stress the greater the surface slope, but as the water column becomes shallower, the water surface slope becomes larger for the same surface stress. The ocean creates frictional drag for the wind, due to the shallow waters along the coastline, and results in the ocean piling up against the coastline. When a strong onshore wind is present, the wind attempts to push the ocean onto the land, thereby massing water landward for stretches of coastline. The forward motion of the hurricane also tends to increase the amount of water that accumulates (Dean & Dalrymple, 2002).

The effect of the changing coastal geometry, coastline shape and bathymetry, plays an important role in the generation of storm surge. Surge in the open ocean generally does not surpass 0.5-m, however in shallow waters, relative to the deep ocean, or in semi-enclosed seas, such as the Gulf of Mexico, storm surge can reach heights over several meters (Pore, 1965; Carter, 1988; Pielke, 1990). During a neap tide, storm surge is likely to increase due to

shallower depths, however the storm surge (storm tide minus astronomic tide) is higher when occurring along with a spring tide (Lennon, 1963; Carter, 1988).

When a hurricane gains intensity, its central pressure reduces causing the underlying water surface to rise. The pressure is lowest near the eye wall, resulting in a bulge of water at that location. On the other hand, the wind velocity is greatest near the eye wall producing an increase of wind shear (Figure 13). The relationship between water surface variation and pressure is a water surface rise of one centimeter for every one millibar drop in pressure; a pressure drop of 100 millibars will result in a water surface rise of one meter (Harris, 1963; Pielke, 1990).

The rotation of the earth affects the storm surge when the storm forces intense currents to flow in the alongshore direction (Dietsche *et al.*, 2007; Kennedy *et al.*, 2011). If a storm forces a current moving south along the east coast of the U.S., the Coriolis force must be balanced by a change in the water level surface to the east of the current. The opposite occurs if the current is moving in a northerly direction. The following formula governs the water surface elevation change due to the Coriolis force:

$$\frac{\partial \eta_c}{\partial x} = \frac{fV}{g} \quad 2.5$$

where η_c is the Coriolis tide; f is the Coriolis parameter; and V is the depth averaged current magnitude (Harris, 1963; Dean & Dalrymple, 2002).

Short-waves (wind-waves) can affect water levels during a storm surge. The generation and propagation of wind-waves can alter peak storm surge elevations, time of peak surge, and water recession after the storm. Wind induced waves are influenced by several factors including

bathymetry, tide-, wind- and wave-induced currents; tide- and surge-induced water level fluctuation; and coastal structures. (Smith *et al.*, 2002; Bunya *et al.*, 2010).

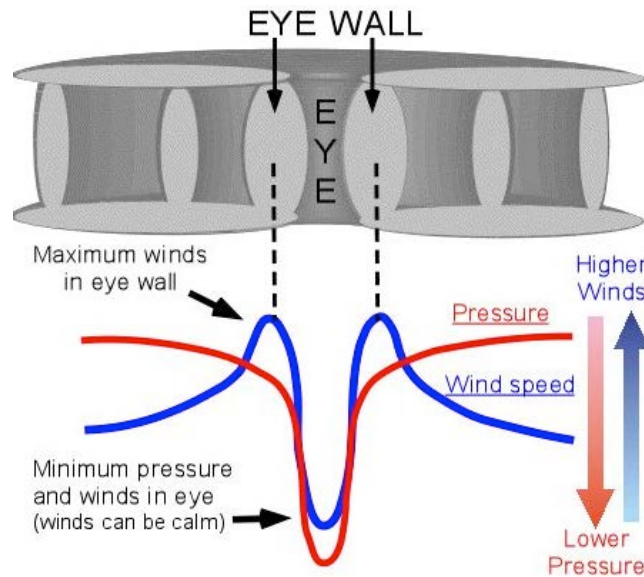


Figure 13 Figure of the hurricane eye wall and a cross-section view of the winds and pressure distributed throughout the storm (Department of Atmospheric Sciences at University of Illinois at Urbana-Champaign, 2010).

Much research has been done to ensure the essential physics are included to successfully simulate astronomic tides and hurricane storm surge across large domains. As remote sensing data collection and processing techniques continue to improve and become more abundant, new methods should be presented and fully tested to further the progression of state-of-the-art hydrodynamic models. However, as presented in the previous literature review, there is a lack of knowledge in shallow water hydrodynamic modeling with respect to resampling bare earth LiDAR points to a FEM, at varying element sizes. As a result, the research presented focuses on this issue.

CHAPTER 3: INTERPOLATION METHODS

Based on published literature, three interpolation methods were selected for this study: linear, inverse distance weighted, and natural neighbor. These methods are easily employed by the software program SMS 10.1 (Aquaveo LLC, 2010). In addition to linear, IDW, and NN interpolations a direct lookup and a basic area averaging schemes are tested. The following sections present a brief description to each interpolation method and its mathematical representations.

3.1 Linear Interpolation

Linear interpolation is the most widely used mathematical representation of a DEM surface due to its simplicity and practicability (Zhu *et al.*, 2005). When using a TIN model, rather than a regular grid DEM, the surface of the TIN triangles is a 3D surface in which a linear plane connects the three vertices, or nodes of the triangles (Figure 14). However, with a regular grid DEM, a linear model represents the surface in the X and Y directions with a constant Z value, representing a flat plane. To compute an unknown elevation value at a point surrounded by points with known elevation values, a linear interpolation first triangulates the known points to form a temporary TIN using a Delaunay triangulation scheme. A Delaunay triangulation guarantees that no vertex of the triangle resides within the interior of any of the circumcircles of the triangular network (Aquaveo LLC, 2011). See Chapter 3 of Hjelle & Dæhlen (2006) for an in depth definition of Delaunay triangulation. Because the TIN surface is assumed to vary

linearly across the triangle, the TIN describes a piecewise linear surface. For a triangle, the equation of the plane is defined by three nodes of known elevations:

$$Ax + By + Cz + D = 0 \quad 3.1$$

where A, B, C , and D are computed by the nodal locations $(x_1, y_1, z_1), (x_2, y_2, z_2), (x_3, y_3, z_3)$.

$$\begin{aligned} A &= y_1(z_2 - z_3) + y_2(z_3 - z_1) + y_3(z_1 - z_2) \\ B &= z_1(x_2 - x_3) + z_2(x_3 - x_1) + z_3(x_1 - x_2) \\ C &= x_1(y_2 - y_3) + x_2(y_3 - y_1) + x_3(y_1 - y_2) \\ D &= -Ax_1 - By_1 - Cz_1 \end{aligned} \quad 3.2$$

Rearranging 3.1 and substituting in 3.2, the plane equation can be represented as:

$$z(x, y) = -\frac{A}{C}x - \frac{B}{C}y - \frac{D}{C} \quad 3.3$$

where $z(x, y)$ is the elevation function at coordinates x and y .

Solving 3.3 for a point located inside triangle ABC yields an elevation value linearly interpolated from nodes ABC (Aquaveo, 2007b).

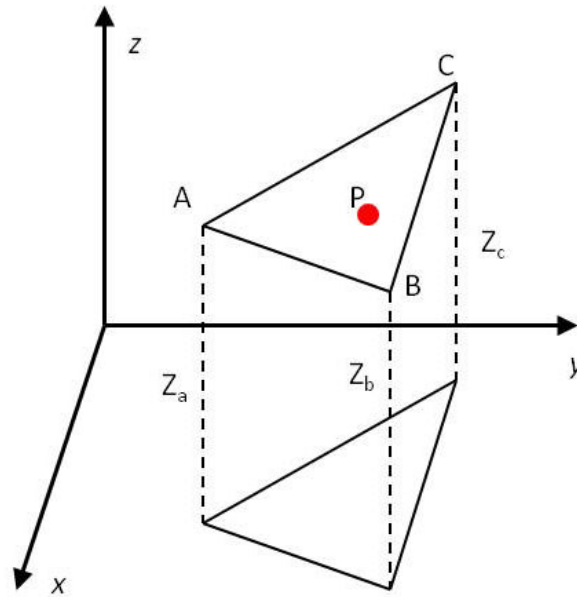


Figure 14 3D representation of a triangle using a linear interpolation.

3.2 Inverse Distance Weighed Interpolation

Another common interpolation technique is inverse distance weighed (IDW). IDW interpolation is based on the assumption that the target point being interpolated should be influenced more by its closest points rather than points farther away (ESRI, 2008). Inverse distance interpolation methods merge the ideas by Voronoi polygons, but with a steady change of the surface (Burrough & McDonnell, 1998). Voroni (or Thiessen) polygons are constructed for each point using the circumcircles of the triangles resulting from the Delaunay triangulation (Hjelle & Dæhlen, 2006). The simplest expression (Shepard's Method) for IDW interpolation is as follows (Shepard, 1968; Aquaveo, 2007a):

$$z(x, y) = \sum_{i=1}^N w_i z_i \quad 3.4$$

where N is the number of known input points, w_i is the weighting function and z_i is the value of point i . For this project, $i = 3$, the four closest points. The weighting function is based on proportionate areas and computed by:

$$w_i = \frac{d_i^{-p}}{\sum_{i=1}^N d_i^{-p}} \quad 3.5$$

where p is a real positive number equaling 2 (power parameter), giving an appropriate result for the purposes of general surface mapping and description (Shepard, 1968). Also, d_i is the horizontal distance of the target point to the input point i :

$$d_i = \sqrt{(x - x_i)^2 + (y - y_i)^2} \quad 3.6$$

where (x, y) is the coordinate of the target point and (x_i, y_i) is the coordinates of input point i .

The following weighting function is used in SMS 10.1 for the IDW interpolation scheme.

$$w_i = \frac{\left[\frac{R - d_i}{Rd_i} \right]^2}{\sum_{i=1}^N \left[\frac{R - d_i}{Rd_i} \right]^2} \quad 3.7$$

where R is the distance from the most distant scatter point. According to Franke & Nielson (1980), this weighting function gives improved results compared to Shepard's equation.

3.3 Natural Neighbor Interpolation

Natural neighbor (NN) interpolation looks for the closest points to an unknown point and applies weights based on proportionate areas. Similar to the linear interpolation method, the known points are triangulated using the Delaunay triangulation method. Next, a Voronoi

diagram is constructed. The Voronoi polygon represents the region of influence around the unknown point. Therefore, each point has an associated area that is a polygon defining the boundaries of strength of the point as shown in Figure 15.

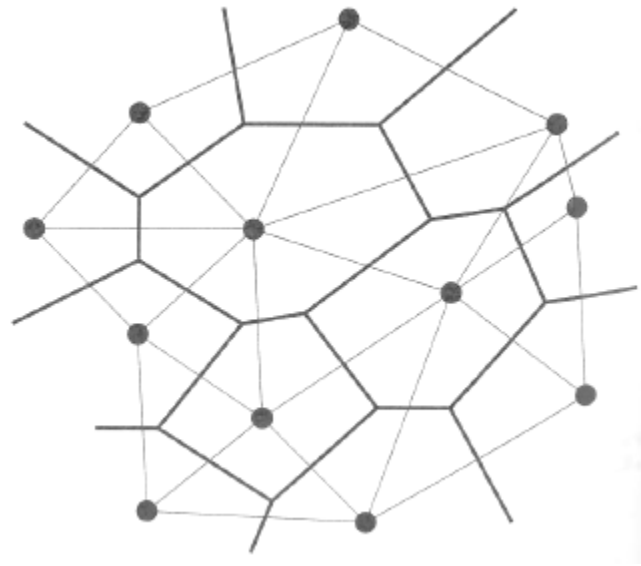


Figure 15 Thiessen polygon resulting from a Delaunay Triangulation. The bold lines are the Thiessen polygons and the thin lines represent the Delaunay triangulation. From (Burrough & McDonnell, 1998) page 114.

To estimate a value at point P, P is inserted as a new point resulting in a new triangulation. Therefore, a new network of Voronoi polygons are created, in which P has its own area of influence that overlaps with the Voronoi region of its neighbors. This determines how P fits into the existing points. The value of P is calculated based on the portion of the area that it borrows from each neighboring polygon in the previous network. For example, if the areas of the contributing polygons are $A_i, i = 1, 2, \dots, N$, then the relative portion borrowed from each of the original areas are (Sibson, 1981):

$$\lambda_i = \frac{A_i}{\sum_{i=1}^N A_i} \quad 3.8$$

Therefore, the value at P (z_p) is the summation of the relative portion of each contributing polygon (λ_i) multiplied by the value of its point z_i :

$$Z_p = \sum_{i=1}^N \lambda_i Z_i \quad 3.9$$

3.4 Area Averaging

For interpolation of a DEM to a finite element mesh, a basic area averaging scheme is employed. Several difference techniques are used. First, a single cell average (direct lookup) assigns the value of the DEM cell that overlays on a given mesh node (Figure 16). Further, the nine cell area (CA) averaging technique uses the nine DEM cells surrounding a given mesh node and averages those nine elevation values for an elevation assignment to the given node (Figure 17). An area averaging of 25, 49, 81, 121, and 169 surrounding cells are also used in the same fashion as the 9 cell area average.

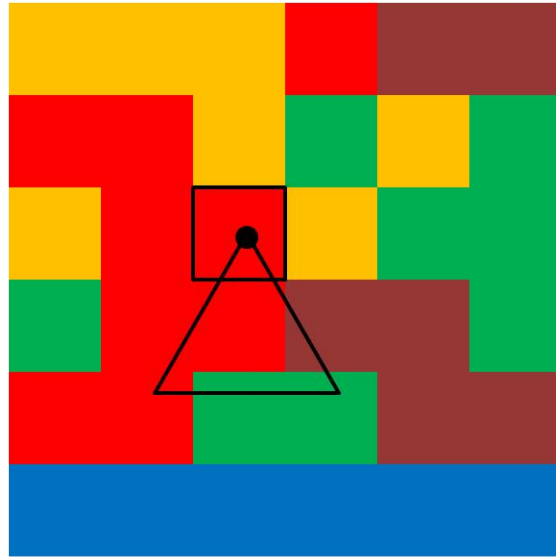


Figure 16 Example of interpolation using a 1 cell average (direct lookup)

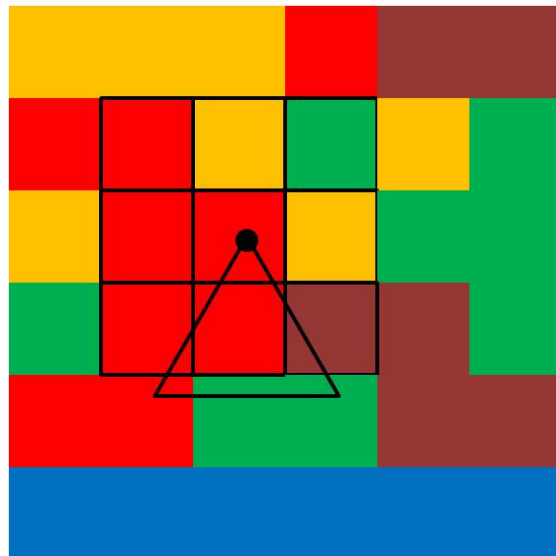


Figure 17 Example of interpolation using a nine cell area averaging scheme

CHAPTER 4: DESCRIPTION OF STUDY DOMAIN

The 130-km Pascagoula River, located in southeastern Mississippi, is contained in the Pascagoula River Basin, which drains approximately 25,000-km² (Figure 18). It is the last unregulated river system in the lower 48 states, facing far less human alteration than other watershed basins of similar scale (Mossa *et al.*, 2003; Perrott, 2007). The Leaf and Chickasawhay River join to form the Pascagoula River, each draining approximately 9,000-km² and 7,700-km², respectively, of the basin.

The Pascagoula River meanders through low-lying flatlands and broad flat plains upstream; however, heavy marshlands are present as it drains into the Gulf of Mexico through Mississippi Sound. The river empties into the Gulf of Mexico via two inlet systems, the East and West Pascagoula. In fact, the east inlet includes its own tributary in the Escatawpa River. The land cover/land use of the basin (Figure 19 and Figure 20) includes largely forested regions, with some agricultural, residential, and mining areas. Marshlands and developed land predominate along the coastline, but dense forest occupies much of the floodplain. The basin topography is generally rolling with low to moderate relief and elevations exceeding 180-m in the north (Oldham & Rushing, 1970; Slack, 1991; Strom, 1998). Much of the Pascagoula River is slow moving with shallow waters and can be heavily influenced by tides propagated from the Gulf of Mexico as far as 55-km upstream, south of Graham Ferry (Takahashi, 2008). The main focus of this study is on the lower Pascagoula River and surrounding marsh areas and floodplain.



Figure 18 Pascagoula River Basin and its rivers

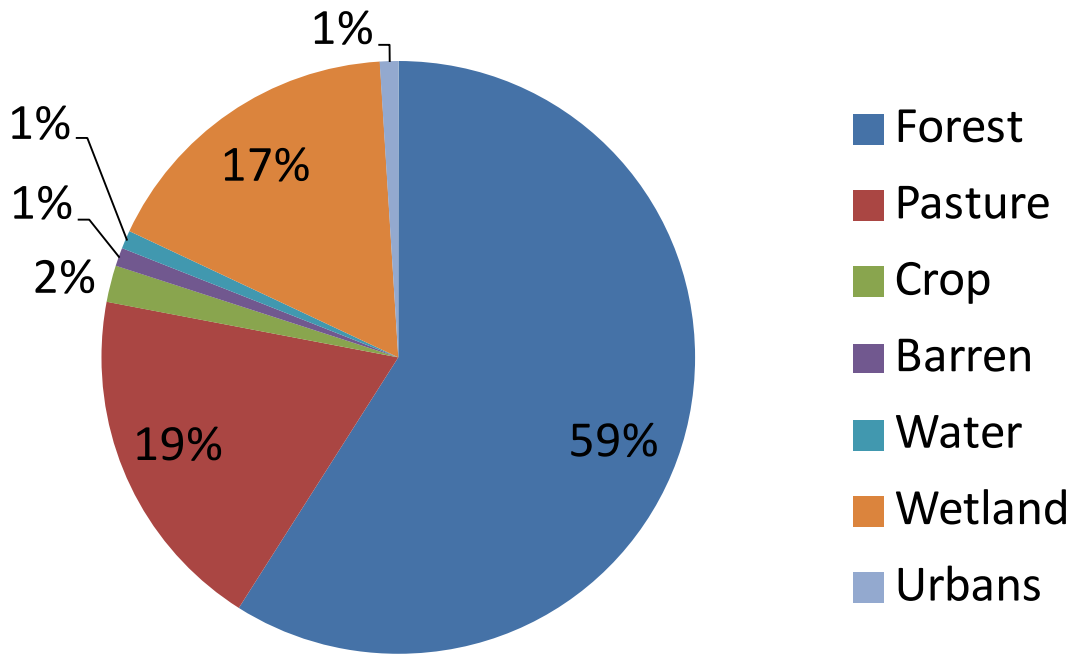


Figure 19 Land cover distribution in the Pascagoula River Basin (Mississippi Department of Environmental Quality, 2001).



Figure 20 2001 National LandCover Data and classification for the Pascagoula River Basin (Homer *et al.*, 2004).

Few publications exist on hydrodynamic numerical modeling of astronomic tides and hurricane storm surge for the Pascagoula River region. Wang (2008) developed a general finite element model of the Pascagoula River, capable of accurately describing astronomic tides fully within the banks of the river. Tides were found to propagate as far upstream as Graham Ferry, MS (55 km upstream). Building on this, Takahashi (2008) added the adjoining floodplain to the Pascagoula River, up to the 1.5-m contour. The inclusion of the floodplain, specifically the marsh regions, drastically improved model results. Including the immediate overland region enabled the tide (astronomic or storm) to inundate and recede, as it would in the natural system. However, there are two shortcomings to the model. First, the floodplain is limited to the 1.5 m contour. As this may be sufficient to accurately simulate astronomic tides, hurricane storm surge has a high likelihood of surpassing this boundary. To fully capture the physics of hurricane storm surge, the model boundary should extend past the 1.5-m contour, at a minimum, the 5 m contour (Takahashi, 2008). Second, the source elevations for the mesh elements in the floodplain were interpolated from an existing storm surge model for southeastern Louisiana (SL15 mesh) (Bunya *et al.*, 2010). Although many portions of the SL15 mesh have elevations derived from bare-earth LiDAR, information is lost when interpolating one finite element mesh to another, especially if they have severely different resolutions.

With previous research in modeling of tides and storm surge in the Pascagoula River and a lack of a state-of-the-art storm surge model, it becomes an excellent region to further investigate the development of a fully developed high-resolution numerical model.

CHAPTER 5: LiDAR DATA ACQUISITION

5.1 LiDAR Requirements for Flood Modeling

Several requirements must be met when acquiring LiDAR for flood modeling studies. In the U.S., these requirements are set forth by FEMA for Flood Hazard Maps as they are the most demanding for LiDAR data. The requirements are published in *Guidelines and Specifications for Flood Hazard Mapping Partners* (FEMA, 2003).

In particular, section A.8 outlines the methods that must be followed when using LiDAR for flood modeling. The post spacing, or ground sampling distance, should never exceed 5-m. DEM point spacing of 5-m or less (data dependent) must have a vertical accuracy of 1.2-ft (36.5-cm) at a confidence level of 95-percent. If data voids (areas within two times the DEM spacing) are present, several adjustments must be made pending the source of the void. If the void is due to a system malfunction during LiDAR collection then a new flight must be completed. Data voids resulting from thick vegetation require additional processing. If the vegetation is thick mangrove or sawgrass, the void may be interpolated from surrounding areas that include mangrove or sawgrass. In addition, if a void in dense vegetation is less than 1-acre similar interpolation methods may be undertaken. If the void is larger than 1-acre, ground surveys may be required to fill in the missing data, unless otherwise decided by a FEMA Lead representative. Data voids caused by the removal of manmade structures in the creation of the bare earth dataset are acceptable.

If artificial peaks or troughs (regions of anomalous elevations) are present in the DEM resulting from systematic errors, environmental conditions, or incomplete post-processing, the Mapping Partner should provide an analysis of the effects of the anomalies on DEM accuracy.

Outliers may be removed if they exceed three standard deviations of the localized region. Up to 10-percent of the worst performing outliers may be removed, however the FEMA Lead is capable of adjusting the percentage of outliers removed.

When used for flood modeling, the data should be delivered as high-resolution, high-accuracy, bare earth ground elevation data. When validating the vertical accuracy, a TIN linear interpolation should be used, not the DEM. The TIN should be constructed using the bare earth points and breaklines.

The data must have a maximum RMSE of 18.5-cm (37-cm accuracy at the 95-percent confidence level) in flat terrain. The vertical accuracy is defined as 1.96 times the RMSE of linearly interpolated elevation, compared to known elevations from high-accuracy test points, assuming a normal distribution:

$$Accuracy_z = 1.96 \times RMSE_z \quad 5.1$$

Vertical accuracy is defined as “the linear uncertainty value, such that the true or theoretical location of the points fall within \pm of that linear uncertainty value 95-percent of the time” (Appendix A, Section A.3) (FEMA, 2003). The factor of 1.96 to convert RMSE to a 95-percent confidence level is found in Greenwalt and Shultz (1962). The factor is based on observations of the normal distribution. It is recommended that if the data does not follow a normal distribution that the 95th percentile be used and should be computed from the error dataset and not from the RMSE.

Because accuracy of LiDAR may vary with changes in landcover type, the American Society for Photogrammetry and Remote Sensing (ASPRS) (ASPRS, 2004) and the National Digital Elevation Program (NDEP) (NDEP, 2004) guidelines advise different vertical accuracies for different landcover types:

- Consolidated vertical accuracy (CVA): vertical accuracy for all land cover types combined
- Fundamental vertical accuracy (FVA): vertical accuracy from checkpoints in the open terrain. The accuracy in the open terrain is assumed to be optimal due to a lack of influence from vegetation and buildings. Also, the errors are assumed to follow a normal distribution and all checkpoints should be used in the calculation of $RMSE_z$ and the 95th percentile is determined by multiplying the $RMSE_z$ by 1.96.
- Supplemental vertical accuracy (SVA): vertical accuracy from landcover types other than open terrain, one or more landcover types may be combined. The 95th percentile should be derived from the error distribution, since the error dataset does not always follow a normal distribution.

5.2 LiDAR Source Data

The study domain is located in portions of Jackson, Hancock and Harrison Counties, Mississippi and western Mobile County, Alabama. The domain is bounded by the 10-m elevation contour in the north, the Gulf of Mexico to the south, and the east and west boundaries taper from the 10-m contour to the shoreline (Figure 21). The size and extent of the domain was established to study storm tide in the Pascagoula River and adjacent floodplain while allowing a

large enough inundation area for surge to fully propagate and not artificially build up along the boundary.

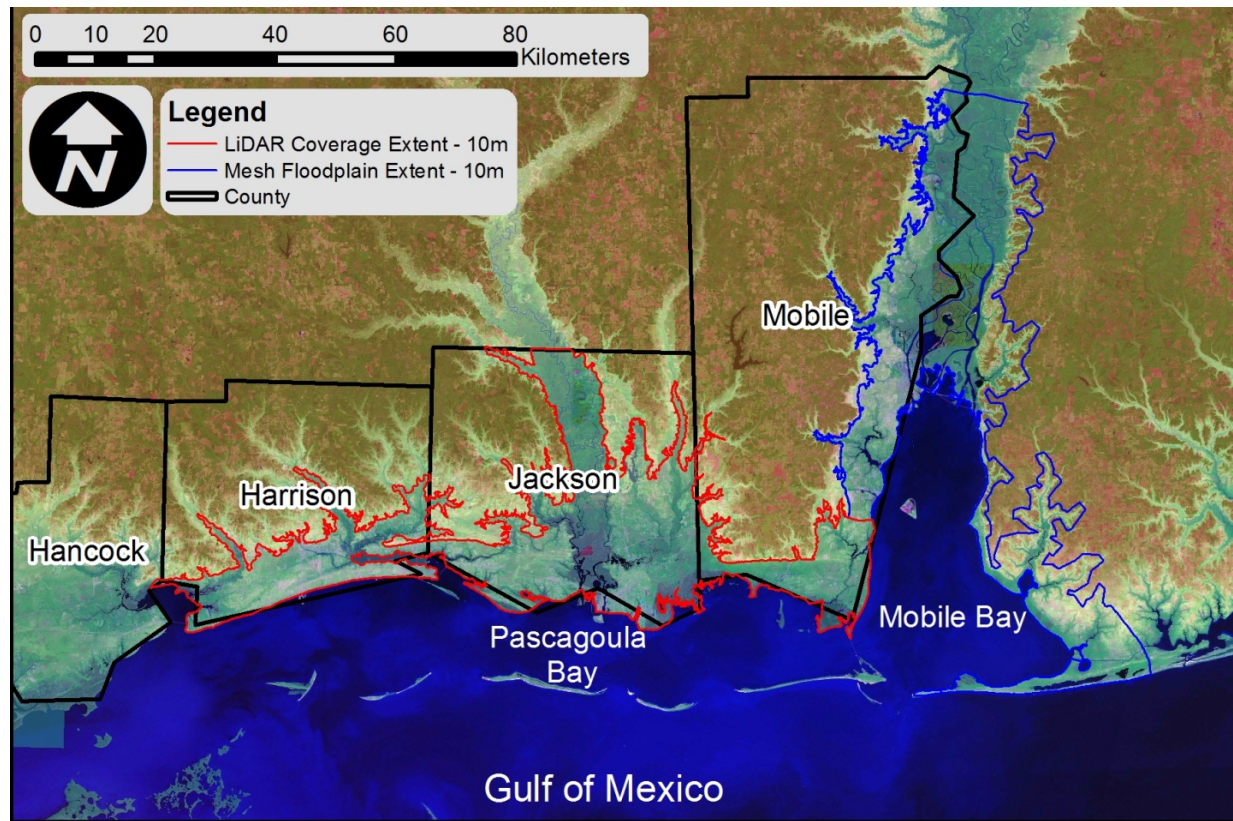


Figure 21 Map of the floodplain boundary (blue + red). The extent of the LiDAR coverage is represented by the red line. Elevation data within the blue boundary was obtained from a previous FEM. The counties are bounded by the black lines. The background is NED (Gesch *et al.*, 2002; Gesch, 2007) elevation data over Landsat satellite imagery (Goslee, 2011).

Three sources of LiDAR data were obtained for the study region by way of counties: 1) Hancock and Jackson Counties, Mississippi; 2) Harrison County, Mississippi; and 3) Mobile County, Alabama.

The LiDAR dataset for Mississippi was obtained through the Mississippi GIS Department. Data acquisition and processing was performed by EarthData International. This

data source covers approximately 477-mi² in Hancock County and 727-mi² in Jackson County, Mississippi, a full coverage of 1,204-mi². The data collected was obtained using the Lecia ALS-50 LiDAR system along with an inertial measuring unit (IMU) and a frequency GPS receiver. It is equipped with a 50-kHz thermal infrared laser that can measure ground point spacing of 1-m to 8-m. Nominal 5-m post spacing was required for the LiDAR data per FEMA guidelines. The data was acquired between February 25 and March 12, 2005. The specifications of the ALS-50 LiDAR system are listed in Table 1.

CheckDEM, a proprietary software program by EarthData International, was used to check a set of control points to the DEM to assess the accuracy of the LiDAR dataset. The data acquisition process resulted in point cloud data, bare-earth data, and 3D hydro-breaklines. Both LAS and ASCII files were delivered for the point cloud and bare earth data sets. Using bare earth points a statistical assessment of Jackson and Hancock Counties resulted in an RMSE of 7.5-and 4.4-cm, respectively (EarthData International, 2005a). Based on Equation 5.1, the accuracy for Jackson and Hancock Counties is 14.7-cm and 8.6-cm, respectively. Only the bare earth dataset was used in this research.

Data acquisition for Harrison County, Mississippi was also performed by EarthData International. The data were collected using a Cessna 210 aircraft equipped with an LH System ALS40 LiDAR system and an IMU and dual frequency GPS receiver. The specifications of the ALS-40 LiDAR system are listed in Table 2. Collection of the data took place on March 8 and 9, 2004 in three flights. The raw data were filtered and above ground features were removed by EarthData International. The data were delivered as LAS and ASCII files for both the point

cloud and bare earth LiDAR points along with 3D hydro-breaklines (EarthData International, 2005c, 2005b).

Data acquisition for Mobile County, Alabama was performed by the U.S. Army Corps of Engineers through Southeast Digital Mapping, LLC. The data collected between February 2 and February 8, 2002 (Southeast Digital Mapping, 2003). Raw bare earth XYZ files were delivered.

Table 1 Hancock & Jackson Counties LiDAR sensor parameters

Sensor Collection Parameters	
Flying Height	3,657 m AMT
Target Airspeed	150 knots
Laser Pulse	29,900 Hz
Field of View	45 Degrees
Scan Rate	17 Hz
Average Swath Width	3,100 m
Post Spacing	5 m

Table 2 **Harrison County LiDAR sensor parameters**

Sensor Collection Parameters	
Flying Height	3,383 m AMT
Target Groundspeed	120 knots
Laser Pulse	20,000 Hz
Field of View	45 Degrees
Scan Rate	11 Hz
Average Swath Width	2,777 m
Post Spacing	5 m

CHAPTER 6: TOPOGRAPHIC ERROR ASSESSMENT METHODOLOGY

6.1 Selection of Test Sites

To assess the error of the bare earth topography in two typical coastal settings, urban and marsh, three test sites were selected in coastal Jackson County, Mississippi (Figure 22). The methods presented are consistent, unless otherwise noted, for each of the three test sites. The first test site covers a forested region and small urban development (Figure 23). The second site is located in a marsh area found between the East and West Pascagoula inlet (Figure 24). The third site is a developed, urban, area (Figure 25).



Figure 22 Pascagoula River, MS with box insets representing accuracy testing sites 1, 2, and 3.



Figure 23 Test Site 1



Figure 24 Test Site 2



Figure 25 Test Site 3

For each test site, inner and outer boundaries were constructed. The outer boundary is 1120-m by 1120-m and the inner boundary is offset by 160-m, yielding an inner 800-m by 800-m region. The bare earth points were clipped to both the outer boundary and the inner boundary as well to the transition zone, the area in between the outer and inner boundary. For the interior domain (i.e. area bounded by the inner boundary), the LiDAR points were randomly sub-divided into two datasets. The first dataset, termed the training dataset, includes 90-percent of the points; the second, termed the test dataset, includes the remaining 10-percent. Figure 26 presents an example of the training, test, and transition zone datasets. The ratio of training to test points yields enough points to test the quality of the processed data without degrading the LiDAR data itself and provides enough samples for statistical calculations (Liu *et al.*, 2007a; Bater & Coops, 2009). The training dataset was used to generate DEMs as well as the source elevations for

interpolation onto FEM nodes, whereas the test dataset was used to assess vertical errors in elevation. Table 3 shows the number of LiDAR points for each test site and the average point spacing of training points within the interior domain (inner boundary).

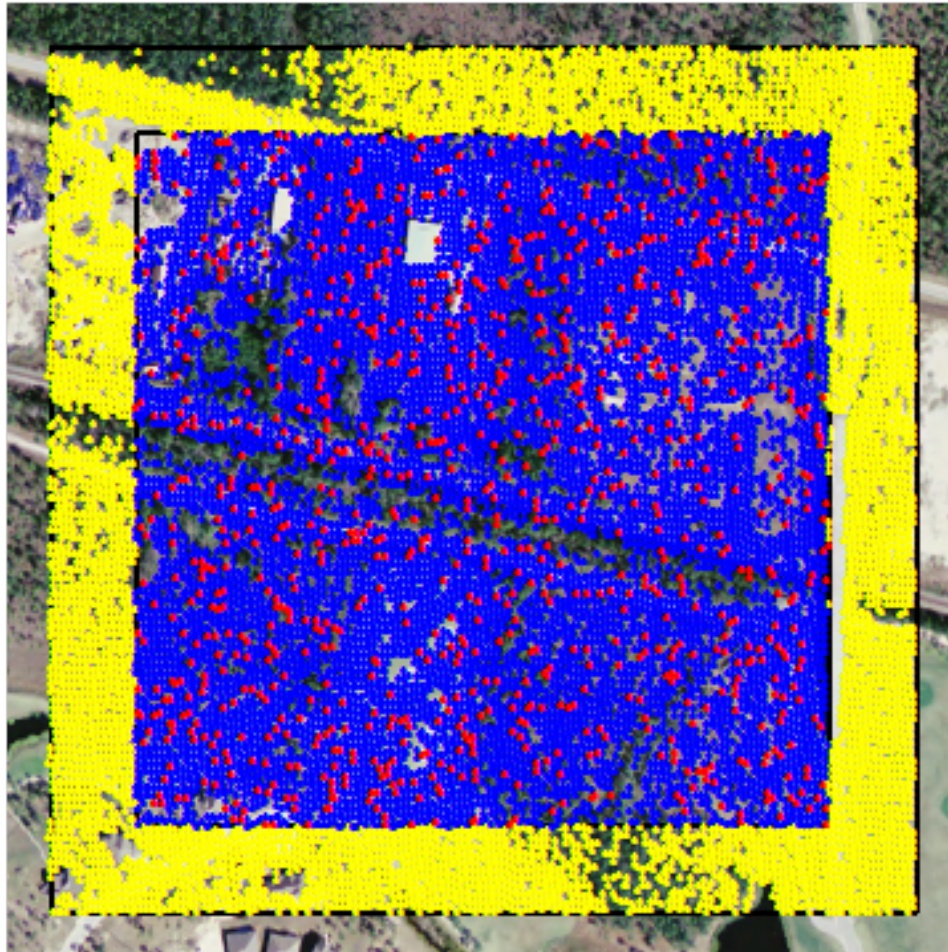


Figure 26 The boundary of the LiDAR coverage for the test sites. The blue and red points indicate the training and test datasets, respectively. The yellow points represent the transition area dataset.

It is important to note that this method was not intended to examine the geodetic accuracy of the collected bare earth LiDAR dataset. The focus is on examining how interpolation functions as well as linear triangular elements and raster DEMs predict and/or represent the

vertical component of the source data. This method is similar to that employed by Bater and Coops (2009).

Table 3 LiDAR point statistics for test sites

Test Site No.	Name	Outer Area (km ²)	Inner Area (km ²)	# Training Points	# Test Points	Average Point Spacing (m)
1	Mixed	1.25	0.64	36,015	4,002	3.39
2	Marsh	1.25	0.64	37,751	4,560	4.11
3	Urban	1.25	0.64	34,465	3,829	4.61

6.2 DEM and Finite Element Mesh Generation

Eight DEMs were produced for each test site. All sites included DEMs at resolutions of 160-m, 80-m, 40-m, 20-m, 10-m, 5-m, 2.5-m, and 1.25-m. The source dataset for all DEMs was the training datasets, merged with the transition dataset. ESRI ArcGIS 10 (ESRI, 2011a) was used to generate all DEMs. The DEM generation method for each test site is similar to that of Medeiros *et al.* (2011) where the terrain dataset (TDS) within ArcGIS was utilized. The TDS is further explained in Chapter 6. Once the Terrain was generated, the Terrain to Raster tool in the 3D Analyst Toolbox was used with a linear interpolation to convert the Terrain to a raster DEM.

Similar to that of the DEMs, eight structured FEMs were developed for each test site, at the same resolutions as the DEMs. The mesh elements were chosen to be equilateral to best depict a regular interval and perfect triangulation for description of topography. Equilateral elements are also the most numerically stable when used in finite element models (Hagen, 2001). The first mesh, 160-m in edge length, was refined, by successively splitting the edge length in

half, to 1.25-m in edge length. Refinement splits the edge length in half, resulting in four sub-elements as depicted in Figure 27.

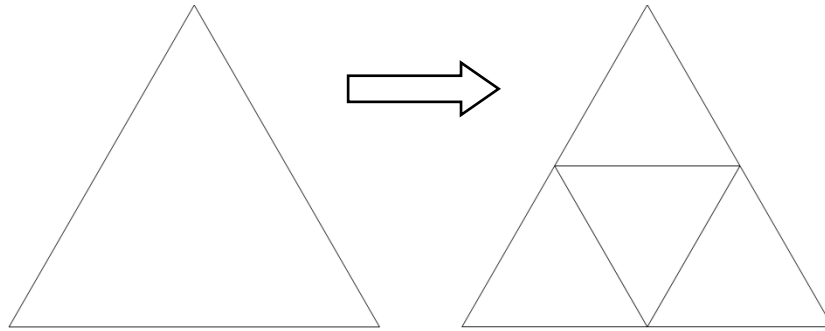


Figure 27 Refinement splits the element into four sub-elements and divides the edge length in half.

The source elevation data used to interpolate elevations onto the FEM nodes was the training dataset merged with the transition dataset, the 5-m DEM, and 10-m DEM. All three were interpolated onto each FEM at each site test using the three interpolation methods in the software package SMS 10.1 (Aquaveo LLC, 2010). The 5-m and 10-m raster DEM was interpolated onto the FEMs using cell area averaging schemes.

6.3 Accuracy Analysis Statistics (RMSE)

Using all DEMs and FEMs for each test site, with elevations obtained via the training dataset, the test dataset points allowed for comparison of the accuracy between all representative surfaces. For each DEM and FEM, vertical errors were computed for each point in the test dataset using the root mean square error (RMSE):

$$RMSE = \sqrt{\frac{\sum_{i=1}^N (M_z(x, y) - I_z(x, y))^2}{N}} \quad 6.1$$

where $M_z(x,y)$ is the measured (LiDAR) elevation, $I_z(x,y)$ is the predicted (interpolated) elevation value at coordinate x,y , and N is the number of points in the test dataset. RMSE is commonly used to measure the precision of DEMs derived from points using interpolation functions (Desmet, 1997; Shi, 2010). In this instance, RMSE is a measure of the global accuracy in the disagreement between the interpolated value and the measured value. Further, if the dataset is normally distributed, $Accuracy_z$ can be measured by Equation 5.1. As stated previously, it is important to note that the elevation value, when compared to the DEMs, is that of the center of the DEM grid cell, while the test points are unlikely to occur at or near the center. This results in some additional error when comparing the test points to the DEM surface (Bater & Coops, 2009).

6.4 Test for Normality

To report results in terms of $Accuracy_z$, as previously discussed in section 4.1 (accuracy = 1.96 times the RMSE for a 95-percent confidence interval), the errors are assumed to be normally distributed. Measures of normality (skewness and kurtosis) and tests for normality (Kolmogorov-Smirnov test using Lilliefors significance correlation and Shapiro-Wilk test) (Shapiro & Wilk, 1965; Lilliefors, 1967) were used to determine if the elevation error follows a normal distribution. Skewness is a measure of symmetry about the mean. A skewness of 0 represents a normal distribution (i.e. symmetrical distribution). Kurtosis is a measure of the height and sharpness of the peak of the distribution in relation to the remaining data. Higher values indicate a sharp, high peak; alternatively, lower values signify a smaller peak. Histograms and normal probability plots offer a visual test of normality. Histograms visually illustrate a dataset's distribution. Normal probability plots, or normal Q-Q plots, are a visual

method to determine if the distribution of a dataset diverges from a theoretical normal distribution. If the datasets distribution follows the theoretical normal distribution, then the dataset follows a normal distribution; however, if it deviates from the theoretical line, the distribution is a sign of non-normality.

Many works have shown that error distribution resulting from LiDAR-derived DEM error is a non-normal distribution, invalidating the typical accuracy equation used in digital terrain modeling (Oksanen & Sarjakoski, 2006; Aguilar & Mills, 2008; Zandbergen, 2008; Hasan *et al.*, 2011; Zandbergen, 2011). ASPRS (2004) Guidelines state (p. 3) that “for error that is not normally distributed, ASPRS recommends $Accuracy_z$ be determined by 95th percentile testing, not by use of $Accuracy_z=1.96*RMSE$.” This is only a recommendation; however, LiDAR is typically reported in terms of both RMSE and $Accuracy_z$. Further, RMSE does not differentiate between positive and negative elevation errors (i.e. RMSE is equal for the error and absolute value of the error).

Supplementary normality tests were conducted. Several outliers in the two example datasets were removed to determine if outliers cause non-normality. Zandbergen (2011) found that outliers significantly altered RMSE when ground truth elevations were compared to a bare earth LiDAR-derived TIN model, but the distributions still did not confirm normality. He recommended employing an outlier removal method to trim the data by 1- to 5-percent prior to computing $RMSE_z$. For this study, outliers were defined as any value which had an absolute Z-score of three or greater (p.42) (Mendenhall & Sincich, 2007). The Z-score was computed by the following equation:

$$Z - score = \frac{(x_{\Delta z} - \bar{x}_{\Delta z})}{\sigma_{\Delta z}} \quad 6.2$$

where $x_{\Delta z}$ is the elevation error at the given point, $\bar{x}_{\Delta z}$ is the mean of all elevation errors in the test dataset, and $\sigma_{\Delta z}$ is the standard deviation of all elevation errors in the test dataset.

Outliers accounted for 1.14-percent and 1.38-percent of the data points for Test Sites 2 and 3, respectively. The $RMSE_z$ (equal to the standard deviation of the errors) decreased 6.93-cm and 0.46-cm for Test Sites 2 and 3, respectively. The $RMSE_z$ decrease is significant for the larger element size, particularly when less than 2-percent of the data was removed.

Table 4 shows the results of the measures and tests for normality for two FEMs for Test Sites 2 and 3 with the full datasets and with outliers removed. Both datasets yield a negative skewness value, indicating the majority of the distribution is concentrated to the right of the mean. The kurtosis value for Test Site 2 is smaller because the peak is not as sharp as the peak for Test Site 3; however, both peaks are well beyond the crest of the normal distribution curve. Both the Lilliefors correlation and Shapiro-Wilk tests can be used to determine normality. If the p -value (probability) is greater than 0.05, the dataset is normally distributed.

Both tests for both Test Site datasets yield a p -value of approximately 0.0, indicating a non-normal distribution. The tests on the datasets with outliers removed show a closer match to a normal distribution, yet the datasets still do not qualify as normally distributed (p -values are still less than 0.05).

Figure 28 presents the error distribution in the 40-m FEM for Test Site 3 and in the 5-m FEM for Test Site 2 as a histogram and a normal probability plot. Figure 29 shows the histogram and normal probability plot for the same datasets, except with outliers removed. The

histograms tend to follow a bell-shaped curve; however, many of the values are clustered about the mean providing a sharp peak in the data. The data about the mean are too narrow and occur at too high of frequency to follow a normal distribution, with several data points near the tails. The normal probability plots further shows strong departure from a normal distribution. Also, the Q-Q plots expose a sigmoid shape, further proving non-normality in the distribution, especially for the datasets with outliers included).

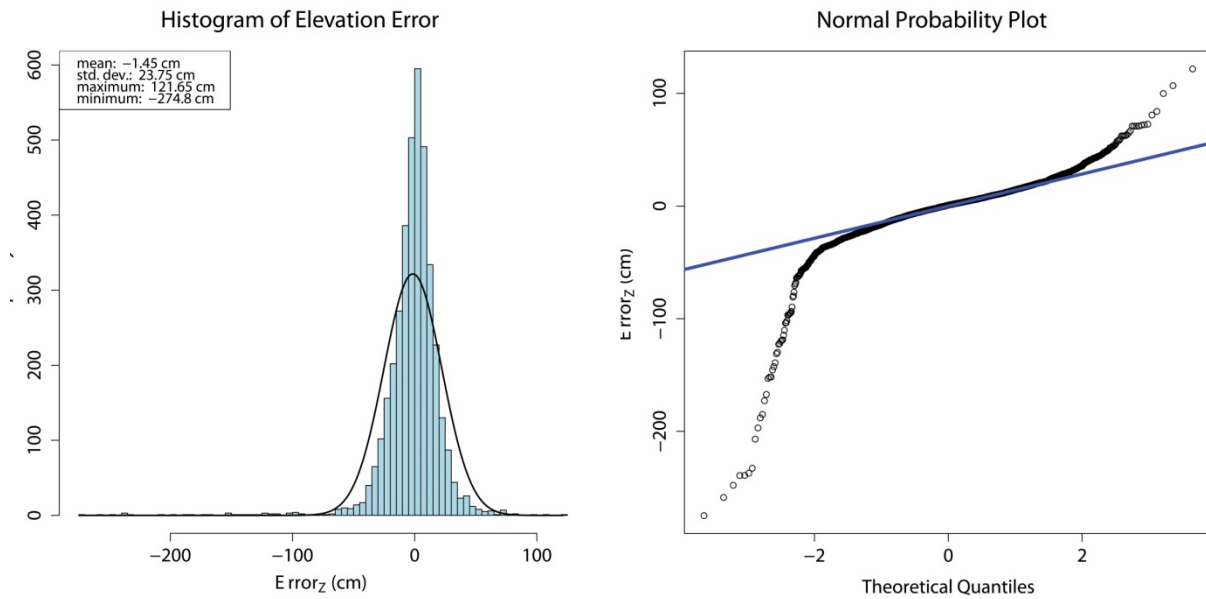
The results obtained complement those of Zandbergen (2011), which demonstrate the propagation of non-normality of elevation error from bare earth LiDAR to a FEM. Since the data shown does not follow a normal distribution, the statistical measures used for vertical errors in elevation were RMSE and the 95th percentile.

Table 4 Normality test results of error distribution

FEM (Interpolation)	n points	Skewness	Kurtosis	Lilliefors*		Shapiro-Wilk	
				Statistic	p-value	Statistic	p-value
40 m Test Site 3 (49CA)	3,829	-3.48	33.55	0.1182	< 0.05	0.759	< 0.05
5 m Test Site 2 (BEL_NN)	4,560	-0.29	5.51	0.0489	< 0.05	0.9751	< 0.05
Outliers Removed (Z-score > 3)							
40 m Test Site 3 (49CA)	3,776	-0.18	4.42	0.0498	< 0.05	0.9826	< 0.05
5 m Test Site 2 (BEL_NN)	4,508	0.01	3.56	0.0373	< 0.05	0.9924	< 0.05

* Kolmogorov-Smirnov test using Lilliefors significance correlation

40 m FEM (49 Cell Averaging) Error



5 m FEM (Training NN) Error

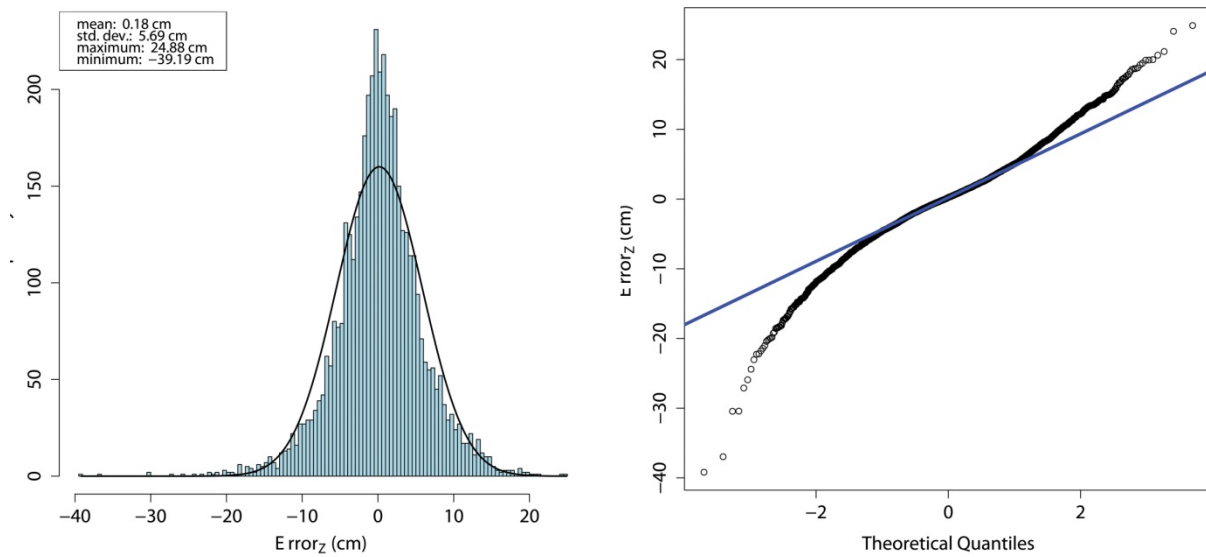
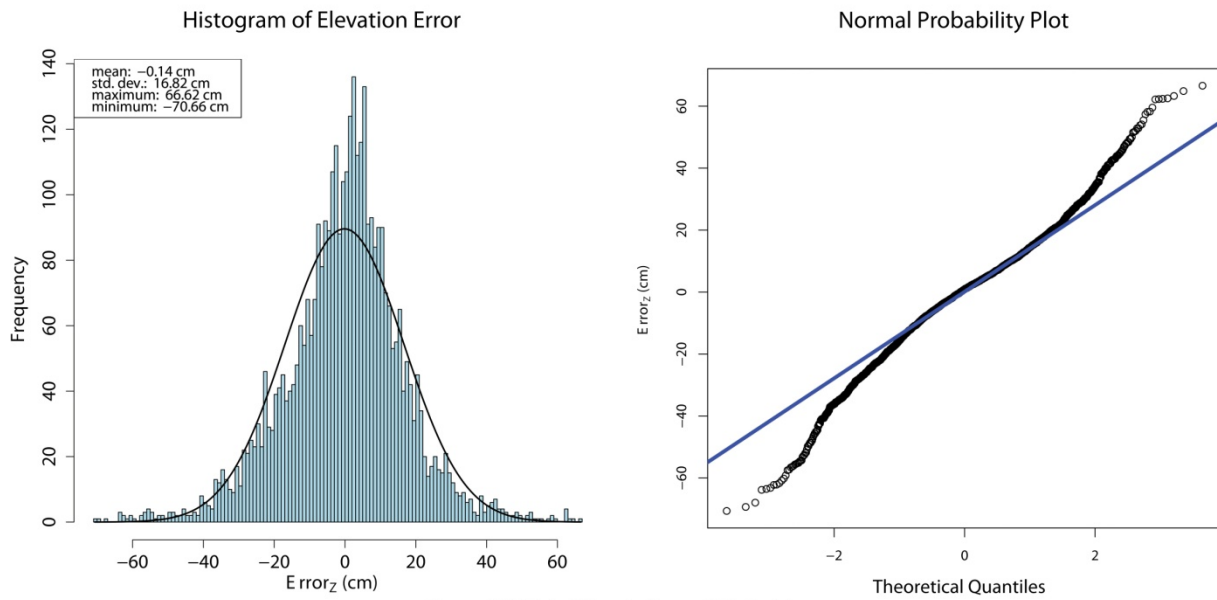


Figure 28 Error distribution in the 40-m FEM (49 cell averaging) for Test Site 3 and in the 5-m FEM (training NN) for Test Site 2.

40 m FEM (49 Cell Averaging) Error



5 m FEM (Training NN) Error

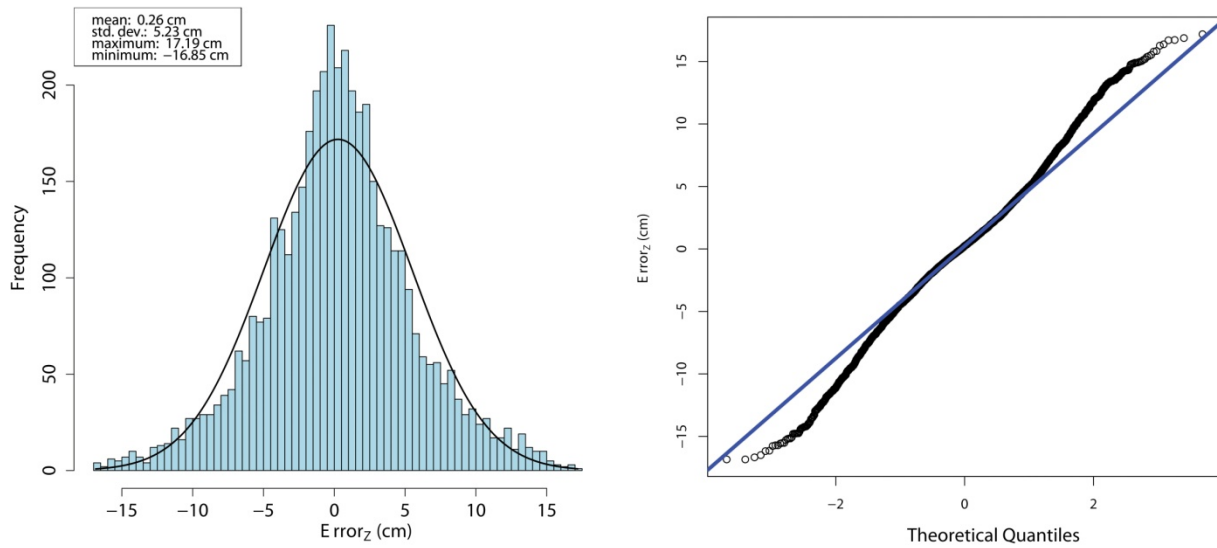


Figure 29 Error distribution in the 40-m FEM (49 cell averaging) for Test Site 3 and in the 5-m FEM (training NN) for Test Site 2 with outliers removed.

6.5 Accuracy Assessment Results

Elevation error was computed in terms of RMSE for vertical differences in interpolated values across the test dataset for the three test sites. RMSE for each FEM and DEM at the locations of each test point in the test dataset are presented. Table 5 presents the RMSE across all FEMs and DEMs that obtained elevations from the training dataset using a linear interpolation. From this table, the DEMs generally contained larger error (up to 10-cm) when compared to the FEMs. This is a consequence of the assumption that the elevation is constant across the raster DEM grid cell. Higher resolution DEMs may perform better as a result of the test points occurring at decreased distances from the grid cell centers (Bater & Coops, 2009). Thus, linear elements have an advantage over raster grid cells, particularly due to the 3D nature of the polygonal faces that make up the surface.

Generally, both the FEMs and DEMs perform similarly at larger scales, 20-m and above, where larger differences occur at smaller element and raster grid cell sizes. The greatest range in error occurs in Test Site 1, both in the FEM and DEM representations. The wide range in error for this site is attributed to the wide range in groundcover, resulting in pockets of dense and sparse bare earth returns. Test Site 1 is characterized by heavily forested regions, roadways, and urban areas. LiDAR returns on the canopy in forested regions and on manmade structures are removed from the raw point cloud in the generation of the bare earth points, leaving artificial fissures in the bare earth dataset. In a similar fashion, Test Site 3 includes more error than Test Site 2. As expected, Test Site 2 has lower error in all sizes as it contains more bare earth LiDAR returns than the other two sites. A significant difference in RMSE is found in Test Site 2 when comparing the FEMs to DEMs across the smaller scale. A 5.7-cm difference occurs for the 1.25-

m size. The large error for the low raster grid cell sizes is likely a result of a lack of LiDAR returns on the water across the marsh. Elevation error on the marsh is sensitive to the constant elevation across the DEM grid cells. Further, the RMSE of Test Site 1 is between Test Site 2 and 3 for element sizes of 10-m and below (Test Site 1 includes landcover types found in Test Sites 2 and 3). However, this is not the case above 10-m in element size because the effect of small-scale variations in slope smoothes out the elevation.

The RMSE results for Test Sites 1, 2, and 3 signify that grid and element mesh resolution is a factor that can affect overall global error in elevation. At Site Number 1, training-to-FEM RMSE is 9.4-cm for an element size of 5-m, relative to RMSE of 53.7-cm for element size of 160-m. In fact, elements sized at 160-m can result in as much as greater than five times the error of that associated with elements sized at or less than 5-m. Note it is not uncommon to use elements sized at or greater than 160-m in shallow water modeling. Generally, as the resolution increases, error decreases showing better fit to the source data.

A comparison of interpolating the 5 m DEM and 10 m DEM onto the FEMs is presented in Table 6 through Table 8, using a linear, IDW, and NN interpolation, for all test sites. The meshes with elevations derived from the 5 meter DEM perform better than the meshes obtained from the 10 m DEM at element edge lengths of 20 m and less. For scales larger than 20 m, both sets of meshes are generally comparable, resulting in similar RMSE. This finding relates to the Shannon-Nyquist theorem presented earlier (Shannon, 1949). Resampling the 10 m DEM to lower than half of its source data density, i.e. 5 m, does not yield increased accuracy. This is shown by comparing all test sites and all FEM sizes at the 5 m resolution and lower when interpolating using the 10 m DEM, for all interpolation schemes.

Table 5 RMSE for all test sites with a linear interpolation of the training dataset onto the FEMs and DEMs

Size (m)	Training to FEM - RMSE (cm)			Training to DEM - RMSE (cm)		
	Site 1	Site 2	Site 3	Site 1	Site 2	Site 3
1.25	9.1	3.1	11.4	9.5	8.8	11.7
2.5	9.1	3.9	11.5	9.9	8.9	11.8
5	9.4	5.9	11.6	11.8	9.4	13.0
10	12.3	8.7	13.8	16.7	10.7	16.2
20	19.1	11.4	20.0	26.9	13.2	21.6
40	29.9	14.1	27.1	39.9	16.1	31.4
80	38.9	16.9	31.4	47.7	17.9	36.4
160	53.7	18.7	50.7	62.3	20.9	41.5

Table 6 RMSE for Test Site 1 using linear, IDW, and NN interpolation from the 5-m and 10-m DEM

Size (m)	5m DEM to Finite Element Mesh - RMSE (cm)			10m DEM to Finite Element Mesh - RMSE (cm)		
	Linear	IDW*	NN	Linear	IDW*	NN
1.25	9.8	10.4	9.8	13.2	19.5	13.2
2.5	9.8	10.1	9.8	13.2	14.1	13.1
5	10.2	10.5	10.2	13.3	13.4	13.1
10	12.4	12.5	12.4	14.4	14.6	14.2
20	18.8	19.1	18.9	18.8	19.3	19.0
40	29.6	29.8	29.7	29.4	29.6	29.4
80	38.6	38.7	38.6	38.0	38.3	38.1
160	53.5	53.3	53.4	53.0	53.2	53.0

*Using three closest points

Table 7 RMSE for Test Site 2 using linear, IDW, and NN interpolation from the 5-m and 10-m DEM

Size (m)	5m DEM to Finite Element Mesh - RMSE (cm)			10m DEM to Finite Element Mesh - RMSE (cm)		
	Linear	IDW*	NN	Linear	IDW*	NN
1.25	6.4	7.9	6.1	9.0	10.9	8.9
2.5	6.5	7.8	6.2	9.0	10.7	9.0
5	67.0	8.6	6.9	9.0	10.6	6.9
10	8.5	9.3	8.6	9.4	11.2	9.3
20	11.1	11.5	11.2	11.1	11.9	11.1
40	13.8	14.0	13.9	13.6	13.9	13.7
80	16.7	16.6	16.8	16.5	16.4	16.6
160	18.7	19.0	19.0	18.5	18.7	18.7

*Using three closest points

Table 8 RMSE for Test Site 3 using linear, IDW, and NN interpolation from the 5-m and 10-m DEM

Size (m)	5m DEM to Finite Element Mesh - RMSE (cm)			10m DEM to Finite Element Mesh - RMSE (cm)		
	Linear	IDW*	NN	Linear	IDW*	NN
1.25	11.8	13.7	11.8	14.5		
2.5	11.8	14.1	11.8	14.5	17.0	14.1
5	12.0	14.4	12.1	14.6	17.3	14.1
10	14.0	15.3	14.1	15.2	18.6	15.1
20	19.7	20.8	20.0	19.7	21.5	20.1
40	26.7	27.3	26.9	26.5	25.7	26.8
80	30.9	32.4	30.9	30.6	29.6	31.1
160	49.0	52.7	50.1	48.4	42.2	50.1

*Using three closest points

Figure 30 shows the 5-m FEM for Test Site 2 with cross-section A. Figure 31 graphically dictates the absolute error along cross-section A (difference between the FEM and test point elevation). The blue boxes correspond to regions along the cross-section with the

largest absolute error, relating to the topographic slope in the FEM. It is shown that a large variance in topographic slope increases the absolute vertical error. Also, a larger element size increases the topographic slope, therefore increasing the error. Figure 32 shows the elevation and absolute error for the 80-m FEM.

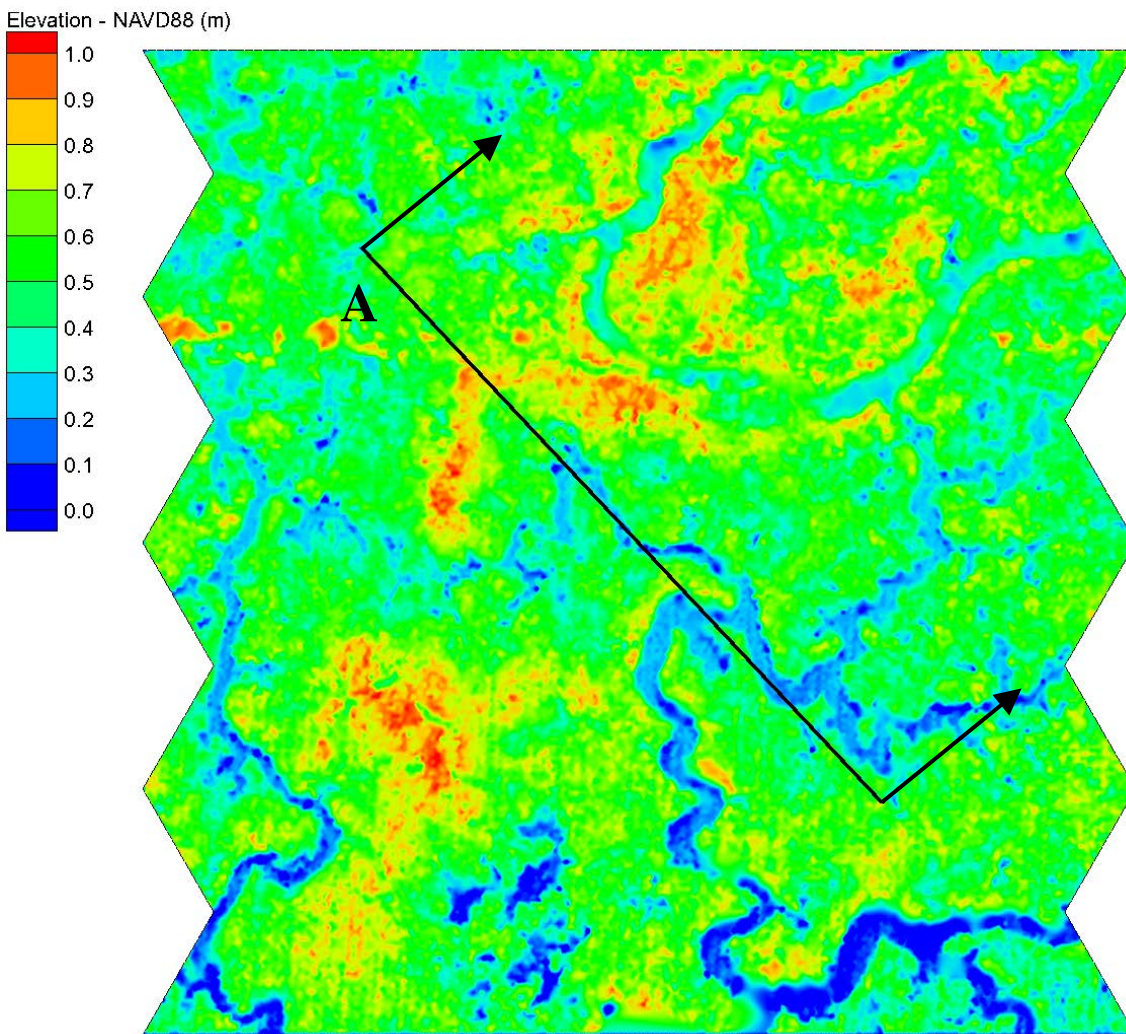


Figure 30 5 m FEM for Test Site 2. The black line represents cross-section A.

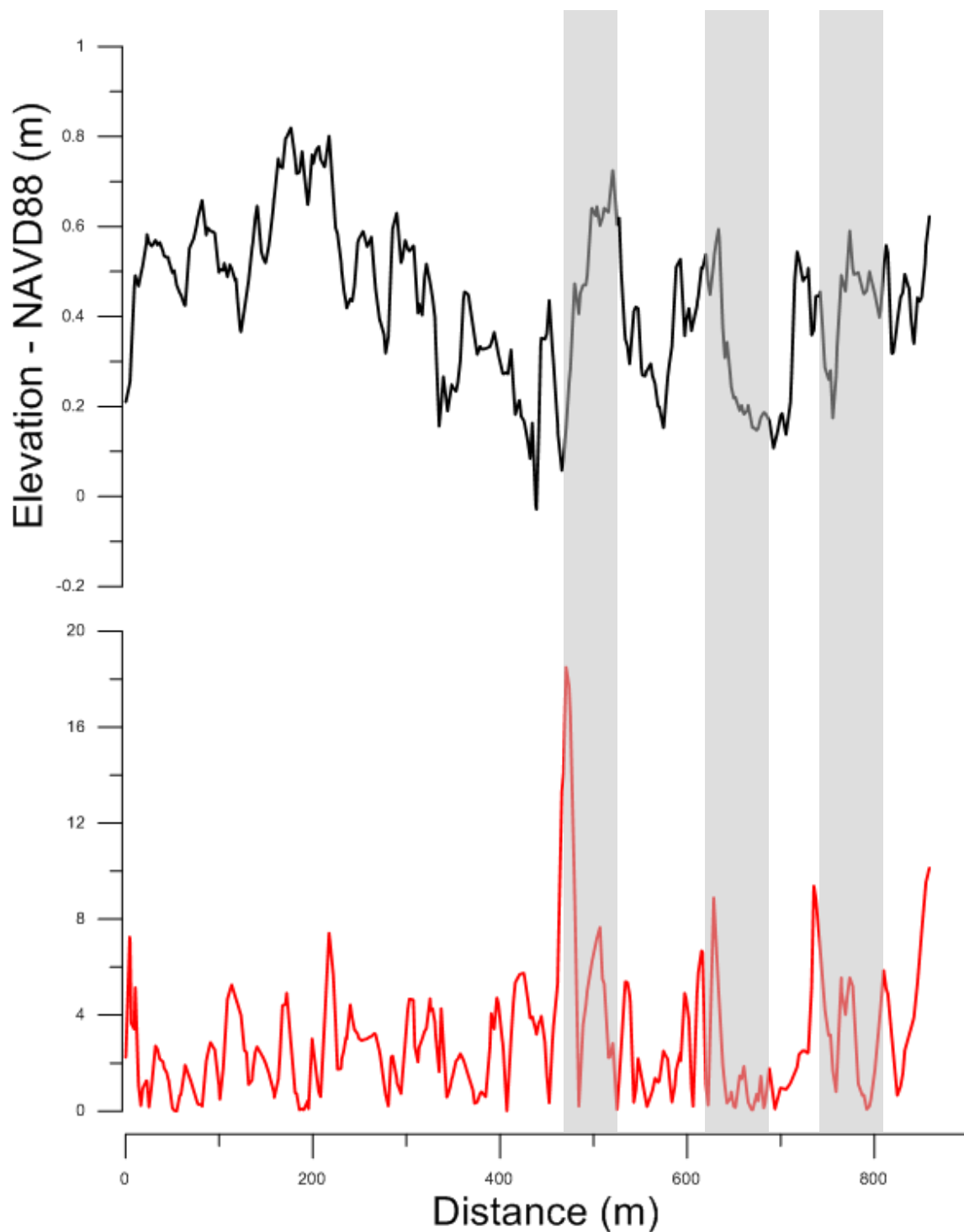


Figure 31 Plot of (top) elevation (m) and (bottom) absolute elevation error (cm) at Test Site 2 for the 5-m FEM along cross-section A. The blue boxes indicate the highest errors along the cross-section correlating with high topographic slopes.

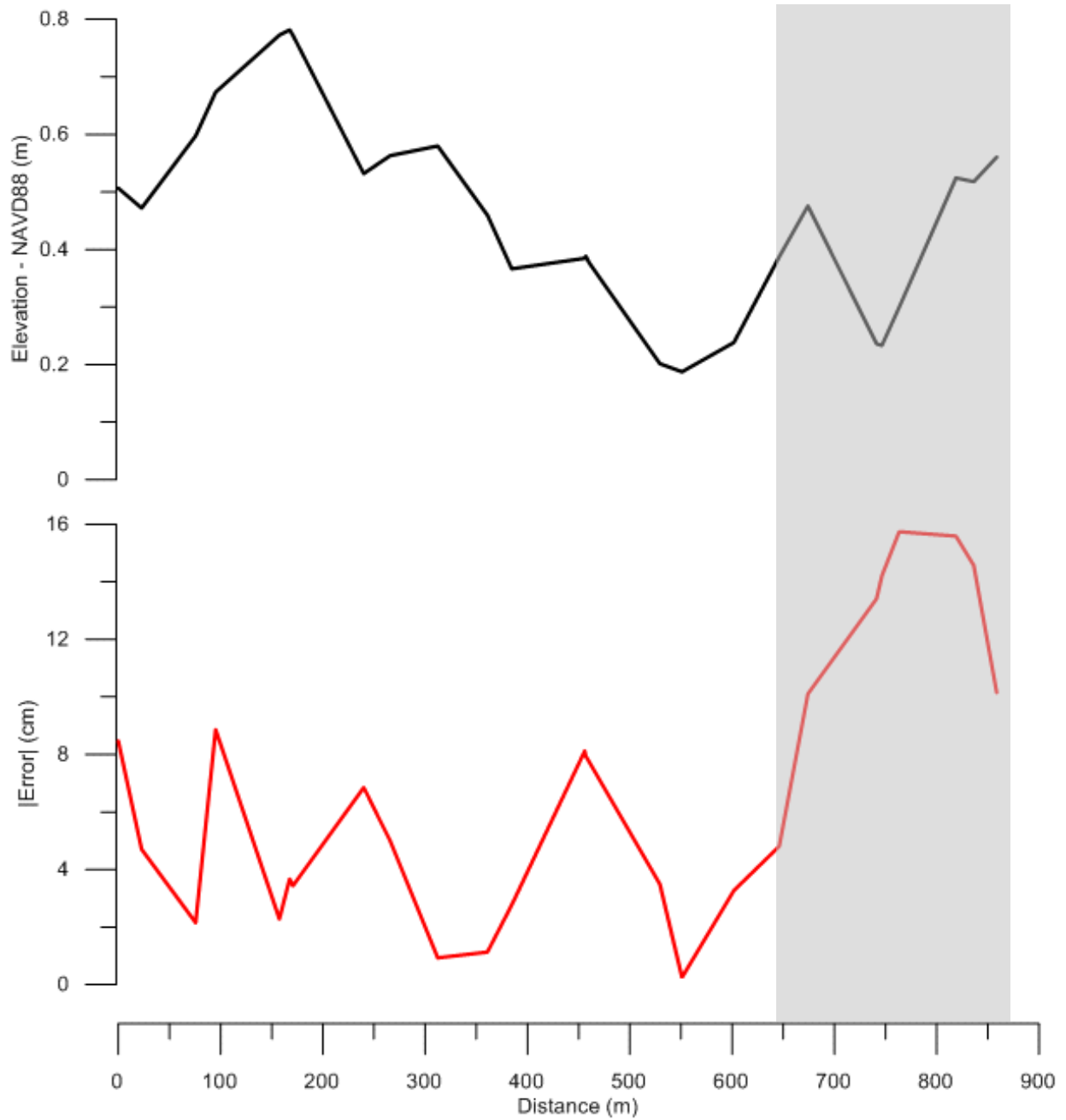


Figure 32 Plot of (top) elevation (m) and (bottom) absolute elevation error (cm) at Test Site 2 for the 80-m FEM along cross-section A.

Figure 33 through Figure 35 present the RMSE for all test sites using the 5-m DEM with cell area averaging techniques to obtain nodal elevations onto the FEM nodes. For mesh sizes of 10-m and below, the direct lookup performed best with the exception of Test Site 2, where the 9 cell average performed better at the 10-m scale. When the FEM size is larger than 10-m, more cells were required to contribute to the averaging scheme to obtain a lower RMSE. However, if too many cells were used, the error increased. The error increased because variations in topographic elevations averaged out (elevation smoothing).

It is interesting to note how the different interpolation methods and number of cells contributing to the average affect the topographic error of the FEMs. An increase of up to 20-cm RMSE was found if a 169 cell average was used versus a linear interpolation for a mesh size of 1.25-m. However, as mesh size increased, the overall RMSE difference between the interpolation techniques decreased, resulting in a few centimeters in increased error.

Since the data does not follow a normal distribution, the 95th and 5th percentile was computed in order to assess the accuracy of each FEM interpolated from the training-derived 5-m DEM (Table 9 through Table 11). The 95th percentile follows a similar trend as RMSE with respect to element size. Smaller elements produced higher accuracy with smaller cell averages. As the element size increased, more neighboring cells were needed to produce higher accuracy. However, if too many cells were used, accuracy decreased (Figure 36 through Figure 38). Additionally, the Shannon-Nyquist theorem (Shannon, 1949) is verified when using the 95th percentile as a means for assessing topographic accuracy. The accuracy in the 1.25-m mesh does not offer any significant decrease in error. In fact, the accuracy decreases as the mesh size decreases in some instances.

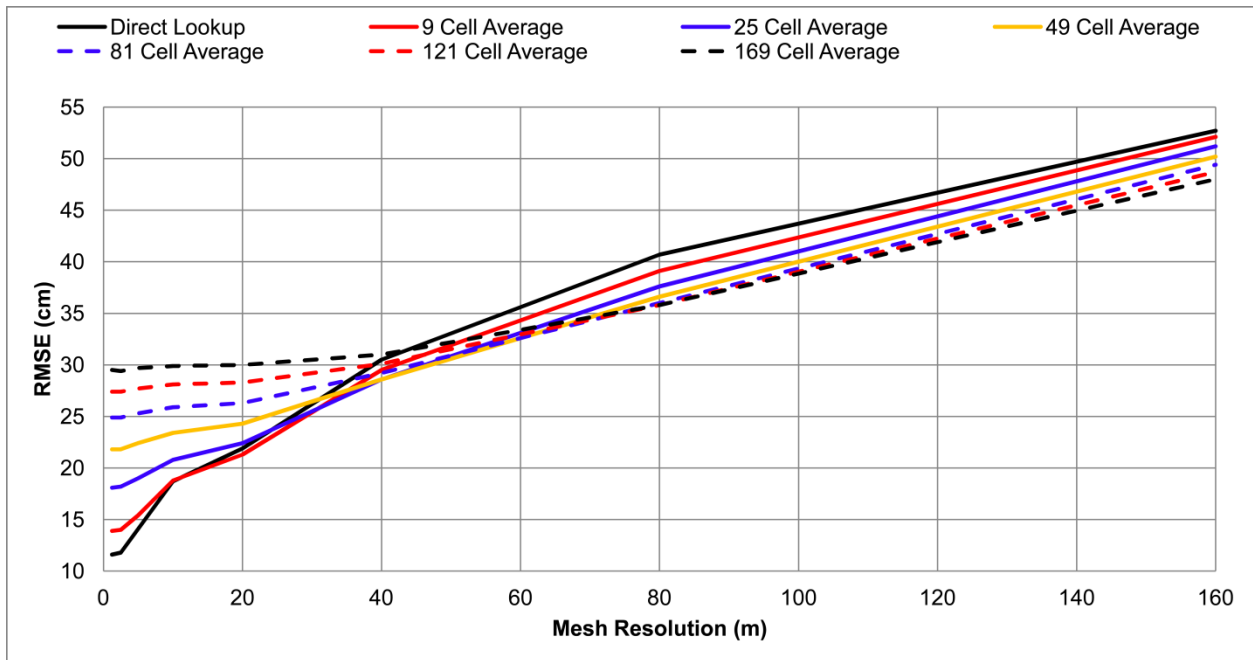


Figure 33 RMSE (cm) for Test Site 1 using area averaging from the 5-m DEM

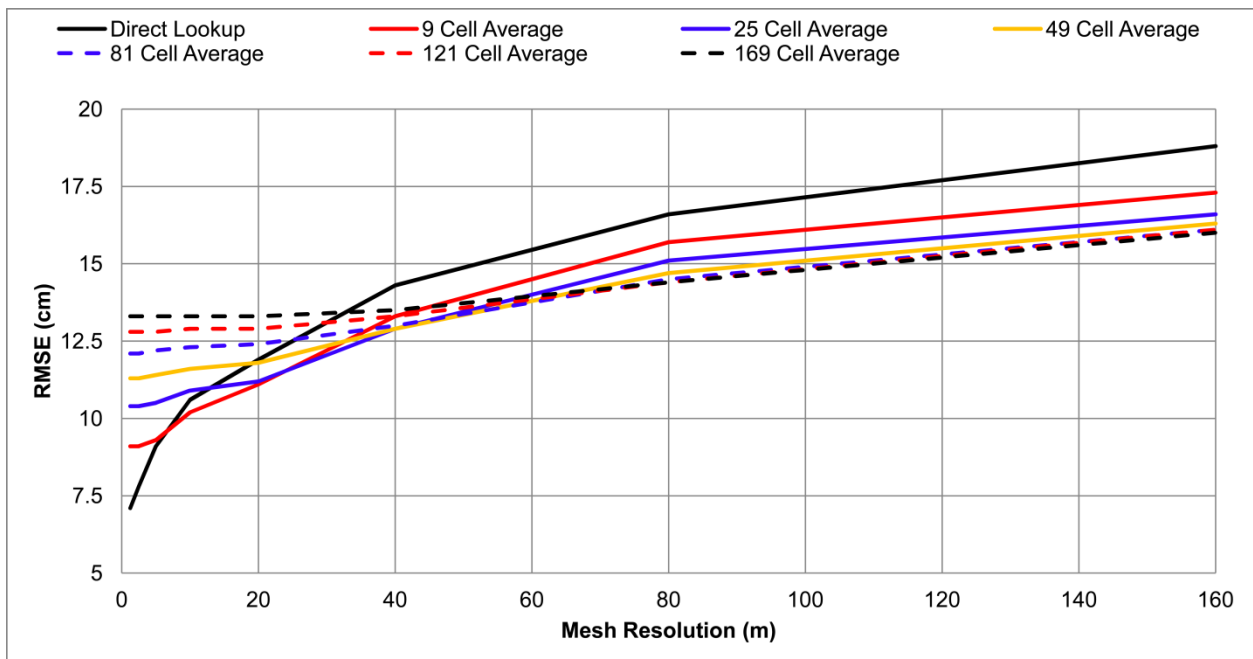


Figure 34 RMSE (cm) for Test Site 2 using area averaging from the 5-m DEM

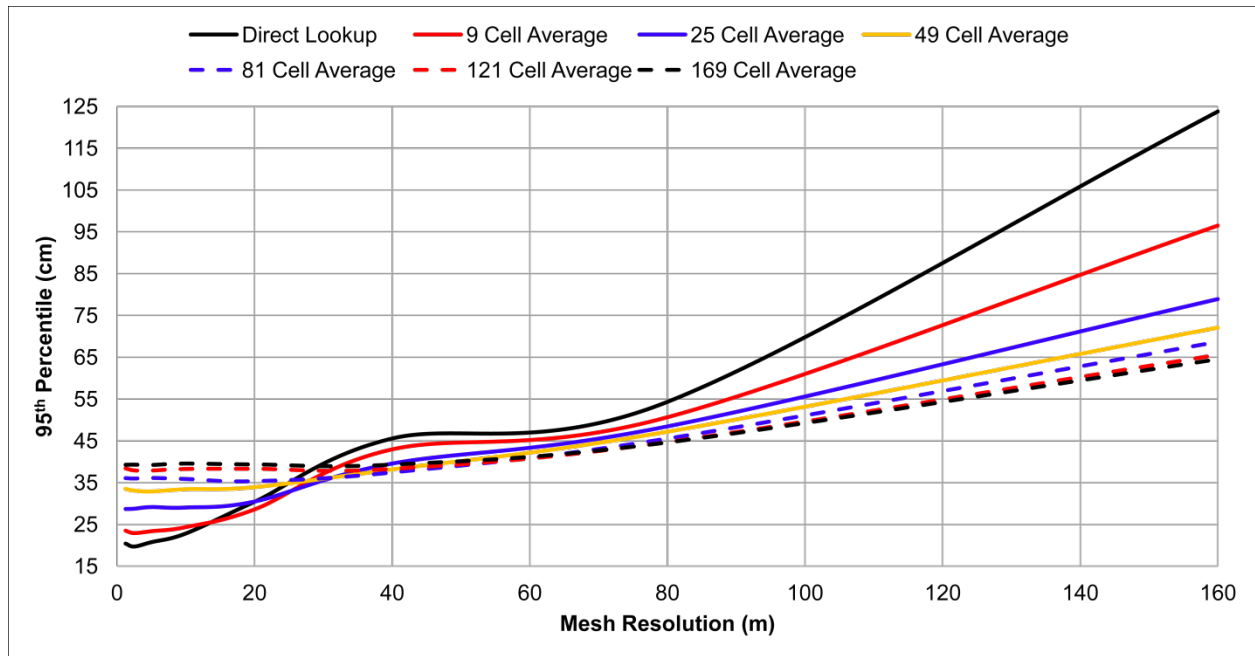


Figure 35 RMSE (cm) for Test Site 3 using area averaging from the 5-m DEM

Table 9 95th and 5th percentiles of elevation errors for Test Site 1 using the 5-m DEM

Size (m)	Direct Lookup		9 Cell Average (cm)		25 Cell Average (cm)		49 Cell Average (cm)		81 Cell Average (cm)		121 Cell Average (cm)		169 Cell Average (cm)	
	95 th	5 th	95 th	5 th	95 th	5 th	95 th	5 th	95 th	5 th	95 th	5 th	95 th	5 th
1.25	23.44	0.54	29.49	0.56	38.41	0.64	47.20	0.79	54.09	0.90	60.65	0.99	65.59	1.02
2.5	23.34	0.56	29.25	0.62	38.33	0.58	47.31	0.80	53.58	0.90	59.26	0.99	65.38	1.05
5	28.51	0.57	32.76	0.63	40.30	0.73	48.77	0.82	55.47	0.91	61.76	1.02	66.37	1.05
10	38.19	0.68	38.95	0.74	43.88	0.80	51.05	0.82	56.68	0.89	61.62	0.92	65.90	7.07
20	45.09	0.78	45.37	0.83	47.76	0.88	52.46	0.93	56.96	0.90	62.01	0.92	65.64	1.06
40	64.70	0.97	62.41	0.84	60.21	0.91	60.53	0.95	61.31	1.01	66.80	0.96	69.18	1.01
80	89.72	1.05	84.68	1.12	83.88	1.02	83.48	1.22	84.28	1.21	80.72	1.13	80.27	1.21
160	102.45	1.43	99.21	1.06	96.85	1.21	95.63	1.11	94.24	1.07	93.22	1.13	92.17	1.22

Table 10 95th and 5th percentiles of elevation errors for Test Site 2 using the 5-m DEM

Size (m)	Direct Lookup		9 Cell Average (cm)		25 Cell Average (cm)		49 Cell Average (cm)		81 Cell Average (cm)		121 Cell Average (cm)		169 Cell Average (cm)	
	95 th	5 th	95 th	5 th	95 th	5 th	95 th	5 th	95 th	5 th	95 th	5 th	95 th	5 th
1.25	14.47	0.36	18.43	0.50	21.20	0.57	22.78	0.61	23.99	0.71	25.30	0.78	26.17	0.78
2.5	15.45	0.37	18.65	0.50	21.05	0.55	22.73	0.58	24.15	0.64	25.36	0.73	26.27	0.77
5	18.50	0.46	19.19	0.49	21.35	0.52	22.71	0.54	24.04	0.64	25.06	0.69	26.08	0.76
10	21.90	0.48	21.21	0.50	22.11	0.57	23.41	0.61	24.74	0.68	25.54	0.73	26.50	0.78
20	24.26	0.63	22.58	0.60	22.89	0.65	23.86	0.61	24.87	0.76	25.71	0.73	26.41	0.75
40	29.51	0.74	27.04	0.71	25.90	0.70	25.78	0.75	25.76	0.81	26.01	0.81	26.49	0.87
80	33.90	0.89	31.45	0.92	29.81	0.91	29.55	0.92	28.89	0.92	28.47	0.84	28.23	0.84
160	39.43	0.97	34.51	1.06	32.66	0.97	32.09	1.06	31.90	1.01	31.51	1.01	31.31	1.01

Table 11 95th and 5th percentiles of elevation errors for Test Site 3 using the 5-m DEM

Size (m)	Direct Lookup		9 Cell Average (cm)		25 Cell Average (cm)		49 Cell Average (cm)		81 Cell Average (cm)		121 Cell Average (cm)		169 Cell Average (cm)	
	95 th	5 th	95 th	5 th	95 th	5 th	95 th	5 th	95 th	5 th	95 th	5 th	95 th	5 th
1.25	20.39	0.46	23.48	0.54	28.69	0.57	33.49	0.68	36.09	0.79	38.39	0.90	39.24	0.93
2.5	19.69	0.43	22.91	0.55	28.76	0.57	33.08	0.69	35.99	0.76	37.91	0.86	39.27	0.92
5	20.73	0.47	23.36	0.58	29.15	0.56	32.87	0.67	36.14	0.79	37.88	0.81	39.20	0.94
10	22.81	0.47	24.34	0.51	29.04	0.59	33.41	0.69	35.89	0.80	38.25	0.87	39.53	0.93
20	30.40	0.59	28.58	0.55	30.48	0.67	33.90	0.78	35.36	0.86	38.29	0.88	39.33	0.93
40	45.54	0.86	42.95	0.76	39.56	0.71	38.15	0.90	37.45	0.89	38.28	0.89	39.29	0.90
80	54.30	1.14	50.64	1.11	48.45	1.12	47.17	1.12	45.55	1.04	44.68	0.97	44.59	0.97
160	123.77	1.72	96.52	1.78	78.91	1.66	72.08	1.37	68.67	1.28	65.57	1.51	64.51	1.33

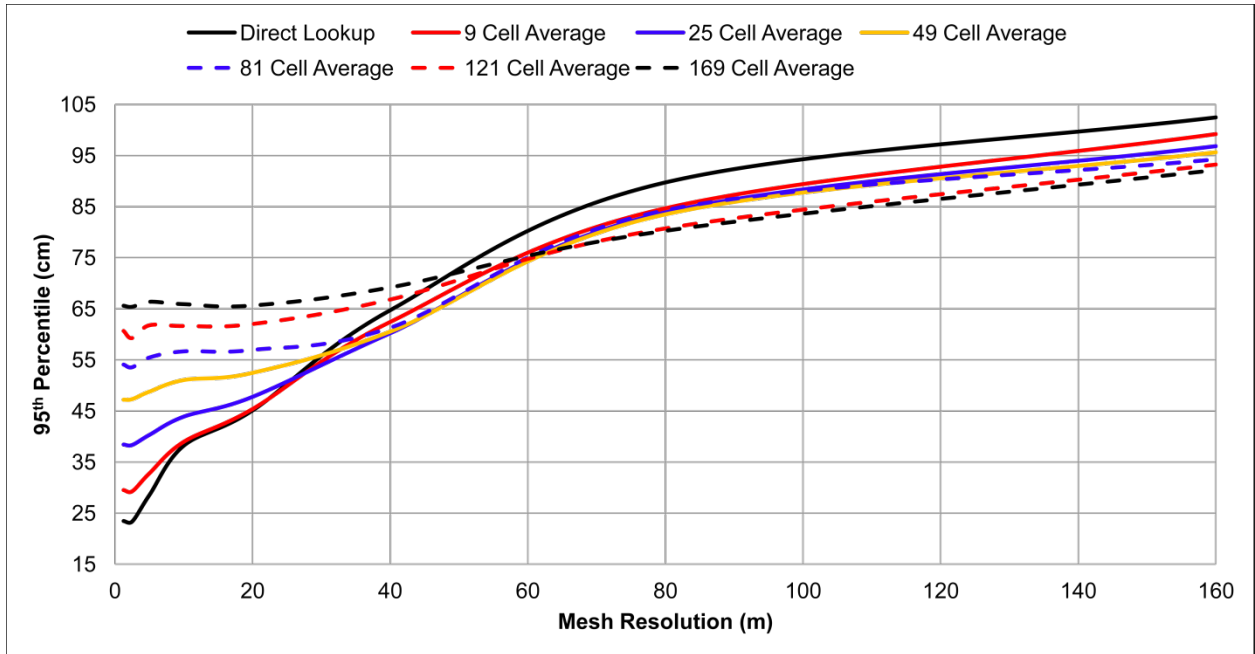


Figure 36 95th percentile for Test Site 1 using area averaging from the 5-m DEM

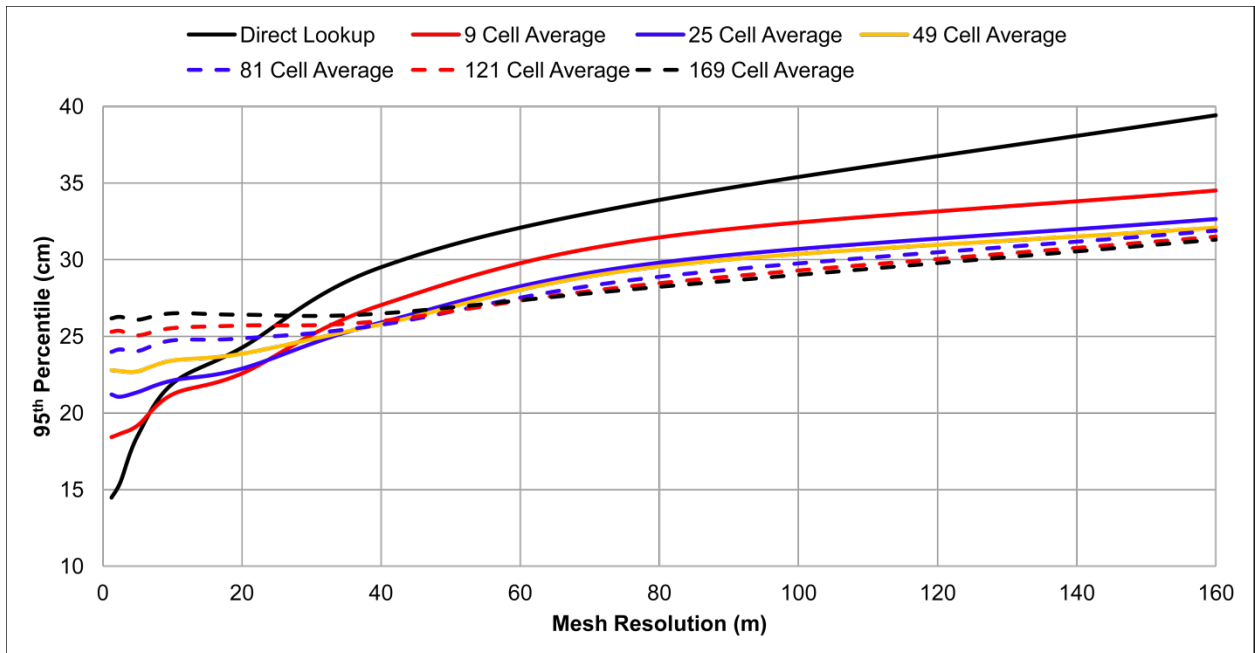


Figure 37 95th percentile for Test Site 2 using area averaging from the 5-m DEM

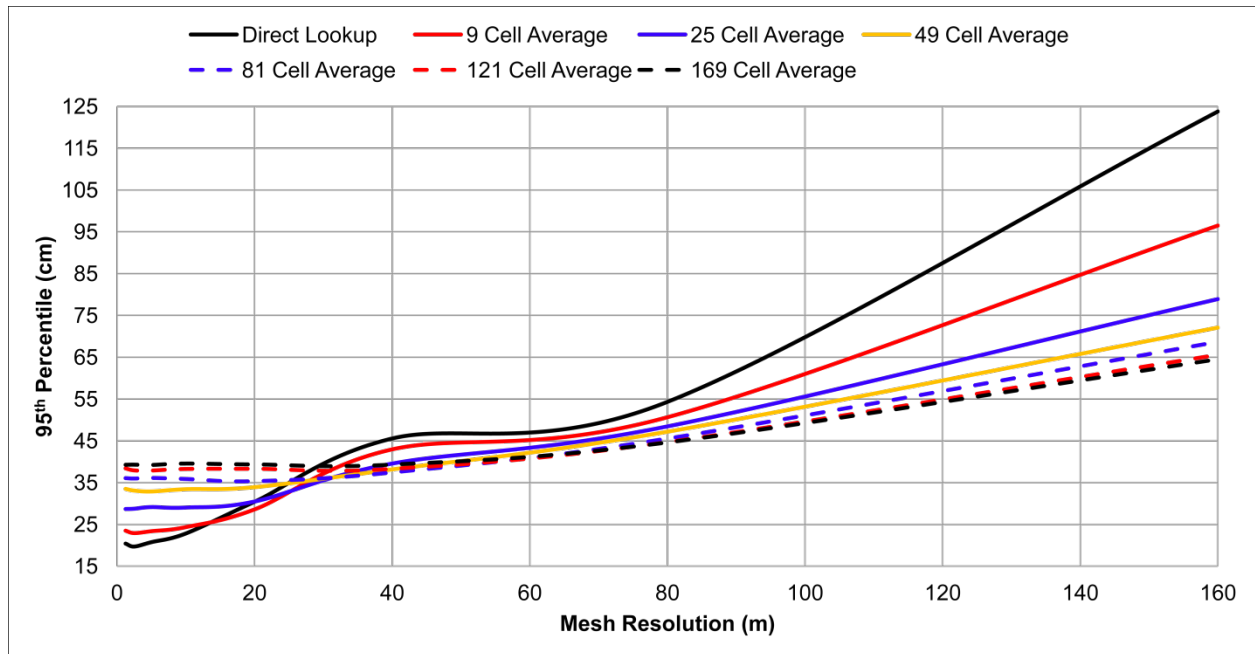


Figure 38 95th percentile for Test Site 3 using area averaging from the 5-m DEM

6.6 Louisiana Test Sites

In order to appreciate the methods presented and results obtained from the error analysis, two additional test sites were chosen in a similar coastal setting; southeastern Louisiana near the Lower 9th Ward and the Mississippi River (Figure 39). Figure 40 and Figure 41 show the urban and marsh area test sites, respectively.

Processed bare earth LiDAR was obtained from the Louisiana State Atlas LiDAR project (Louisiana State University, 2009). The LiDAR report stated an RMSE of 11.064-cm when referenced to 120 survey locations for the entire LiDAR coverage area (Watershed Concepts, 2004).

The Louisiana Urban Test Site has an 1120-m by 1120-m outer boundary and an inner offset of 160-m. The second test site, the marsh area, has an outer boundary of 500-m by 500-m

with an interior boundary offset by 50-m. This site is smaller because three sides are bounded by water features where LiDAR points have been removed to solely represent the bare earth terrain. The methods and computations are similar to that of the previous test sites in southern Mississippi.



Figure 39 Southern Louisiana test site locations outlined in red.

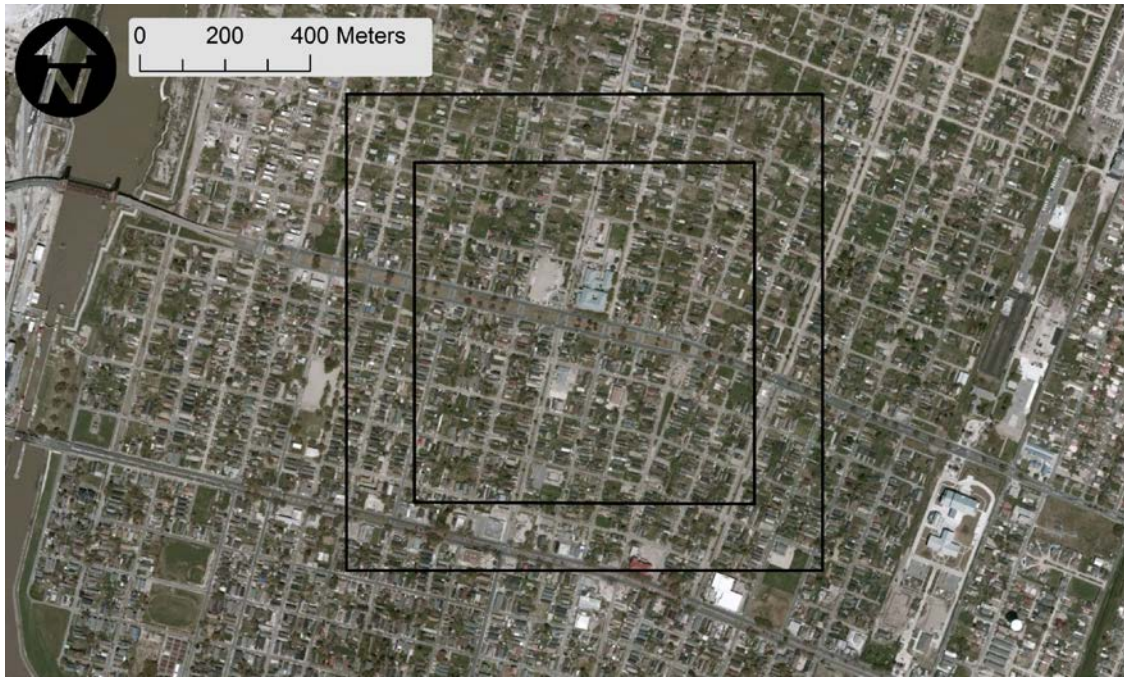


Figure 40 Louisiana Urban Test Site with the outer and inner boundary in black

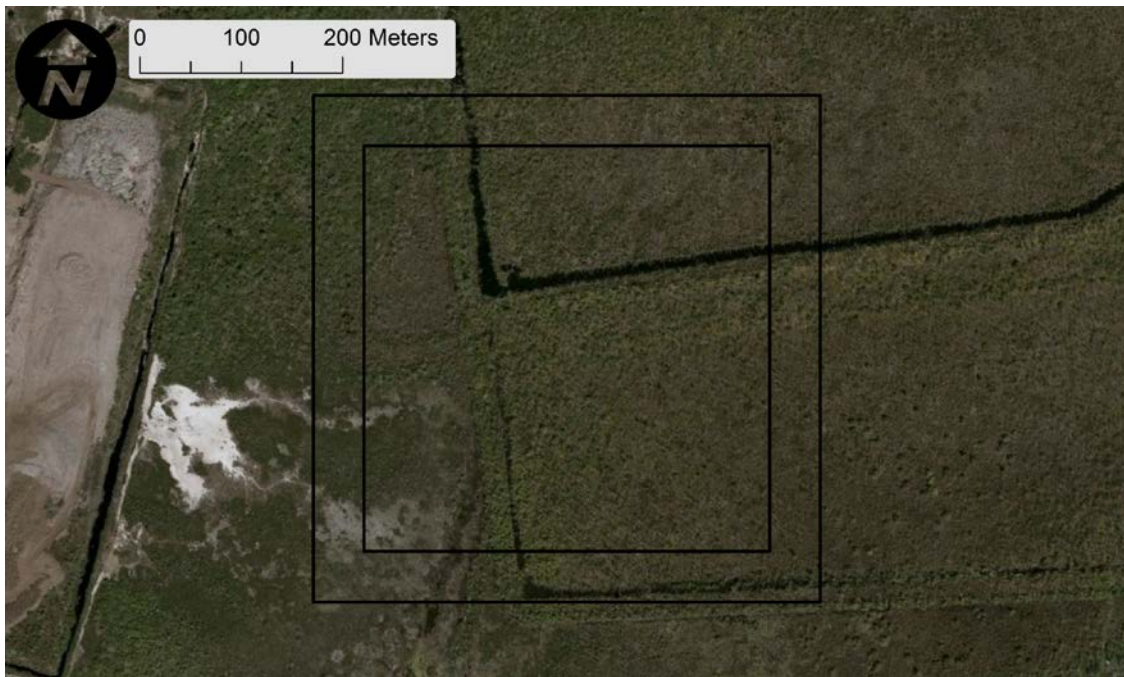


Figure 41 Louisiana Marsh Test Site with the outer and inner boundary in black

Elevation error was computed in terms of RMSE equivalent to the Pascagoula test sites. Table 12 presents the RMSE across all FEMs and DEMs that obtained elevations from the training dataset using a linear interpolation. The Marsh Test Site is limited to a maximum of 20-m due to its boundary size and that it's bordered by water; elements larger than 20-m would yield erroneous results. Similar to the results shown in Table 5 for the Pascagoula test sites, the DEMs contain more topographic error compared to the FEMs at the same scale. The higher resolution DEMs tend to perform better than the lower resolution DEMs. Also, the training dataset to DEM error reaches a minimum at a grid size of 2.5-m and the error slightly increases with a grid size of 1.25-m, for the Marsh Test Site, hence decreasing the grid size does not always decrease the error. Similarly, for the Urban Test Site, the error is not significantly decreased when the mesh or DEM size is less than 2.5-m. This finding follows the Shannon-Nyquist theorem (Shannon, 1949). Since the bare earth LiDARs point spacing is about 5-m, decreasing the sampling size to less than half the 5-m source data density (2.5-m) tends to no longer decrease the error. Results obtained in Table 12 show that DEM grid and element size can significantly alter the topographic accuracy. Errors range from 6.3-cm to 19.5-cm for the Urban Test Site, a difference of almost 0.5-ft.

Table 12 RMSE for all both test sites with a linear interpolation of the training dataset onto the finite element meshes and DEMs

Size (m)	Training to FEM - RMSE (cm)		Training to DEM - RMSE (cm)	
	Urban	Marsh	Urban	Marsh
1.25	6.3	10.7	6.5	10.9
2.5	6.3	10.7	6.8	10.6
5	6.7	10.8	7.7	11.6
10	8.3	11.4	10.1	12.2
20	11.4	14.2	13.0	16.9
40	14.6	-	16.6	-
80	16.8	-	20.6	-
160	19.5	-	23.0	-

Comparing interpolation of the 5-m DEM and 10-m DEM to each of the FEMs is shown in Table 13 and Table 14 for a linear, IDW, and NN interpolation. For each mesh size and test site, errors were less for the 5-m DEM as the source elevation rather than the 10-m DEM. Error differences are larger for the smaller mesh sizes (around 2-cm) and less at element sizes of 20-m and larger. It was expected that meshes with element sizes of 20-m and larger would perform similarly, as found for the Pascagoula test sites, and it follows the Shannon-Nyquist theorem (Shannon, 1949).

Table 13 RMSE for the Urban Test Site using linear, IDW, and NN interpolation from the 5-m and 10-m DEM

Size (m)	5m DEM to FEM- RMSE (cm)			10m DEM to FEM - RMSE (cm)		
	Linear	IDW*	NN	Linear	IDW*	NN
1.25	6.9	8.2	6.8	8.8	9.1	8.6
2.5	6.9	8.2	6.9	8.9	8.9	8.6
5	7.1	8.6	7.1	8.9	8.8	8.6
10	8.3	9.1	8.3	9.1	9.2	9.0
20	11.2	11.6	11.3	11.2	11.4	11.3
40	14.4	14.7	14.4	14.1	14.3	14.2
80	16.7	16.9	16.7	16.5	16.7	16.5
160	19.6	19.7	19.6	19.5	19.9	19.6

*Using three closest points

Table 14 RMSE for the Marsh Test Site using linear, IDW, and NN interpolation from the 5-m and 10-m DEM

Size (m)	5m DEM to FEM- RMSE (cm)			10m DEM to FEM - RMSE (cm)		
	Linear	IDW*	NN	Linear	IDW*	NN
1.25	10.9	11.1	10.8	11.7	12.1	11.6
2.5	10.9	11.4	10.8	11.7	11.9	11.6
5	11.0	12.0	10.9	11.7	11.8	11.6
10	11.3	11.9	11.2	11.9	11.9	11.9
20	13.9	14.2	13.9	13.4	13.8	13.6

*Using three closest points

Figure 42 and Figure 43 present RMSE for the Urban and Marsh Test Sites using the 5-m DEM with direct lookup and area averaging methods to interpolate nodal elevation for the FEM. For mesh sizes of 1.25-m and 2.5-m, direct lookup performed best for the urban area and 1.25-m

to 5-m for the marsh area. For both Test Sites, as the mesh elements became large, topographic error was reduced when more DEM grid cells were included in the averaging scheme; however, if too many grid cells were used, the error began to increase. As expected, accuracy in the marsh area tends to improve when using less DEM grid cells than the urban area. The marsh topography is relatively uniform with minimal gaps in data since it does not contain manmade features like the urban test site.

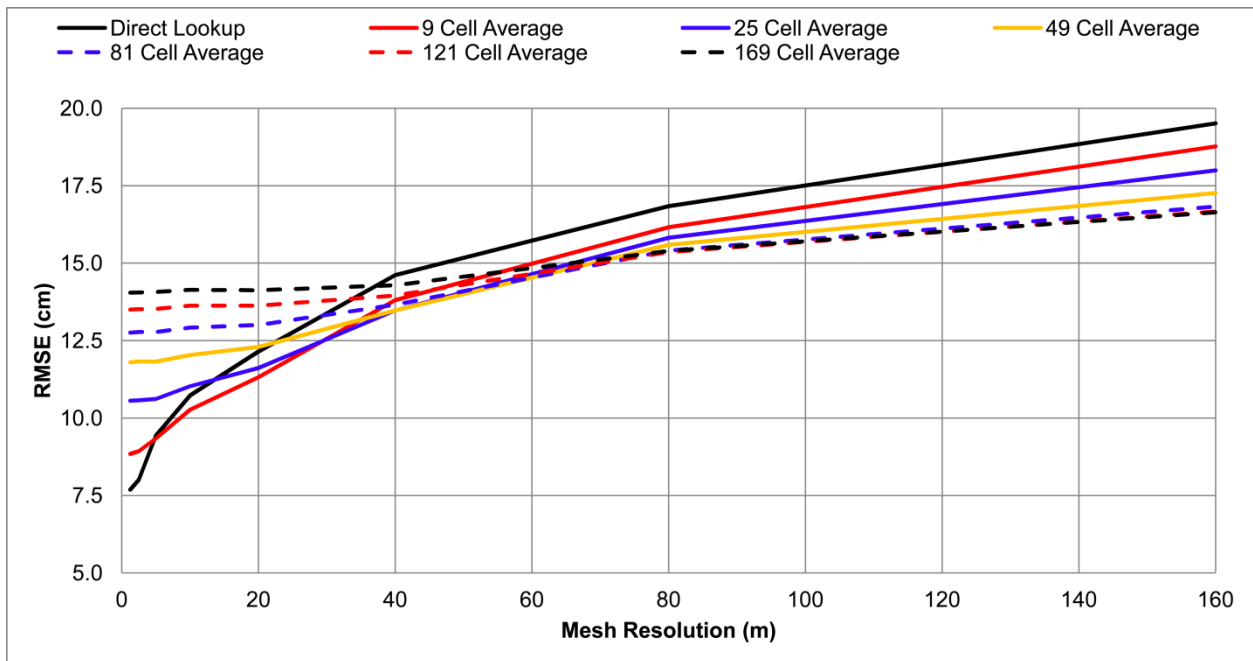


Figure 42 RMSE (cm) for the Urban Test Site using area averaging from the 5-m DEM

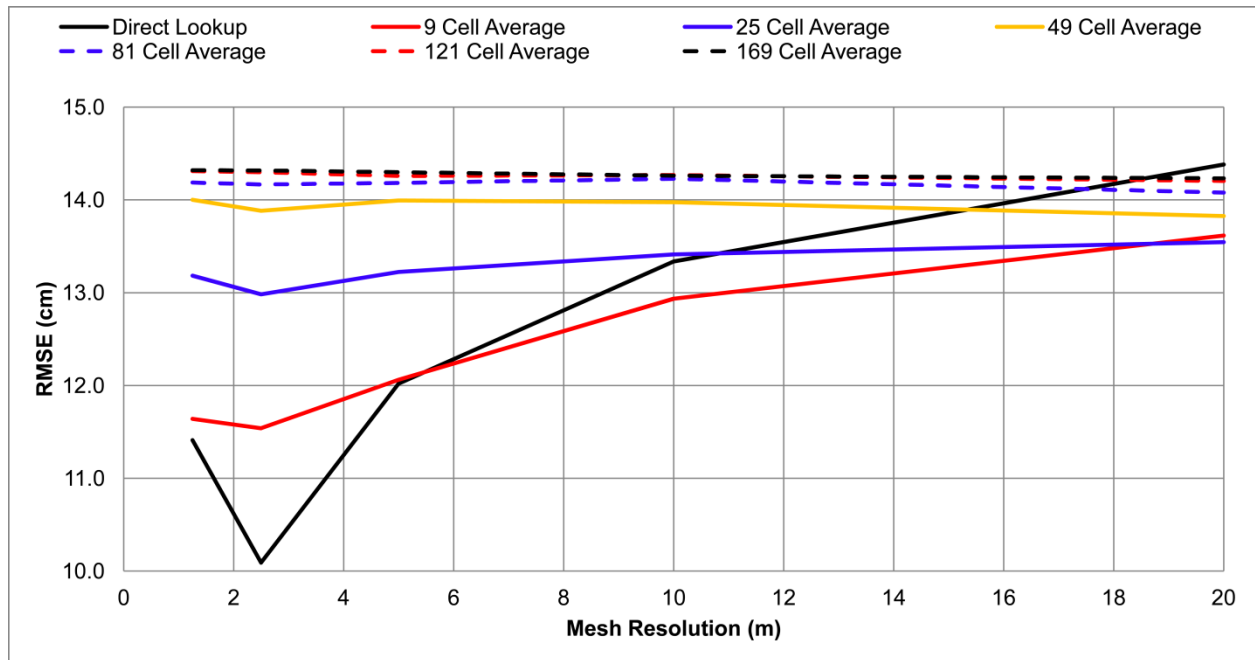


Figure 43 RMSE (cm) for the Mash Test Site using area averaging from the 5-m DEM

6.7 Preliminary Conclusions

The first finding is that vertical errors in elevation do not follow a normal distribution. Careful consideration should be exercised when reporting vertical accuracy as related specifically to $RMSE_z$. The results obtained during this preliminary error assessment confirm the validity of using a DEM as an elevation source for a FEM, as current practice dictates. Software tools popular in geospatial analysis such as ESRI ArcGIS (ESRI, 2011a) and Global Mapper (Blue Marble Geographics, 2011) are fine tuned for working with raster DEM products rather than irregular spaced points. Secondly, the results demonstrate that the Shannon-Nyquist theorem (Shannon, 1949) holds true for terrain grid resolution. It is shown that having a DEM or FEM size less than half that of the data density yields no significant decrease in RMSE. Also, DEM size can be related to element size. Results show that if an element size is 20 -m, a 10-m

DEM should suffice, rather than using the bare earth or a higher resolution DEM as the elevation source, in terms of topographic error. Careful consideration should be exercised when choosing a DEM grid size or FEM size with respect to the data capacity and computational resources available.

Between three interpolating routines (linear, IDW, and NN) as well as DEM direct lookup and cell averaging, cell averaging generally performed better than the other methods, for element sizes larger than 20-m. With respect to only the interpolation methods, linear and NN performed best, with IDW resulting in increased error when non bare earth features are removed. Linear is preferred over NN due to its simple parameterization and efficient algorithm. Linear interpolation also performs faster than IDW. In all, cell averaging is the method of choice when element edge lengths are larger than 20-m. As well, cell averaging performs faster than linear, IDW, and NN.

Chapter 9 will use the methodology presented on three large regions of coastal Mississippi to compare topographic and hydrodynamic error.

CHAPTER 7: DEM DEVELOPMENT

7.1 Terrain Dataset

ESRI ArcGIS 10.0 (ESRI, 2011a) was the software program utilized to develop all DEMs. The methods outlined are similar to those employed by Medeiros *et al.* (2011) wherein a terrain dataset (TDS) within ArcGIS was utilized. A TDS is a multiresolution, TIN-based surface constructed from surface measurements that are stored in a geodatabase. The measurements are usually LiDAR, sonar and other photogrammetric sources. TDS are stored in a feature dataset within a personal or file geodatabase, or Spatial Database Engine (SDE). Not only can surface point measurements be stored and used, but other feature classes can be incorporated into the TDS such as polyline and polygon shapefiles (i.e. breaklines). The rules of the TDS dictate how features within the feature dataset are used in the terrain. The advantage of the TDS is how it stores data. It does not actually store surfaces as a raster or TIN, it references feature classes stored in a geodatabase for faster data retrieval and TIN surface derivation on the fly (ESRI, 2011b). Another advantage of the TDS over other methods is the storage capability of geodatabases. Since a typical 465-m² (5000-ft²) of LiDAR point cloud data can contain roughly 1.1 million points (Coggin, 2008), data management and size limitation become an issue when working with large areas. Feature datasets have the ability to store multipoint shapefiles for use in a TDS. An ESRI multipoint shapefile is a geometry type that can represent thousands of points that are grouped into one individual shape. Therefore a few thousands records can store millions of points using the multipoint feature class. Since a file geodatabase (fGDB) can store a

TDS of up to one terabyte (TB), it is convenient to employ a TDS when working with high-density LiDAR data (Medeiros *et al.*, 2011). One other capability of a TDS is the “TDS to Raster” function. A TDS can be converted to a raster, in which a grid cell size and interpolation method (linear or natural neighbor) is specified (ESRI, 2011b).

The procedure for creating a topographic DEM is similar to that of Medeiros *et al.* (2011), except that it is updated for ArcGIS 10.0 and slightly modified for this study:

1. Create a fGDB and a feature dataset.
2. Use the Point File Information tool in the 3D Analyst Toolbox to create a point file feature class for the LiDAR dataset. This provides information on the dataset such as point spacing and total number of points. The point spacing is needed in the next step.
3. Convert bare earth text (*.txt) (LiDAR) data to a multipoint feature class using the ASCII 3D to Feature class tool in the 3D Analyst Toolbox. During this process, a Z Factor of 0.3048 was specified to convert elevations units of feet to meters.
4. Convert all multipoint features classes to a common horizontal datum. For this study UTM Zone 16N was used.
5. Remove (clip) all LiDAR points and other feature class data that do not fall within the project boundary. This includes LiDAR points that fall inside the bathymetric dataset (i.e. rivers, lakes and bays) and points that lie outside the area of interest.
6. Import the clipped multipoint feature class into the feature dataset.
7. Import any additional feature classes such as breaklines and the project boundary polygon into the feature dataset. Note: All feature classes imported into the feature dataset must be projected to the same coordinate system.

8. Build the TDS within the feature dataset. The parameters used are in Table 15. A window size with a point selection method of Z Minimum was used for pyramid generation and the default pyramid values computed by ArcGIS 10.0 were employed.
9. The Terrain to Raster tool in the 3D Analyst Toolbox was used to convert the terrain to a raster. A required input parameter is the size of the raster grid cells and interpolation scheme. A linear interpolation was used.

Table 15 Parameters used during generation of the Terrain (ESRI, 2011a; Medeiros *et al.*, 2011)

Feature Class	Height Source	Surface Feature Type (SFTType)
LiDAR Points	Shape	Mass points (data source containing elevations of points)
Hydro 3D Breaklines	Shape	Hard Line (place a TIN triangle edge along the line and defines an interruptions in slope or surface smoothness)
Model Boundary Polygon	Shape	Hard Clip (Similar to hard line, except triangulation stops and does not continue on the other side of the line)

7.2 Test and Training Data

In order to fully evaluate the accuracy of the DEMs, two sub-datasets were derived from the each equilateral test regions' bare earth LiDAR dataset, training and test dataset (Desmet, 1997; Chaplot *et al.*, 2006; Bater & Coops, 2009). This was done using the 'Subset Features' tool in the ArcGIS Geostatistical Analyst Toolbox wherein the training dataset was produced by randomly selecting 90-percent of the LiDAR points with the test dataset consisting of the

remaining 10-percent. This was done for the purpose of assessing the quality of the DEM without destroying the reliability of the LiDAR data itself. In general, the TDS was built from the training dataset, completely withholding the test points. This process is not intended to examine the actual precision of the terrain represented by the LiDAR and DEM surface, but rather to validate the tools and parameters (interpolation scheme and grid size) used to predict elevations at unknown locations (Bater & Coops, 2009).

7.3 Raster DEM Generation

Seven grid sizes of 1.25-m, 2.5-m, 5-m, 10-m, 20-m, 40-m and 80-m were generated for each region. Two of the grid sizes were determined based on the point density of the raw, bare earth LiDAR, 5-m and 2.5-m. The minimum point spacing for all LiDAR tiles is 3.5-m (~11.5-ft). The average post spacing for all LiDAR tiles is ~5.2-m (~17-ft). General rules of thumb deem a DEM with grid size less than that of the original source data density is insufficient (McCullagh, 1988; Florinsky, 1998, 2002; Liu *et al.*, 2008); however, a DEM raster cell size of 2.5-m and 1.25-m is used to test this rule based on the Shannon-Nyquist theorem (Shannon, 1949; Hengl, 2006). Other cell sizes were tested alongside 1.25-m, 2.5-m, and 5-m to evaluate how the larger DEM grid cell sizes compared to the lower magnitude cell sizes.

7.4 Results of LiDAR DEM Generation

Using the methodology described in the previous section, a total of 21 land-only DEMS were produced, seven for each equilateral region, from the training dataset. The boundary of the training equilateral region is described in the following chapter. Figure 44 through Figure 47 present each DEM from a grid cell size of 1.25-m to 80-m resolution. It is clear that as the grid

size is increased, the quality of the DEM, in terms of visual appearance, degrades. Elevations become smoothed and pixilation starts to appear, especially with the 40-m and 80-m DEMs.

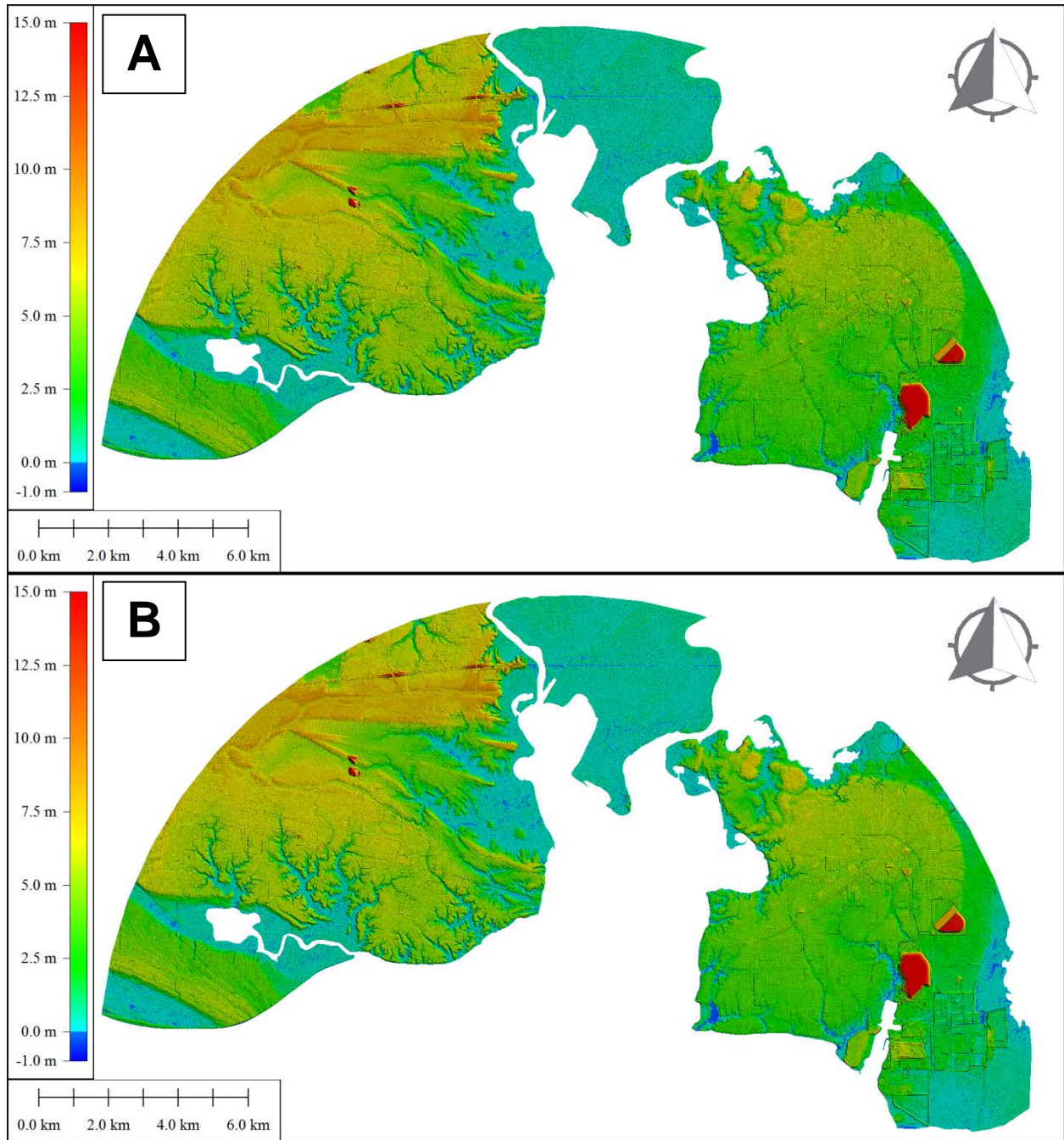


Figure 44 A) 1.25-m training dataset-derived DEM
B) 2.5-m training dataset-derived DEM

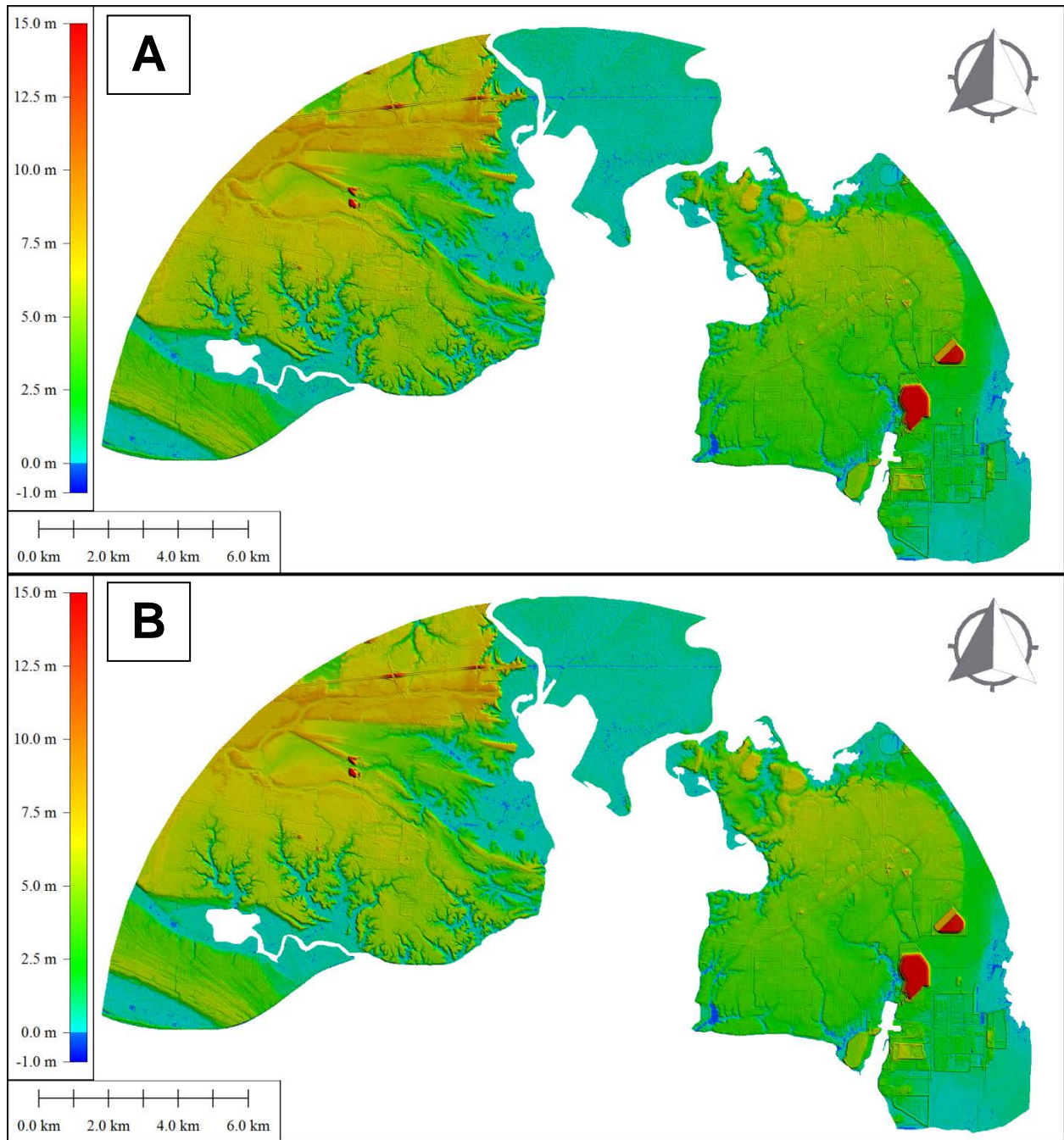


Figure 45 A) 5-m training dataset-derived DEM B) 10 m training dataset-derived DEM

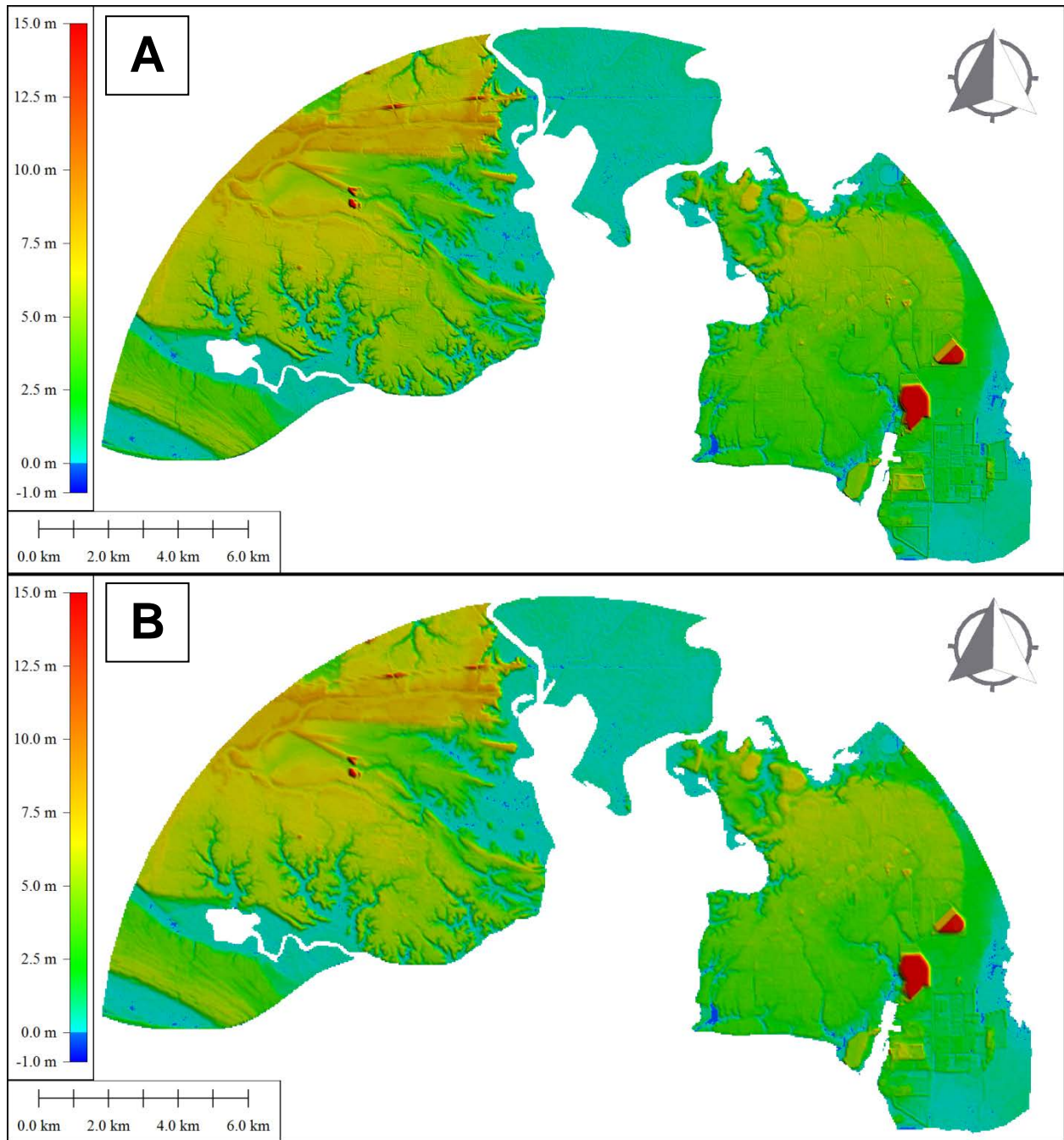


Figure 46 A) 20-m training dataset-derived DEM
B) 40-m training dataset-derived DEM

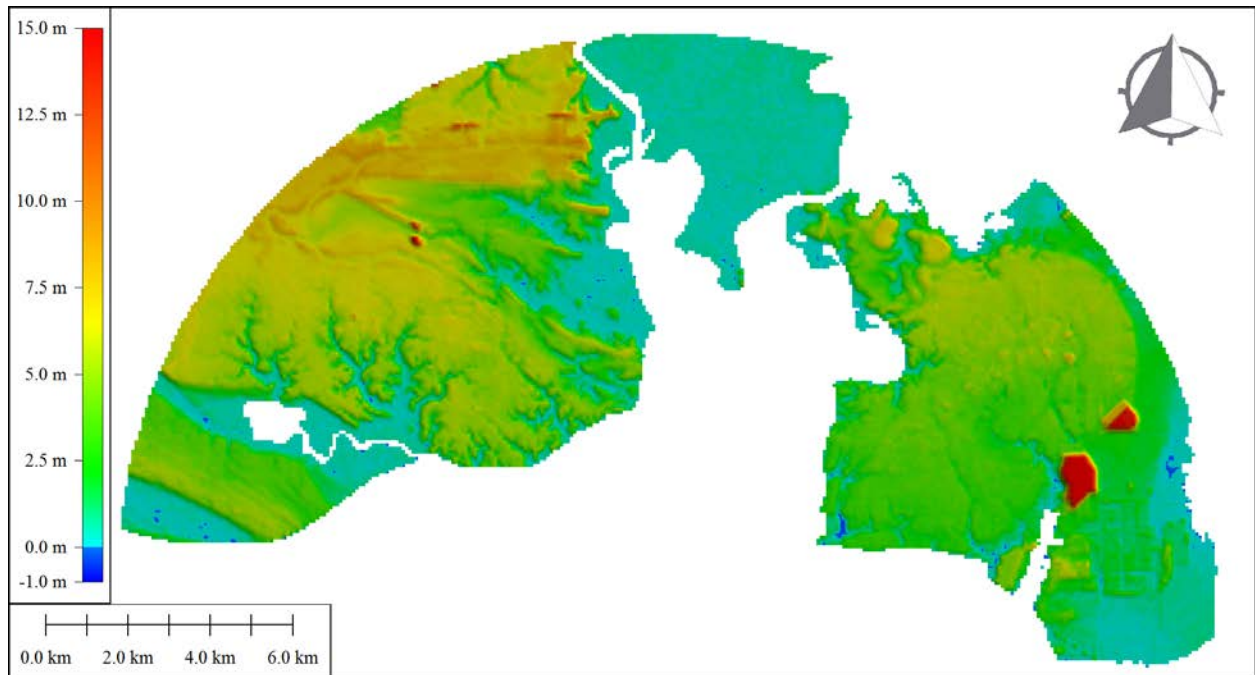


Figure 47 80-m training dataset-derived DEM

Vertical error between the training-derived DEMs and the test dataset was assessed in terms of RMSE (see Equation 6.1). Table 16 presents the RMSE for each equilateral region training-derived DEM when compared to the test point dataset. As expected, RMSE increases with DEM size. Also, the Shannon-Nyquist theorem (Shannon, 1949) is further validated for use with terrain datasets. When the grid size is decreased from 5-m to 2.5-m, RMSE is reduced by 1.5-cm, 0.6-cm, and 1.9-cm, for the left, center, and right zones, respectively. Further reducing from 2.5-m to 1.25-m in cell size yields RMSE of 0.4-cm, 0.2-cm, and 0.6-cm, for the left, center, and right zones, respectively. RMSE does not significantly reduce when decreasing the DEM size to lower than of half the source data density, ~5-m. Further, the scale of RMSE compares well to the results obtained in Chapter 5 with respect to the RMSE in the DEMs for Pascagoula Test Sites One, Two, and Three (Table 5). The left and right equilateral zones

contain a mix of urban, marsh, and forested regions whereas the center region is exclusively marsh area. For example, Pascagoula Test Site One was characterized by urban and forested regions and yielded an RMSE of 9.9-cm for a grid size of 2.5-m. The left and right Zones with a grid size of 2.5-m contain an RMSE of 10.6-cm and 11.1-cm, respectively. These values complement the RMSE yielded in the Pascagoula Test Sites. Pascagoula Test Site Two, the marsh area, had an RMSE of 8.9-cm with a grid size of 2.5-cm. The center zone is exclusively marsh and contains an RMSE of 8.9-cm for a grid size of 2.5-m. Again, this matches well with the preliminary Pascagoula Test Sites. This trend continues for all grid sizes.

Table 16 RMSE of each training-derived DEM when compared to the test points

Size (m)	Left Zone DEM RMSE (cm)	Center Zone DEM RMSE (cm)	Right Zone DEM RMSE (cm)
1.25	10.2	8.7	10.5
2.5	10.6	8.9	11.1
5	12.1	9.5	13.0
10	16.3	11.3	18.4
20	24.4	14.0	29.2
40	38.6	17.3	44.4
80	59.7	20.5	66.4

7.5 Seamless Pascagoula Floodplain DEM Generation

With an average minimum element size in the in-bank Pascagoula model of ~10-m (presented in Chapter 8) and with the DEM RMSE results presented in Table 16, a 5-m DEM was created using 100-percent of the bare earth LiDAR points for the entire study area (refer Figure 21) using the methods presented in section 7.1. Breakline data was also incorporated. The topographic DEM was then merged with the bathymetric dataset. Figure 49 through Figure 53 present the seamless bathymetric/topographic 5-m DEM of the Pascagoula study region.

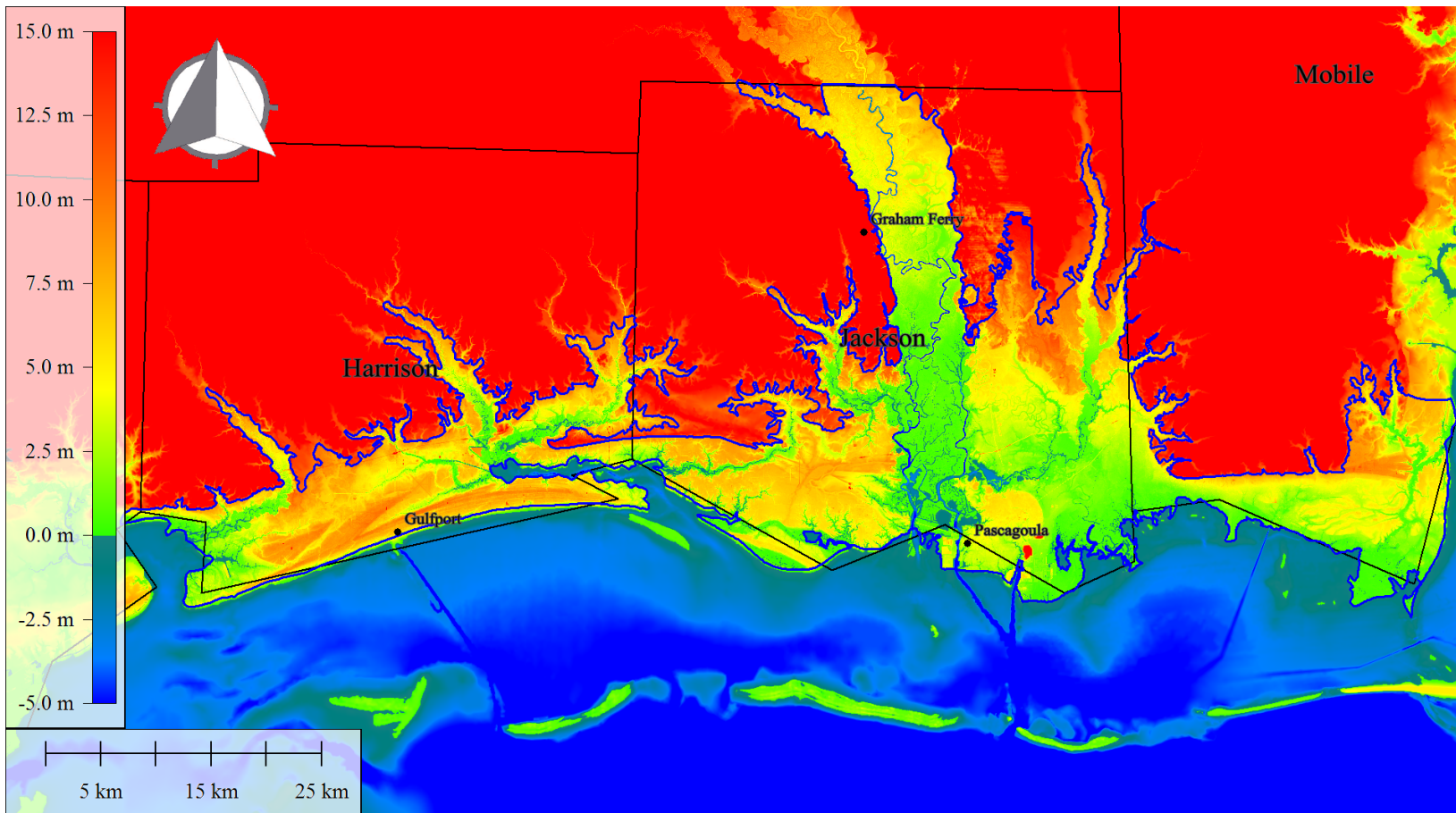


Figure 48 Seamless 5-m DEM of study including offshore bathymetry. The blue line is the mesh boundary. Elevations beyond the mesh boundary are obtained from the NED 1-arc-second DEM (Gesch *et al.*, 2002; Gesch, 2007).

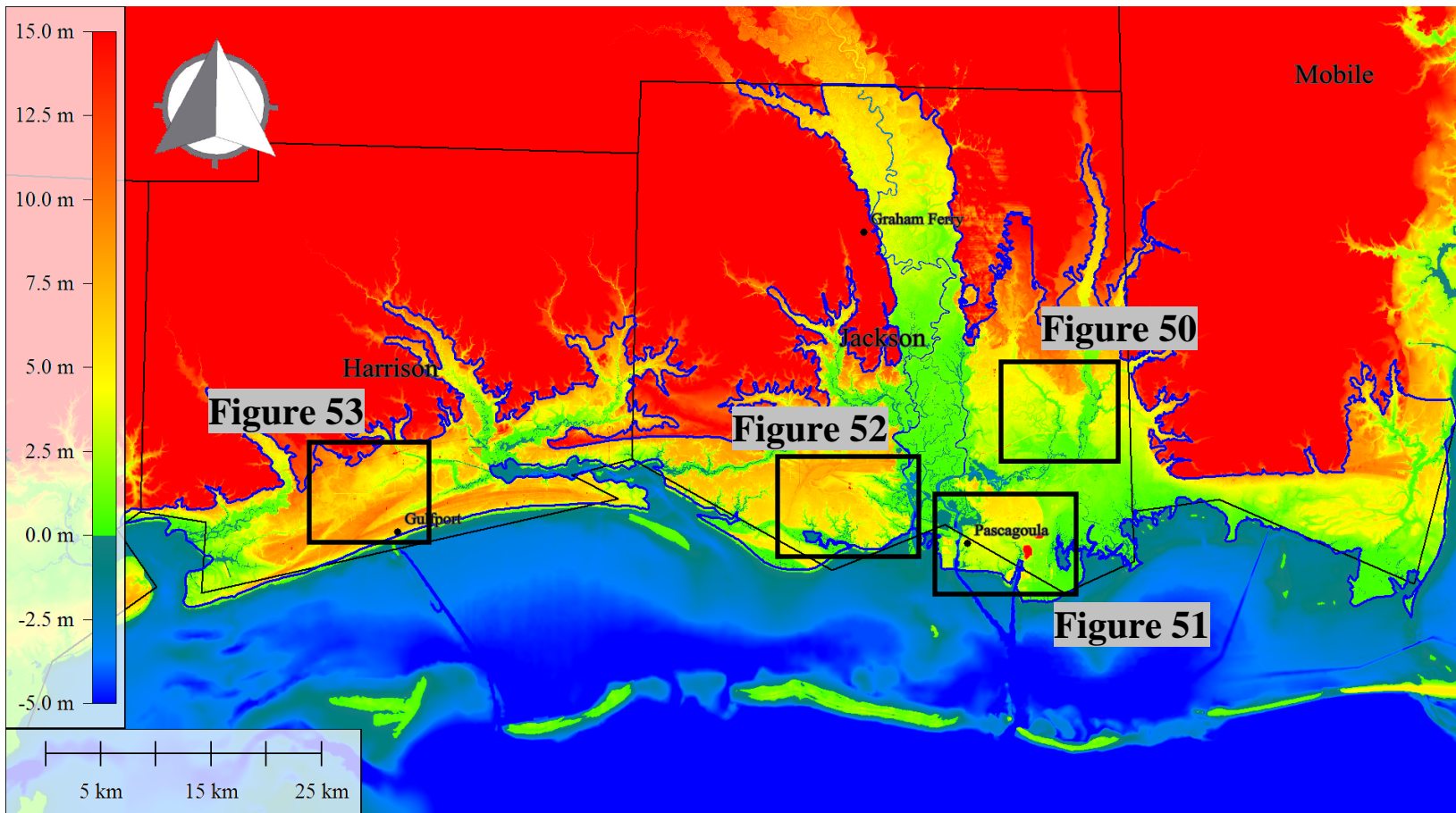


Figure 49 Inset boxes for zooms of the 5-m DEM found in Figure 50 through Figure 53.

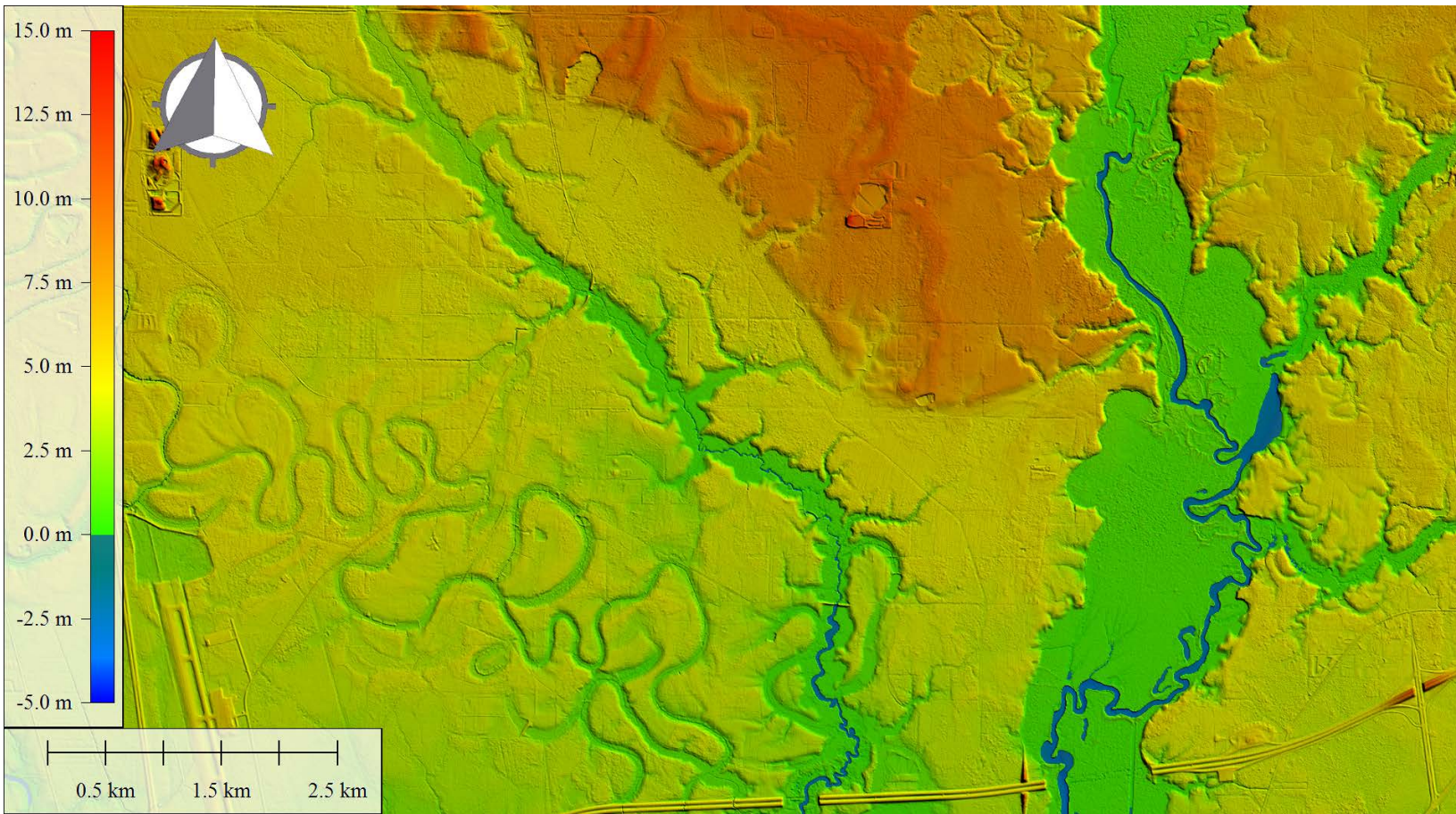


Figure 50 5-m DEM near the upper Escatawpa River

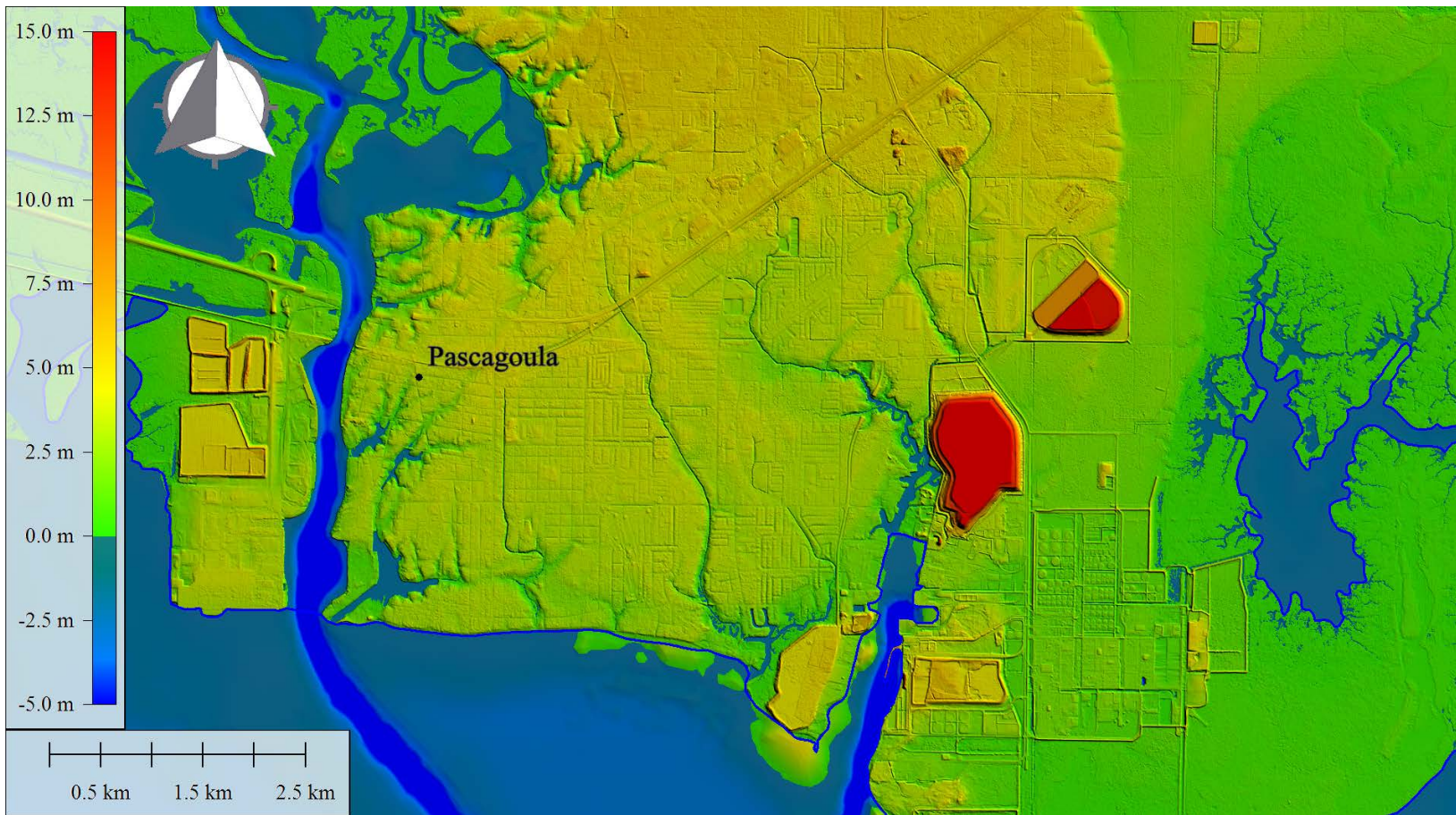


Figure 51 5-m DEM near the East Pascagoula Inlet and Port of Pascagoula with floodplain boundary (blue line).

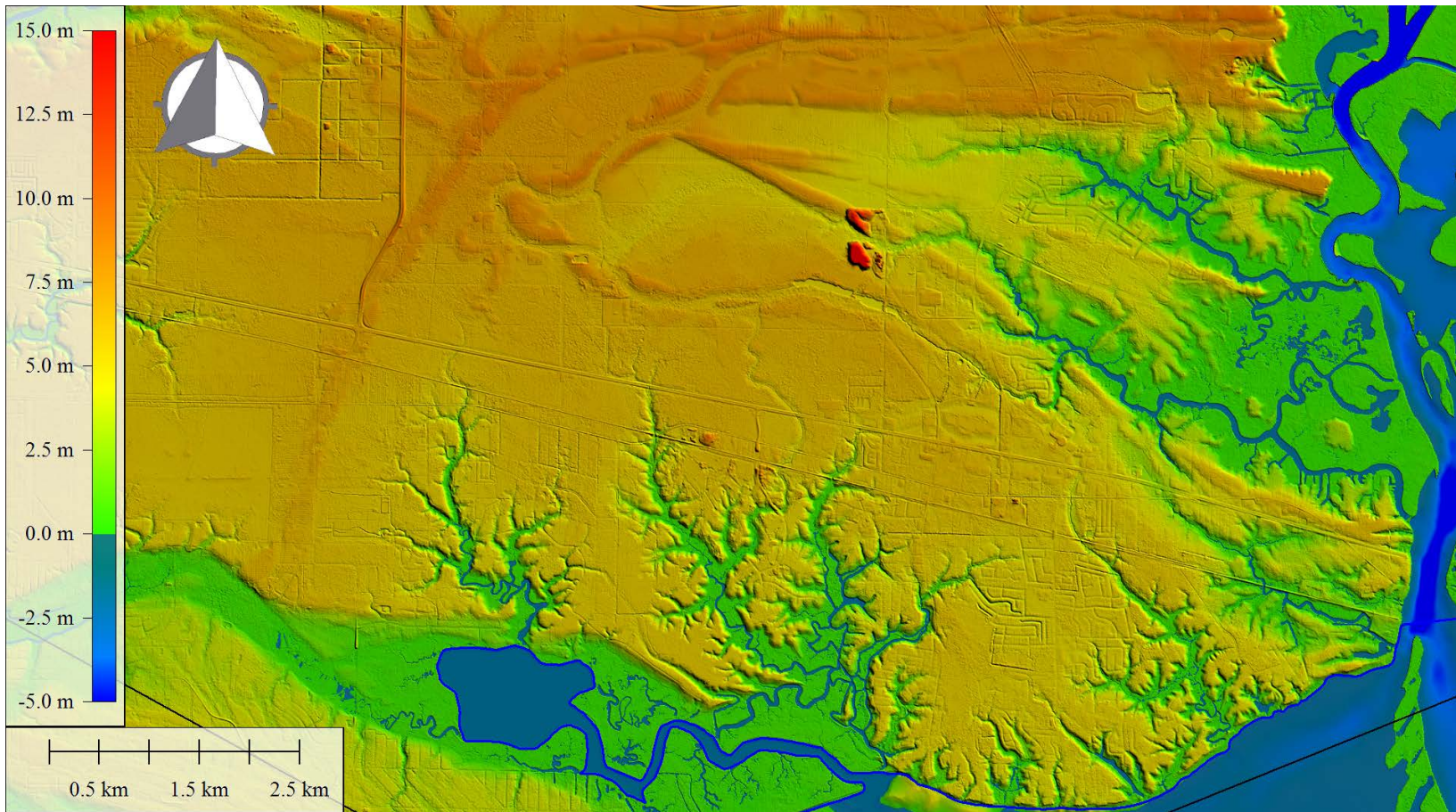


Figure 52 5-m DEM near the West Pascagoula Inlet and Graveline Bay with the floodplain mesh boundary (blue line).

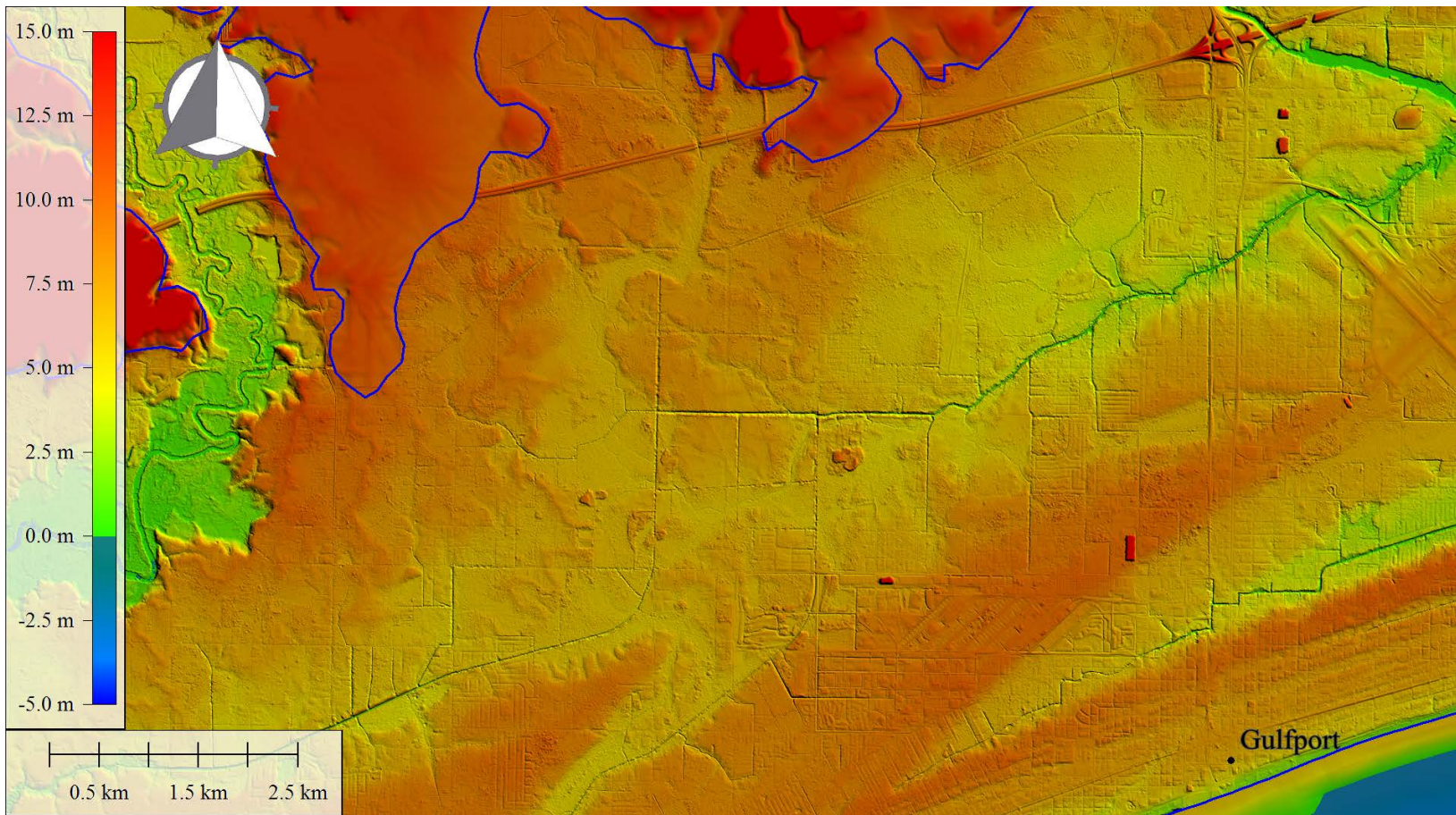


Figure 53 5-m DEM near Gulfport Mississippi. The blue line is the floodplain mesh boundary. Elevation beyond the blue line is from the NED 1-arc-second DEM (Gesch *et al.*, 2002; Gesch, 2007).

CHAPTER 8: FINITE ELEMENT MESH DEVELOPMENT

To accurately simulate water levels and currents due to astronomic tides and hurricane winds a hydrodynamic numerical model must include proper geometric description and be large enough in geographic extent to incorporate the associated boundary conditions and circumvent unrealistic boundary effects. A large domain approach allows boundary conditions to reside in the deep ocean and for the storm's natural propagation from the deep ocean onto the continental shelf and floodplain to occur entirely within the model domain (Blain *et al.*, 1994; Dietrich *et al.*, 2011; Kennedy *et al.*, 2011). The domain herein is discretized using triangular finite elements. Large elements are placed in the deep ocean where small scale dynamics are minor and small elements are placed near the continental shelf and coastline, in bays and rivers as well as in the adjacent floodplain where small scale dynamics are essential toward obtaining accurate results (Hagen *et al.*, 2000; Hagen, 2001; Hagen *et al.*, 2001; Hagen & Parrish, 2004; Roberts, 2004; Westerink *et al.*, 2004; Hagen *et al.*, 2006; Coggin, 2011; Salisbury *et al.*, 2011).

The development of each FEM used in this study is presented here. The chapter is broken into two main sections. The first section describes the development of the in-bank (water only) mesh. The second section describes the development of the floodplain mesh and the modifications of the mesh that were made to test hydrodynamic accuracy.

This study is not intended to validate a numerical model for tides and storm surge; rather the following chapter describes a physical application to test the affect topography has on maximum water levels from tides and hurricane winds and pressures.

8.1 In-Bank Mesh Development

The interconnectedness of the coastal system including the open ocean, bays, rivers, intertidal zones, marshes, and overland areas play a major role in the behavior of hydrodynamics in the Pascagoula region (Takahashi, 2008; Wang, 2008). This interconnectedness presents many complexities to the modeler desiring to simulate hydrodynamics within the Pascagoula region. Therefore, it is essential to initially simplify the problem.

First, two-water only meshes were developed to simulate astronomical tides for the lower Pascagoula River, as described in the following section. Constructing an in-bank mesh simplifies the mesh generation process in several ways. Discretizing (i.e. meshing) the water bodies allows proper mesh transitioning techniques to be applied from the deep ocean to the shoreline, which is important for tides and storm surge (Hagen *et al.*, 2006). Since a majority of the high-resolution is near or at the coastline, accurate placement and dimensioning is essential. Additionally, the coastline is typically represented as the zero-elevation contour, allowing element edges to align with an accurate contour elevation. It has been proven ,within the ADCIRC model (Luettich *et al.*, 1992), that more accurate results are found when element edges are aligned with elevation contours (Roberts, 2004; Coggin, 2008).

Second and most importantly, resolution in the adjacent floodplain is largely dependent on the resolution in the water areas. Channels and inlets must be properly discretized since they convey the majority of the flow and have steep bathymetric gradients. Therefore water areas tend to have the most resolution (Roberts, 2004).

8.1.1 Digitization of Model Boundary

The first step was digitization of the shoreline boundary. The shoreline boundary includes the open ocean shoreline, islands, river banks and other waterways. The digitization was done with the aid of aerial photography, 5-m LiDAR-derived DEM, and LiDAR-derived breaklines. When river boundaries were found along heavy forestation it became difficult to locate the shoreline because of the tree canopies. In this case, the DEM was used to delineate the boundary between water and land. At this point, only river banks were digitized and many of the marsh areas within the East and West inlet were avoided since they are not constantly wetted. These areas are reserved for inclusion in the floodplain mesh.

The next step, after the boundary was digitized, was to determine the extent at which to cut the existing Western North Atlantic Tidal (WNAT) model domain (Hagen *et al.*, 2006) (Figure 54 and Figure 55). Note that the WNAT mesh was used as the base mesh, to which the high-detailed Pascagoula region is appended, to provide proper boundary forcing at the open ocean boundary as well as include a large enough domain to capture the full extent of meteorological forcings (Blain *et al.*, 1994; Kennedy *et al.*, 2011). The WNAT mesh, or 53K mesh (Hagen *et al.*, 2006), contains approximately 53,000 nodes, and spans the western North Atlantic Ocean, Caribbean Sea and Gulf of Mexico. The open ocean boundary extends the 60° west meridian from Glace Bay, Nova Scotia, to the vicinity of Corocora Island in eastern Venezuela. The location of the incision in the 53K mesh is important to provide suitable element transition from the large deep ocean elements (order of 100-km) to the smaller elements located in the Pascagoula Bay and riverine network (order of 10-m) (Figure 56). The final digitized

boundary containing the river banks, islands, and off-shore boundary is represented by a series of polylines and polygons in Figure 57.

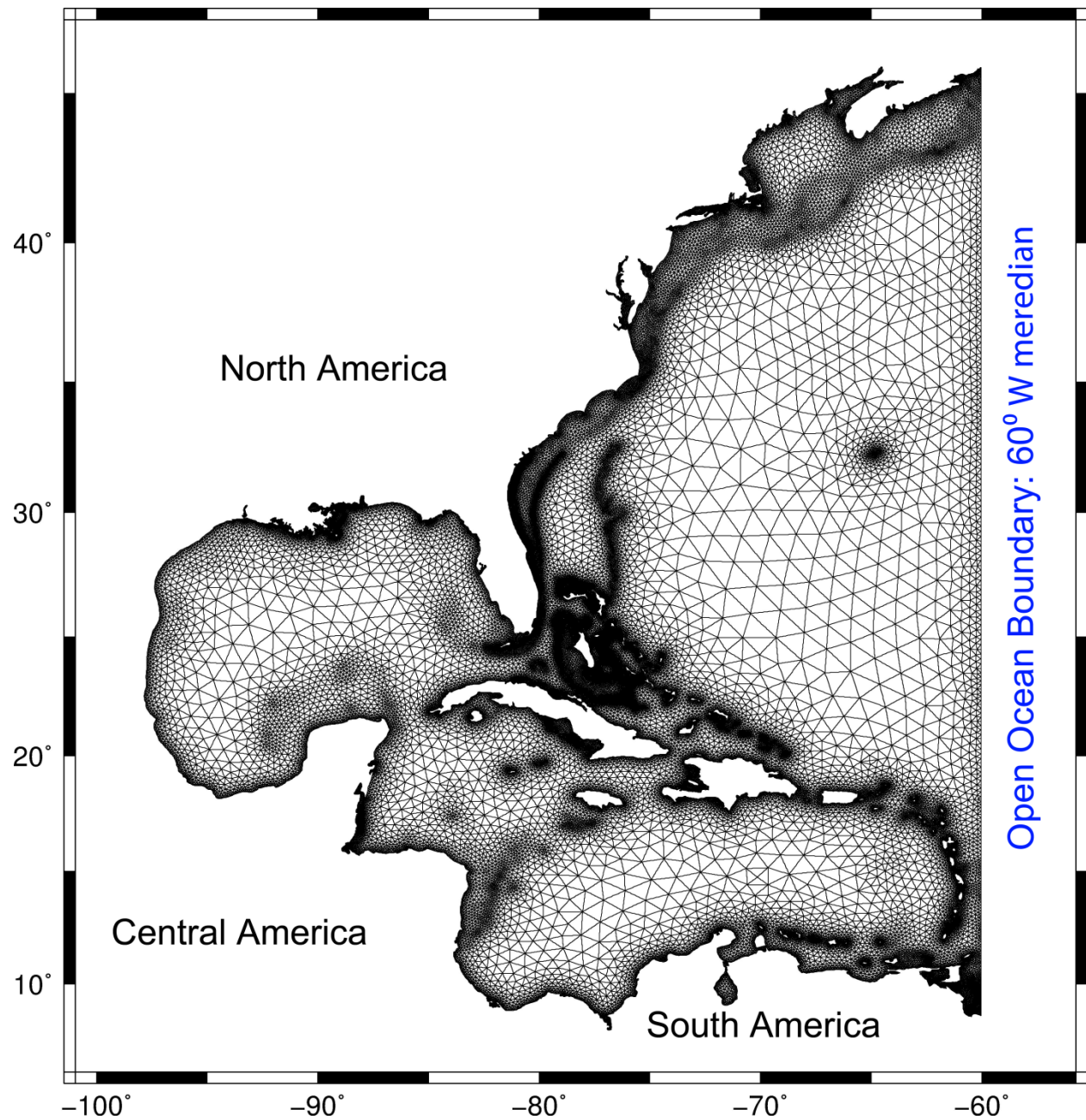


Figure 54 53K mesh (Hagen *et al.*, 2006)

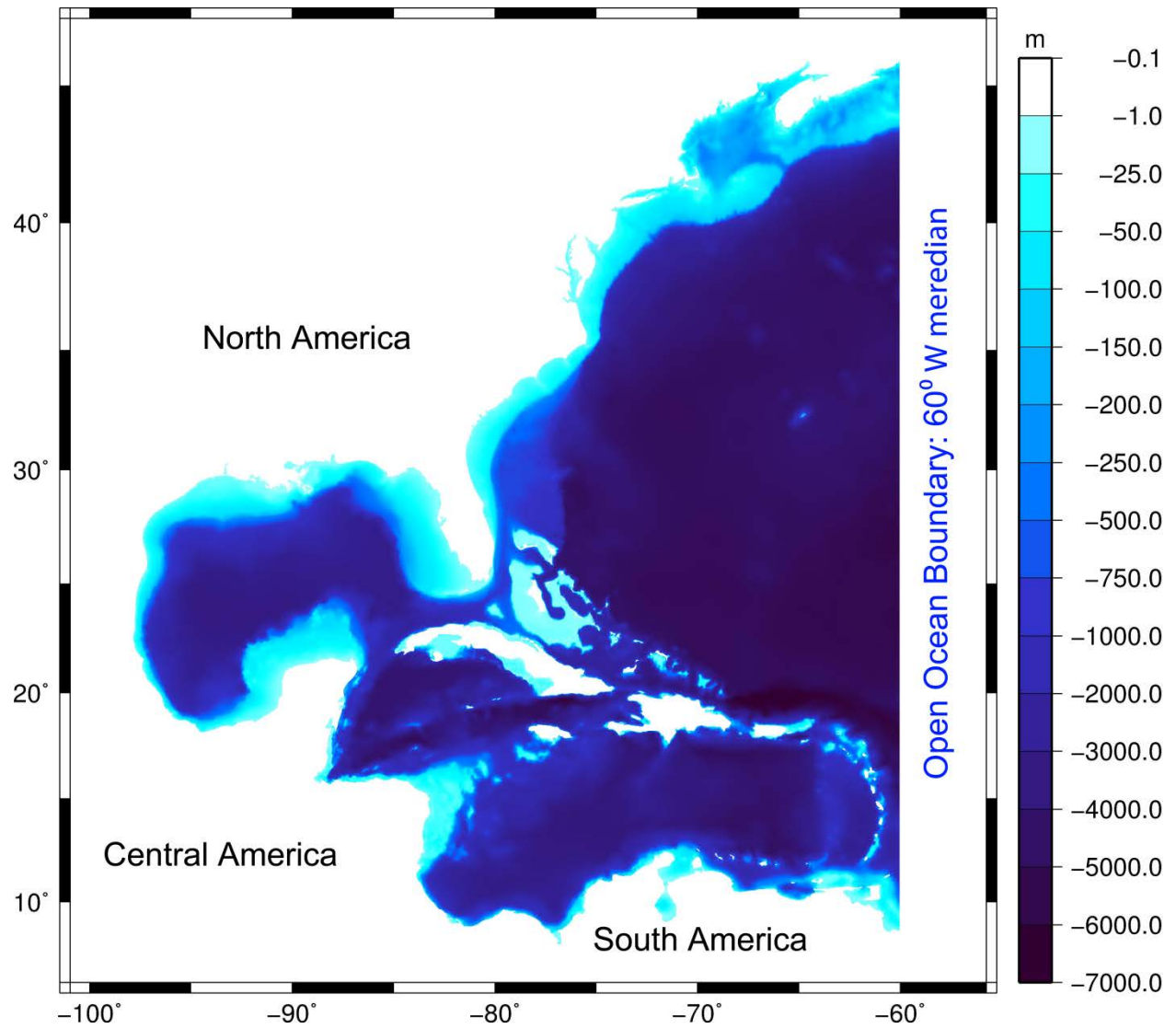


Figure 55 53K mesh bathymetry (Hagen *et al.*, 2006)

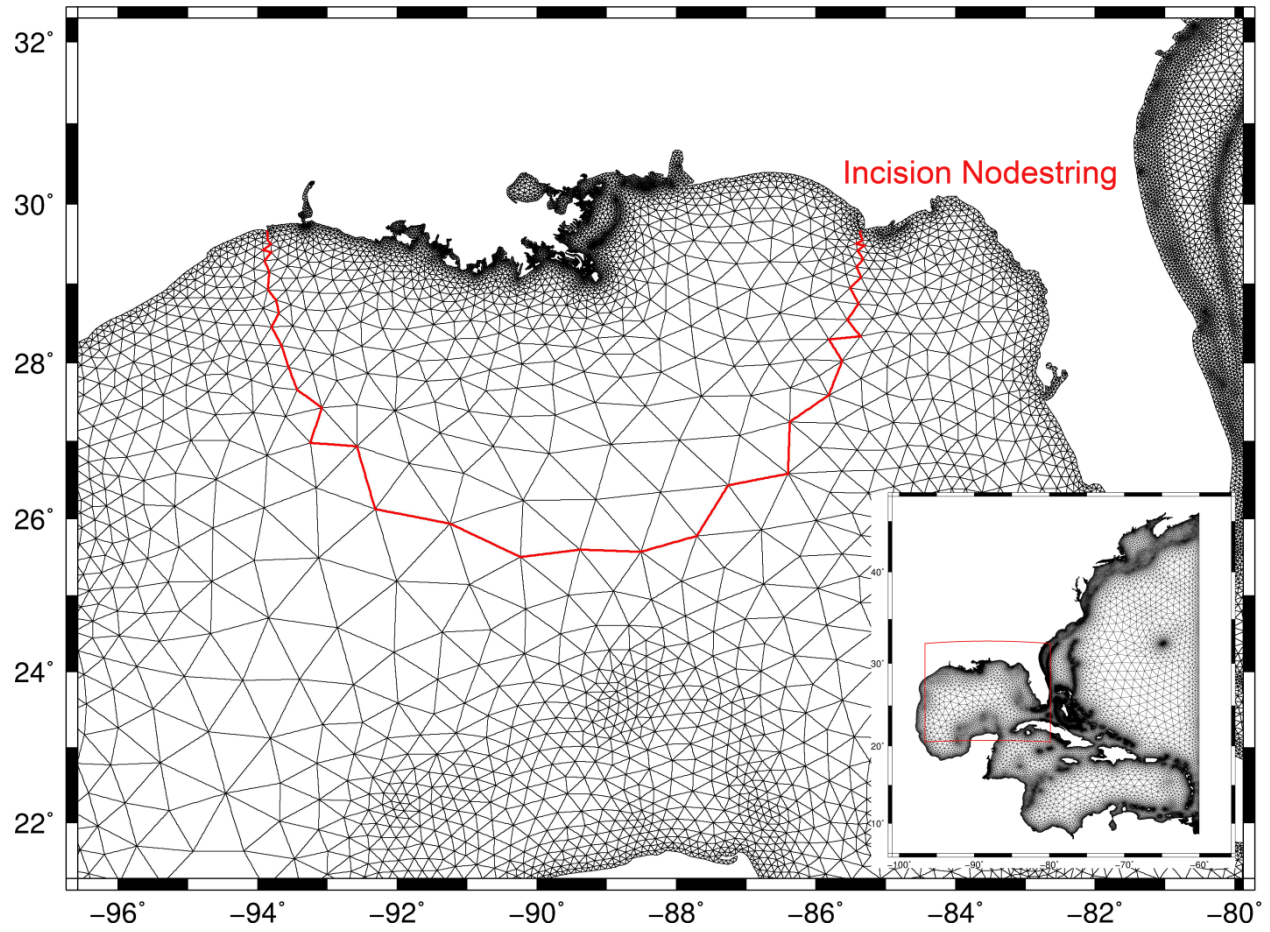


Figure 56 Location of the incision on the 53K mesh

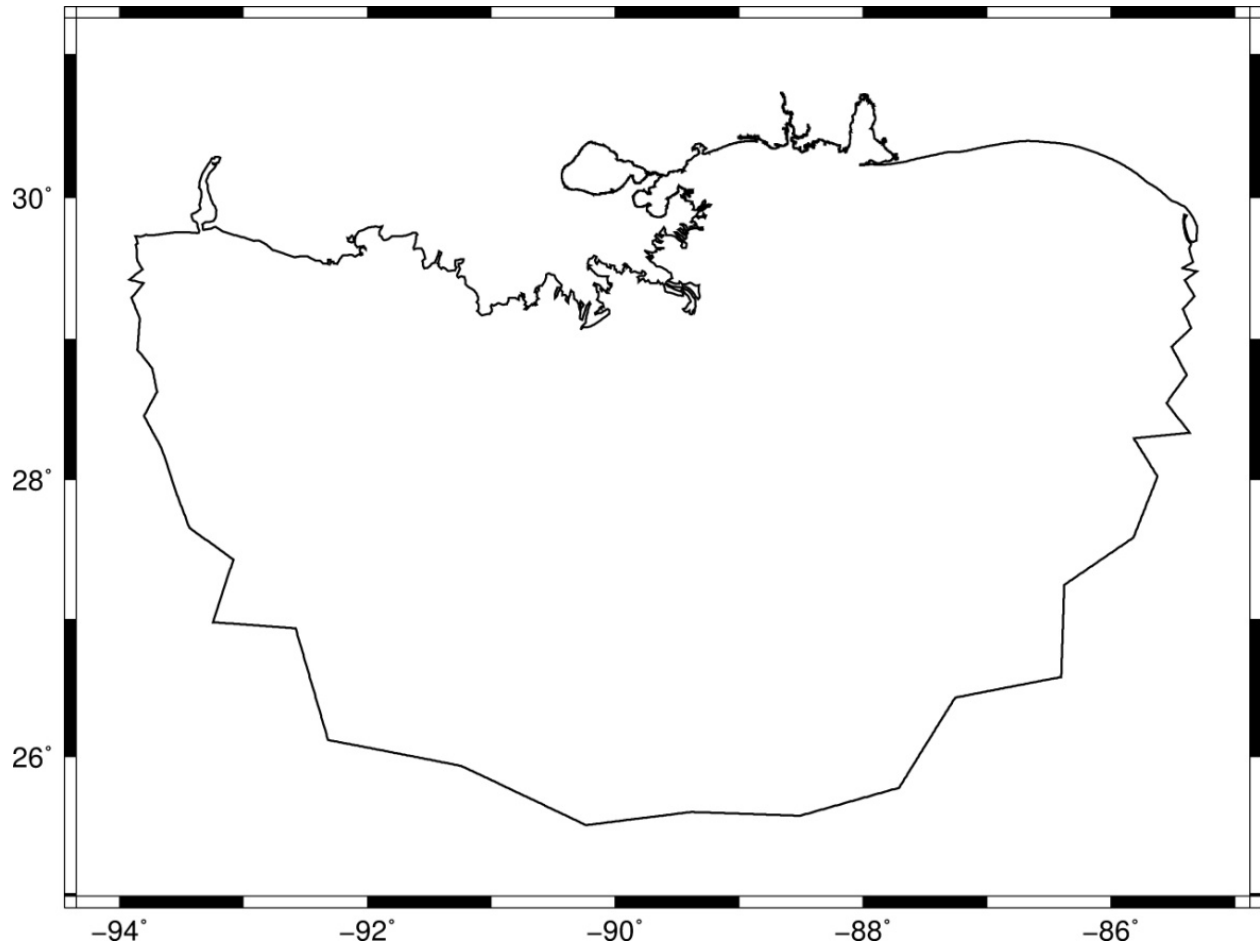


Figure 57 Final digitized boundary excluding islands

8.1.2 Triangulation

The next step was to triangulate within the digitized boundary. For this, the paving algorithm in the Surface-water Modeling System (SMS) computer program (Aquaveo LLC, 2010) was used. Two different versions of in-bank meshes (differing in mesh resolution) were constructed to determine if mesh element size in the river was sensitive to astronomic tides. In-bank mesh number 1 is at relatively lower resolution and the other, in-bank mesh number 2, is at a relatively higher resolution. For the first in-bank mesh (in-bank mesh number 1), one central rule was followed throughout the meshing procedure; that a minimum of three elements had to

span across a channel. This enables a description of the channel's geometry, for the worst cases, depicting a trapezoidal cross-section (Figure 58). The second in-bank mesh includes higher resolution than the aforementioned mesh. Throughout much of the river, elements were about 10-m in edge length.

For both in-bank meshes high-resolution was acceptable not only in the Pascagoula River and Bay, but also around dredged shipping channels, near the Mississippi River, and along the numerous barrier islands surrounding the area. Once paving was complete, manual adjustments were made to remove nodes that contained four (kites) or eight (pinwheels) or more elements. These areas are known to potentially cause numerical instabilities. Additionally, alterations were made to present a visually appealing triangulation to provide proper element transition in terms of elemental area as well as removing elements that contain small interior angles. Numerical instabilities may also arise if the elements' surface areas change too rapidly in space.

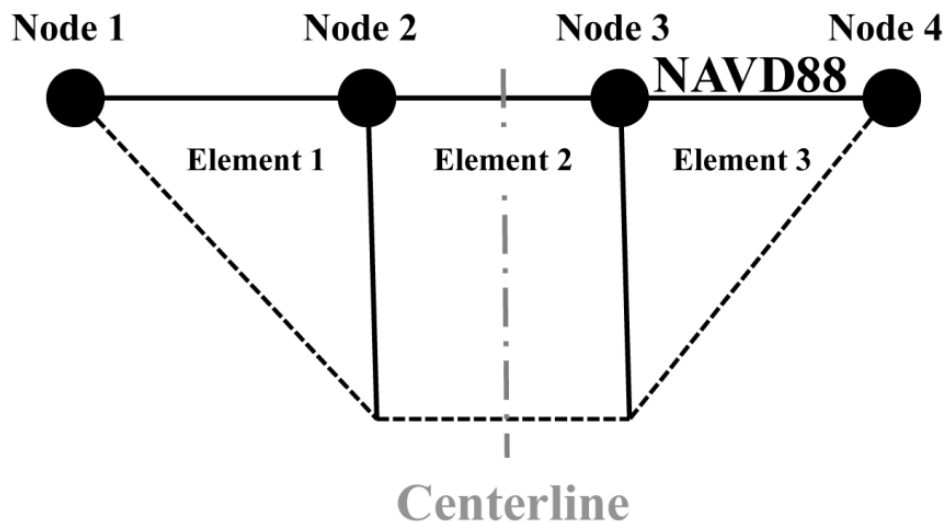


Figure 58 Three elements across the channel representing a trapezoidal cross-section

Figure 59 shows the difference between the relatively low- and high-resolution in-bank FEM for a portion of the West Pascagoula inlet. The first in-bank mesh consists of 346,269 nodes and 661,515 elements (Figure 60). With the utilization of the unstructured FEM, the largest elements are 143-m and the smallest elements are 8-m in edge length. In the Pascagoula River, element sizes range between 75-m to 8-m in side length. A detailed image of the mesh can be found in Figure 61.

The second in-bank mesh (in-bank mesh number 2) consists of 695,588 nodes and 1,342,642 elements. In-bank mesh number 2 includes much higher resolution in the river than the previous mesh. Within the Pascagoula River, mesh elements, on average, are 10-m in element edge length. This was done in order to test proper transitioning of the river bank to high-resolution (order of tens of meters) elements located within the floodplain.

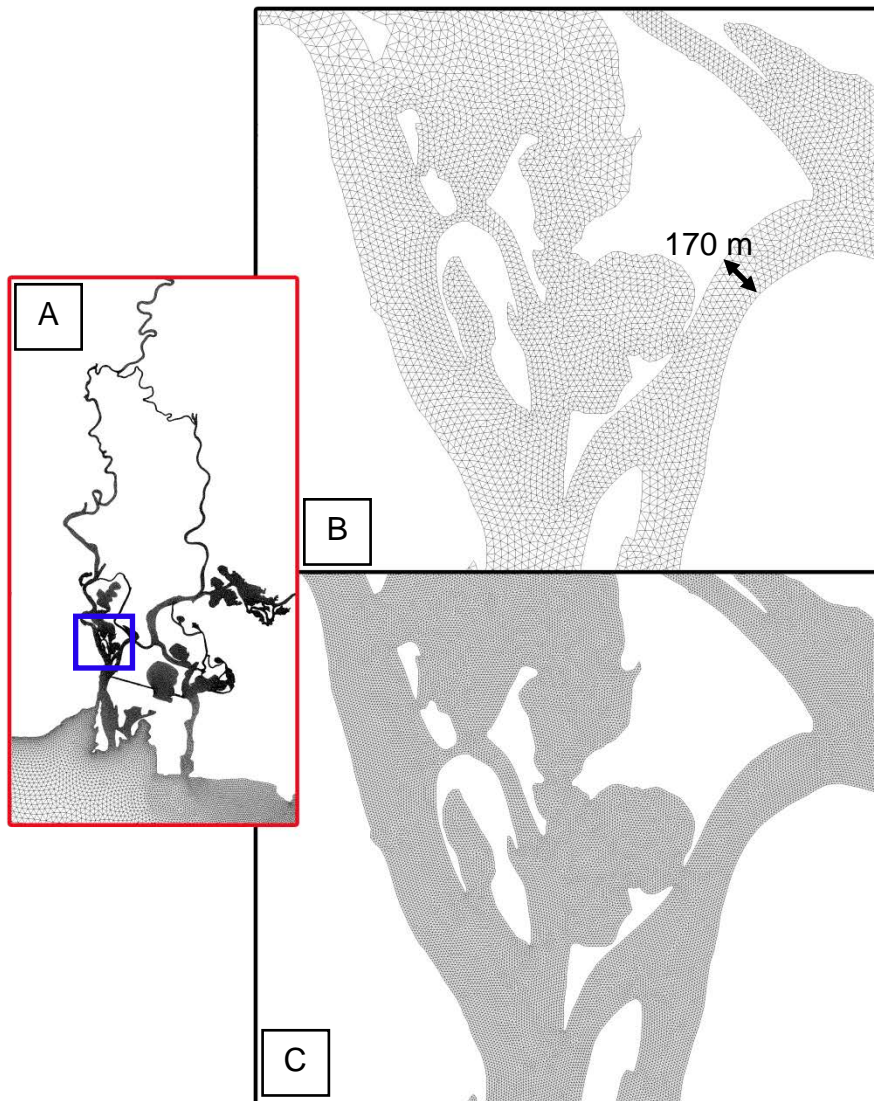


Figure 59 A) Localized frame of the in-bank Pascagoula River mesh with blue inset box
 B) relatively low-resolution in-bank FEM
 C) relatively high-resolution in-bank FEM

8.1.3 Bathymetry

The final step was to interpolate the bathymetry onto the FEM nodes. Several sources of bathymetric data were used, as obtained from previously developed FEMs (Figure 62). These include the SL15 (Bunya *et al.*, 2010), FLPH_AL, and a previous in-bank model for the

Pascagoula River (Wang, 2008). The SL15 (Southeastern Louisiana) mesh was used in a storm surge model developed at the University of Notre Dame by Dr. Joannes Westerink for the Federal Emergency Management Agency (FEMA) (Bunya *et al.*, 2010). It contains approximately 2.2 million nodes and highly resolves the coast and overland regions of southeastern Louisiana. It is a product of the earlier EC2001 U.S. East Coast and Gulf of Mexico astronomic tide model and the S08 southern Louisiana storm surge model (Blain *et al.*, 1994; Mukai *et al.*, 2002; Westerink *et al.*, 2008). The SL15 bathymetry was used for areas east of Pascagoula Bay, and in the deep waters of the Gulf of Mexico.

The FLPH_AL mesh was a mesh developed at the University of Central Florida by Dr. Scott Hagen and his team for FEMA to produce new digital flood insurance rate maps (DFIRMs) for parts of the Florida Panhandle and coastal Alabama (Northwest Florida Water Management District, 2011). It provides high resolution along the Florida Panhandle's shoreline as well as in the bays and Gulf Intracoastal Waterway (GIWW) system. This bathymetry was used east of Pascagoula Bay along the shoreline and continental shelf up to Saint Joseph Bay, Florida.

The bathymetry for the Pascagoula River was obtained from an existing Pascagoula River mesh developed by Wang (2008). Wang used river cross-sections from a USGS study (Turnipseed & Storm, 1995) and developed a toolbox to interpolate known bathymetric points between each of the river cross-sections to unknown locations.

All bathymetry data were merged into a single dataset which was then linearly interpolated onto each in-bank FEM. Figure 63 through Figure 65 show bathymetry at different scales for the areas around the Pascagoula River. Many features are highly resolved within the in-bank mesh: the Mississippi delta region where the Mississippi River empties into the Gulf of

Mexico; the shipping channel south of Chandeleur Sound; Lake Pontchartrain and Lake Borgne; Pascagoula Bay, Mobile Bay and its shipping channels; and of course, the Pascagoula River system.

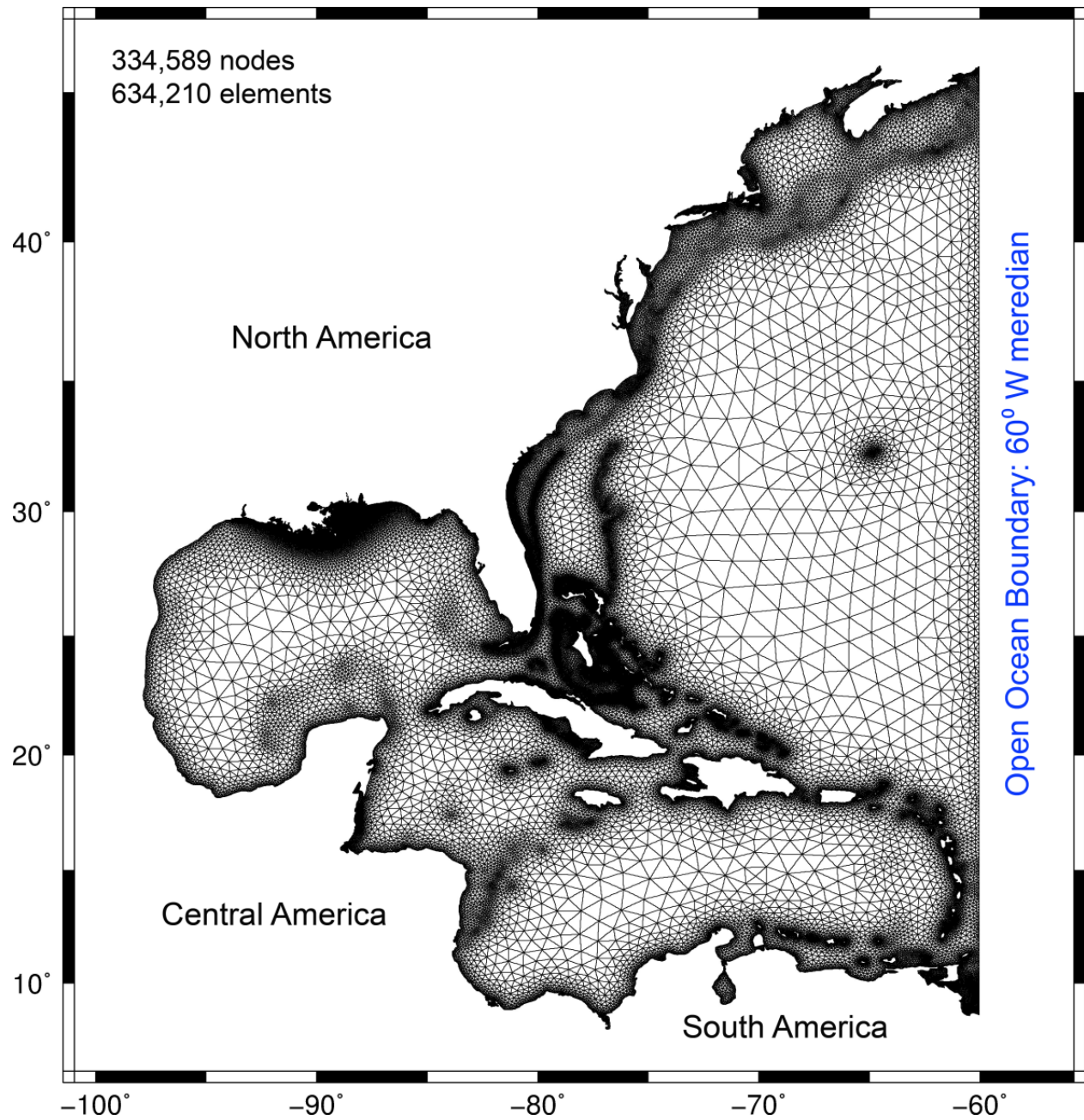


Figure 60 Pascagoula River in-bank finite element mesh. The mesh consists of 334,589 nodes and 634,210 elements. It extends from the deep Atlantic Ocean and Gulf of Mexico into Pascagoula Bay and into the Pascagoula River.

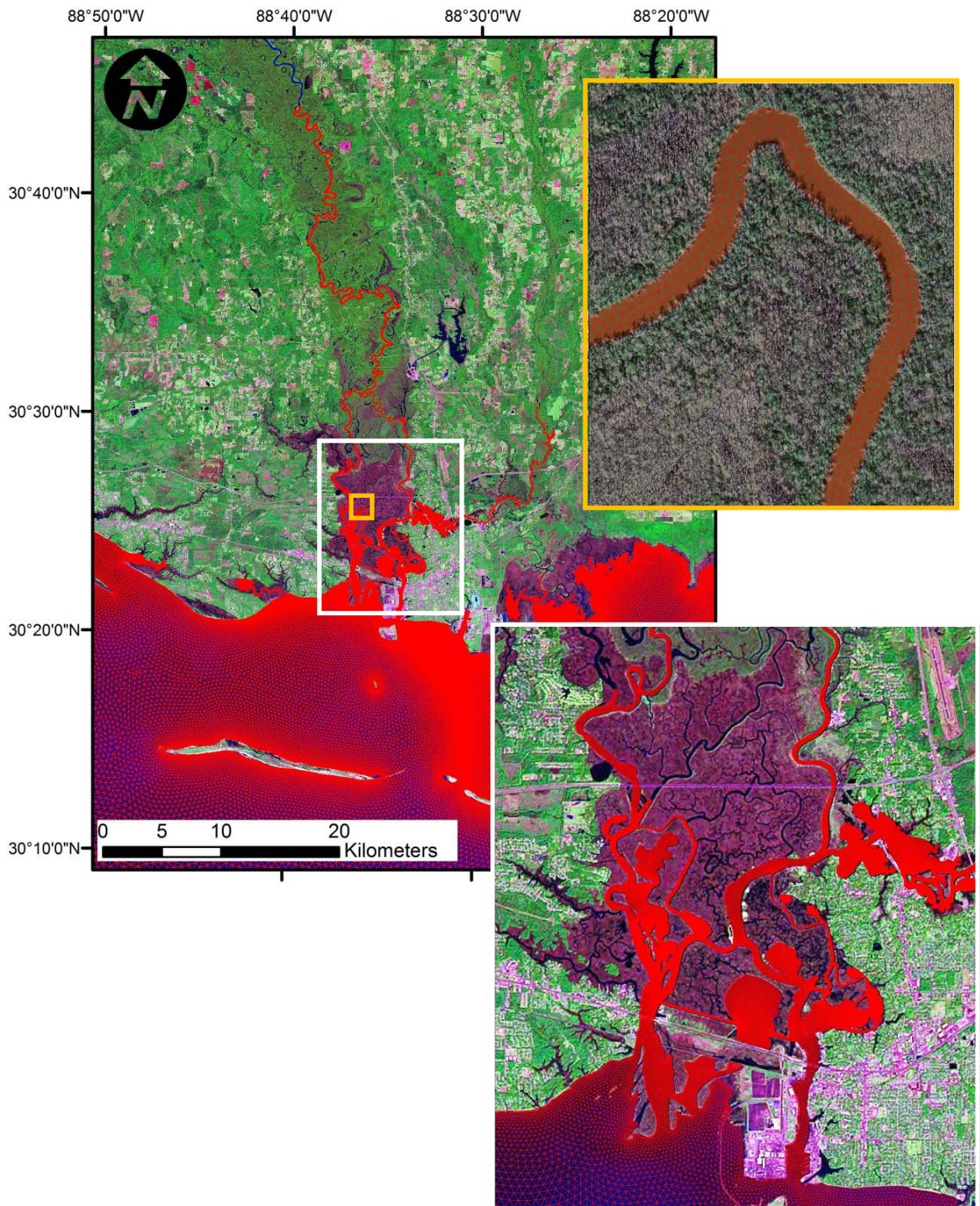


Figure 61 Triangulation of the Pascagoula Bay and River. The mesh elements are outlined in red. The background imagery is LANDSAT satellite imagery and aerial photography.

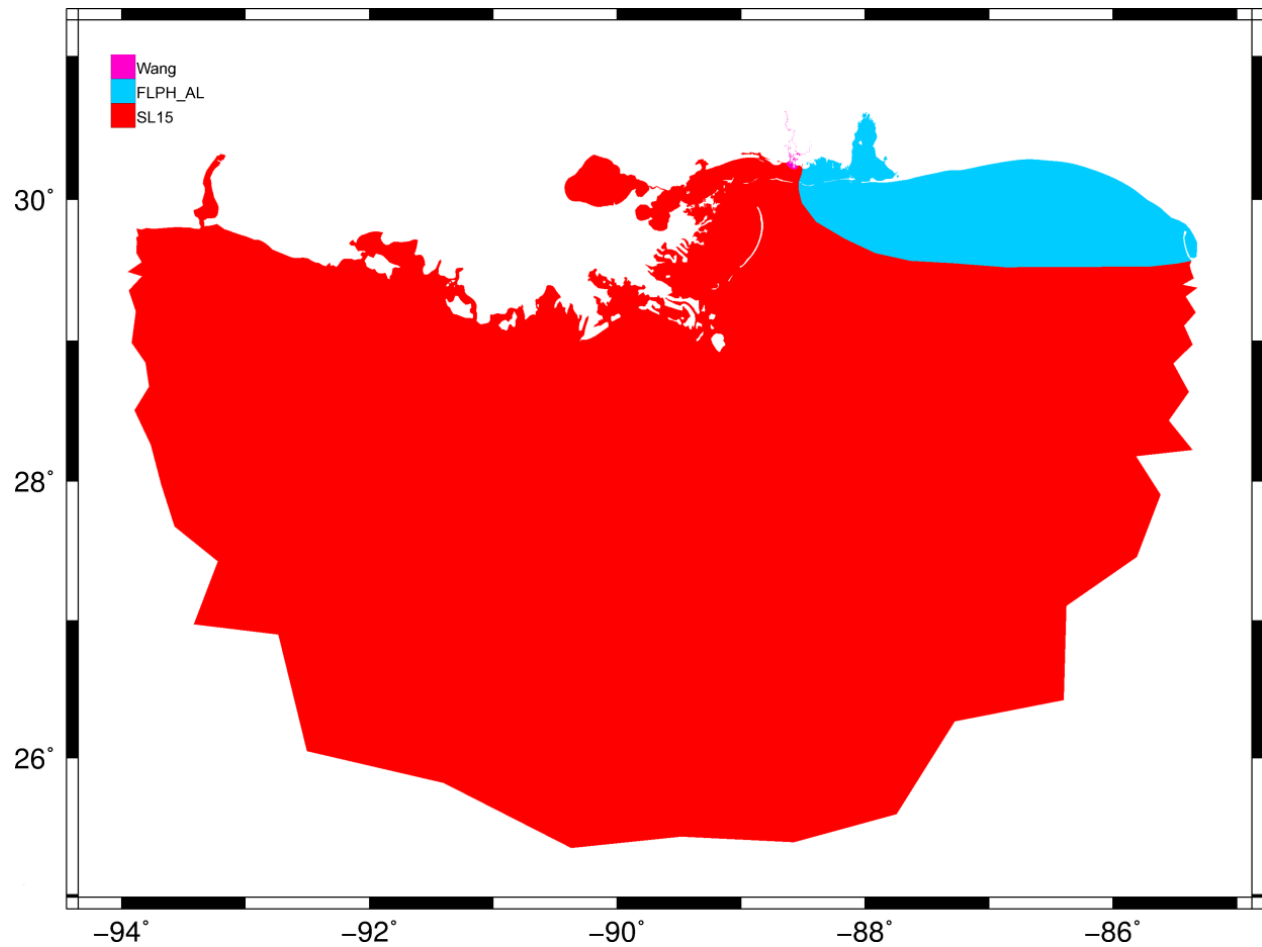


Figure 62 Sections which utilized different bathymetry sources. The red indicates elevations taken from SL15 (Bunya *et al.*, 2010), blue from FLPH_AL (Northwest Florida Water Management District, 2011), and purple from Wang (2008).

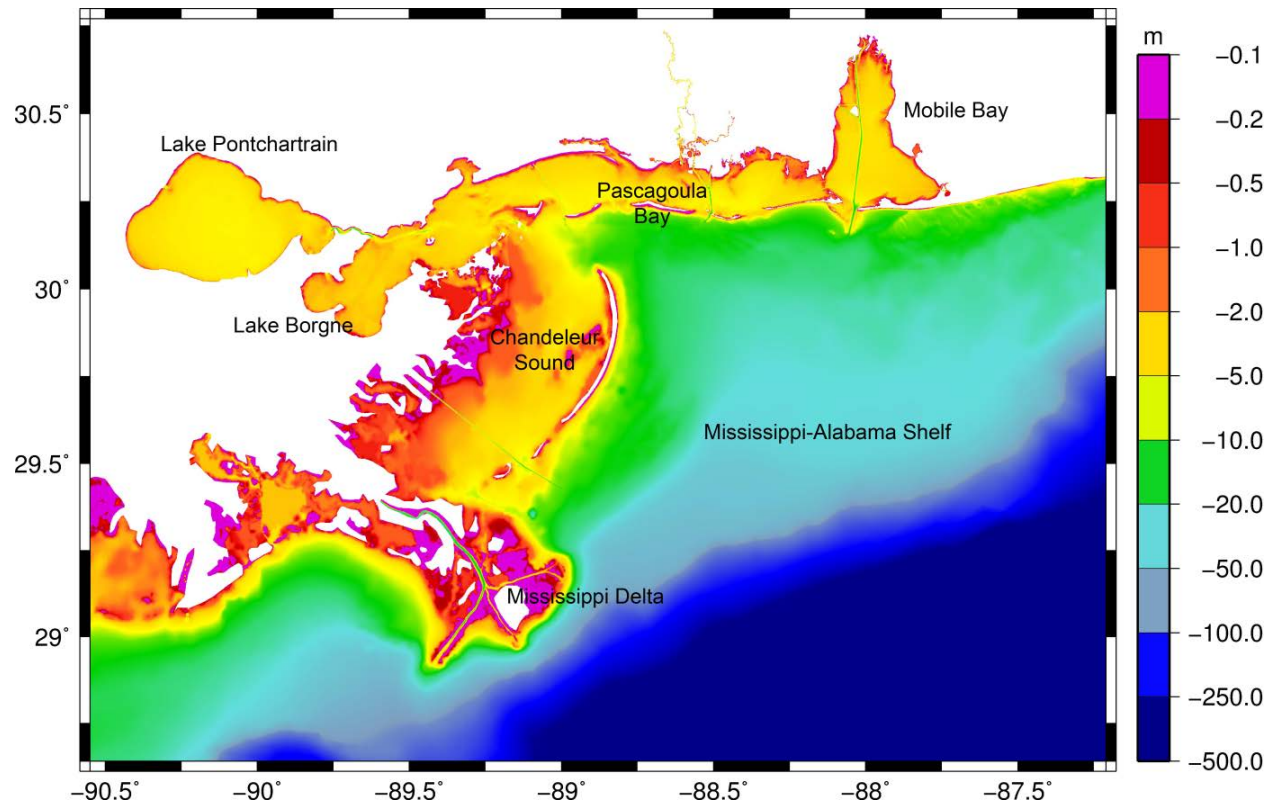


Figure 63 In-bank model bathymetry around Louisiana, Mississippi, and Alabama. Key features include the Mississippi-Alabama Shelf, Mississippi Delta, Chandeleur Sound and the shipping channels around southeastern Louisiana, Pascagoula Bay, and Mobile Bay.

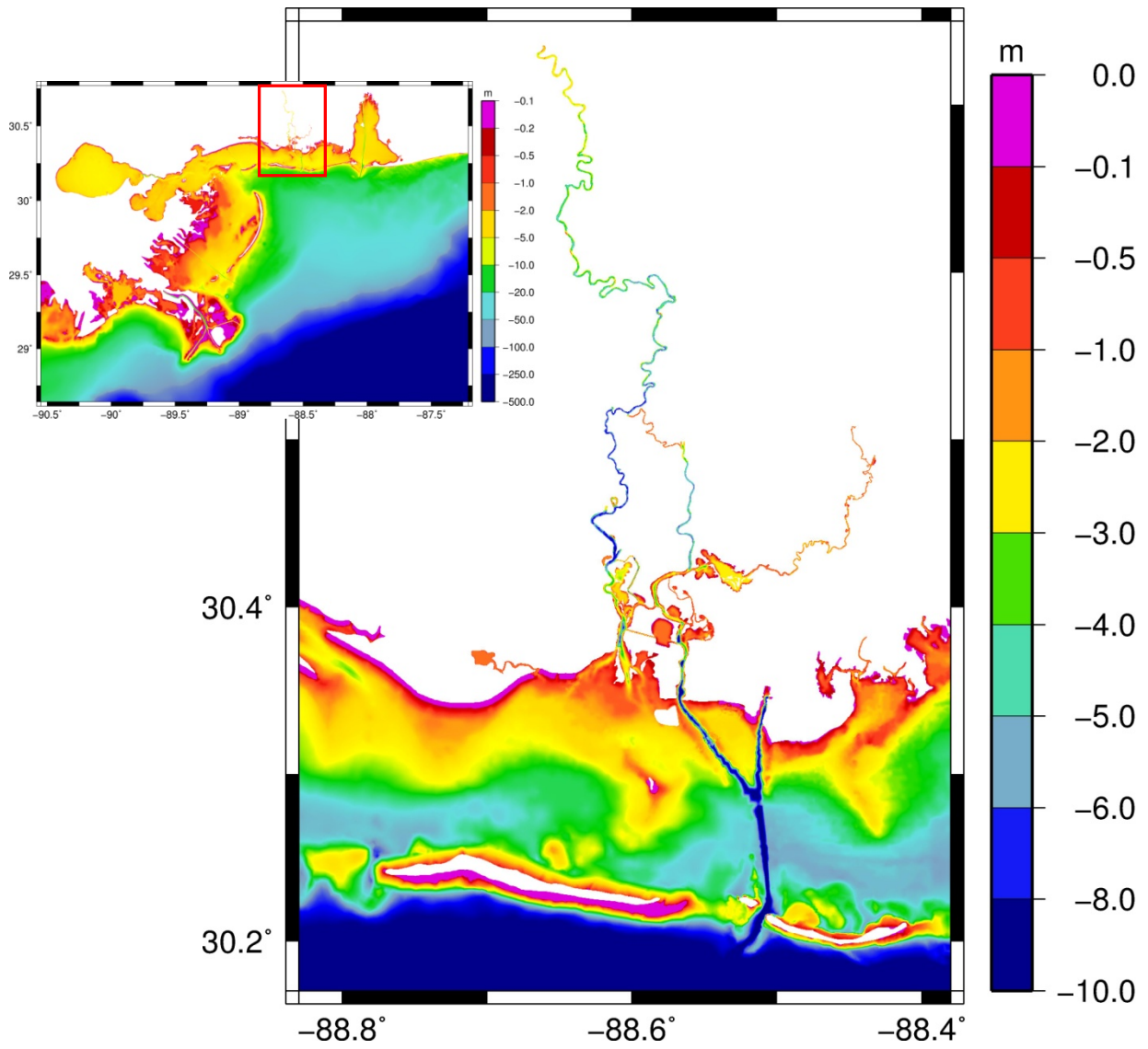


Figure 64 In-bank model bathymetry for the Pascagoula River.

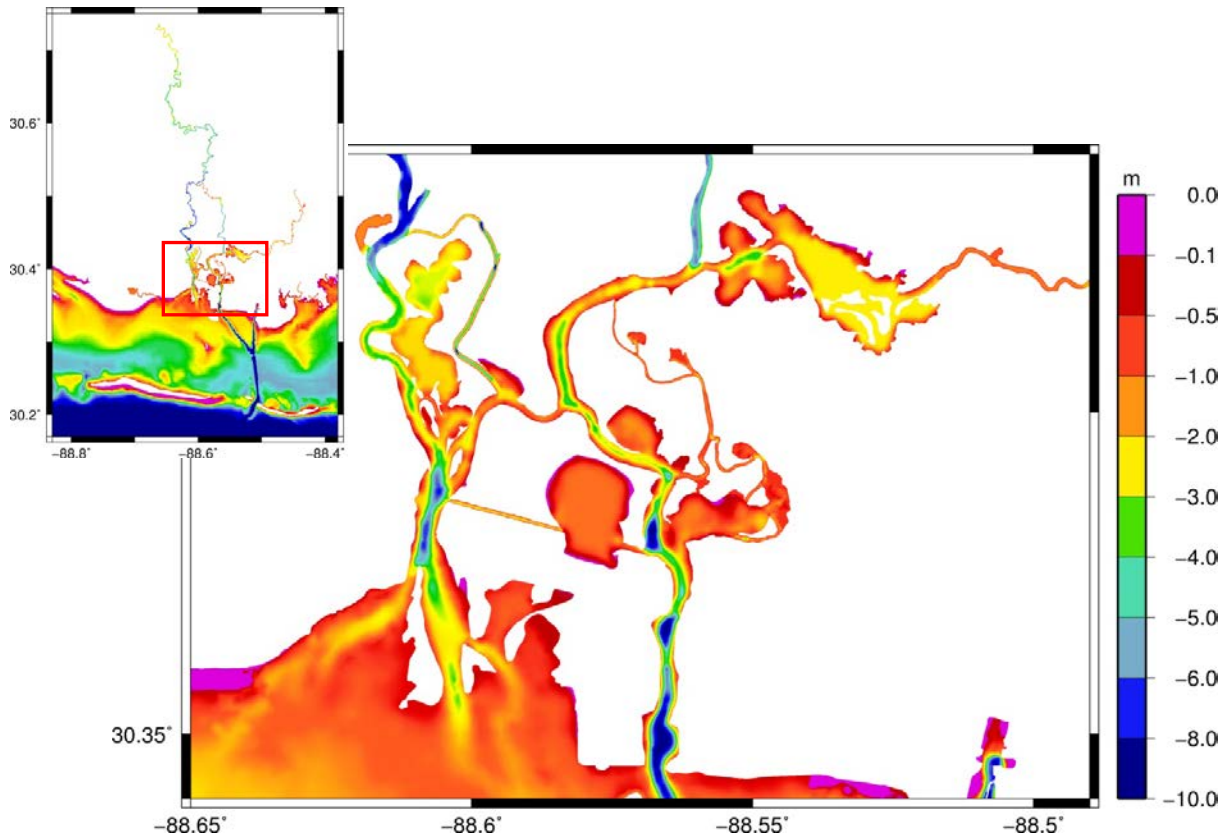


Figure 65 In-bank model bathymetry around the east and west Pascagoula inlets.

8.2 Floodplain Mesh Development

Building on the in-bank model, the model domain must encompass the floodplain to fully study overland flooding due to hurricane storm surge and astronomic tides. In the following sections two major items are discussed: 1) development of the three equilateral test regions and 2) development of the remaining floodplain.

8.2.1 Equilateral Regions

The methods presented in Chapter 6 to evaluate topographic accuracy are applied to three regions around the Pascagoula River and immediate coastal shoreline. These regions cover a

larger area than those presented prior in order to test overall global topographic and hydrodynamic accuracy via astronomic tides and hurricane storm surge from Hurricane Katrina. Figure 66 and Figure 67 and present the three zones, left, center, and right with the in-bank mesh elements and Landsat satellite imagery background, respectively. They are bounded by a semi-circular arc and the shoreline of the Pascagoula Bay and River. The left and right regions contains a mixture of common coastal features such as marshlands, urban, and dense forest with the center region exclusively marsh.

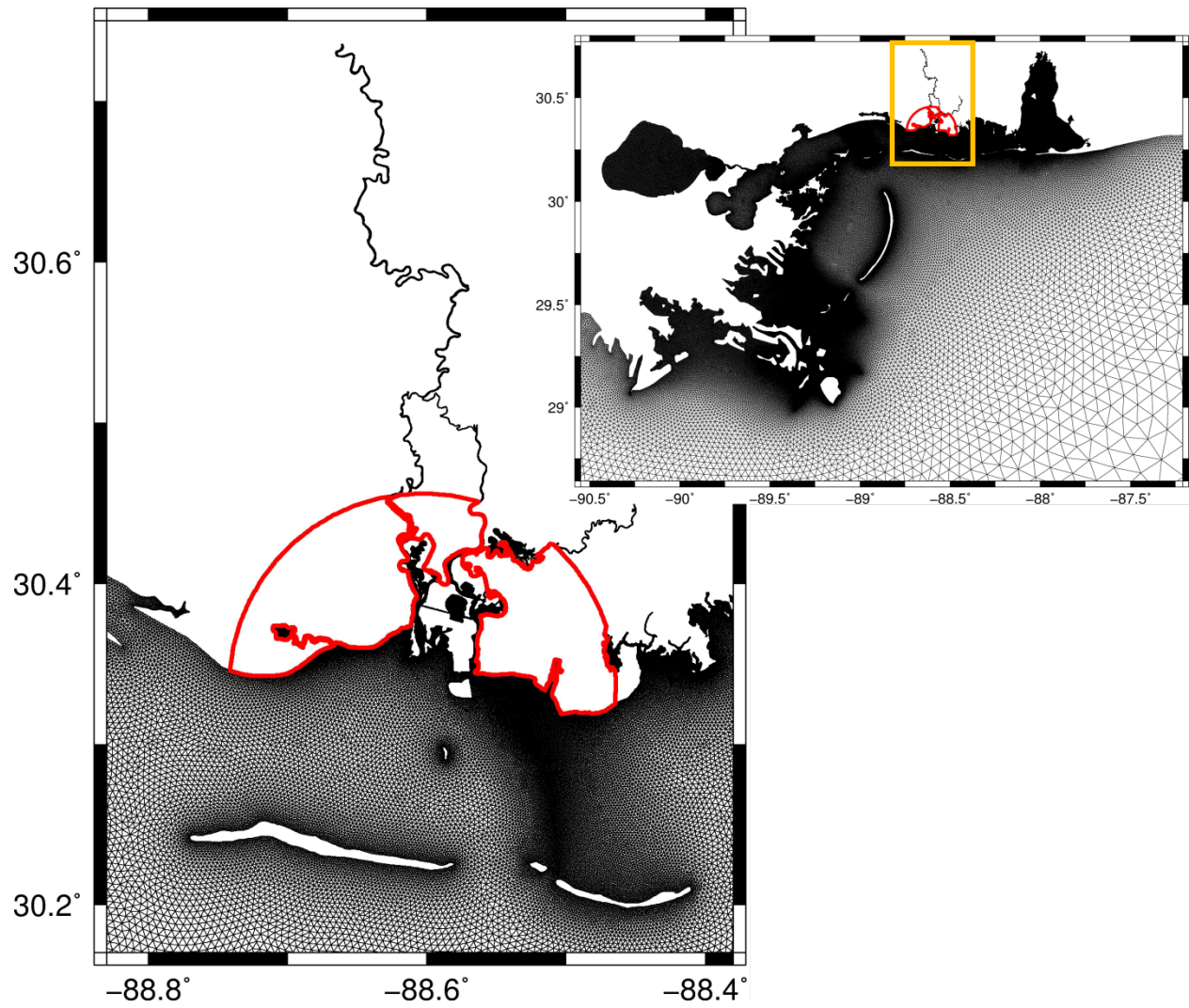


Figure 66 Equilateral regions in red and the triangular finite elements in black

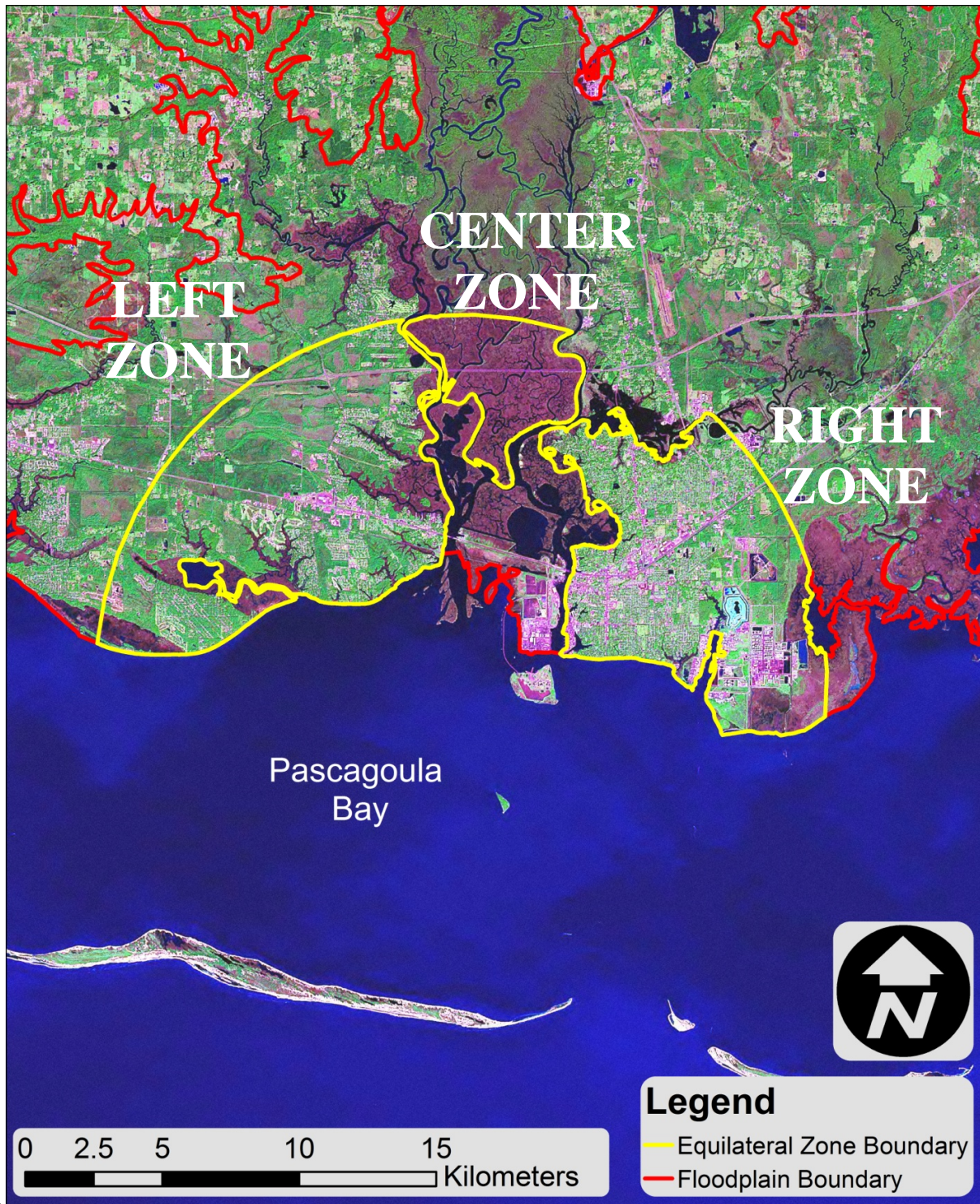


Figure 67 Left, center, and right zones outlined in yellow. The model floodplain boundary is in red. The background image is Landsat (Goslee, 2011).

Within each zone, equilateral elements were applied at four resolutions: 160-m, 80-m, 40-m, and 20-m. A transition zone was constructed to incorporate true equilateral elements within each zone. The transition zone ensures proper element transitioning from the elements along the shoreline, which are varying in element size and non-equilateral, to the equilateral elements of sizes 160-m, 80-m, 40-m, and 20-m. It is also used in the topographic accuracy assessment to ensure interpolation is not affected by a lack of source data along the interior boundary. To establish the size of the transition zone (distance from shoreline to pure equilaterals), one major geometric criterion was followed, \mathcal{A} -ARC (Adjacent Element Area Ratio Criteria). \mathcal{A} -ARC is a measure of mesh irregularity in which a ratio is computed based on the areas of adjacent elements. Some finite element models may experience numerical noise and/or instabilities when the mesh contains irregularities. The default \mathcal{A} -ARC ratio set within SMS (Aquaveo LLC, 2010) is 0.5 (small:big). Therefore, the ratio of $A_1:A_2$ should be a maximum of 0.5, as shown in Figure 68. It has been proven through truncation error analysis (Hagen, 2001) that elements changing in area too rapidly will decrease accuracy (Parrish, 2007).

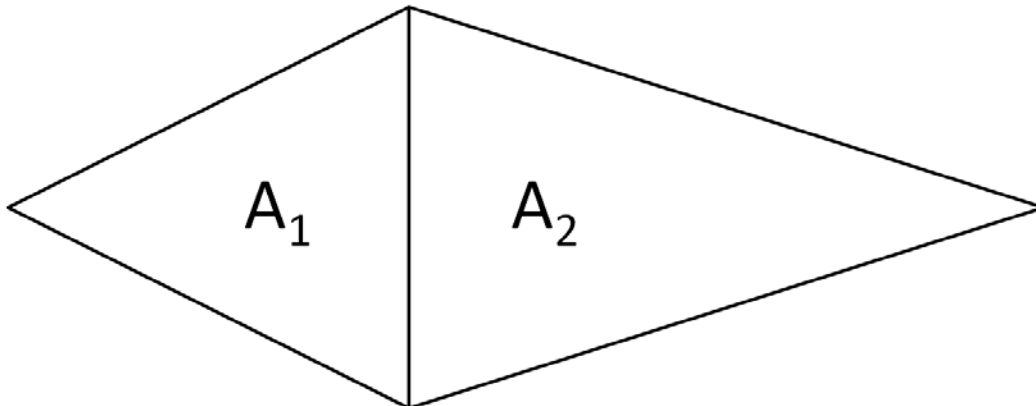


Figure 68 \mathcal{A} -ARC criteria for the area of one and two, A_1 and A_2 , respectively. The ratio shown is $A_1:A_2 = 0.5:1$.

\mathcal{A} -ARC was reformulated for element edge lengths to compute a proper transition distance between the in-bank elements and target equilateral element size:

$$a = \frac{2(3)^{3/4}}{3} A^{1/2} \quad 8.1$$

where a is the element edge length (for an equilateral element all edge lengths are equal and the height is $= a\sqrt{3}/2$) and A is the elements area. To determine the length of the transition (i.e. buffer) zone, Equation 8.1 was applied to find the smallest element edge length along the shoreline and increase element area with an \mathcal{A} -ARC ratio of 0.5 (small:big) until an element edge length of 160-m (the largest equilateral element size being the worst case with respect to element size transition within the buffer zone) was reached. This yielded a transition length of about 360-m. Based on this method, an interior buffer of 360-m was applied to each of the transition zones. Figure 69 presents the three zones and the applied 360-m interior buffer. The 360-m buffer is wide enough to provide a proper transition of elements and small enough where inundation due to astronomic tides and hurricane storm surge will inundate a large amount of area within the interior of the equilateral zones.

Figure 70 presents the 160-m equilateral mesh (black triangles), transition zone (blue triangles), and in-bank mesh (red triangles) merged together. The equilateral zone and buffer zone (transition zone) boundaries were converted to arcs in SMS (Aquaveo LLC, 2010). Equilateral elements were generated in the interior of each zone and the paving tool within SMS was used to triangulate from the shoreline to the equilateral elements. Some manual editing was performed to keep consistent with the \mathcal{A} -ARC ratio. This process was repeated for the 80-m, 40-m, and 20-m equilateral elements (Figure 70 through Figure 72).

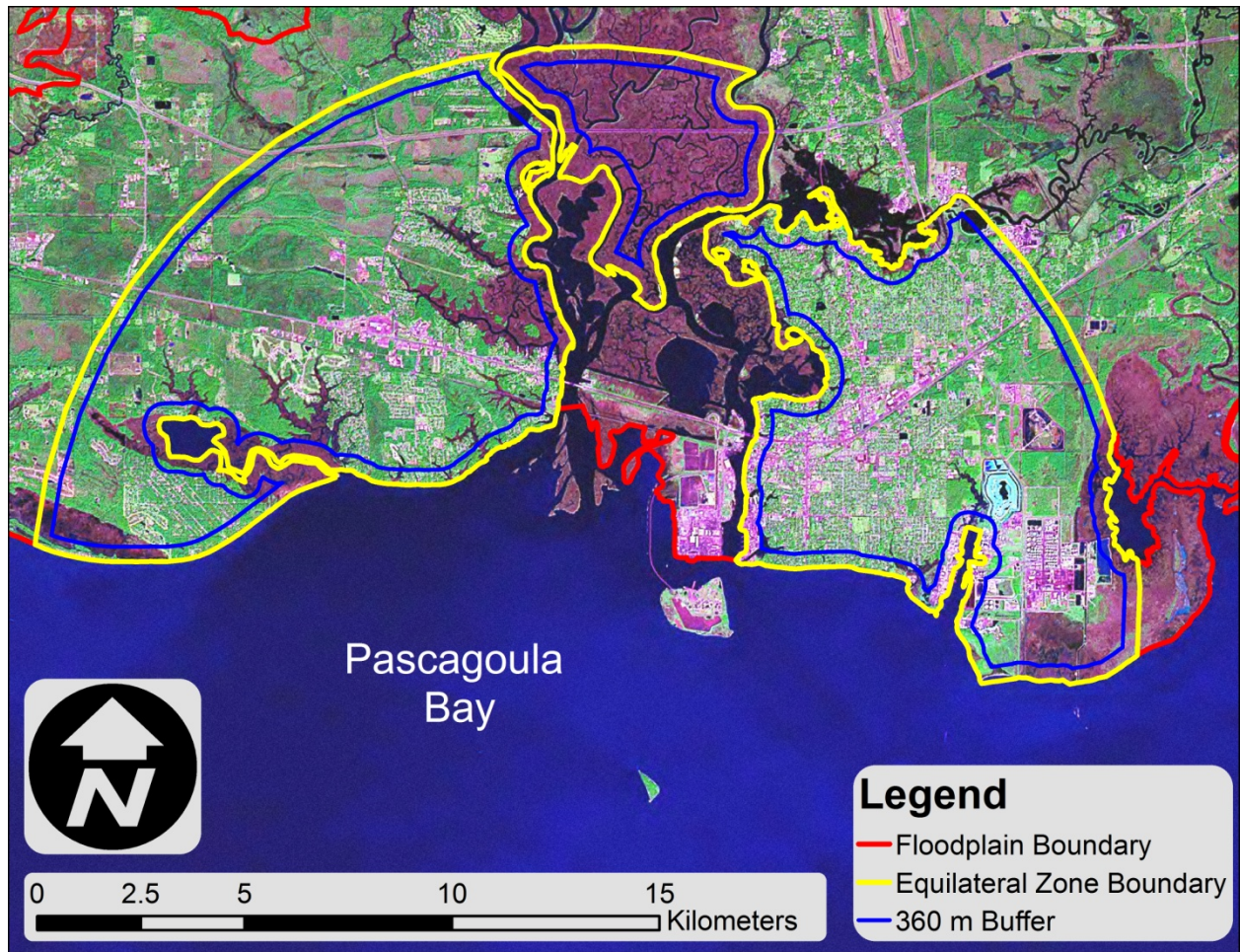


Figure 69 Left, center, and right zones outlined in yellow. The interior buffer regions are bounded by the blue boundary. The red line is the floodplain boundary.

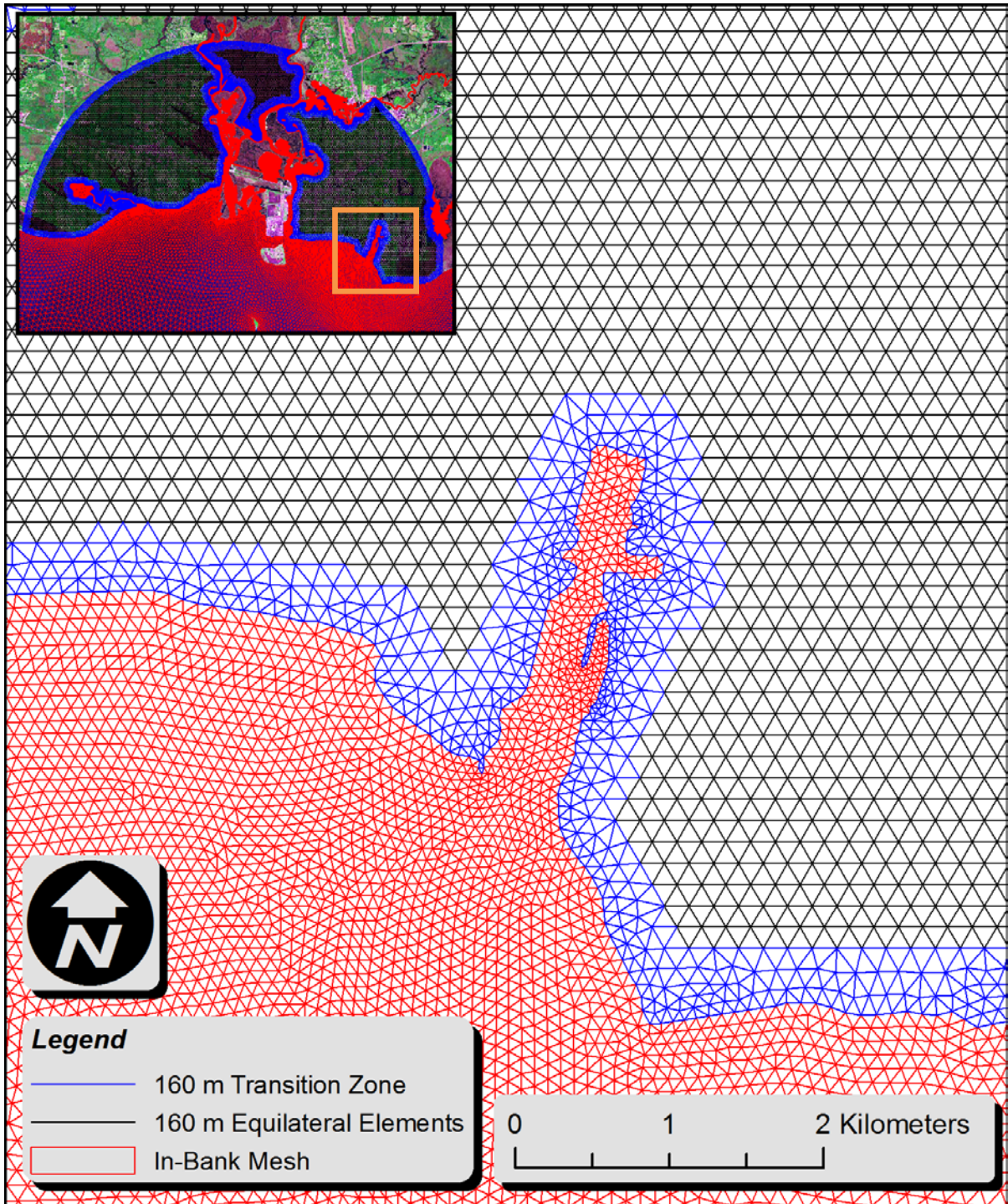


Figure 70 Zoom in on the Pascagoula Port located in the Right Equilateral Zone. The red triangles represent the in-bank triangular elements, the blue is the transitional elements following the geometric criteria, and the black elements are the 16-m equilateral elements.

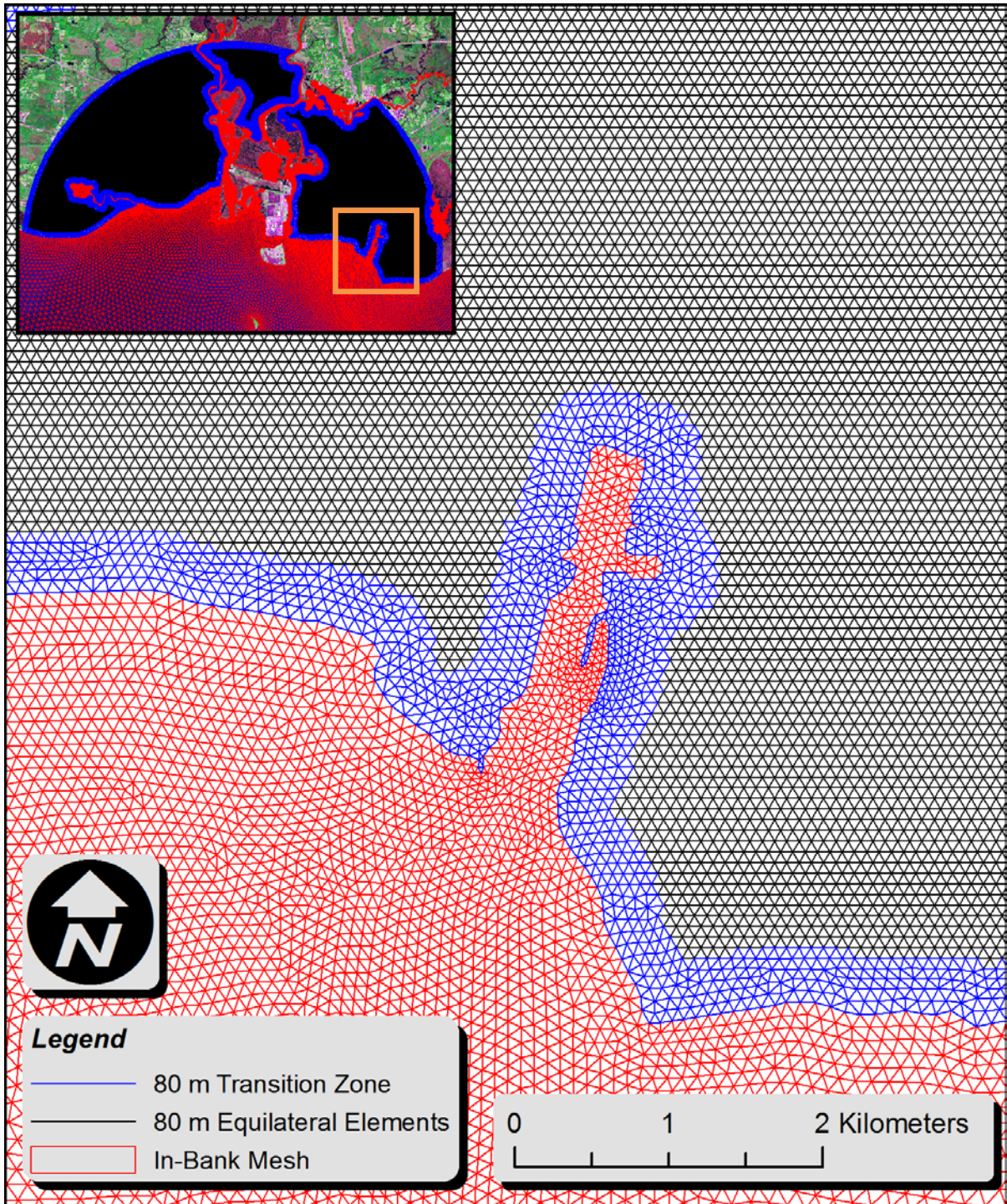


Figure 71 Zoom in on the Pascagoula Port located in the Right Equilateral Zone. The red triangles represent the in-bank triangular elements, the blue is the transitional elements following the geometric criteria, and the black elements are the 80-m equilateral elements.

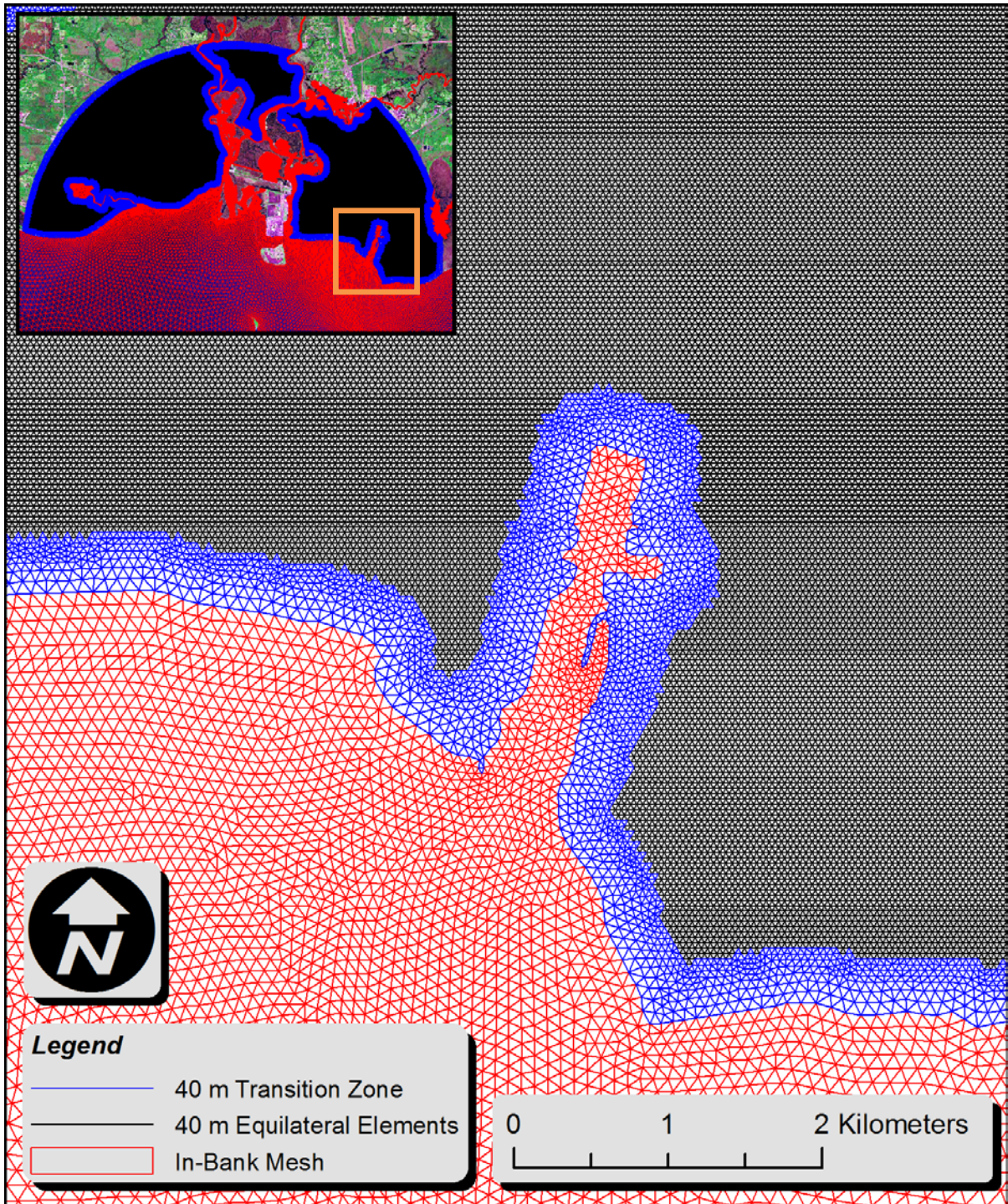


Figure 72 Zoom in on the Pascagoula Port located in the Right Equilateral Zone. The red triangles represent the in-bank triangular elements, the blue is the transitional elements following the geometric criteria, and the black elements are the 40-m equilateral elements.

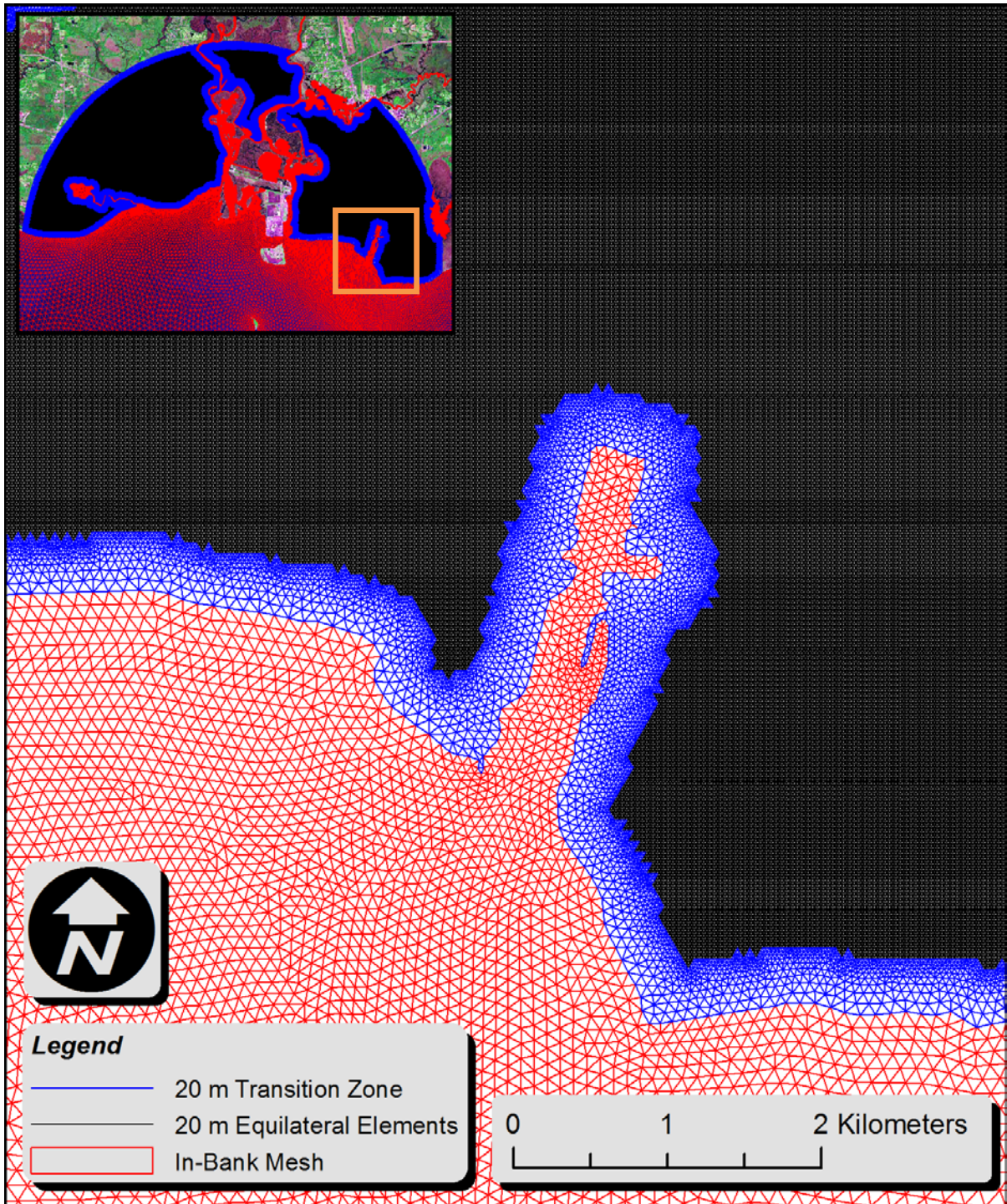


Figure 73 Zoom in on the Pascagoula Port located in the Right Equilateral Zone. The red triangles represent the in-bank triangular elements, the blue is the transitional elements following the geometric criteria, and the black elements are the 20-m equilateral elements.

8.2.2 Remaining Floodplain Mesh

The remaining area of the floodplain is discretized around the equilateral transition zone and bounded by the 10-m contour and adjoining shoreline. Figure 74 shows the floodplain boundary (red line), existing mesh coverage area (blue line), and the equilateral regions (orange boundary). Vertical features were hand digitized by creating arcs along significant topographic gradients. The arcs were forced as element edges at specific resolutions during paving. It has been proven for the ADCIRC model, that forcing element edges along topographic features improves model results (Roberts, 2004; Coggin, 2008). The 1-arc-second (30-m) National Elevation Dataset (NED) (Gesch *et al.*, 2002; Gesch, 2007), Landsat satellite imagery (Gesch *et al.*, 2002; Gesch, 2007), bare earth LiDAR-derived 5-m DEM (discussed in the next chapter), and aerial photography were used to digitize the vertical features. Figure 75 and Figure 76 show the digitized boundaries as black arcs with both the NED and Landsat data as the background image, respectively. Along the interior, mesh resolution of vertical feature arcs ranged from 50-m to 150-m and was 200-m along the mesh boundary. Varying the mesh resolution was achieved by adjustments to the nodal density along the boundary and vertical feature arcs using the “Redistribute vertices” tool in SMS. The tool redistributes vertices along an arc by three methods: 1) specified spacing, 2) number of segments with a bias function, and by 3) minimum and maximum spacing. When transitioning element sizes, all three methods were utilized, with the first method providing a brute force transition and the other two adjusting the vertex distribution by automated methods in SMS. After the boundary and interior arcs had proper vertex spacing, the region between the floodplain boundary and equilateral area was paved using a triangular paving method using SMS 10.1 (Aquaveo LLC, 2010). The floodplain was split into

four sections to speed up mesh generation time. The sections were split by raised features or raised features were connected to form a boundary. All four segments were then appended together as one grid file. Figure 77 presents a section of the mesh with the digitized vertical features (purple) and the mesh elements (black) over the 5 m DEM.

A transitional area was meshed to merge the LiDAR coverage area and the FLPH_AL mesh. The FLPH_AL mesh was used for the area around the shoreline of Mobile Bay to the 10-m contour (Figure 74). Figure 78 shows the breakdown of each mesh. The red area is the floodplain mesh developed for this study, the light blue is the mesh to transition from the Pascagoula floodplain to the FLPH_AL mesh, and the dark blue is the FLPH_AL mesh.

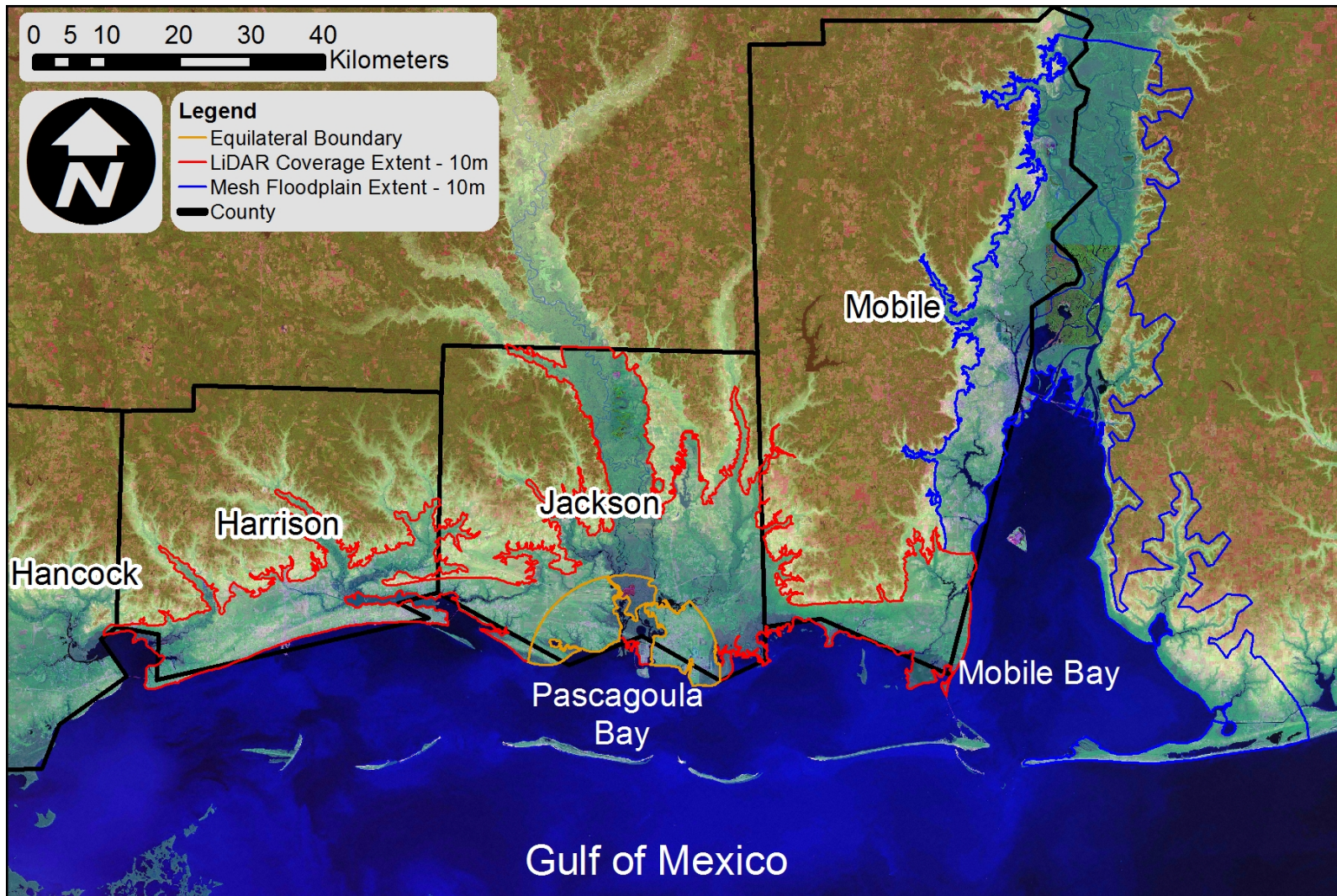


Figure 74 The extent of the LiDAR coverage is represented by the red line. The equilateral region is the orange boundary. Nodal placement and elevation data within the blue boundary was obtained from a previous FEM. The counties are bounded by the black lines. The background is NED (Gesch *et al.*, 2002; Gesch, 2007) elevation data over Landsat satellite imagery (Goslee, 2011).

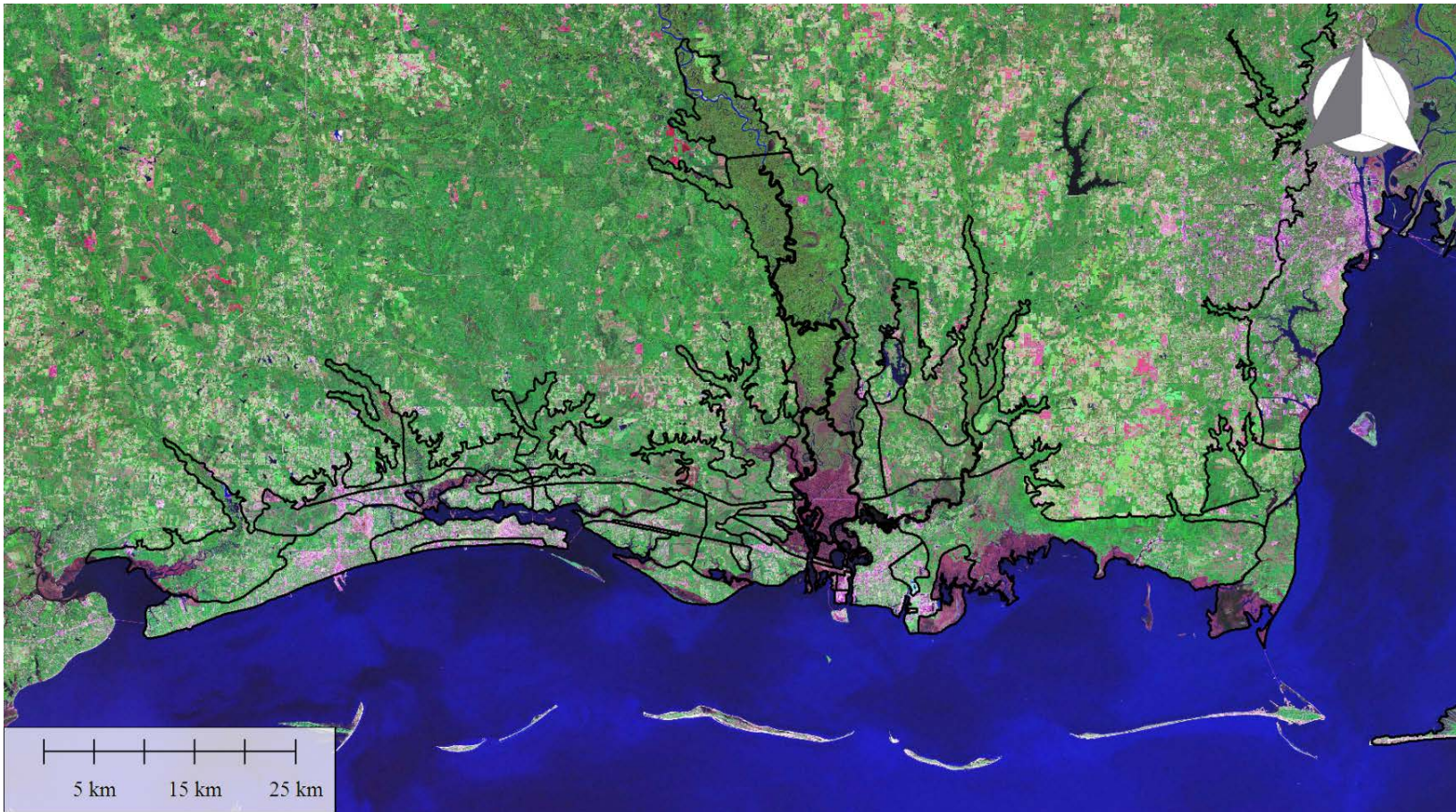


Figure 75 Digitized boundaries for use in floodplain mesh development (black). The background image is Landsat satellite imagery (Goslee, 2011).

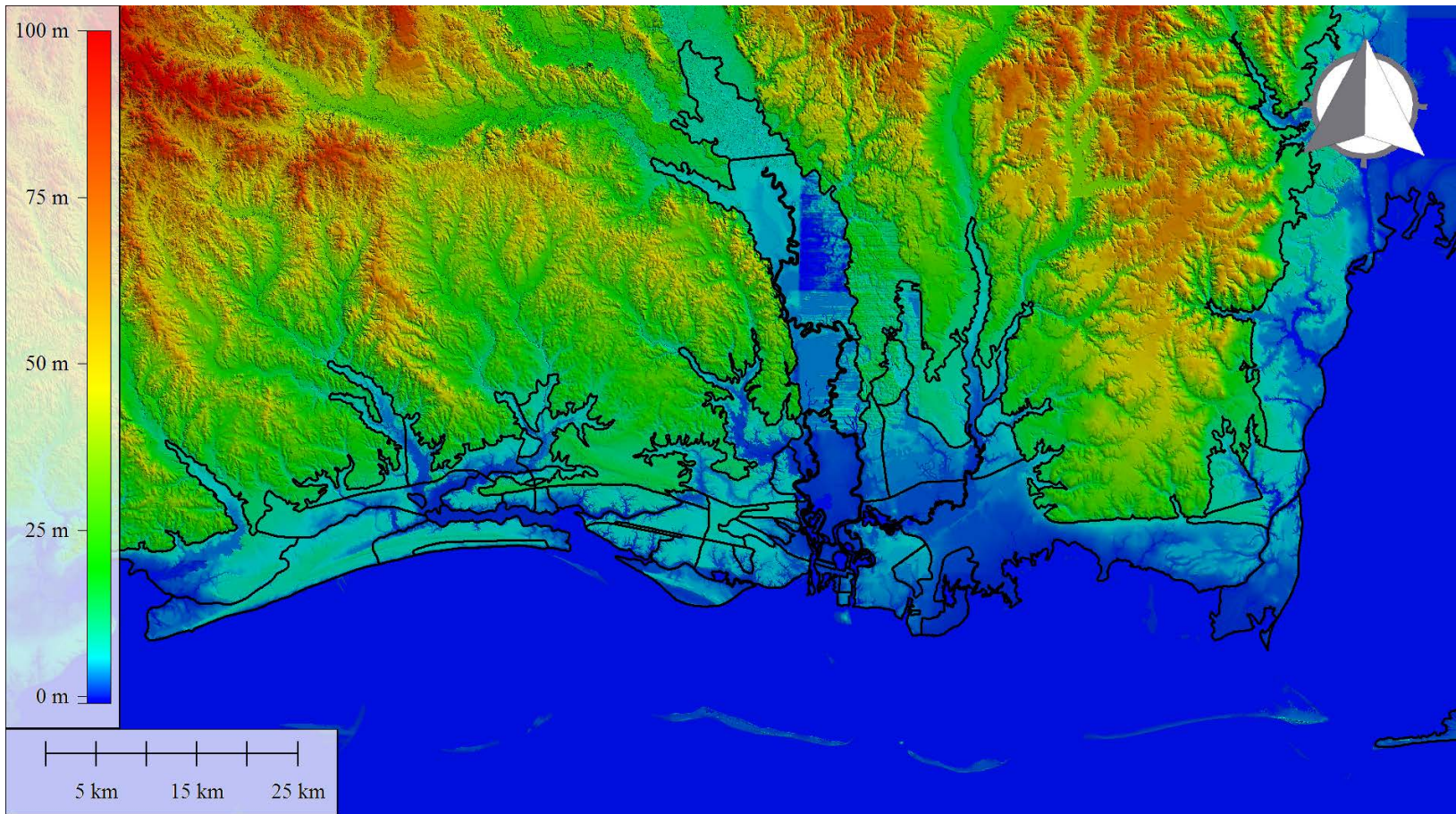


Figure 76 Digitized boundaries for use in floodplain mesh development (black). The background is 1-arc-second (30 m) NED DEM (Gesch *et al.*, 2002; Gesch, 2007).

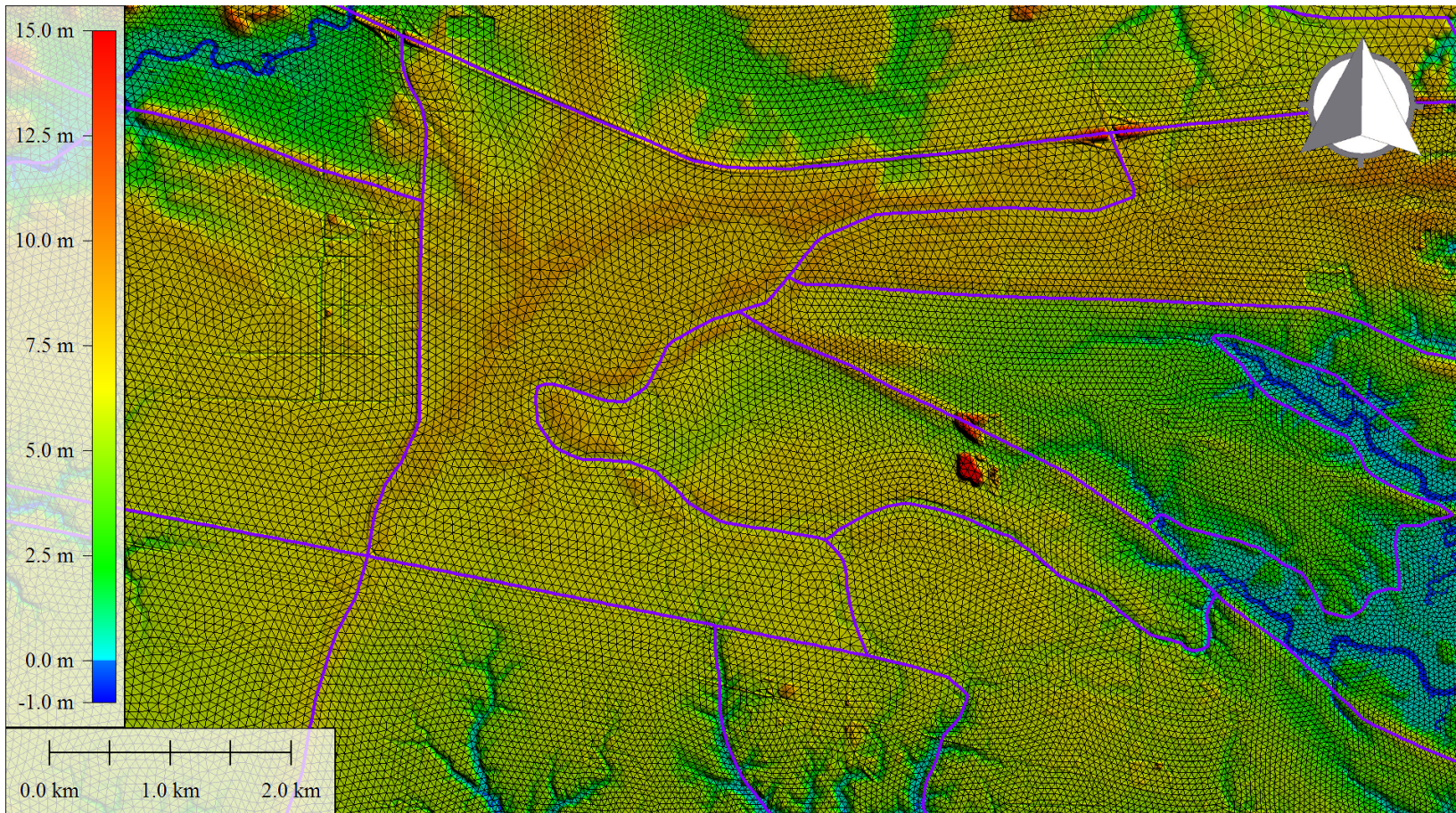


Figure 77 Digitized vertical feature arcs (purple) used as element (black triangles) edges. The background is the bare earth LiDAR-derived 5-m DEM.

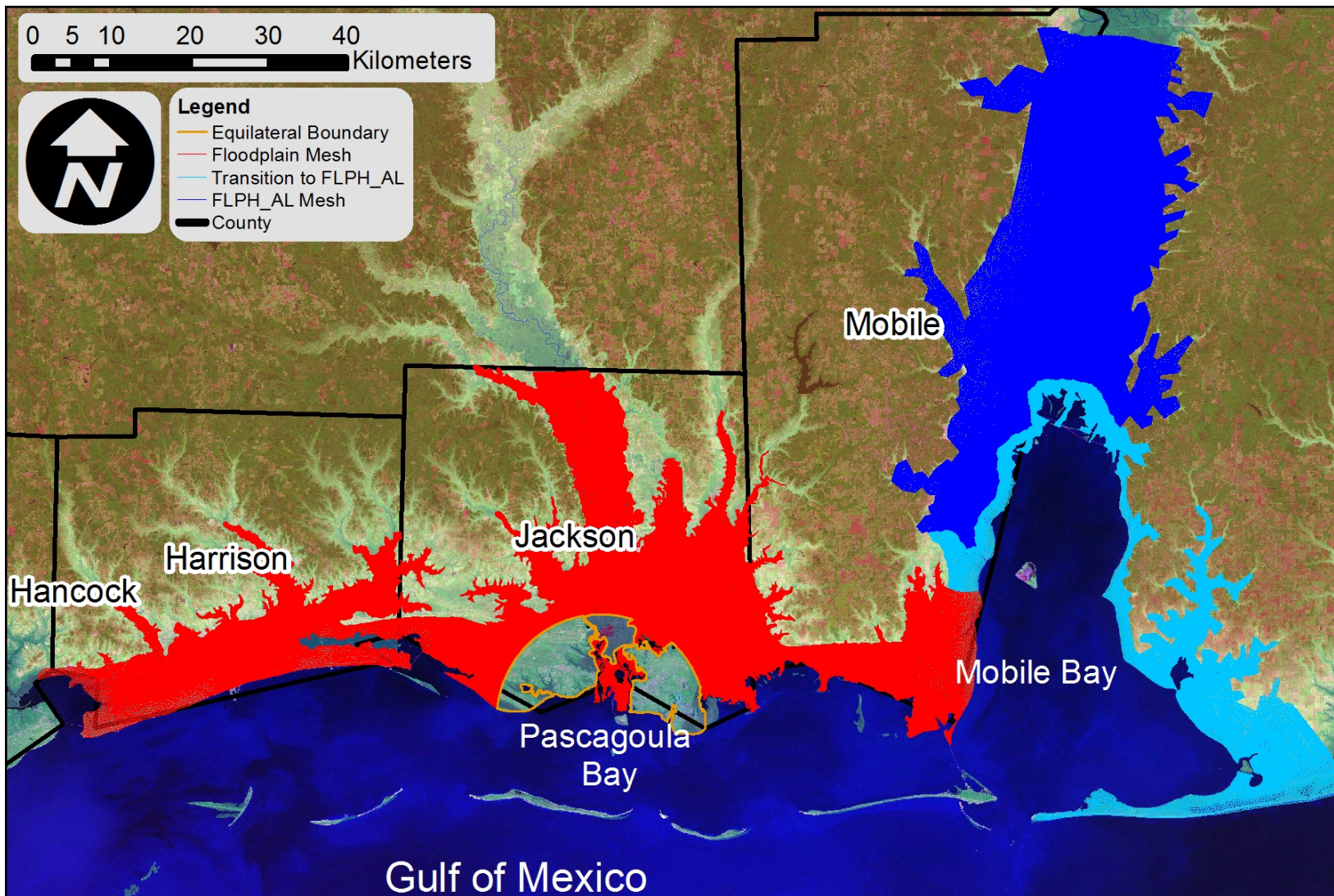


Figure 78 Floodplain mesh in red, transition to FLPH_AL mesh (light blue), and FLPH_AL mesh (blue). The equilateral zones are bounded by the orange boundary. The background is Landsat (Goslee, 2011).

8.2.3 Mesh Node Interpolation

Before merging the floodplain mesh to in-bank mesh number 1, topographic values above NAVD88 must be assigned to the mesh nodes. The bare earth LiDAR-derived 5-m DEM discussed in Chapter 7 (Figure 48) was the source elevation dataset used for the floodplain regions outside the equilateral areas and the equilateral transition zones. The interpolation scheme used is that defined by Coggin (2008) and explained in Chapter 2 Section 2.2. The method applies a control area polygon using the connected elements' centroids as vertices and averages the DEM cells within each control polygon (Figure 10). Figure 79 presents the FEM with elevations, without the equilateral regions, merged to the in-bank model. Chapter 9 presents the interpolation of the topography to the equilateral mesh nodes.

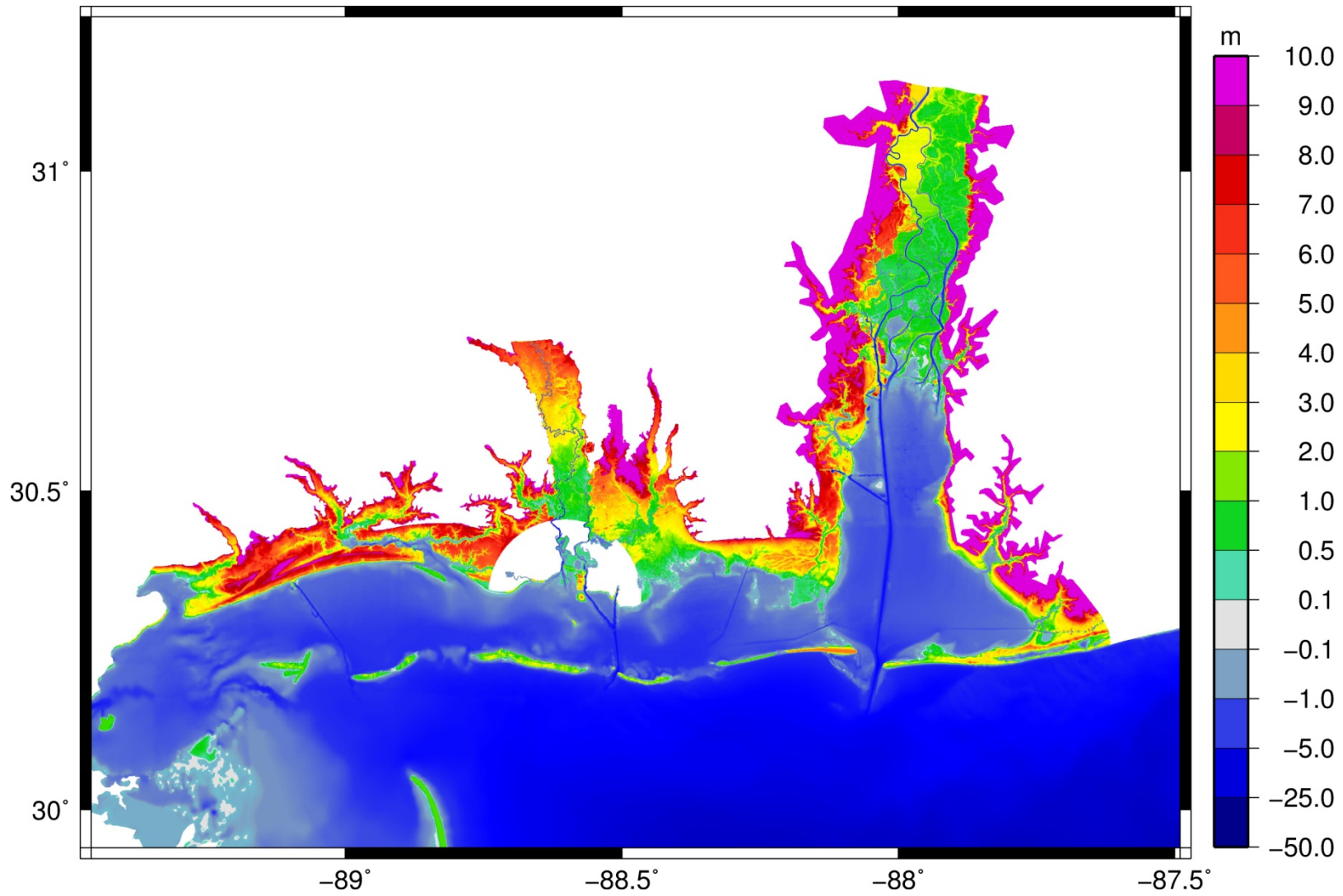


Figure 79 Floodplain mesh (withholding the equilateral zones) merged to in-bank mesh number 1. The contours are elevations with respect to NAVD88.

CHAPTER 9: LARGE DOMAIN TOPOGRAPHIC ERROR ASSESSMENT

Assessment of topographic error for the three large regions discussed in Chapter 8 surrounding the Pascagoula River in southern Mississippi is presented (Figure 67). First, a comparison of the training dataset and training-derived 5-m DEM interpolated to four equilateral FEMs (160-m, 80-m, 40-m, and 20-m) in each region is discussed. Second, an assessment of neighboring DEM grid cell averaging techniques is shown. The general methods are consistent with those presented in Chapter 6 on the equilateral zones developed in Chapter 8.

9.1 Equilateral Mesh Node Interpolation

Equilateral element mesh nodes for all four element edge lengths (160-m, 80-m, 40-m, and 20-m) obtained elevations from two sources with varying interpolation schemes. Development of the equilateral meshes for each zone was discussed in Chapter 7. The two elevation sources are the training dataset and the training dataset-derived 5-m raster DEM generated in Chapter 6 Section 2 and Chapter 7, respectively. Linear, NN, and IDW interpolation schemes were employed using SMS 10.1 (Aquaveo LLC, 2010). Direct lookup (1 cell average) and multiple cell area averaging (9, 25, 49, 81, 121, 169, 225, 289, 361, and 441 neighboring cell area averages) with the 5-m DEM was interpolated with a FORTRAN code specifically developed for this research. Details for each interpolation method were discussed in Chapter 3.

9.2 Accuracy Assessment Results and Discussion

Elevation error was computed in terms of RMSE (Equation 5.1) and the 95th percentile for vertical differences in interpolated values across the test dataset for the three equilateral regions. RMSE and 95th percentile for each FEM from differences at the locations of each test point in the test dataset are presented. Table 17 and Table 18 show RMSE for each FEM with elevation interpolated from the training dataset and training-derived 5-m raster DEM using linear, IDW, and NN. For each test region, linear and NN interpolation outperformed IDW, regardless of the source elevation dataset. Linear interpolation performed computationally faster than the IDW and NN methods.

RMSE was generally equivalent for the Left and Right Zones; however, the Center Zone achieved significantly less RMSE. Note how the Center Zone is primarily marsh with no areas of thick vegetative canopy and manmade structures are non-existent. As shown previously, increased error typically arises in regions of gradients in elevation. Since the marsh area is characterized by smoothly varying topography, RMSE was expected to be minimal, regardless of the element size employed, which was the case here with these results. Put simply, large elements are able to capture small topographic gradients approximately as well as smaller elements.

For the Left and Right Zones, RMSE varies drastically with a range of about 45-cm (~1.5-ft) between element edge lengths of 20-m to 160-m. RMSE for the 160-m equilateral meshes in the Left and Right Zones average about 65-cm (~2-ft), which is a considerable error for global elevations, especially for a low-lying coastal region where large gradients in slope are minimal. A large increase in error with increasing element size was expected due to the

variability in landcover types and topographic roughness of the Left and Right Zones. Interpolation using the training-derived 5-m DEM yield lower RMSE than the training dataset for all interpolation methods and mesh sizes tested. Therefore the 5-m DEM was selected as the source elevation dataset.

Table 17 RMSE of the training data interpolated to each FEM using a linear, IDW, and NN method compared to the test dataset

Training BEL to FEM – RMSE (cm)									
	Left			Center			Right		
Size (m)	Linear	IDW	NN	Linear	IDW	NN	Linear	IDW	NN
20	16.7	18.3	16.9	11.9	12.7	12.0	20.2	21.7	20.4
40	26.3	27.3	26.5	14.9	15.5	15.0	30.4	31.3	30.7
80	42.2	42.8	42.4	17.6	18.2	17.8	42.4	43.1	42.6
160	68.4	68.9	68.6	20.2	20.80	20.4	62.9	63.5	63.0

*Using three closest points

Table 18 RMSE of the training-derived 5-m DEM interpolated to each FEM using a linear, IDW, and NN method compared to the test dataset

Training-derived 5m DEM to FEM – RMSE (cm)									
	Left			Center			Right		
Size (m)	Linear	IDW	NN	Linear	IDW	NN	Linear	IDW	NN
20	16.3	18.0	16.3	11.5	11.9	11.6	19.7	20.9	19.8
40	25.9	26.9	25.9	14.4	14.7	14.5	29.6	30.2	29.7
80	41.8	42.3	41.8	17.1	17.3	17.1	41.7	42.2	41.8
160	68.1	68.4	68.2	19.8	20.2	19.9	62.3	62.6	62.4

*Using three closest points

Figure 80 through Figure 82 illustrate RMSE using cell area averaging methods from the training-derived 5-m DEM for each FEM. The figures contain a large amount of information on

the effects of mesh element size and interpolation method on topographic error. For example, in Figure 80, the lowest RMSE was obtained via coupling the 20-m equilateral element with the 9 CA interpolation method. Conversely, if a 441 CA interpolation was used for the same 20-m equilateral mesh, the error increases from 17.2-cm to 38.9-cm, an amount of 21.7-cm (0.7-ft). An 80-m equilateral mesh produced the same error as the 20-m mesh with the 441 CA method. Additionally, RMSE increased if too many neighboring cells were averaged because the total area from the DEM in relation to the element size was too large and overlapped adjacent elements. The range of RMSE between all interpolation methods was higher in the lower mesh size; however, it decreased as the mesh element size increased beyond 100-m, especially for the Left and Right Zones which contain larger error than the Center Zone. As a result, the number of cells used in computing the average was more influential for smaller elements than larger elements.

In terms of RMSE, a general trend was observed with the cell averaging method (Table 19). Regardless of the topographic characteristics and landcover for each region, the best performing interpolation (lowest RMSE) was consistent for each equilateral element size. For the 160-m equilateral elements, many of the large neighboring averages produced equivalent RMSE or differences within 1 cm of one another.

The 95th percentile for each mesh interpolated from the training-derived 5 m DEM was computed to assess vertical accuracy since topographic elevation errors were found to be non-normal (Figure 83 through Figure 85). As expected, the 95th percentile, with respect to mesh resolution, was similar to RMSE with smaller elements yielding an increase in accuracy and larger elements containing less accuracy.

In terms of topographic accuracy using the 95th percentile, the cell averaging method with the highest accuracy for a given mesh resolution generally matched the cell average method with the smallest RMSE (Table 20). Minor variations occurred in relation to the best performing cell averaging technique, though differences were within 1-cm. Results were used to develop a cell averaging relationship of minimal topographic error and accuracy for a given element size

The following equation computes the number of neighboring cell averages based on the results in Table 19:

$$CA = \begin{cases} 1 & \text{for } \mathbb{N} < 1 \\ [2(\mathbb{N}) + 1]^2 & \text{for } \mathbb{N} \geq 1 \end{cases} \quad 9.1$$

where $\mathbb{N} = 0.25(\Delta_M)/\Delta_{DEM}$ and is the number of DEM grid cells to move around the current cell in all directions, Δ_M is the mesh element size, and Δ_{DEM} is the DEM grid cell size.

Table 21 shows Equation 9.1 applied to a 5-m DEM with element sizes form 1.25-m to 160-m. The results are identical to those in Table 19 for element sizes of 20-m, 40-m, 80-m, and 160-m. To test Equation 9.1 on element sizes less than 20-m, it was applied to the Test Sites presented in Chapter 6 (Table 22). Results show the validity of Equation 9.1 for each element size for a 5-m DEM cell size.

From the data and equations presented, an interpolation algorithm was developed for interpolating a 5-m DEM to a FEM using average element size to determine the number of neighboring DEM grid cells to be used in the averaging scheme.

Further, the RMSE and 95th percentile for all sites (both Pascagoula and New Orleans) provide a basis for determining topographic uncertainty for a coastal area in the Northern Gulf of Mexico given a particular mesh size and interpolation scheme.

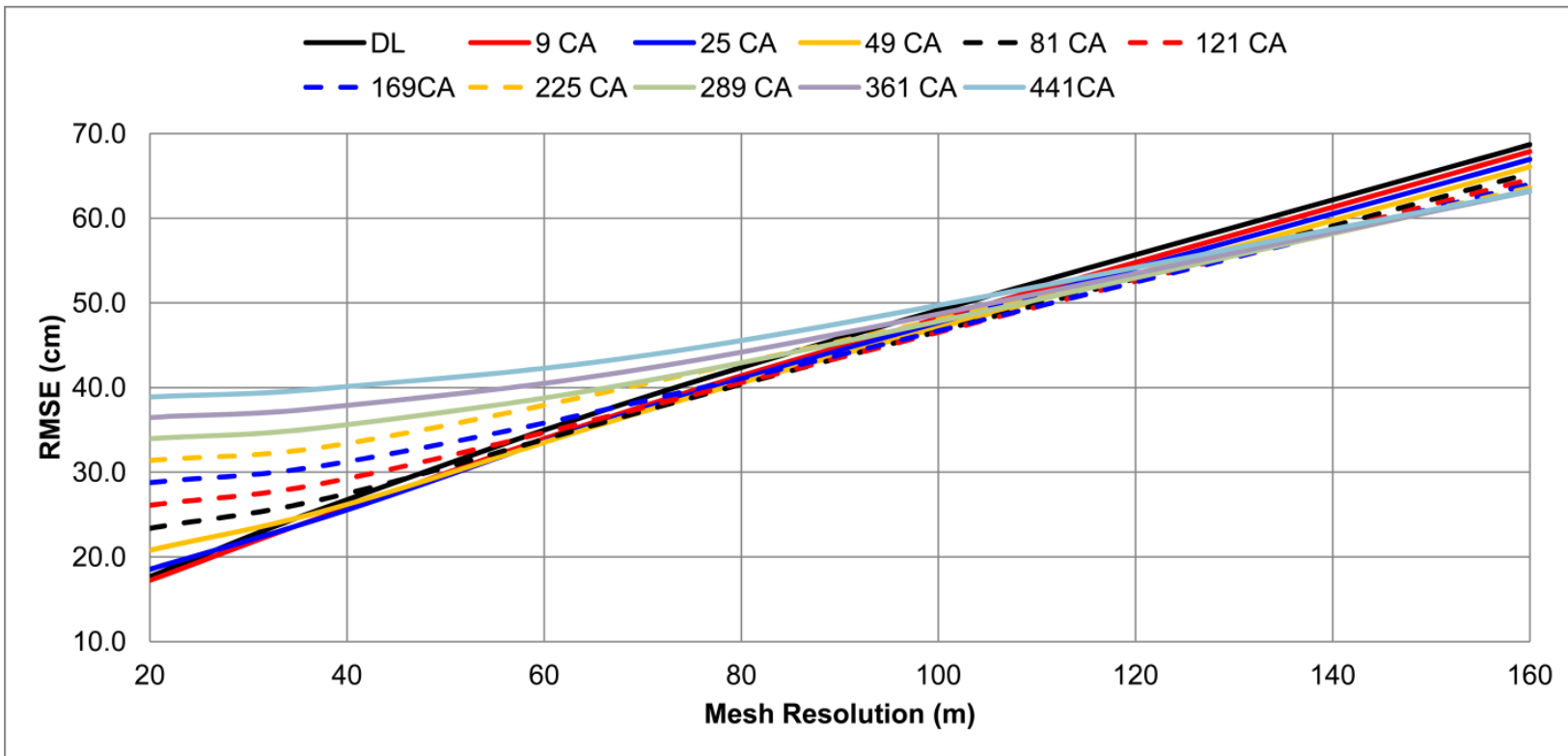


Figure 80 RMSE of the training-derived 5-m DEM interpolated to each FEM for the Left Zone using a direct lookup and area averaging method from 9 to 441 neighboring cells.

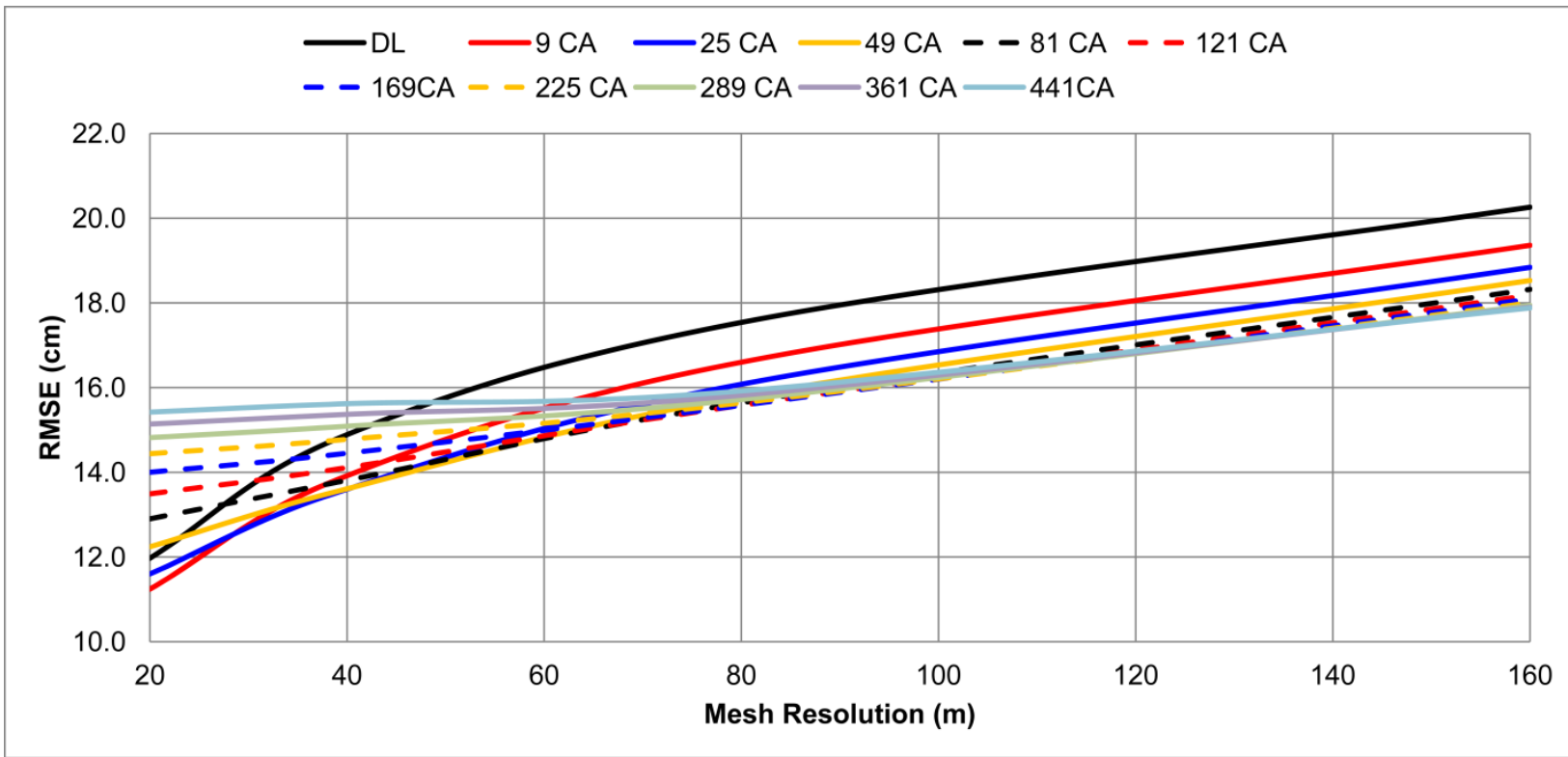


Figure 81 RMSE of the training-derived 5-m DEM interpolated to each FEM for the Center Zone using a direct lookup and area averaging method from 9 to 441 neighboring cells.

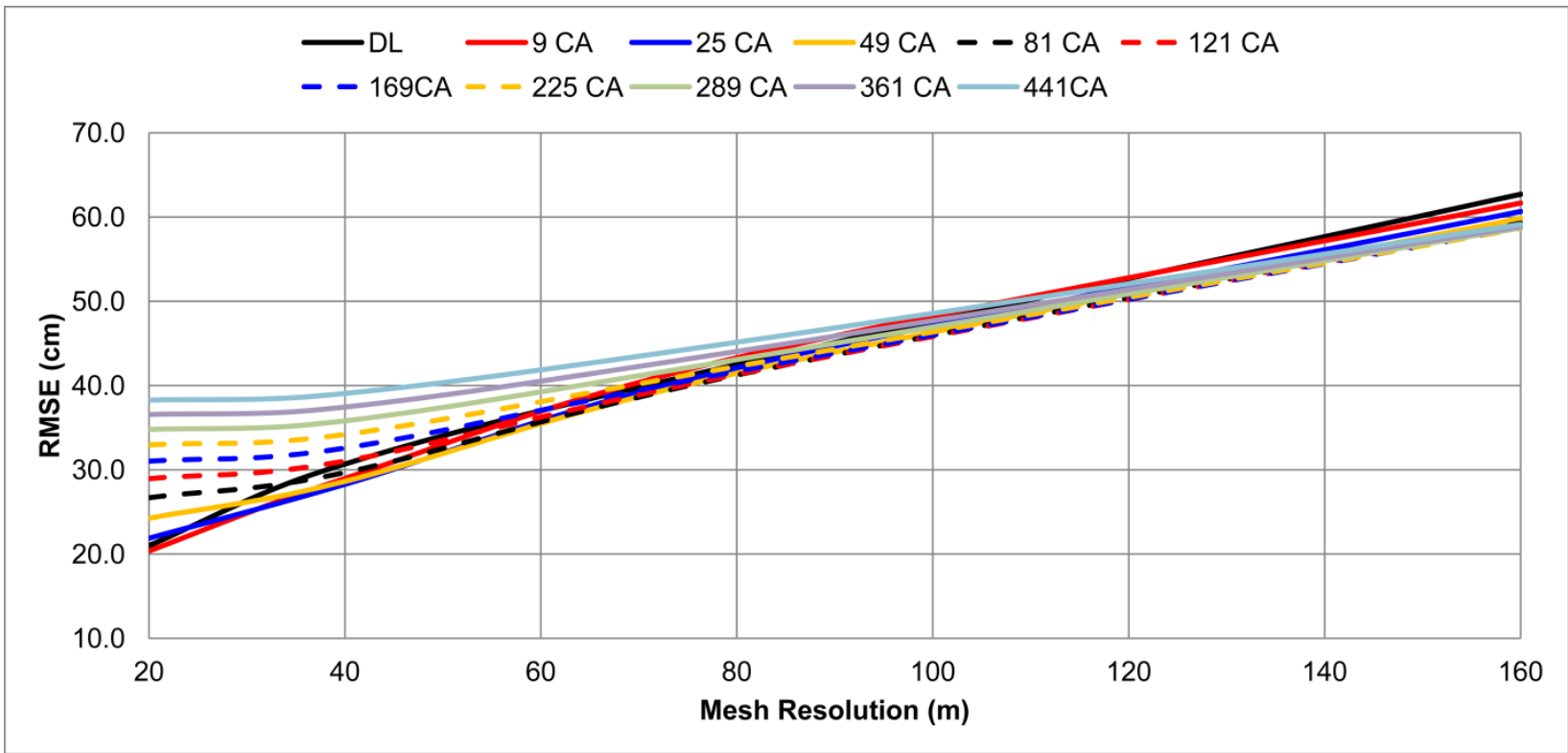


Figure 82 RMSE of the training-derived 5-m DEM interpolated to each FEM for the Right Zone using a direct lookup and area averaging method from 9 to 441 neighboring cells.

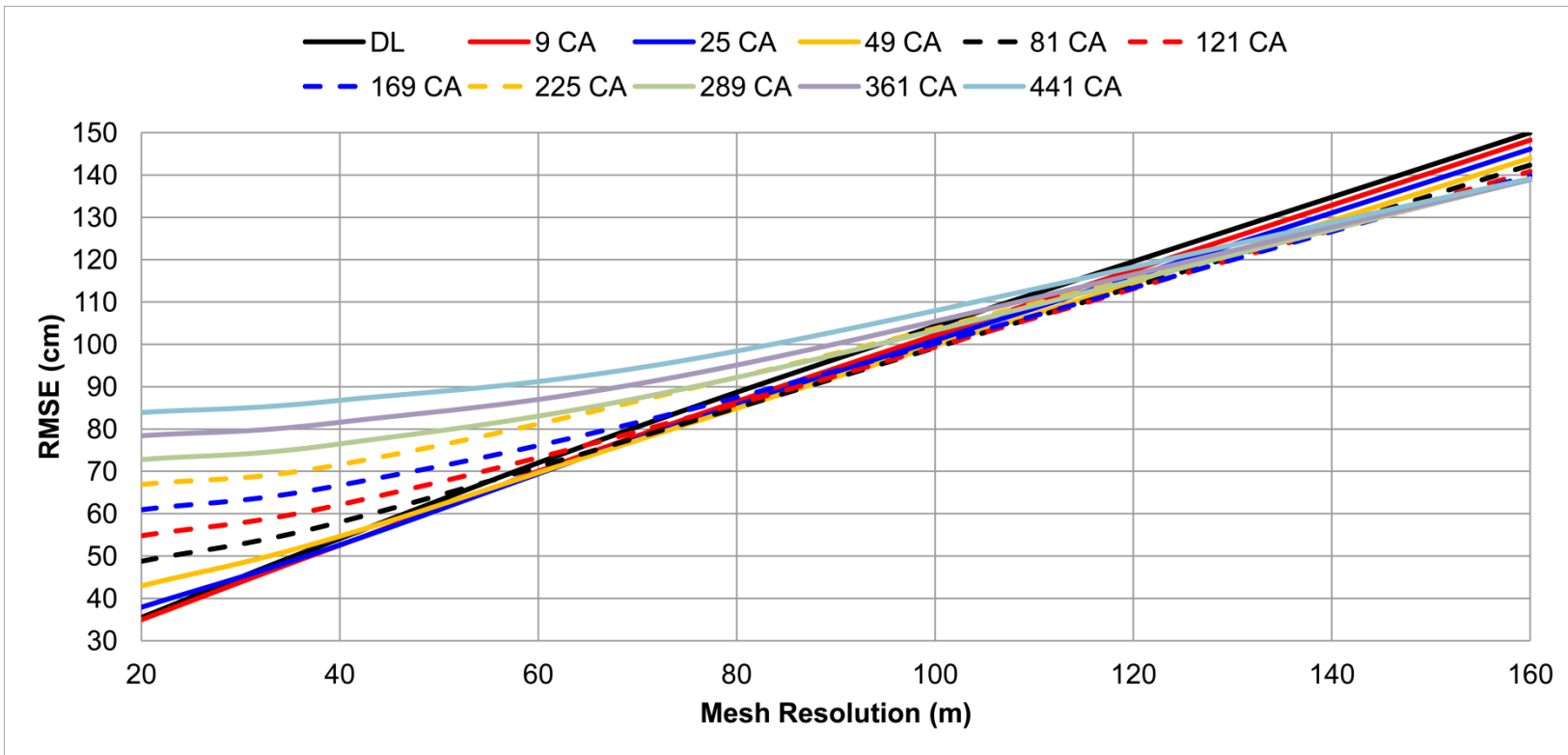


Figure 83 95th percentile of the training-derived 5-m DEM interpolated to each FEM for the Left Zone using a direct lookup and area averaging method from 9 to 441 neighboring cells.

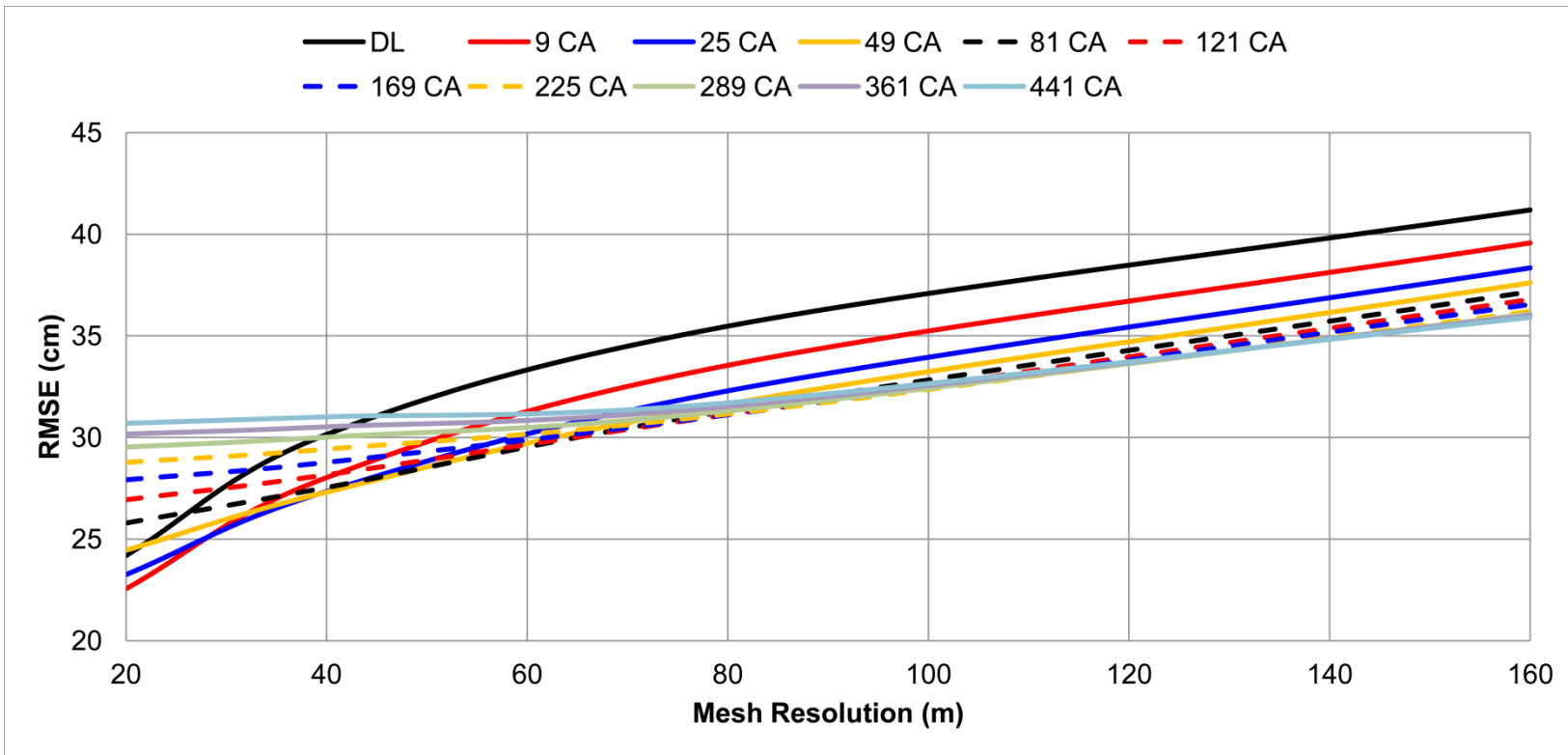


Figure 84 95th percentile of the training-derived 5-m DEM interpolated to each FEM for the Center Zone using a direct lookup and area averaging method from 9 to 441 neighboring cells.

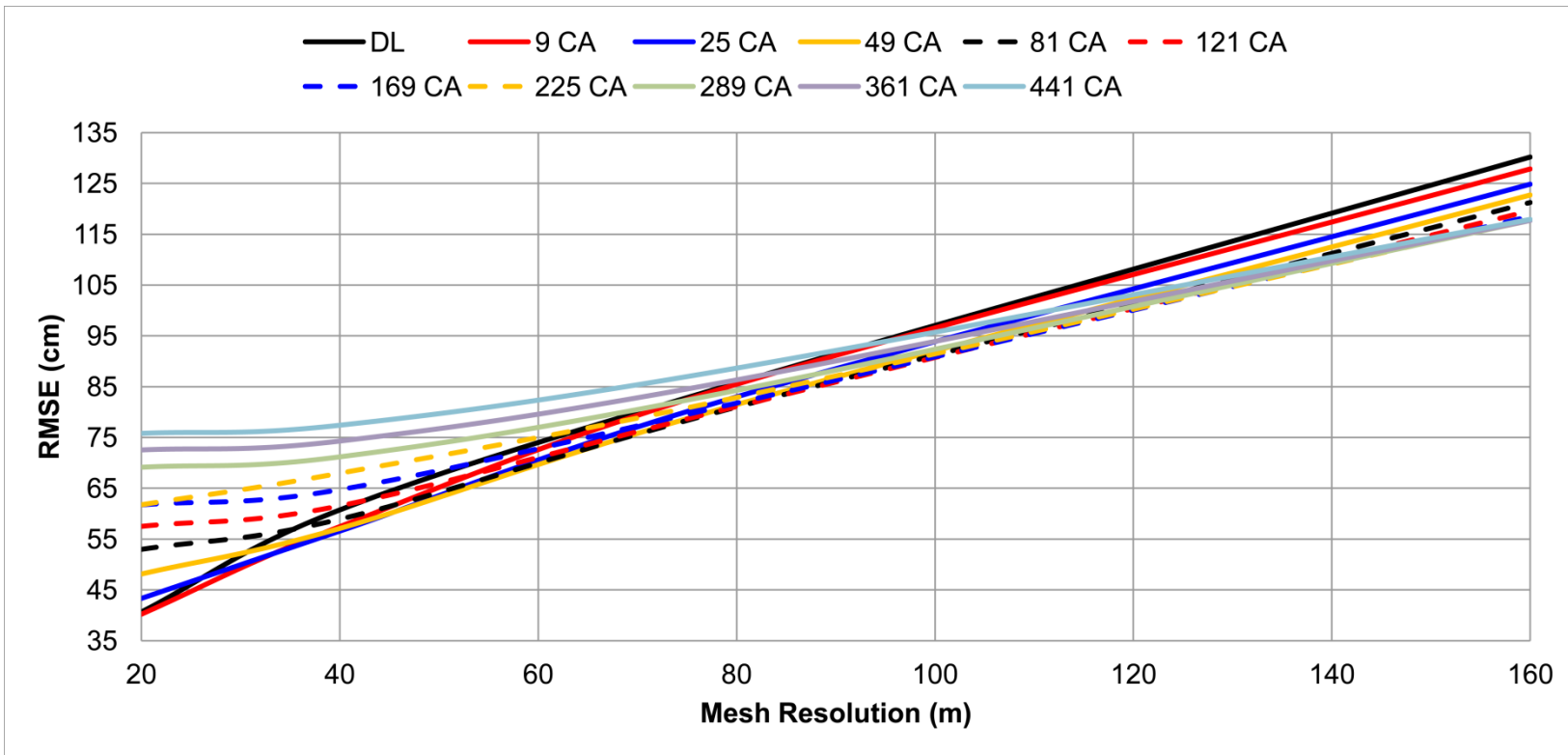


Figure 85 95th percentile of the training-derived 5-m DEM interpolated to each FEM for the Right Zone using a direct lookup and area averaging method from 9 to 441 neighboring cells.

Table 19 Best performing cell averaging method for each equilateral FEM zone at each equilateral element size in terms of RMSE

Δ_M	Left	Center	Right
20	9 CA	9 CA	9 CA
40	25 CA	25 CA	25 CA
80	81 CA	81 CA	81 CA
160	289, 361, 441 CA	289, 361, 441 CA	225, 289 CA

*Multiple entries suggest RMSE was within 1 cm of the lowest value

Table 20 Best performing cell averaging method for each equilateral FEM zone at each equilateral element size in terms of the 95th percentile

Δ_M	Left	Center	Right
20	DL	9 CA	9 CA
40	9, 25CA	25, 49 CA	25 CA
80	49, 81 CA	81 CA	81 CA
160	225, 289, 361 CA	169, 225, 289, 361 CA	225, 289, 361 CA

*Multiple entries suggest accuracy was within 1 cm of the lowest value

Table 21 Equation 9.1 applied for each element size in Table 19 with a 5-m DEM

Δ_M	Δ_{DEM}	N	CA
1.25	5	0.0625	1
2.5	5	0.125	1
5	5	0.25	1
10	5	0.5	1
20	5	1	9
40	5	2	25
80	5	4	81
160	5	8	289

Table 22 Best performing cell averaging method for each equilateral FEM for each Test Site near Pascagoula and New Orleans presented in Chapter 6

Δ_M	Test Site 1	Test Site 2	Test Site 3	NLA_Urban	NLA_Marsh
1.25	DL	DL	DL	DL	DL
2.5	DL	DL	DL	DL	DL
5	DL	DL	DL	9 CA	DI
10	DI	9 CA	DL	9 CA	9 CA
20	9 CA	9 CA	9 CA	9 CA	9, 25 CA
40	25 CA	25 CA	25 CA	25, 49 CA	-
80	81, 121 CA	81, 121 CA	81, 121 CA	81, 121 CA	-
160	169 + CA	169 CA +	169 CA +	169 CA +	-

CHAPTER 10: NUMERICAL CODE DOCUMENTATION

The following chapter presents a description of the numerical code used in this study.

10.1 Numerical Model Description

In modeling long-wave processes of tidal flow and hurricane storm surge in oceanic and coastal environments, the shallow water equations may be used to approximate currents and the variation of water levels. The shallow-water formulation is valid since the horizontal extent of long-wave hydrodynamics is much larger than that of the water depth (Kolar *et al.*, 1994).

10.2 Governing Equations

In this study, the depth integrated equations of mass and momentum are solved by the ADCIRC-2DDI (Advanced Circulation Two-dimensional depth integrated) code to compute water level deviation, ζ , and currents in x and y directions, U and V , respectively. The equations are subject to incompressibility, Boussinesq and hydrostatic pressure approximations. The governing equations are the continuity (Eq. 10.1) and momentum equations (Eq. 10.2) and (Eq. 10.3). They are expressed in a Cartesian coordinate system in primitive form as (Westerink *et al.*, 1994a):

$$\frac{\partial \zeta}{\partial t} + \frac{\partial UH}{\partial x} + \frac{\partial VH}{\partial y} = 0 \quad 10.1$$

$$\frac{\partial U}{\partial t} + U \frac{\partial U}{\partial x} + V \frac{\partial U}{\partial y} - fV = -\frac{\partial}{\partial x} \left[\frac{p_s}{\rho_0} + g(\zeta - \alpha\eta) \right] + \frac{1}{H} M_x + \frac{\tau_{sx}}{\rho_0 H} - \tau_* U \quad 10.2$$

$$\frac{\partial V}{\partial t} + U \frac{\partial V}{\partial x} + V \frac{\partial V}{\partial y} - fU = -\frac{\partial}{\partial y} \left[\frac{p_s}{\rho_0} + g(\zeta - \alpha\eta) \right] + \frac{1}{H} M_y + \frac{\tau_{sy}}{\rho_0 H} - \tau_* V \quad 10.3$$

where ζ = free surface elevation relative to the geoid; U, V = depth-averaged horizontal velocities; $H = \zeta + h$ = total water column; h = bathymetric depth relative to the geoid; $f = 2\Omega \sin \phi$ = Coriolis parameter; Ω = angular speed of the Earth; ϕ = degrees latitude; p_s = atmospheric pressure at the free surface; g = acceleration due to gravity; η = Newtonian equilibrium tide potential; α effective Earth elasticity factor; ρ_0 = reference density of water;

τ_{sx}, τ_{sy} = applied free surface stress; $\tau_* = C_f \frac{(U^2 + V^2)^{1/2}}{H}$ = bottom stress; C_f = bottom friction

coefficient; $M_x = E_{h_2} \left[\frac{\partial^2 UH}{\partial x^2} + \frac{\partial^2 UH}{\partial y^2} \right]$ = depth integrated horizontal diffusion/dispersion, x

direction; $M_y = E_{h_2} \left[\frac{\partial^2 VH}{\partial x^2} + \frac{\partial^2 VH}{\partial y^2} \right]$ = depth integrated horizontal diffusion/dispersion, y

direction; E_{h_2} = horizontal eddy diffusion/dispersion coefficient. Reid (1990) gives a practical expression for the Newtonian equilibrium tide potential expressed as:

$$\eta(\lambda, \phi, t) = \sum_{nj} C_{jn} f_{jn}^{TP}(t_0) L_j(\phi) \cos \left[\frac{2\pi(t-t_0)}{T_{jn}^{TP}} + \nu_{jn}^{TP}(t_0) \right] \quad 10.4$$

where C_{jn} = constant characterizing the amplitude of tidal constituent n of species j ; f_{jn}^{TP} = time-dependent nodal factor; ν_{jn}^{TP} = time-dependent astronomical argument; $j = 0, 1, 2$ = tidal species ($j = 0$, declinational; $j = 1$, diurnal, $j = 2$, semidiurnal); $L_0 = 3\sin^2 \phi - 1$; $L_1 = \sin(2\phi)$; $L_2 = \cos^2(\phi)$; λ, ϕ = degree longitude and latitude, respectively; t_0 = reference time; T_{jn}^{TP} = period of constituent n of species j .

In addition to Cartesian form, the equations can be expressed in spherical form. ADCIRC-2DDI maps these spherical coordinate equations onto a rectilinear coordinate system using the Carte Parallelogrammatique Projection (CPP) (Pearson, 1990). The primitive shallow water equations in spherical coordinates are (Westerink *et al.*, 1994a):

$$\frac{\partial \zeta}{\partial t} + \frac{1}{R \cos \phi} \left(\frac{\partial UH}{\partial \lambda} + \frac{\partial (VH \cos \phi)}{\partial \phi} \right) = 0 \quad 10.5$$

$$\begin{aligned} \frac{\partial U}{\partial t} + \frac{1}{R \cos \phi} U \frac{\partial U}{\partial \lambda} + \frac{1}{R} V \frac{\partial U}{\partial \phi} - \left(\frac{\tan \phi}{R} U + f \right) V = \\ - \frac{1}{R \cos \phi} \frac{\partial}{\partial \gamma} \left[\frac{P_s}{\rho_0} + g(\zeta - \alpha \eta) \right] + \frac{1}{H} (M_\lambda) + \frac{\tau_{s\lambda}}{\rho_0 H} - \tau_* U \end{aligned} \quad 10.6$$

$$\begin{aligned} \frac{\partial V}{\partial t} + \frac{1}{R \cos \phi} U \frac{\partial V}{\partial \lambda} + \frac{1}{R} V \frac{\partial V}{\partial \phi} - \left(\frac{\tan \phi}{R} U + f \right) U = \\ - \frac{1}{R} \frac{\partial}{\partial \phi} \left[\frac{P_s}{\rho_0} + g(\zeta - \alpha \eta) \right] + \frac{1}{H} M_\phi + \frac{\tau_{s\phi}}{\rho_0 H} - \tau_* V \end{aligned} \quad 10.7$$

where R = radius of the Earth.

The equations presented are discretized in space by linear finite elements and in time by a finite difference scheme (Luettich *et al.*, 1992). The use of a finite element scheme in the primitive form gives rise to spurious mode problems and numerical instabilities. To resolve this without artificial damping, the equations were reformulated to use the generalized wave continuity equation (GWCE) coupled with the momentum conservation equations (Kinnmark, 1985). Thus, ADCIRC-2DDI employs the GWCE rather than the primitive continuity equation (Westerink *et al.*, 1994a). The reformulated continuity equation using the GWCE in spherical coordinates is expressed as (Kolar *et al.*, 1994):

$$\begin{aligned}
& \left[\frac{\partial^2 \zeta}{\partial t^2} + \tau_0 \frac{\partial \zeta}{\partial t} - \frac{1}{R \cos \phi} \frac{\partial}{\partial \lambda} \left[\frac{1}{R \cos \phi} \left(\frac{\partial U U H}{\partial \lambda} + \frac{\partial U V H}{\partial \phi} \right) - \left(\frac{\tan \phi}{R} U + f \right) V H \right] \right. \\
& \left. - \frac{H}{R \cos \phi} \frac{\partial}{\partial \lambda} \left(\frac{p_s}{\rho_0} + g(\zeta - \alpha \eta) \right) + \frac{E_{h_2}}{R \cos \phi} \frac{\partial^2 \zeta}{\partial \lambda \partial t} \right. \\
& \left. + \frac{\tau_{s\lambda}}{\rho_0} - (\tau_* - \tau_0) U H \right] \\
& - \frac{1}{R} \frac{\partial}{\partial \phi} \left[\frac{1}{R \cos \phi} \left(\frac{\partial H U V}{\partial \lambda} + \frac{\partial H V V \cos \phi}{\partial \phi} \right) + \left(\frac{\tan \phi}{R} U + f \right) U H \right. \\
& \left. - \frac{H}{R} \frac{\partial}{\partial \phi} \left(\frac{p_s}{\rho_0} + g(\zeta - \alpha \eta) \right) + \frac{E_{h_2}}{R} \frac{\partial^2 \zeta}{\partial \phi \partial t} + \frac{\tau_{s\phi}}{\rho_0} - (\tau_* - \tau_0) V H \right] \\
& - \frac{\tan \phi}{R} \left(\frac{\partial V H}{\partial t} + \tau_0 V H \right) = 0
\end{aligned} \tag{10.8}$$

where τ_0 is a weighting factor constant in both space and time.

10.3 ADCIRC Bottom Friction Formulation

Recall, the bottom stress term, τ_* , represented in the shallow water equations (10.2) and 10.3. The bottom stress can be computed via a quadratic formulation as a function of the depth integrated velocity (Luettich *et al.*, 1992):

$$\tau_* = C_f \frac{\sqrt{U^2 + V^2}}{H} \tag{10.9}$$

where C_f = the bottom friction factor. Either a constant bottom friction factor or spatially varying friction factor can be assigned. In order to vary bottom friction with bathymetric depth, like Manning's formula, Luettich and Westerink (2006) implemented a hybrid bottom friction formulation:

$$C_f = C_{f_{\min}} \left[1 + \left(\frac{H_{break}}{H} \right)^\theta \right]^{-\gamma/\theta} \tag{10.10}$$

where $C_{f_{\min}}$ = minimum bottom friction coefficient; H_{break} = break depth; H = depth of the water column; θ = dimensionless parameter which that determines how rapid the hybrid bottom friction relationship approaches its deep and shallow water limits (10-m is recommended); γ = dimensionless parameter which that determines how the friction factor increases as the water depth decreases (a value of 1/3 is recommended for a Manning type friction law). When the water depth is above H_{break} (i.e. $H > H_{break}$), the bottom frictions approaches a quadratic function of depth averaged velocity where:

$$C_f = C_{f_{\min}} \quad 10.11$$

If the water depth is below H_{break} (i.e. $H < H_{break}$), equation (10.10) is employed.

Alternative implementation incorporates Manning's n into the bottom friction formulation. The bottom friction coefficient as a function of Manning's n is (Atkinson *et al.*, 2011):

$$C_f = \frac{g}{H^{1/3}} n^2 \approx \frac{g}{h^{1/3}} n^2 \quad 10.12$$

where g = acceleration due to gravity; $H = \zeta + h$ = depth of the entire water column; h = bathymetric depth; n = Manning's n coefficient. Incorporating (Eq. 10.12) into (Eq. 10.9) yields a bottom friction formulation that is a function of Manning's n and depth integrated velocity:

$$\tau_* = g \frac{n^2}{h^{1/3}} \sqrt{\frac{U^2 + V^2}{H}} \quad 10.13$$

For nodes with a bathymetric depth greater than the break depth (10-m), the minimum bottom friction is set to $C_{f_{\min}}$. A typical value of $C_{f_{\min}}$ is 0.003 is employed (Mukai *et al.*, 2002; Blanton *et al.*, 2004; Bacopoulos, 2009; Bunya *et al.*, 2010).

CHAPTER 11: MODEL SETUP

11.1 Astronomic Tide Model Setup

For all tidal simulations, the boundary conditions applied and model parameters remain unchanged, unless noted otherwise. The model is setup in a geographic coordinate system with advective terms disabled. Seven tidal constituents (K1, O1, M2, S2, N2, K2, and Q1) (Table 23) force the model as water levels along the open ocean boundary (60° west Meridian) as well as tidal potential forcings within the interior of the domain (Equation 10.4). The harmonic data is obtained from the global ocean model of Le Provost *et al.* (1998) except in shallow areas along the open ocean boundary where the tidal elevation data are inaccurate. In these locations, long term tidal records are used to adjust the harmonic data accordingly (Westerink *et al.*, 1994b). The model forcings are ramped over a 10-day period with a hyperbolic ramp function (Luettich *et al.*, 1992) and continued for a total simulation length of 45 days with a time step of 1-second and 0.25-seconds, for the in-bank mesh numbers 1 and 2, respectively. The time steps are computed based on the Courant number criteria for model stability. For the last 30-days (day 15 to 45) of the simulation, water levels are harmonically analyzed at selected locations using the built in harmonic analysis tool in ADCIRC-2DDI.

The hybrid bottom friction formulation (Eq. 10.10) is applied with the incorporation of Manning's n parameterization (Eq. 10.13). A constant Manning's n of 0.02 is used with $C_{f_{\min}} = 0.0025$; $H_{break} = 10 - m$; $\theta = 10$; and $\lambda = 1/3$. The horizontal eddy viscosity coefficient is set to 5 m²/sec and a depth-dependent GWCE weighting factor, τ_0 , is enabled. The wetting

and drying option is turned on with the minimum bathymetric depth equal to 0.1-m (Luettich & Westerink, 2006).

Table 23 Tidal constituents used to force the ADCIRC model.

Tidal Constituent	Name	Period (hr)	Frequency (rad/s)
M ₂	Principal lunar semidiurnal	12.42	0.000140518902509
K ₁	Luni-solar diurnal	23.93	0.000072921158358
O ₁	Principal lunar diurnal	25.82	0.000067597744151
N ₂	Larger lunar elliptic	12.66	0.000137879699487
K ₂	Luni-solar semidiurnal	11.97	0.000145842317201
Q ₁	Larger lunar elliptic diurnal	26.87	0.000064958541129
S ₂	Principal solar semidiurnal	12.00	0.000145444104333

11.2 Coupled Tide and Storm Surge Model Setup

The following methods and parameters were used to setup the ADCIRC model for a coupled tide and storm surge simulation. Hurricane Katrina is the storm of record for coastal Mississippi therefore it is the meteorological event used in this thesis (Figure 86). A 21.5-day simulation is performed, divided into two separate simulations (Table 24). First, a 15.5-day astronomic tide only simulation is performed from a cold start. The model is setup in a geographic coordinate system with advective terms disabled and seven tidal constituents (Table 23) force the model along the open ocean boundary, as well as tidal potential. The nodal factor and equilibrium arguments are adjusted to start on 08/10/2005 at 00:00 UTC. The forcings are ramped over a 10-day period with the last 5.5-days in steady-state. Next, a 6-day simulation of

astronomic tides and wind and pressures from Hurricane Katrina is performed from a hot start of the prior 15.5-day tide only model, yielding a total simulation length of 21.5-days. A 1-day is hyperbolic tangent ramping period (Luettich *et al.*, 1992) is included to initialize the added aerodynamic forcing.

Table 24 Breakdown of the 21.5-day astronomic tide and storm surge simulation

Simulation	Total Run Time (days)	Ramp Time (days)	Steady-State Time (days)	Run Start UTC	Run End UTC
Tides	15.5	10.0	5.5	08/10/2005 00:00	08/25/2005 12:00
Tides + Katrina	6	1.0	5	08/25/2005 12:00	08/31/2005 12:00

The coupled tide and storm surge simulations include a time-step of 1-second for the 160-m, 80-m and 40-m equilateral mesh and a 0.5-second time-step for the 20-m mesh to provide numerical stability concerning the Courant number criterion.

The winds and pressures for Hurricane Katrina are included over the computational domain at 15-minute intervals and are interpolated onto the mesh nodes. Figure 87 illustrates the nested boundaries of the wind and pressure fields.

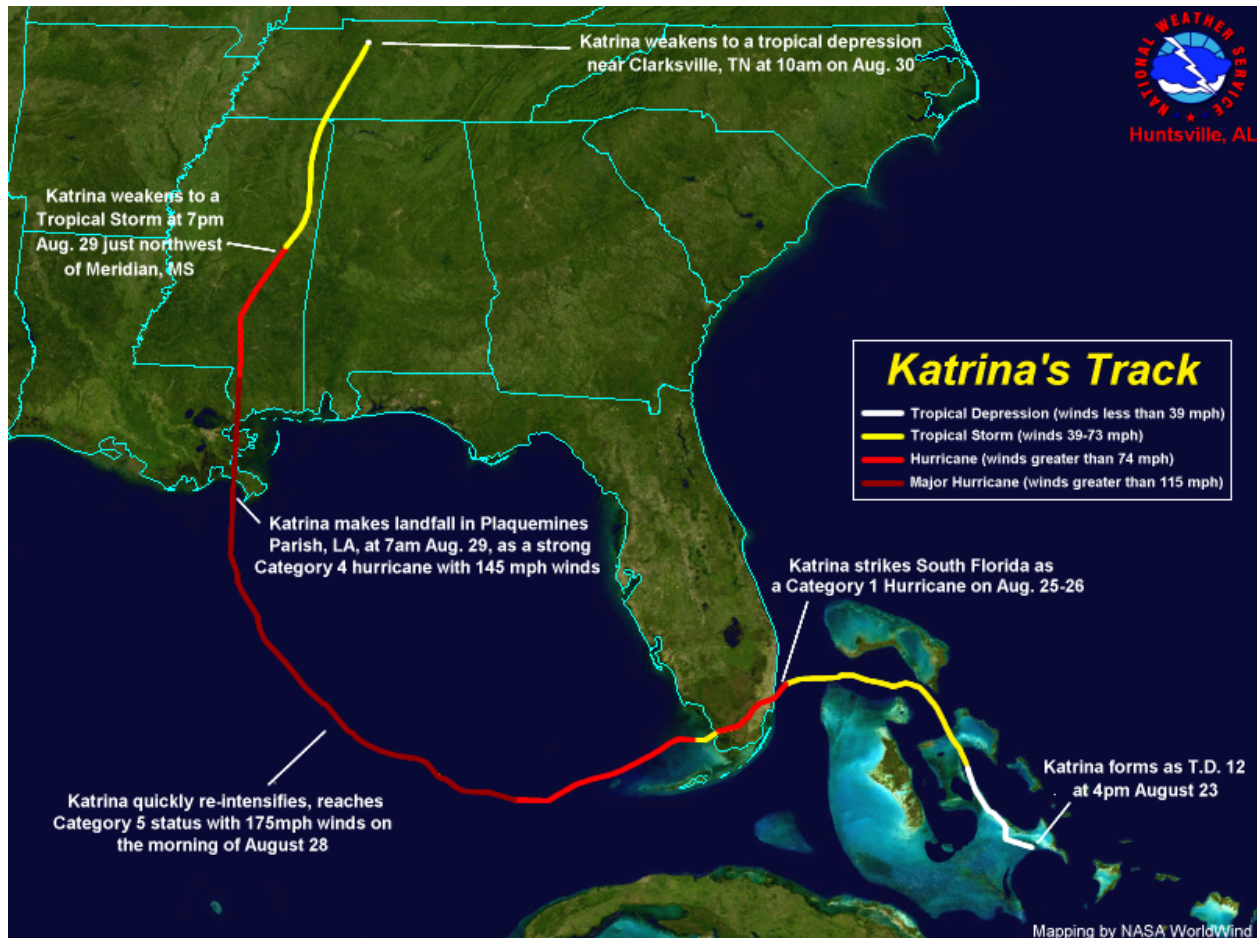


Figure 86 Hurricane Katrina storm track – courtesy of NASA

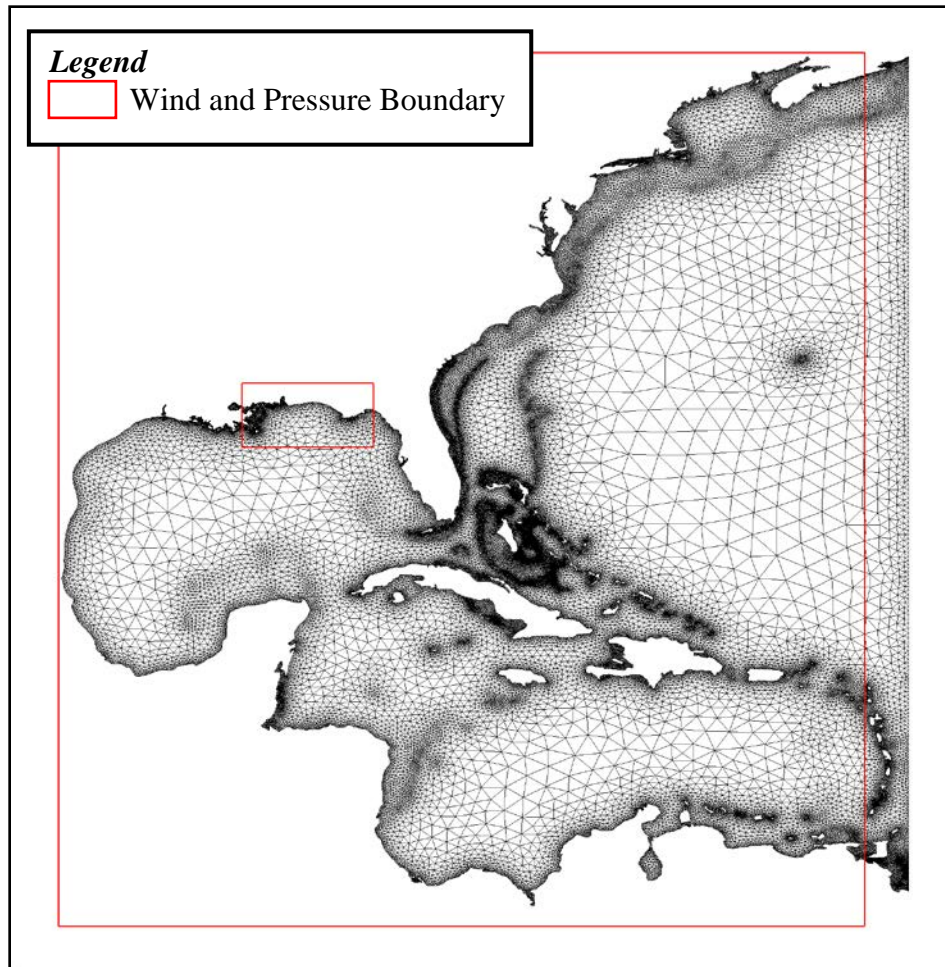


Figure 87 **Extents of the wind and pressure fields**

The hybrid bottom friction formulation (Eq. 10.10) is applied with the incorporation of Manning's n (Eq. 10.13). Manning's n is specified by use of the 1992 NLCD LULC database with $C_{f_{\min}} = 0.0025$; $H_{break} = 10$ m; and $\theta = 10$. Horizontal eddy viscosity coefficients of 2.0 and 20.0, generally, are used for initially wet and dry nodes, respectively. A depth-dependent GWCE weighting factor, τ_0 , is employed: If the average element edge length is less than 500-m, $\tau_0 = 0.03$, otherwise 0.005 is used for depths greater than 10-m, and 0.02 for depths less than

10-m, with respect to NAVD88. The wetting and drying option is turned on with the minimum bathymetric depth equal to 0.01-m (Luettich & Westerink, 2006).

ADCIRC-2DDI allows the incorporation of several spatially varying friction parameters: Manning's n , directional effective roughness length (z_0), and surface canopy. Manning's n is an isotropic parameter to estimate flow resistance, in this case the bare-earth surface (Figure 88).

z_0 and surface canopy relate to the aerodynamic forcing. ADCIRC represents aerodynamic forcing by wind and pressure fields. Wind is included in the model as a surface stress on the water column. Wind speed is converted to a wind surface stress and is computed by a standard quadratic drag law:

$$\frac{\tau_{s\lambda}}{\rho_0} = C_D |W_{10}| W_{10-\lambda} \quad 11.1$$

and

$$\frac{\tau_{s\phi}}{\rho_0} = C_D |W_{10}| W_{10-\phi} \quad 11.2$$

C_D is defined by Garrett's drag formula (Garratt, 1977):

$$C_D = \frac{(0.75 + 0.67W_{10})}{1000} \quad 11.3$$

W_{10} is the 10-minute "sustained" wind speed acting at 10-m above the water. To convert 30-minute "sustained" winds to 10-minute "sustained" winds C_D is multiplied by a wind multiplier, $\mu = 1.09$:

$$C_D = \frac{\mu(0.75 + 0.67W_{10})}{1000} \quad 11.4$$

The value of 1.09 is based on an assumption of an approximate 9-percent increase in wind speed ($\sqrt[3]{1.3} = 1.09$) (Bunya *et al.*, 2010; Hagen *et al.*, 2011).

For atmospheric pressures, the inverted barometer effect is used. This adjusts the water-column height based on the difference in ambient atmospheric pressure and the lower pressure introduced within a tropical storm:

$$\zeta^p = \frac{(\bar{p} - p)}{\rho_w g} \quad 11.5$$

where ζ^p is the equivalent water-column height; \bar{p} is the ambient atmospheric pressure (1013 mb); p is the local atmospheric pressure and g is the gravitational constant (9.81-m/s²).

z_0 is an anisotropic parameter (in 12-directions) that approximates upwind roughness effects. The values change based on the wind direction. z_0 is important in decreasing the speed of marine based winds over the land surface as well as masking the wind when it is blowing from off-shore to on-shore. See Westerink *et al.* (2008) for a detailed description for adjusting W_{10} based on wind reduction factors. Figure 89 shows wind reduction for wind blowing from west to east and Figure 90 shows wind reduction for a wind blowing from south to north. Surface canopy is a parameter used to “turn off” the wind stress in areas where the wind is unable to fully penetrate the tree canopy (Figure 91) and little momentum is transferred from the wind field to the water column (Westerink *et al.*, 2008; Atkinson *et al.*, 2011).

All three attributes are assigned to ADCIRC mesh nodes through the use of the 1992 USGS National Land Cover Data (NLCD) (Vogelmann *et al.*, 2001). Table 25 illustrates the frictional values for each NLCD land class (Bunya *et al.*, 2010). Assignment of a frictional value is based on a direct lookup table.

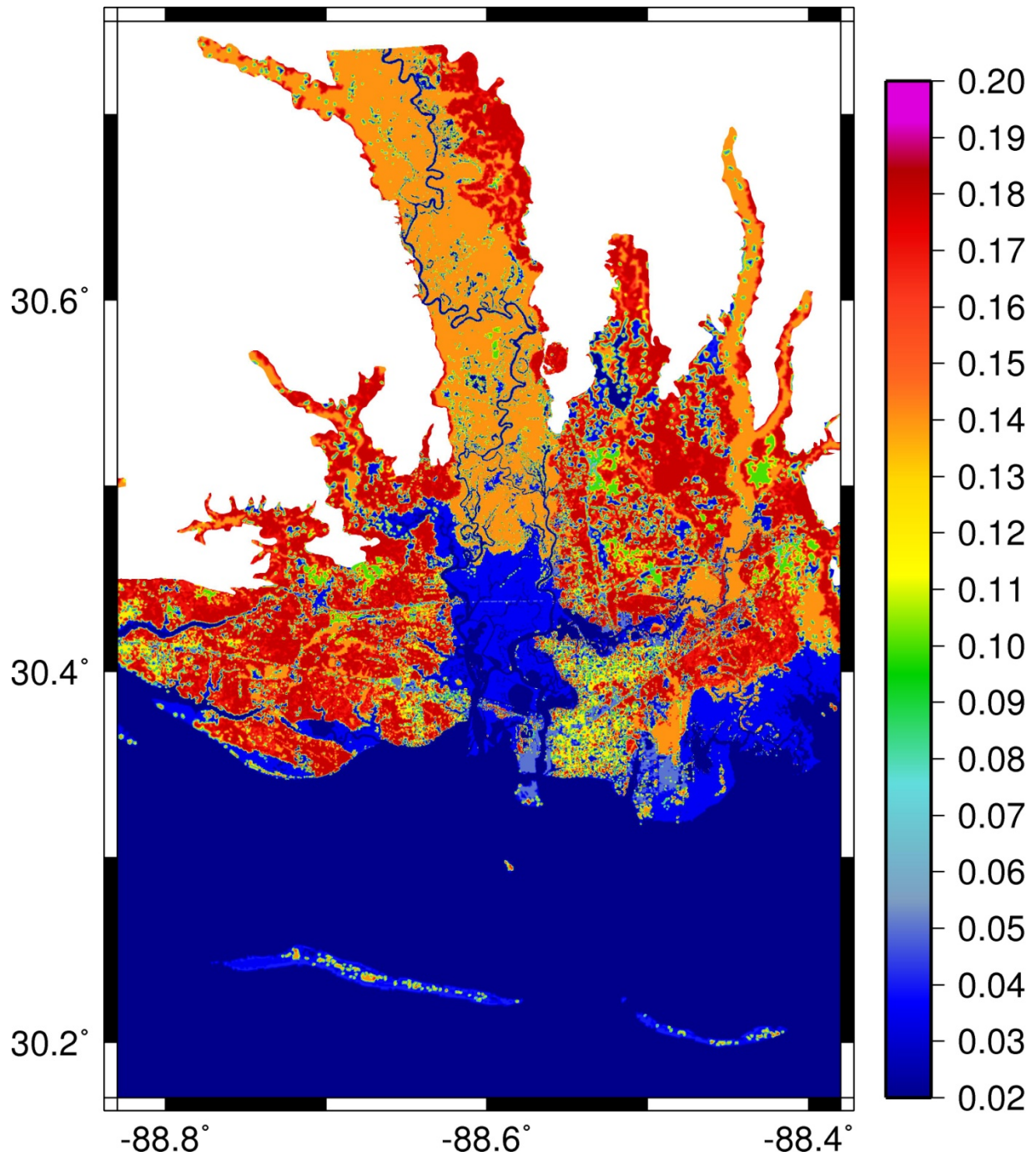


Figure 88 Manning's n for the Pascagoula River and surrounding floodplain. Values were obtained via direct lookup from Table 25 based on the 1992 NLCD landcover classification. Hotter colors represent higher resistance to flow.

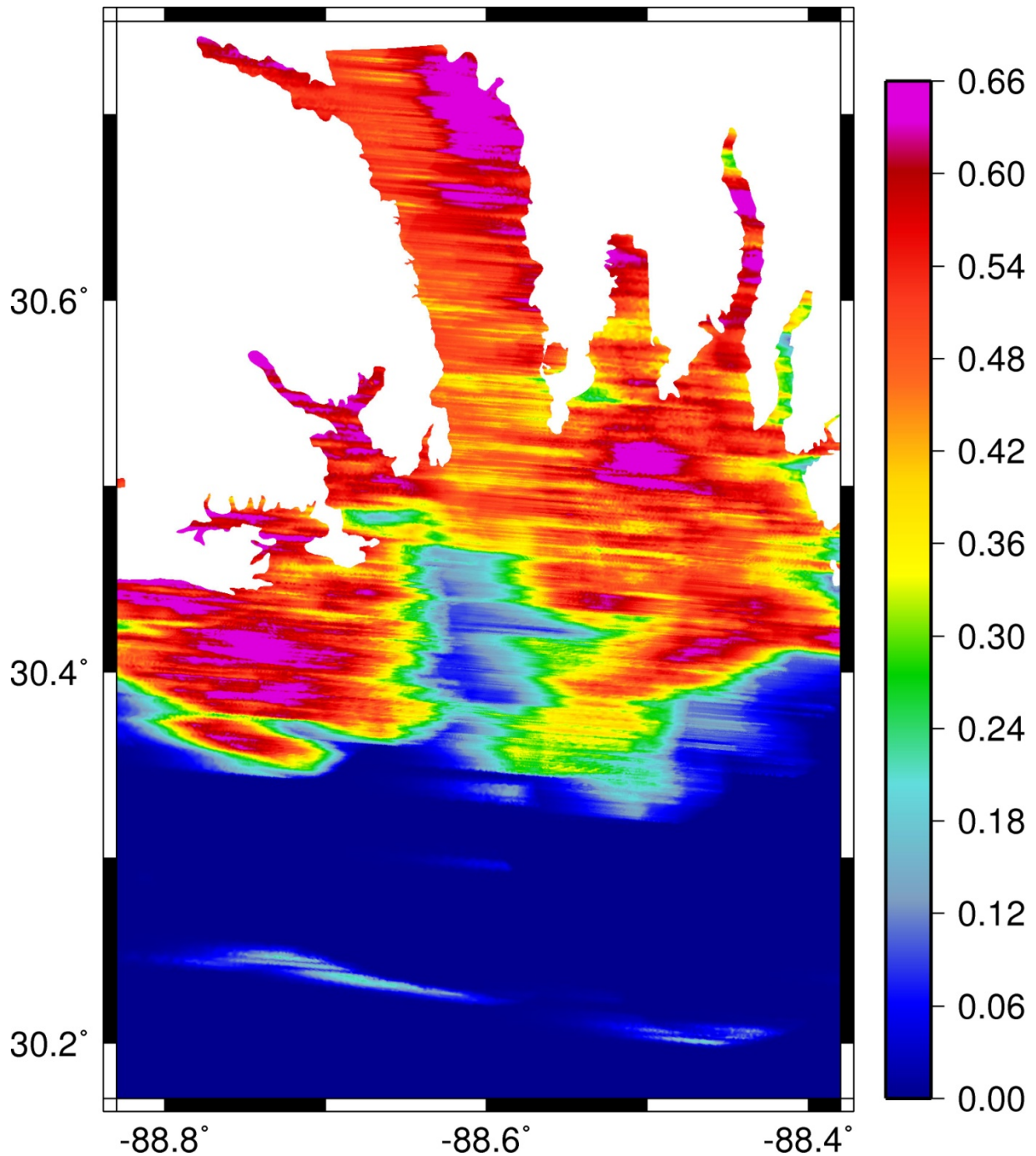


Figure 89 Wind reduction factors (Z_0) for the Pascagoula River and surrounding floodplain with a wind blowing from west to east. Values were obtained via direct lookup from Table 17 based on the 1992 NLCD landcover classification. Hotter colors represent higher wind reduction than the cooler colors.

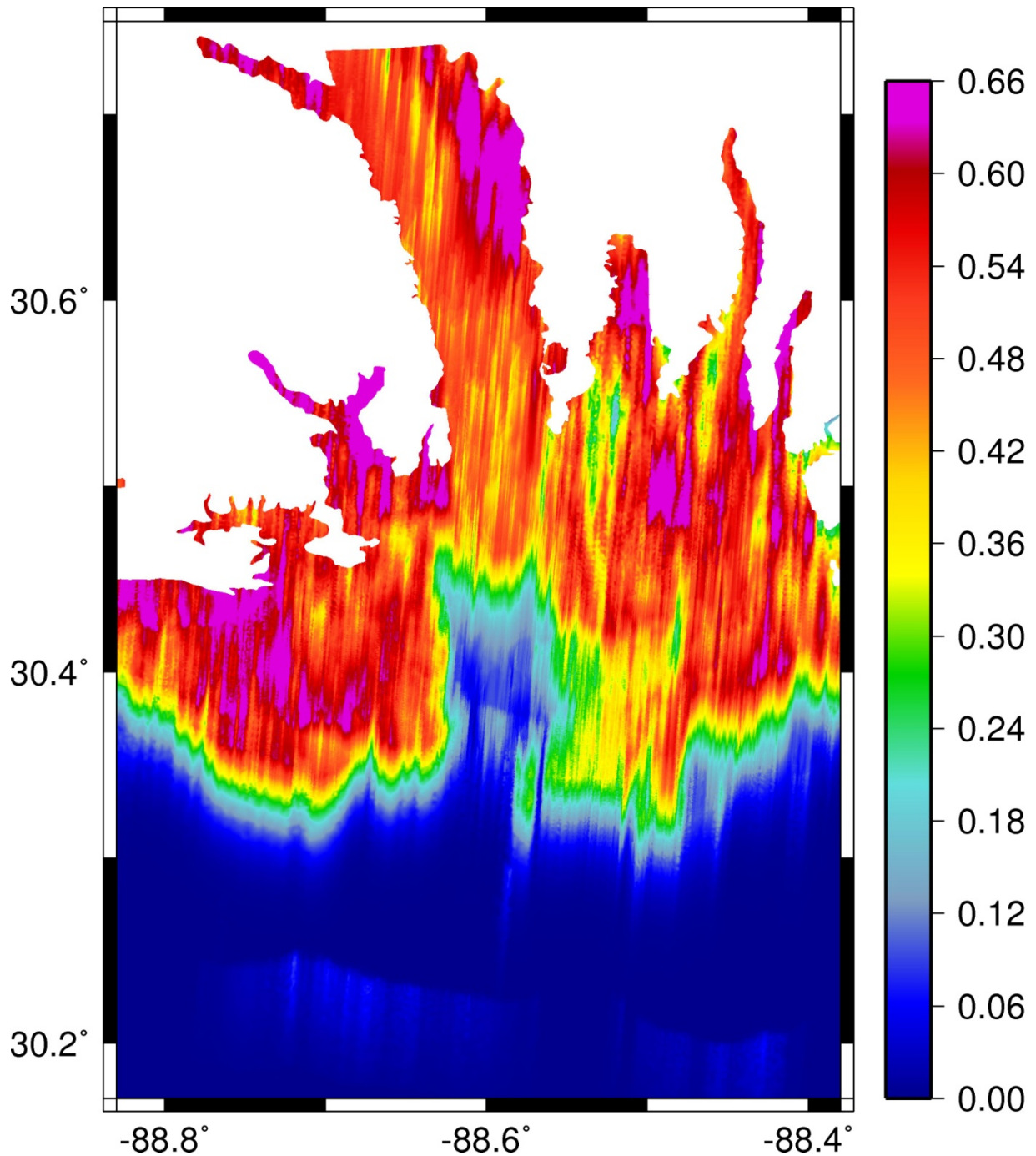


Figure 90 Wind reduction factors (Z_0) for the Pascagoula River and surrounding floodplain with a wind blowing from south to north. Values were obtained via direct lookup from Table 17 based on the 1992 NLCD landcover classification. Hotter colors represent higher wind reduction than the cooler colors.

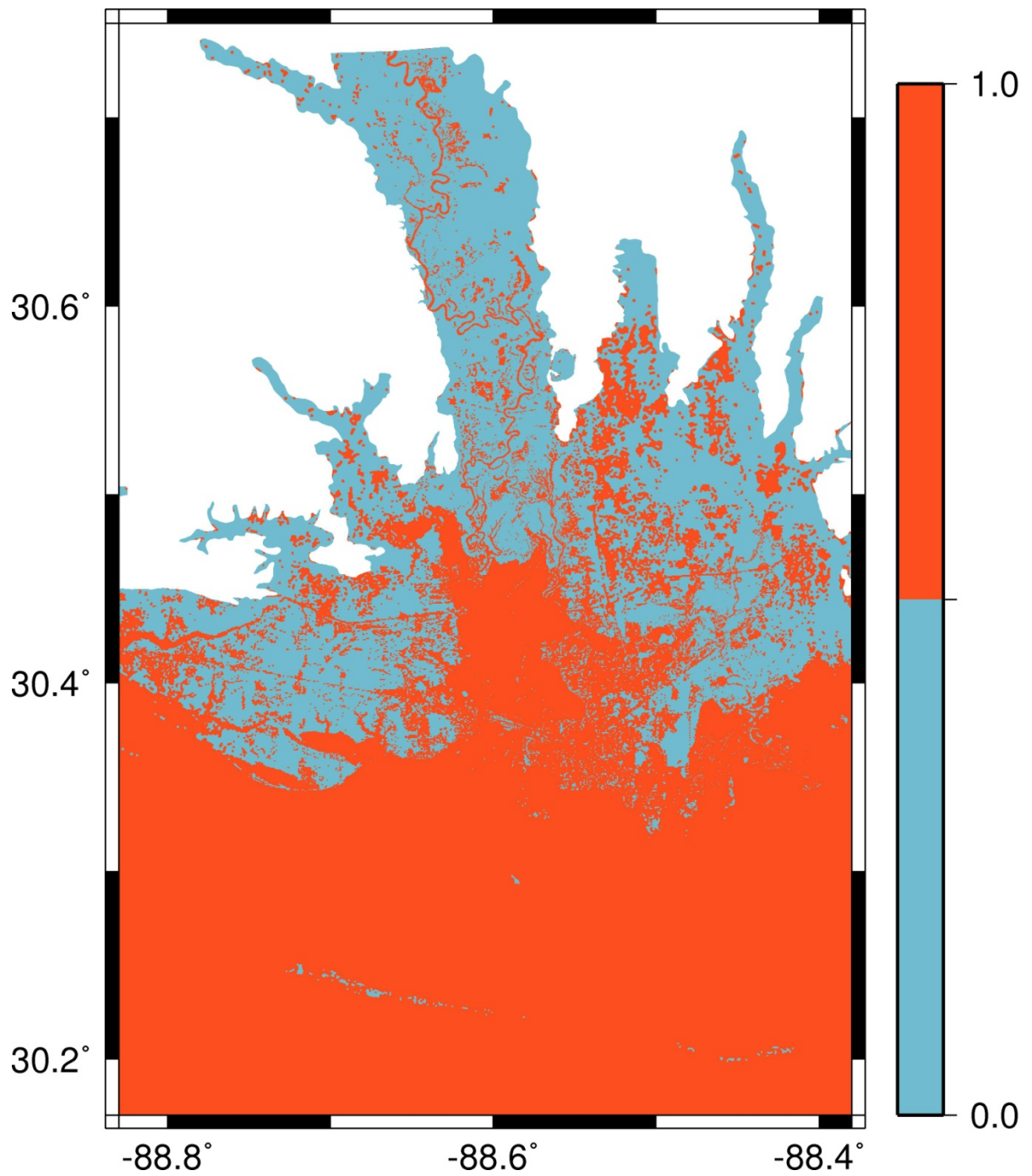


Figure 91 Surface canopy coefficients for the Pascagoula River and surrounding floodplain. Values were obtained via direct lookup from Table 17 based on the 1992 NLCD landcover classification. Wind is turned off for nodes with a value of 0 and wind is enabled for nodes with a value of 1.

Table 25 Manning's n , surface roughness, and canopy values obtained by using the 1992 LULC database (Bunya *et al.*, 2010).

NLCD Class	Description	Manning n	Z0	Canopy
11	Open water	0.020	0.001	1
12	Ice/Snow	0.022	0.012	1
21	Low residential	0.120	0.330	1
22	High residential	0.121	0.500	1
23	Commercial	0.050	0.390	1
31	Bare rock/sand	0.040	0.090	1
32	Gravel pit	0.060	0.180	1
33	Transitional	0.100	0.180	1
41	Deciduous forest	0.160	0.650	0
42	Evergreen forest	0.180	0.720	0
43	Mixed forest	0.170	0.710	0
51	Shrub land	0.070	0.120	1
61	Orchard/vineyard	0.100	0.270	1
71	Grassland	0.035	0.040	1
81	Pasture	0.033	0.060	1
82	Row crops	0.040	0.060	1
83	Small grains	0.035	0.050	1
84	Fallow	0.032	0.040	1
85	Recreational grass	0.030	0.050	1
91	Woody wetland	0.140	0.550	0
92	Herbaceous wetland	0.035	0.110	1

CHAPTER 12: MODEL RESULTS

12.1 Astronomic Tide Results

The following section presents results from an astronomic tide simulation using both in-bank models (high- and low-resolution). This is to verify that the in-bank models accurately describe the physical interaction of the daily tides before moving forward with more intense storm surge forcing. The results will be analyzed both qualitatively and quantitatively. Plots of resynthesized water levels will be presented as well as statistical measures. Five NOS stations (Figure 92) and four USGS stations (Figure 93) are used to compute historical versus computed water levels and verify both models performance with respect to tides. As previously mentioned, this study is not intended to validate a tide model of the Pascagoula River; however, the historical water levels are compared to simulated water levels to simply show the model generally captures the physical processes of the system.

Eight water level stations are selected to compare historical (measured) and simulated tidal harmonics. The eight stations cover a broad extent of the study area, encompassing the coastal shoreline of Alabama (Mobile Bay), and into Mississippi including upstream reaches of the Pascagoula and Escatawpa River.

Each of the two in-bank models are forced with tides using ADCIRC-2DDI, described in Chapter 10, with the parameters presented in Chapter 11. The 23 harmonically analyzed constituents attained from the model are presented in Table 26. These constituents are compared to those from the NOS and USGS stations. The NOS tidal stations include 37 historical tidal

constituents (The solar annual [SA] and solar semi-annual [SSA] are removed) (Table 27). It should be noted that the historical tidal constituents from the NOS stations contain only astronomic tides, as the tidal simulation only simulates astronomical tides. Other factors such as river inflow and meteorological forcings (i.e. wind and pressures) are not included in the historical tidal constituents. At the USGS water level stations, historical tidal constituent data is not available. In order to obtain historic tidal constituent data at these locations, USGS water levels were acquired for a total length of 31 days. The water level data for the four USGS water level stations were analyzed by Wang (2008) and 35 tidal constituents were extracted from the water levels using the T_TIDE MATLAB code (Pawlowicz *et al.*, 2002).

A tidal resynthesis is performed by recomposing all individual tidal constituents into a single tidal signal function, $T(t)$:

$$T(t) = Z_0 + \sum_N H_n f_n \cos[\omega_n t - g_n + (V_n + u_n)] \quad 12.1$$

The only unknown parameters are Z_0 and the amplitudes and phases, H_n and g_n . Commonly, Z_0 represents a local mean sea level (MSL), therefore it is a known parameter. The nodal adjustment parameters, f_n and u_n , along with the terms $\omega_n t$ and V_n combined represent the phase angle of the Equilibrium tidal constituent where V_n is the equilibrium phase angle for constituent n (Pugh, 2004). In order to begin the resynthesis at the start of a tidal epoch the nodal adjustment parameters are removed (i.e. $f_n = 1$ and $g_n = 0$).

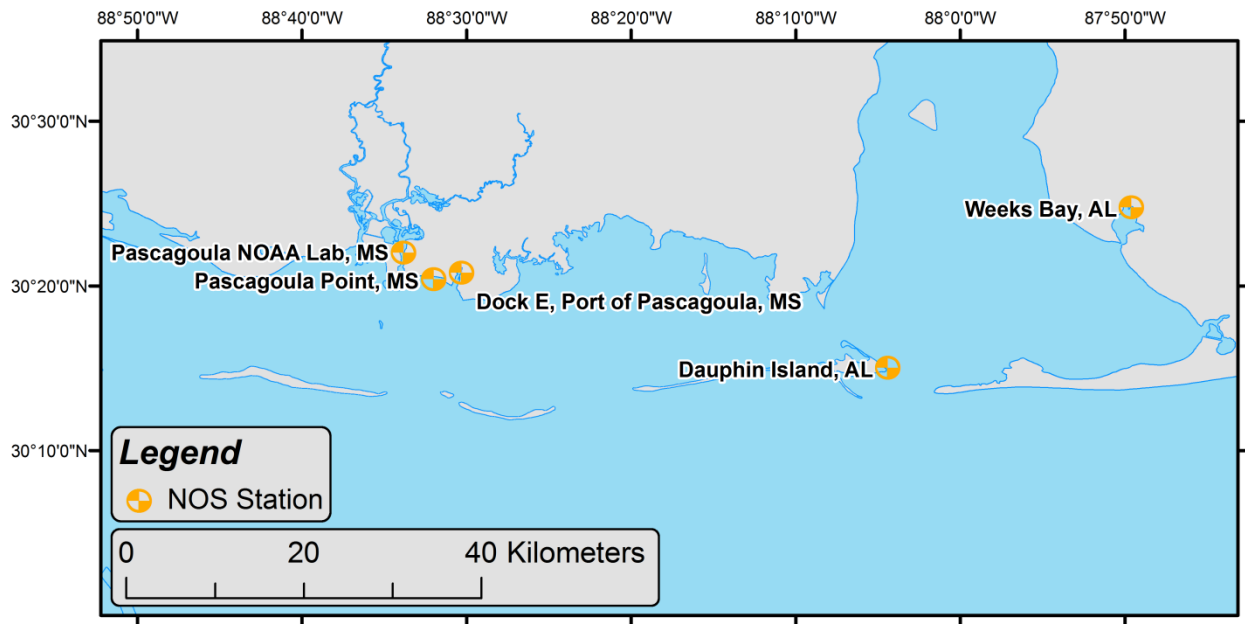


Figure 92 Location of NOS stations located within the in-bank Pascagoula model domain.

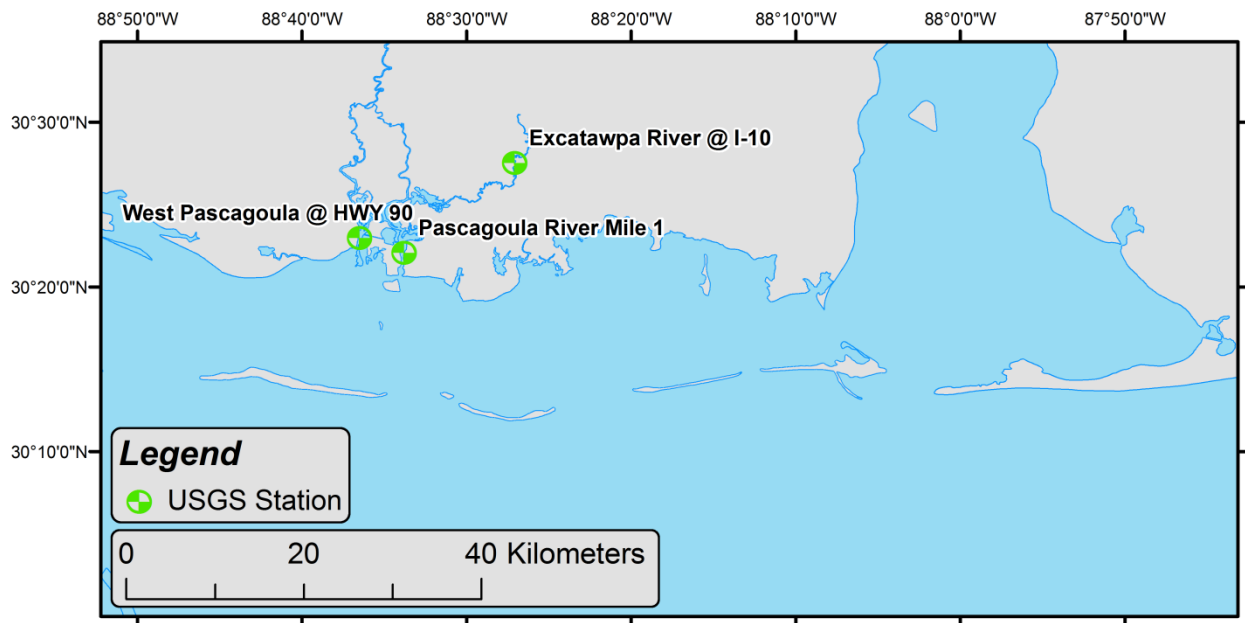


Figure 93 Location of USGS stations located within the in-bank Pascagoula model domain.

Table 26 23 tidal constituents applied in harmonic resynthesis - constituent names gathered from (Kojima, 2005)

Tidal Constituent	Constituent Name	Period (hr)	Frequency (rad/s)
M ₂	Principal lunar semidiurnal constituent	12.42	0.000140519
S ₂	Principal solar semidiurnal constituent	12.00	0.000145444
N ₂	Larger lunar elliptic semidiurnal constituent	12.66	0.000137880
K ₁	Luni-solar diurnal constituent	23.93	0.000072921
M ₄	Shallow water overtides of principal lunar constituent	6.21	0.000281038
O ₁	Principal lunar diurnal constituent	25.82	0.000067598
M ₆	Shallow water terdiurnal constituent	4.14	0.000421557
MN ₄	Shallow water quarter diurnal constituent	6.27	0.000278399
MU ₂ =2MS ₂	Variational constituent	12.87	0.000135594
MM=MN	Lunar monthly constituent	661.31	0.000002639
MSF=SM	Lunisolar synodic fortnightly constituent	354.37	0.000004925
Q ₁	Larger lunar elliptic diurnal constituent	26.87	0.000064959
P ₁	Solar diurnal constituent	24.07	0.000072523
2SM ₂	Shallow water semidiurnal constituent	11.61	0.000150369
L ₂ =2MN ₂	Smaller lunar elliptic semidiurnal constituent	12.19	0.000143158
K ₂	Luni-solar semidiurnal	11.97	0.000145842
M ₈	Shallow water eighth diurnal constituent	3.11	0.000562076
MS ₄	Shallow water quarter diurnal constituent	6.10	0.000285963
STEADY	Principal water level	∞	0.000000000
MNS ₂	Arising from the interaction between MN and S ₂	13.13	0.000132954
2MN ₆	Shallow water twelfth diurnal constituent	4.17	0.000418918
MSN ₆	Arising from the interaction between M ₂ , N ₂ and S ₂	4.12	0.000423843
M ₁₀	Shallow water tenth diurnal constituent	2.48	0.000702595

Table 27 37 tidal constituents gathered from the NOS tidal stations - constituent names gathered from (Kojima, 2005)

Tidal Constituent	Constituent Name	Period (hr)	Frequency (rad/s)
M2	Principal lunar semidiurnal constituent	12.42	0.000140519
S2	Principal solar semidiurnal constituent	12.00	0.000145444
N2	Larger lunar elliptic semidiurnal constituent	12.66	0.000137880
K1	Luni-solar diurnal constituent	23.93	0.000072921
M4	Shallow water overtides of principal lunar constituent	6.21	0.000281038
O1	Principal lunar diurnal constituent	25.82	0.000067598
M6	Shallow water terdiurnal constituent	4.14	0.000421557
MK3	Shallow water terdiurnal constituent	8.18	0.000213440
MN4	Shallow water quarter diurnal constituent	6.27	0.000278399
NU2	Larger lunar evectional constituent	12.63	0.000138233
S6	Shallow water overtides of principal solar constituent	6.21	0.000436332
MU2=2MS2	Variational constituent	12.87	0.000135594
2N2	Lunar elliptical semidiurnal second-order constituent	12.91	0.000135240
OO1	Lunar diurnal	22.31	0.000078245
LAM2	Smaller lunar evectional constituent	12.22	0.000142805
S1	Solar diurnal constituent	24.00	0.000072722
M1	Smaller lunar elliptic diurnal constituent	24.83	0.000070282
J1	Smaller lunar elliptic diurnal constituent	23.10	0.000075560
MM=MN	Lunar monthly constituent	661.31	0.000002639
MSF=SM	Lunisolar synodic fortnightly constituent	354.37	0.000004925
MF	Lunisolar fortnightly constituent	327.86	0.000005323
RHO	Larger lunar evectional diurnal constituent	26.72	0.000065312
Q1	Larger lunar elliptic diurnal constituent	26.87	0.000064959
T2	Larger solar elliptic constituent	12.02	0.000145245

Table 27 37 tidal constituents gathered from the NOS tidal stations - constituent names gathered from (Kojima, 2005)

Tidal Constituent	Constituent Name	Period (hr)	Frequency (rad/s)
R2	Smaller solar elliptic constituent	11.98	0.000145643
2Q1	Larger elliptic diurnal	28.01	0.000062319
P1	Solar diurnal constituent	24.07	0.000072523
2SM2	Shallow water semidiurnal constituent	11.61	0.000150369
L2=2MN2	Smaller lunar elliptic semidiurnal constituent	12.19	0.000143158
K2	Luni-solar semidiurnal	11.97	0.000145842
M8	Shallow water eighth diurnal constituent	3.11	0.000562076
MS4	Shallow water quarter diurnal constituent	6.10	0.000285963

Figure 94 through Figure 102 present plots of the resynthesized historical data and model output for each of the nine water level recording stations, shown in Figure 92 and Figure 93. Each plot depicts the water surface elevation, in meters, from the datum (NAVD88) (y-axis) versus a 14-day time period (x-axis) to capture a full spring-neap tidal cycle. The black curve is the historical data, the red curve is water levels from in-bank model number 1 and the blue curve is water levels from in-bank model number 2. If the red curve is not visible, it resides behind the blue curve, suggestive of a small difference between the two red and blue curves.

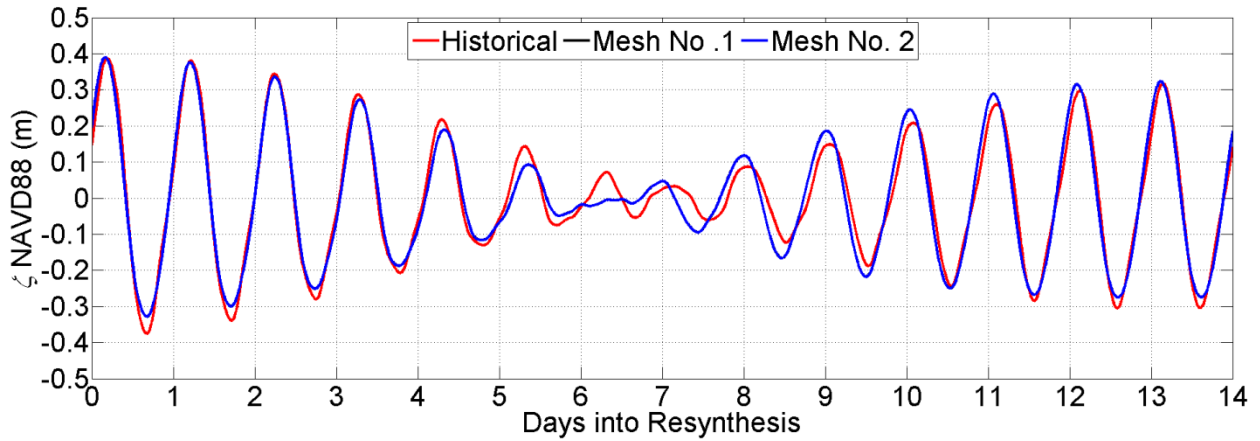


Figure 94 A resynthesis of historical (red) and modeled (black and blue) tidal constituents for a complete spring and neap tidal cycle at tidal station NOS 8732828 – Weeks Bay, Alabama.

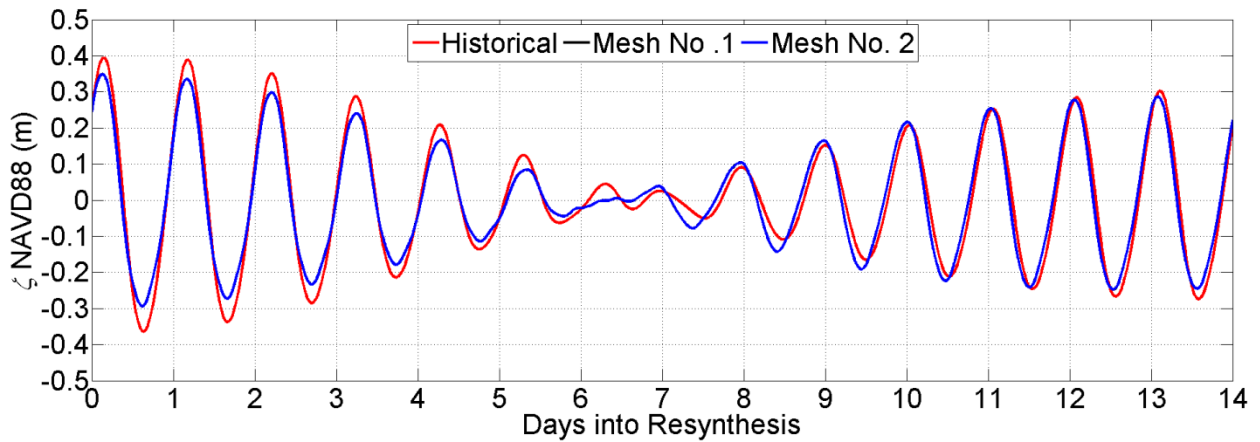


Figure 95 A resynthesis of historical (red) and modeled (black and blue) tidal constituents for a complete spring and neap tidal cycle at tidal station NOS 8735180 – Dauphin Island, Alabama.

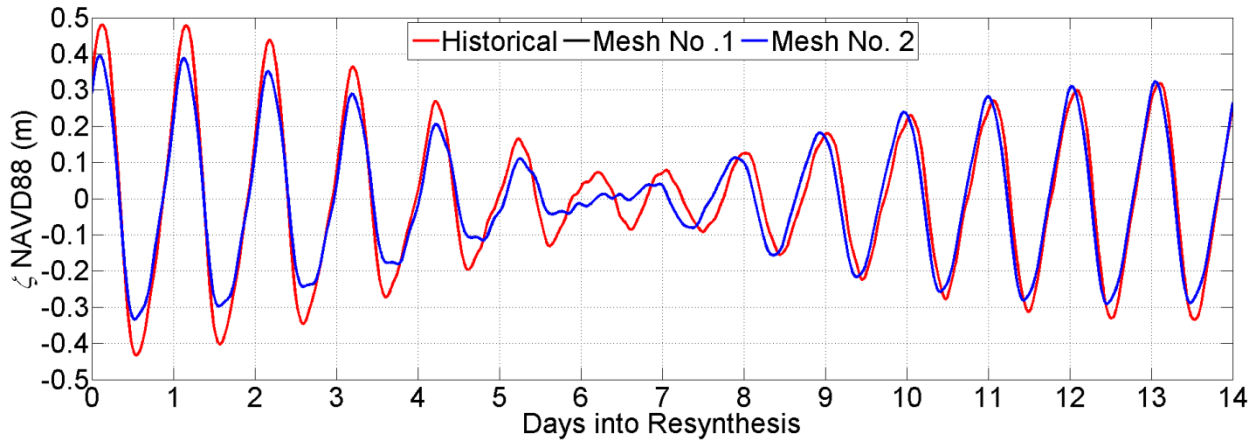


Figure 96 A resynthesis of historical (red) and modeled (black and blue) tidal constituents for a complete spring and neap tidal cycle at tidal station NOS 8741041 – Dock E Port of Pascagoula, Mississippi.

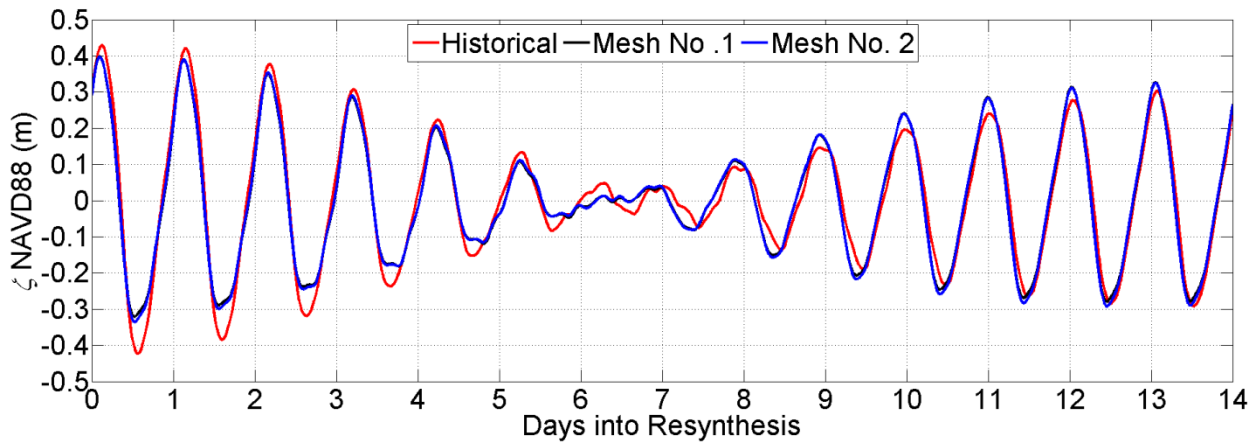


Figure 97 A resynthesis of historical (red) and modeled (black and blue) tidal constituents for a complete spring and neap tidal cycle at tidal station NOS 8741196 – Pascagoula Point, Mississippi.

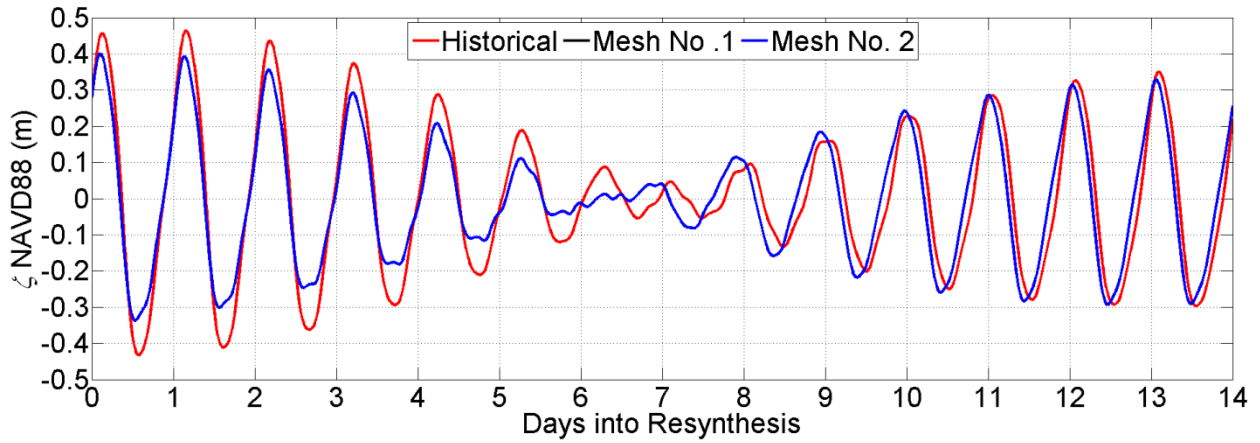


Figure 98 A resynthesis of historical (red) and modeled (black and blue) tidal constituents for a complete spring and neap tidal cycle at tidal station NOS 8741533 – Pascagoula NOAA Lab, Mississippi.

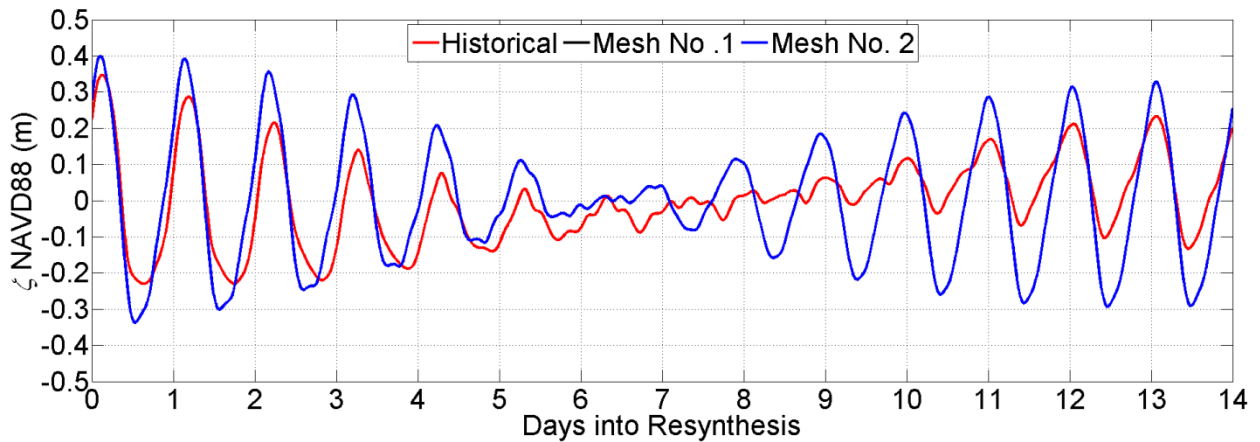


Figure 99 A resynthesis of historical (red) and modeled (black and blue) tidal constituents for a complete spring and neap tidal cycle at water level station USGS 02480212 – Pascagoula River mile 1, Pascagoula, Mississippi.

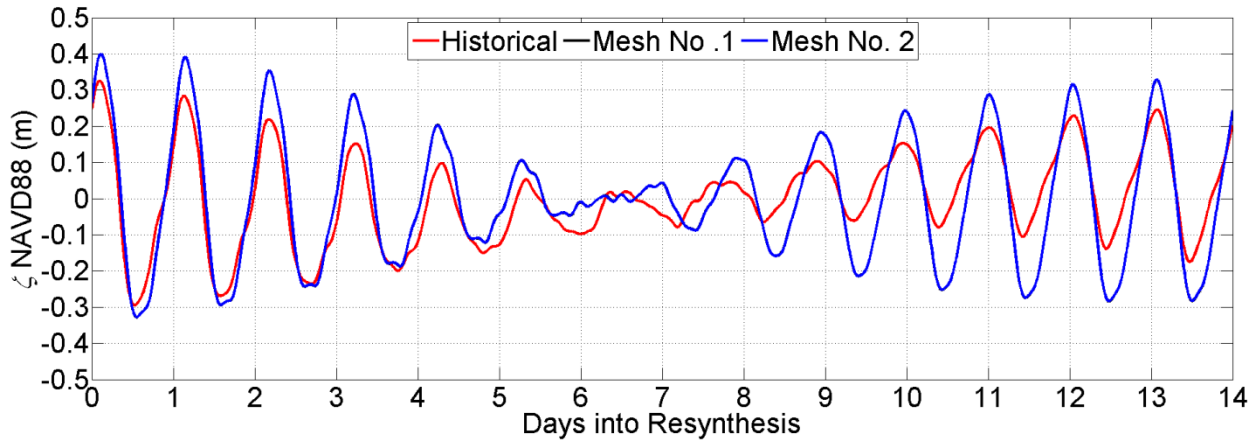


Figure 100 A resynthesis of historical (red) and modeled (black and blue) tidal constituents for a complete spring and neap tidal cycle at water level station USGS 02480285 – West Pascagoula River at Highway 90 at Gautier, Mississippi.

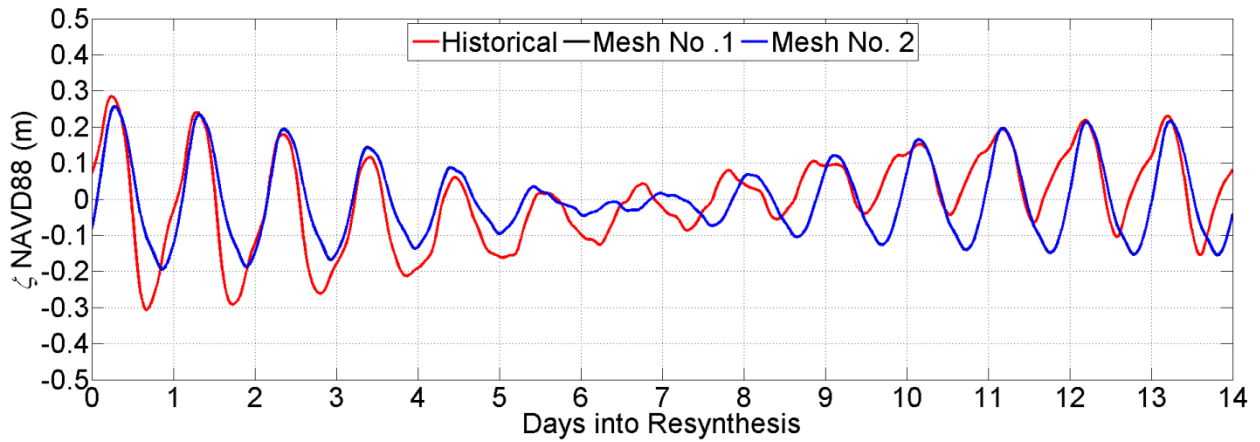


Figure 101 A resynthesis of historical (red) and modeled (black and blue) tidal constituents for a complete spring and neap tidal cycle at water level station USGS 0248018020 – Escatawpa River at I-10 near Orange Grove, Mississippi.

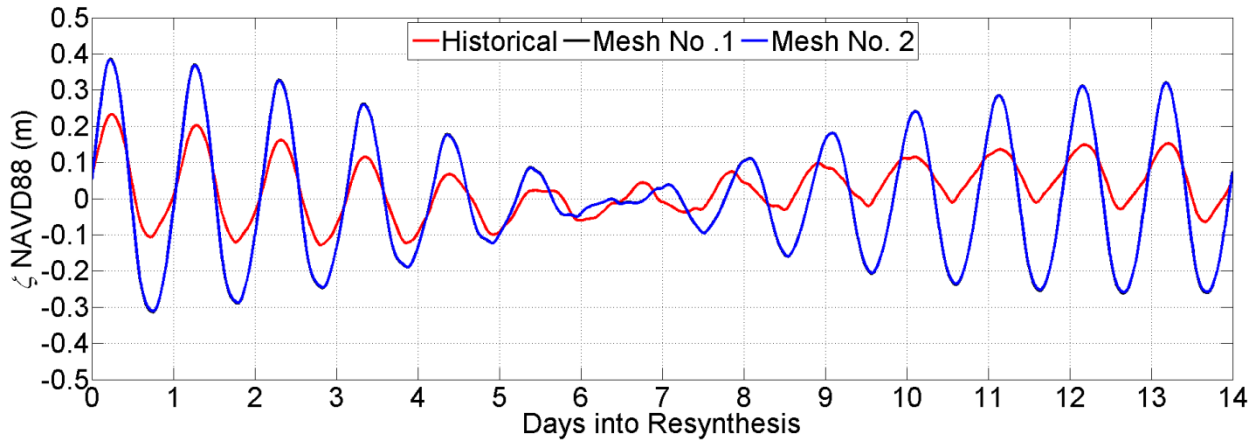


Figure 102 A resynthesis of historical (red) and modeled (black and blue) tidal constituents for a complete spring and neap tidal cycle at water level station USGS 02479310 – Pascagoula River at Graham Ferry, Mississippi.

RMSE is computed at each water level station for both in-bank models. RMSE is expressed as:

$$RMSE = \sqrt{\frac{\sum_{i=1}^N (Hist_i - Mod_i)^2}{N}} \quad 12.2$$

where $Hist_i$ and Mod_i are the water surface elevations at time index i for the historical and modeled tidal elevation, respectively. RMSE provides a way to estimate the difference in historical and model tidal signal for the entire 14-day period. RMSE is computed to quantitatively determine that the higher resolution in-bank mesh (in-bank mesh number 2) performs better than in-bank mesh number 1. It is not used to validate either model. Table 28 presents the RMSE for all stations for each in-bank mesh.

Table 28 RMSE for all 9 stations for both in-bank models.

Agency	Station No.	Station Name	<u>RMSE (cm)</u>	
			Mesh 1	Mesh 2
NOS	8732828	Weeks Bay	3.42	3.42
NOS	8735180	Dauphin Island	3.52	3.52
NOS	8741041	Dock E, Port of Pascagoula	5.51	5.51
NOS	8741196	Pascagoula Point	3.58	3.51
NOS	8741533	NOAA Lab	6.83	6.83
USGS	2480212	Pascagoula River @ MI 1	10.59	10.60
USGS	2480285	W. Pascagoula River	8.28	8.28
USGS	248018020	Escatawpa River	9.02	9.05
USGS	2479310	Graham Ferry	11.21	11.12

In general, results for both in-bank tidal simulations depict a well performing model, producing reasonable results. However, some disagreement occurs between the historical and modeled data. For all NOS stations, the model under-predicts tidal amplitude for the first seven days of the spring-neap tidal cycle. During the remaining 7-days, the amplitude of the modeled data better predicts that of the historic data. As the stations move upstream into the Pascagoula River (USGS), the model over-predicts the amplitude, except in the Escatawpa River, where the flood tides for the first 7-days are similar to the historic data, but the ebb tides are under-predicted. During the last 7-days, the ebb tides are over-predicting the tidal amplitude. It is apparent in Figure 99 that at station USGS 02480212 there is a slight phase difference. The models flood and ebb tide amplitudes generally arrive before the historic peaks and troughs during the first seven days of the tidal cycle.

Furthermore, by evaluating the tidal signals for mesh 1 and mesh 2, it can be concluded that the higher resolution in-bank model (in-bank mesh number 2) does not improve the tidal results with respect to in-bank model number 1. As long as the river channel is described as a

trapezoidal cross-section (Figure 58), proper tidal flow is captured regardless of how well it is resolved. However, both meshes utilize the same source of bathymetry. If higher-resolution bathymetry was available and used for in-bank mesh number 2, tide results may improve.

12.2 Storm Surge Results

A comparison of maximum inundation extent and maximum water levels from adjustments made to the floodplain mesh (160-m, 80-m, 40-m, and 20-m equilateral regions) during simulated storm tide are presented. Recall that for each mesh, the only difference occurs within the equilateral boundary (transition zone and pure equilateral elements). Differences in maximum water levels and inundation area between each simulation are not extreme, but are significant. Figure 103 illustrates the maximum inundation area combining all simulations, the maximum of maximums (MOM). The MOM is the maximum water level, globally, for all simulations. Therefore inundation extent of the MOM represents the maximum possible inundation area for the suite of results. Much of the land area in each of the equilateral zones (orange boundary) is inundated, with the Center Zone completely flooded.

The response to adjustments in topographic representation in the equilateral regions maximum water level is both local and non-local. Figure 104 graphically compares the MEOW (maximum envelope of water) of each storm surge simulation to the MOM. Minor differences are observed within each equilateral region between the MOM and each simulations respective MEOW, however differences do occur. Larger differences in inundation are observed in regions outside the equilateral zones, especially around the upper Escatawpa River (Figure 105). The largest difference is noticed in the 40 m mesh, followed by the 80-m mesh, and the 160-m and 20-m mesh producing minimal differences.

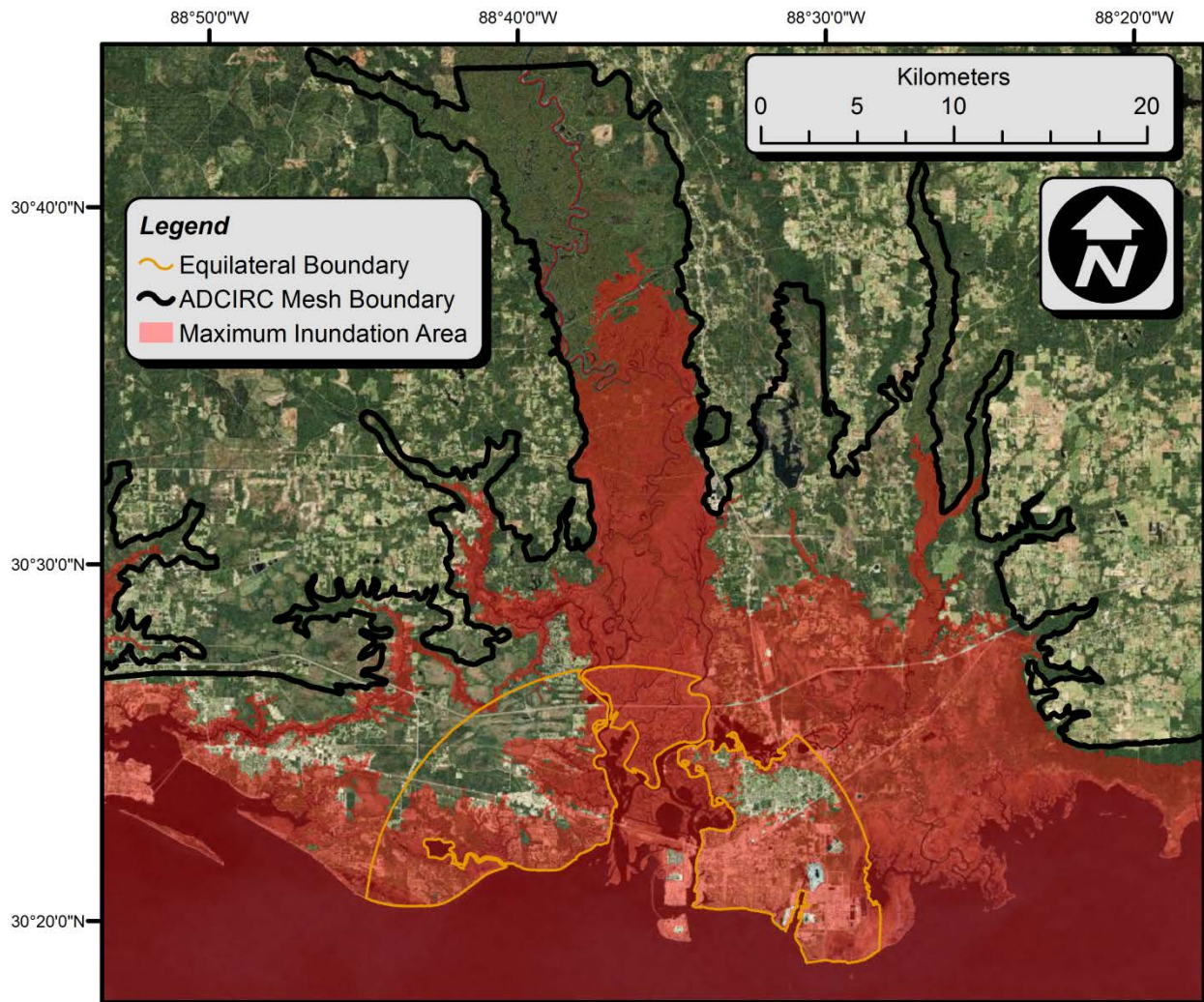


Figure 103 Maximum inundation area (or maximum of maximums) for the four ADCIRC meshes. The black line is the ADCIRC mesh boundary.

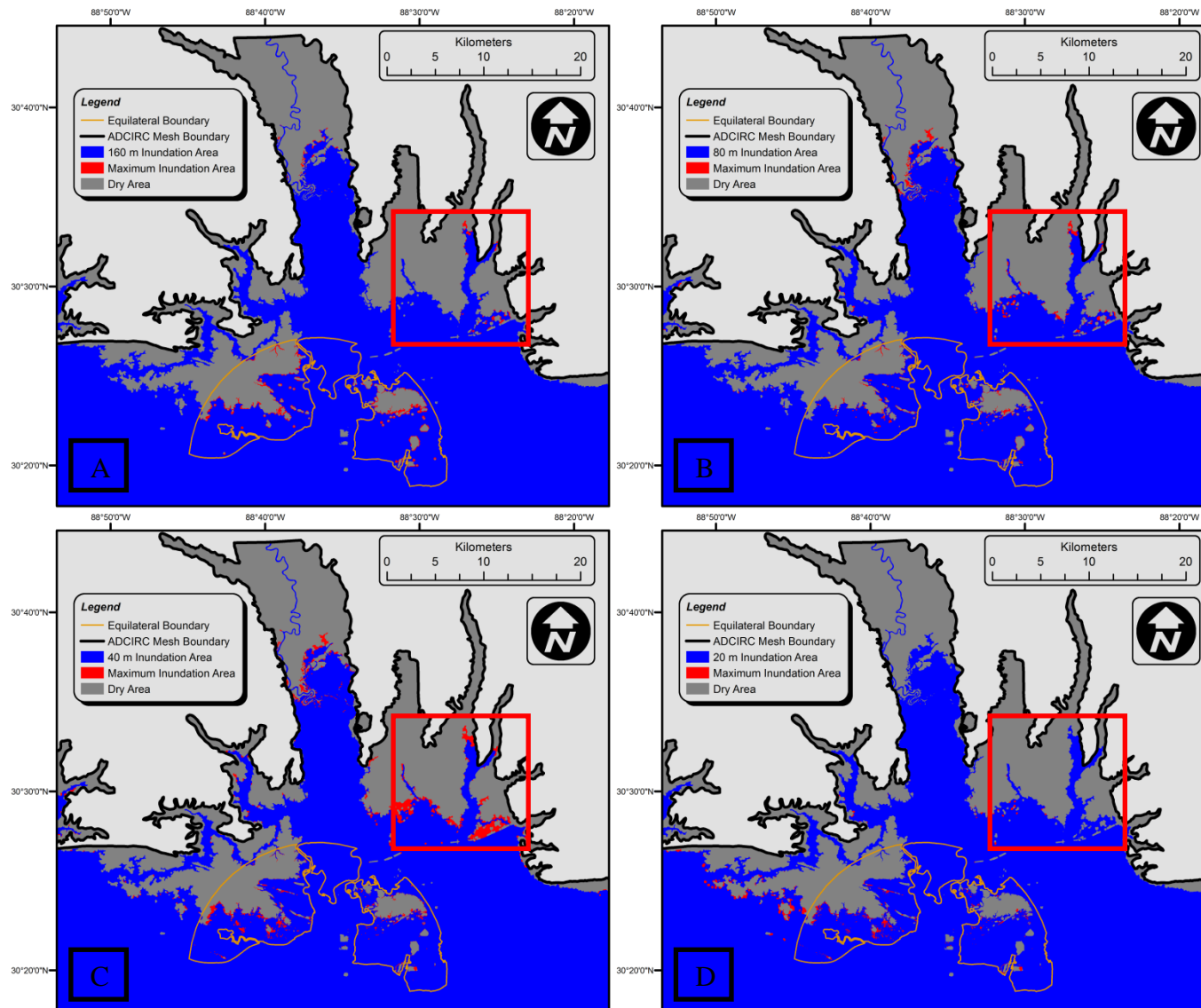


Figure 104 The total inundation area (blue) over the inundation area from the MOM (red) for A) 160-m, B) 80-m, C) 40-m, and D) 20-m equilateral meshes. Figures in the red inset box are shown in Figure 105.

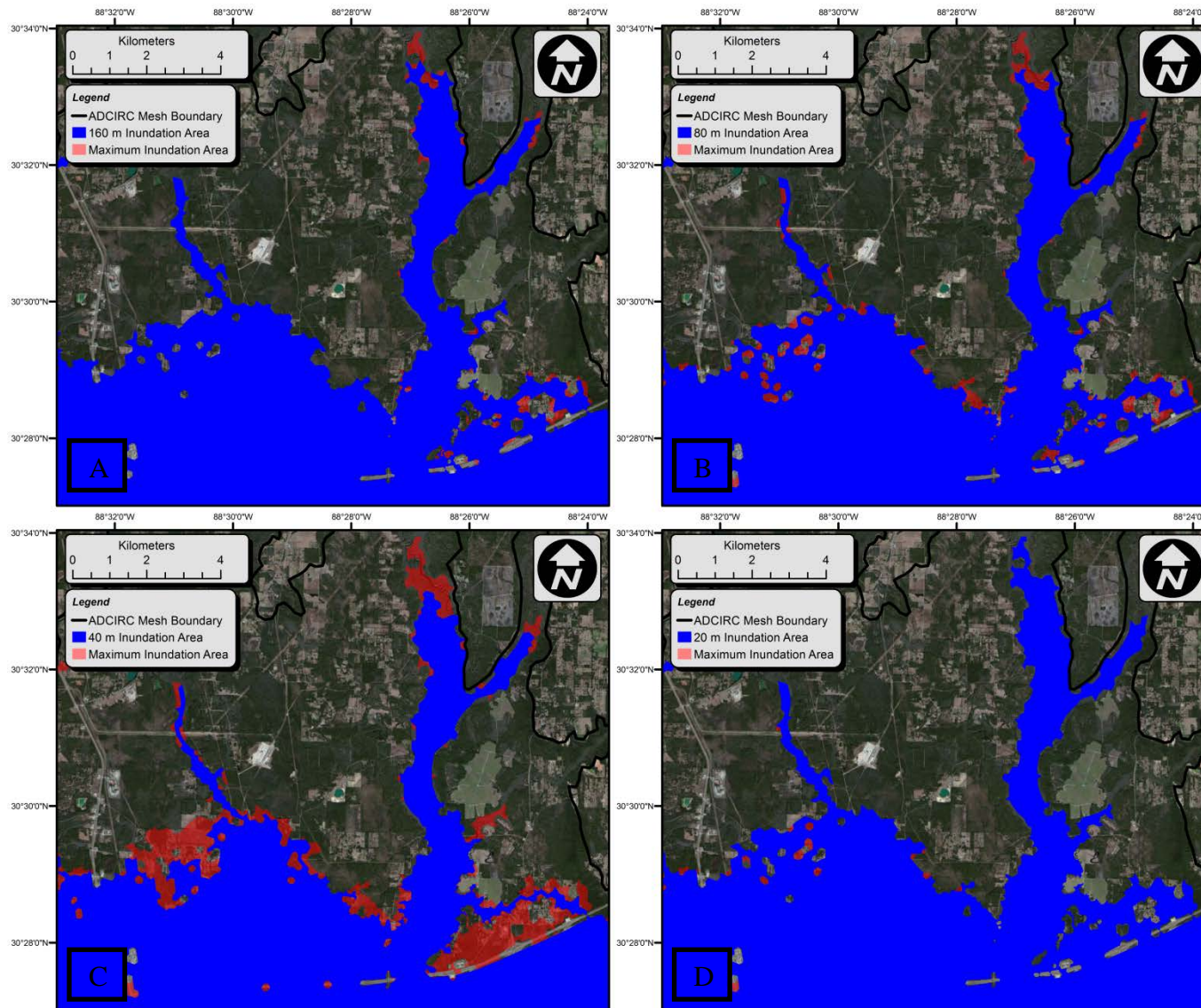


Figure 105 The total inundation area (blue) over the inundation area from the MOM (red) for A) 160-m, B) 80-m, C) 40-m, and D) 20-m equilateral meshes for red inset from Figure 104.

Figure 106 highlights the mesh that contributes to the highest water level in the MOM and similarly, Figure 107 shows the mesh that contributed to the lowest water level in the MOM. Figure 108 illustrates the 5-m DEM for the Pascagoula region for comparing the inundation extent to the topography. The 160-m equilateral mesh contributed a great deal of the highest water levels in the low-lying marsh regions and creeks and tributaries. The 80-m equilateral mesh produced the highest water levels along the coastal shoreline, coastal marsh areas, and into the shallower waters of the bays surrounding Pascagoula, MS. The 40-m mesh contributed to the highest water levels just offshore. Additionally, the 20-m equilateral mesh supplied the highest water level in the further extents of the inundation area which are along the highest inundated topographic elevations. For example, in the Left Equilateral Zone, the area around HWY 90 is colored red for the 20-m equilateral zone. Further upstream along the Escatawpa River, the 20-m mesh contributed the highest water level in close proximity to the Mississippi Sandhill Crane National Wildlife Refuge along I-10 as well as the further inundation extent of the Pascagoula River. On the other hand, the 20-m equilateral mesh contributed to the lowest water levels offshore, along the immediate coastal shoreline and into the marsh areas surrounding both Pascagoula River inlets (Figure 107). Within the floodplain, the 40-m equilateral mesh contributed the lowest water levels from the MOM. These results further demonstrate changes in water levels and inundation extent in regions nearby and away from the local topographic changes.

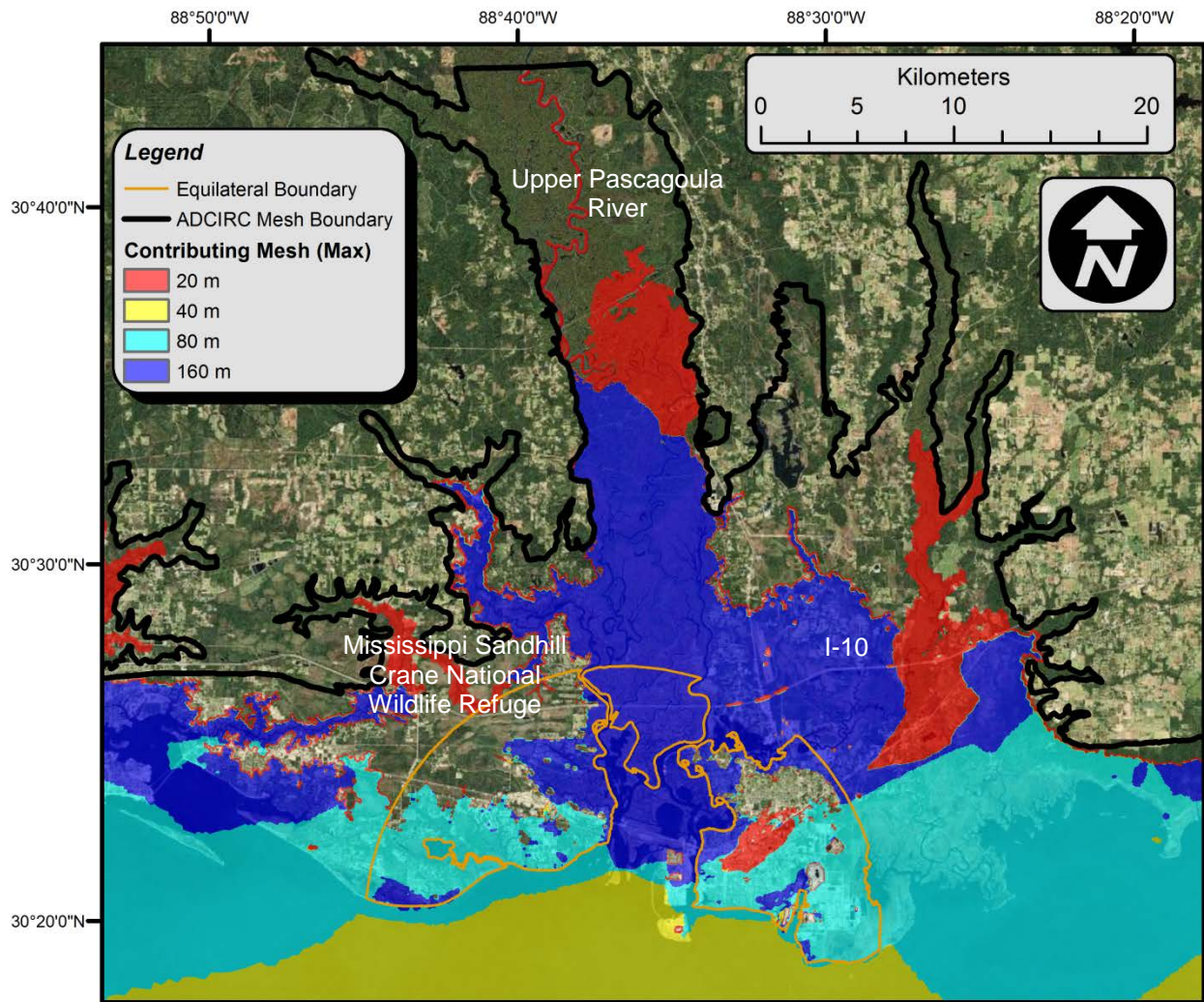


Figure 106 Equilateral mesh contributing to the MOM

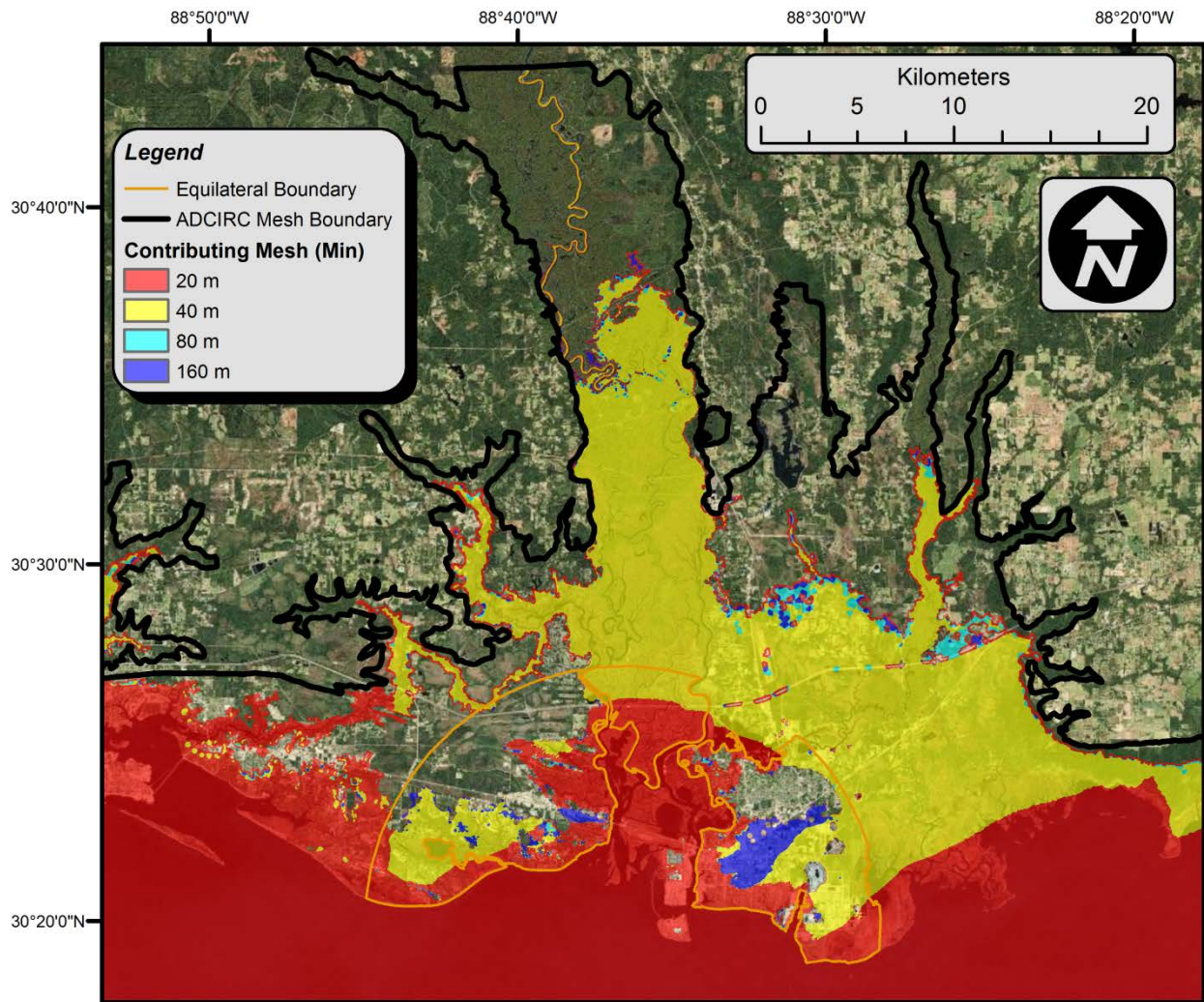


Figure 107 Equilateral mesh contributing to the lowest water level from the MOM.

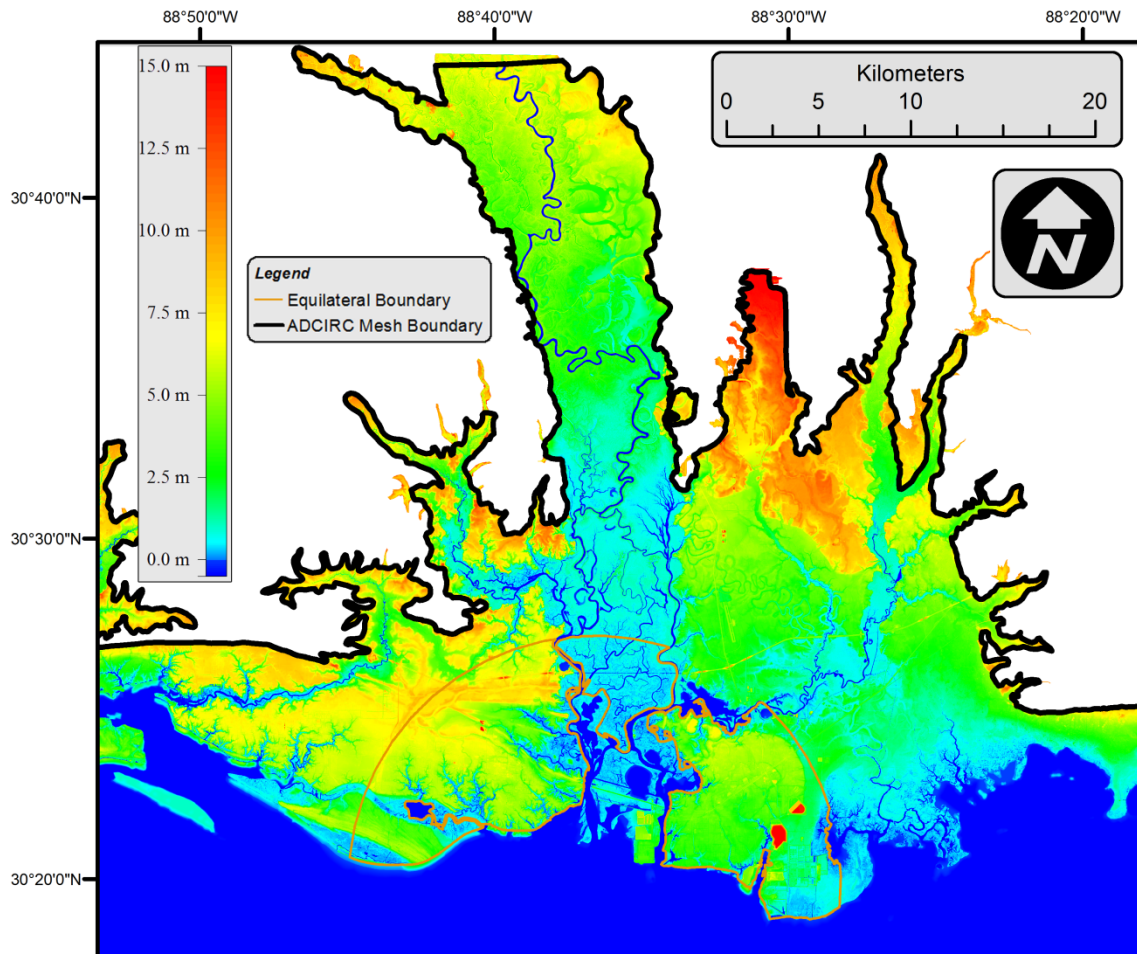


Figure 108 5-m DEM with ADCIRC mesh boundary (black) and equilateral zones (orange). Elevations are referenced to NAVD88.

Figure 109 through Figure 114 present the difference in maximum water levels between each of the four simulations. Differences in inundation less than 1-cm and areas that remained dry during the simulation are colored as transparent. First, Figure 109 shows the differences between the extremes of the equilateral mesh resolutions, 160-m and 20-m. Differences in water levels are as much as 16-cm for much of the marsh area and differences occurring well beyond the equilateral zones. Some of the largest observed differences, over 30-cm (1-ft), are found when subtracting from the 40-m mesh. Maximum water levels in the floodplain are generally

less than the other mesh resolutions, including the 20-m mesh. Also, differences in water levels occur offshore, away from the equilateral regions.

Results show the local and non-local response to in both inundation extent and maximum water levels in for local changes in topography. In other words, the representation of the ground surface has a strong influence on inundation extent and total water levels in areas outside the adjusted topographic features.

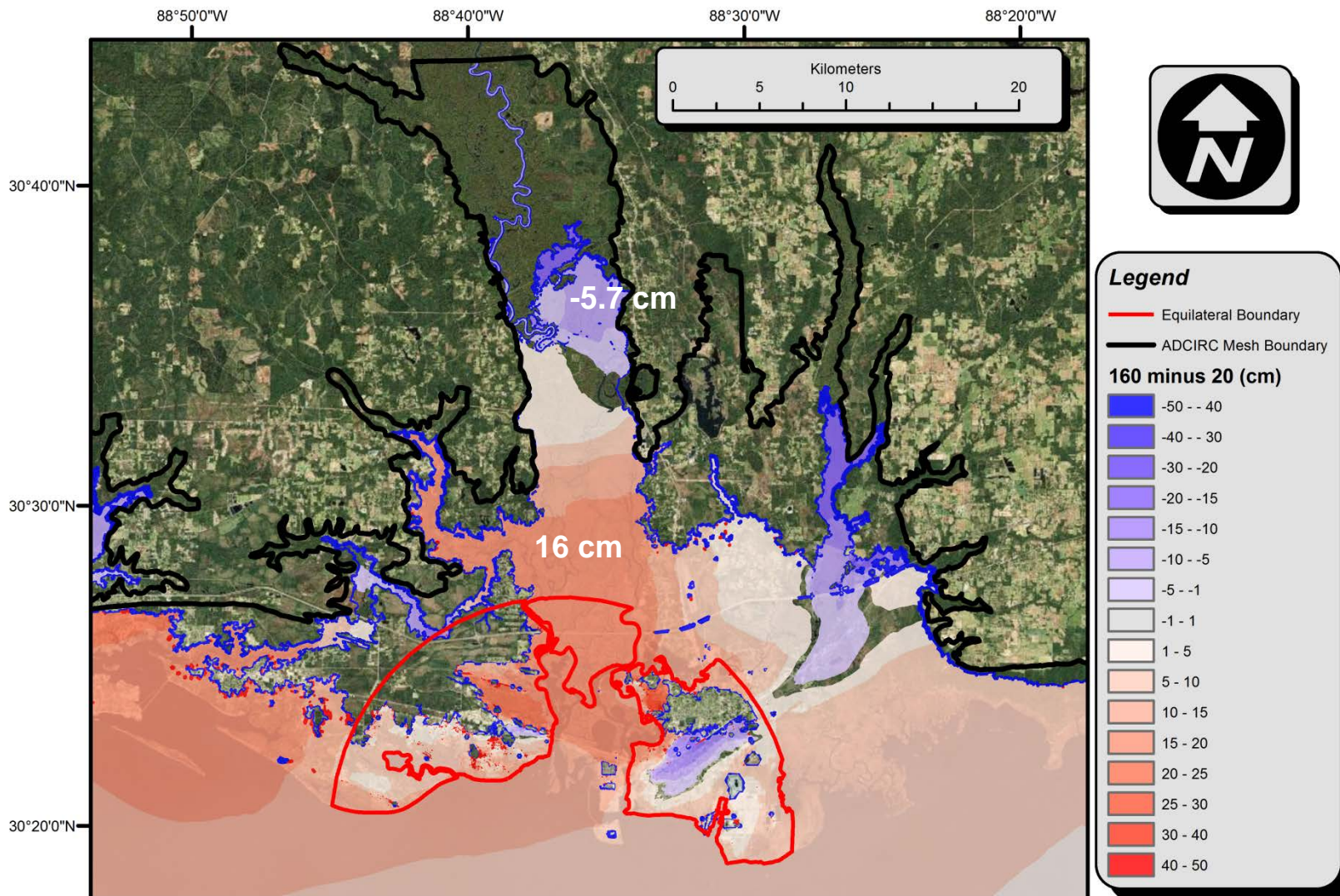


Figure 109 Difference in maximum water levels between the 160-m and 20-m equilateral mesh simulations. Hot colors represent higher water levels for the 160-m mesh and cool colors are higher water levels for the 20-m mesh.

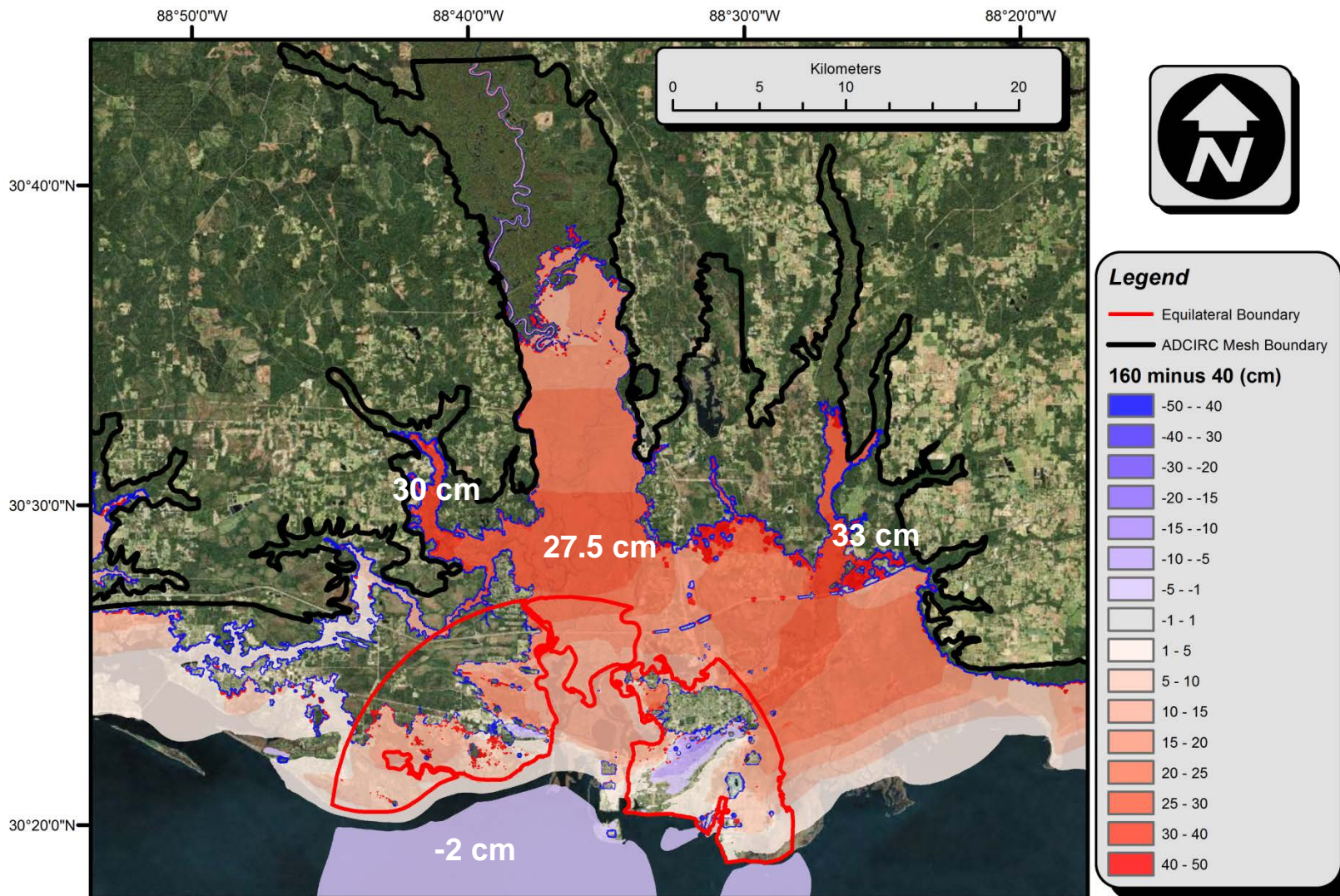


Figure 110 Difference in maximum water levels between the 160-m and 40-m equilateral mesh simulations. Hot colors represent higher water levels for the 160-m mesh and cool colors are higher water levels for the 40-m mesh.

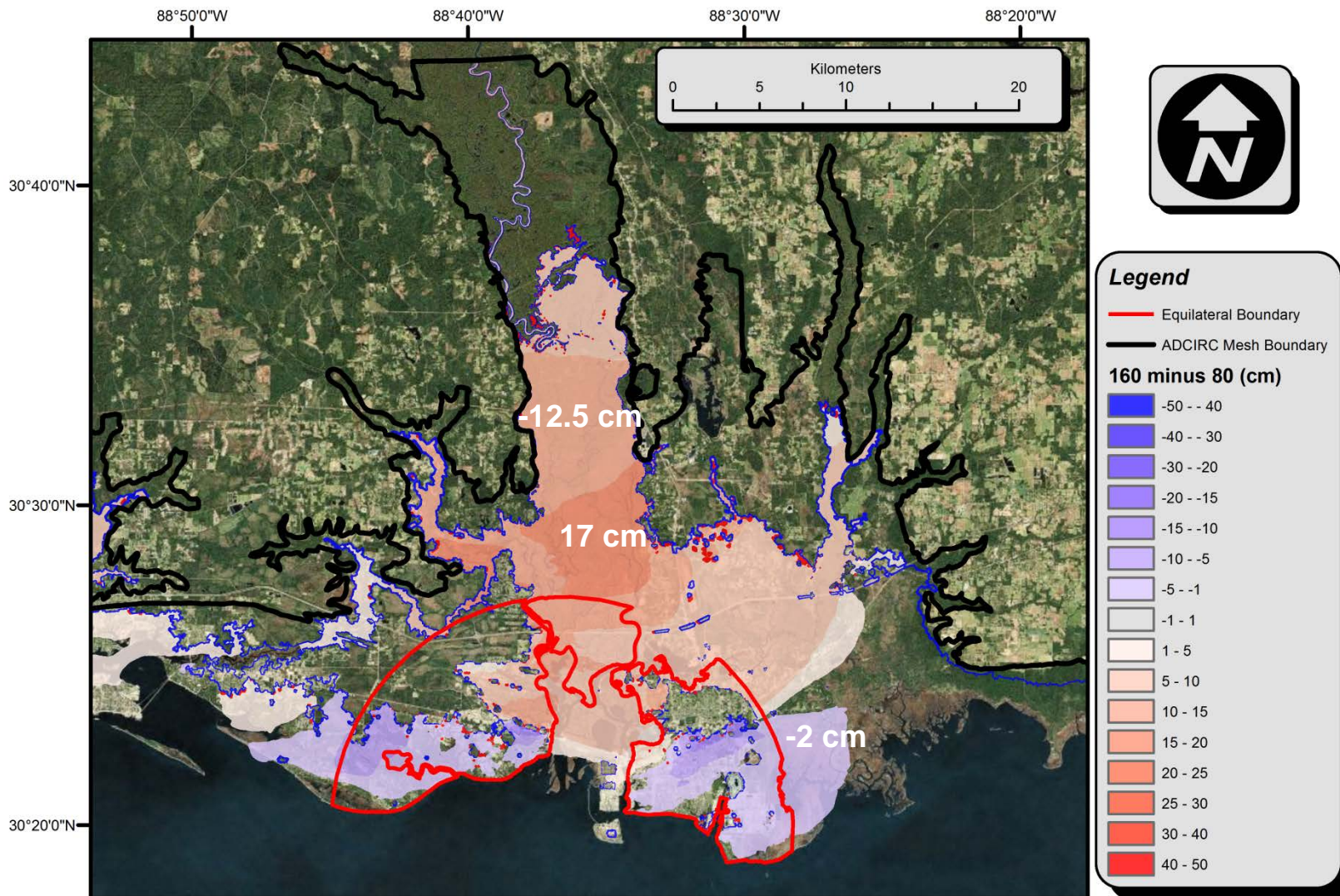


Figure 111 Difference in maximum water levels between the 160-m and 80-m equilateral mesh simulations. Hot colors represent higher water levels for the 160-m mesh and cool colors are higher water levels for the 80-m mesh.

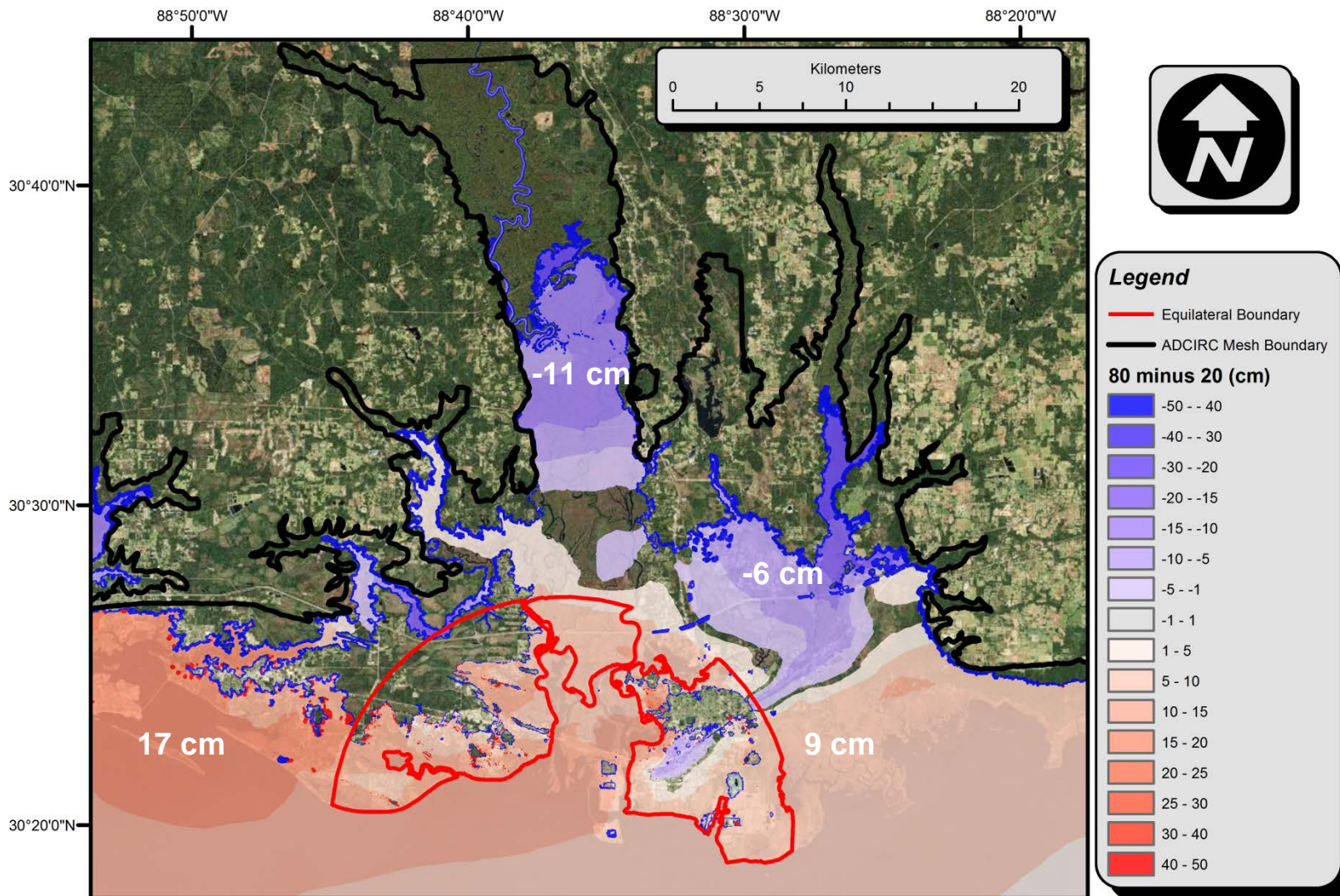


Figure 112 Difference in maximum water levels between the 80-m and 20-m equilateral mesh simulations. Hot colors represent higher water levels for the 80-m mesh and cool colors are higher water levels for the 20-m mesh.

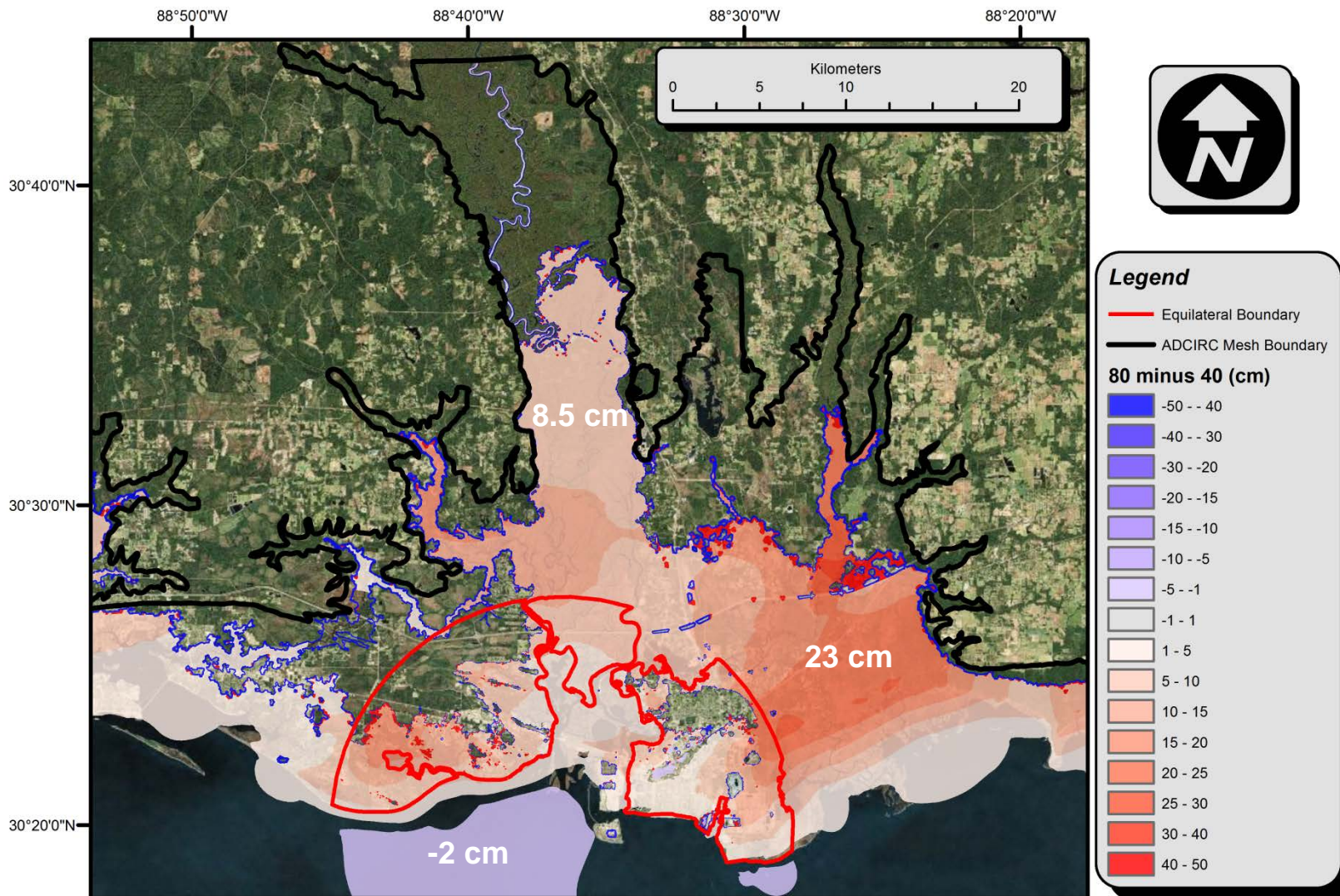


Figure 113 Difference in maximum water levels between the 80-m and 40-m equilateral mesh simulations. Hot colors represent higher water levels for the 80-m mesh and cool colors are higher water levels for the 40-m mesh.

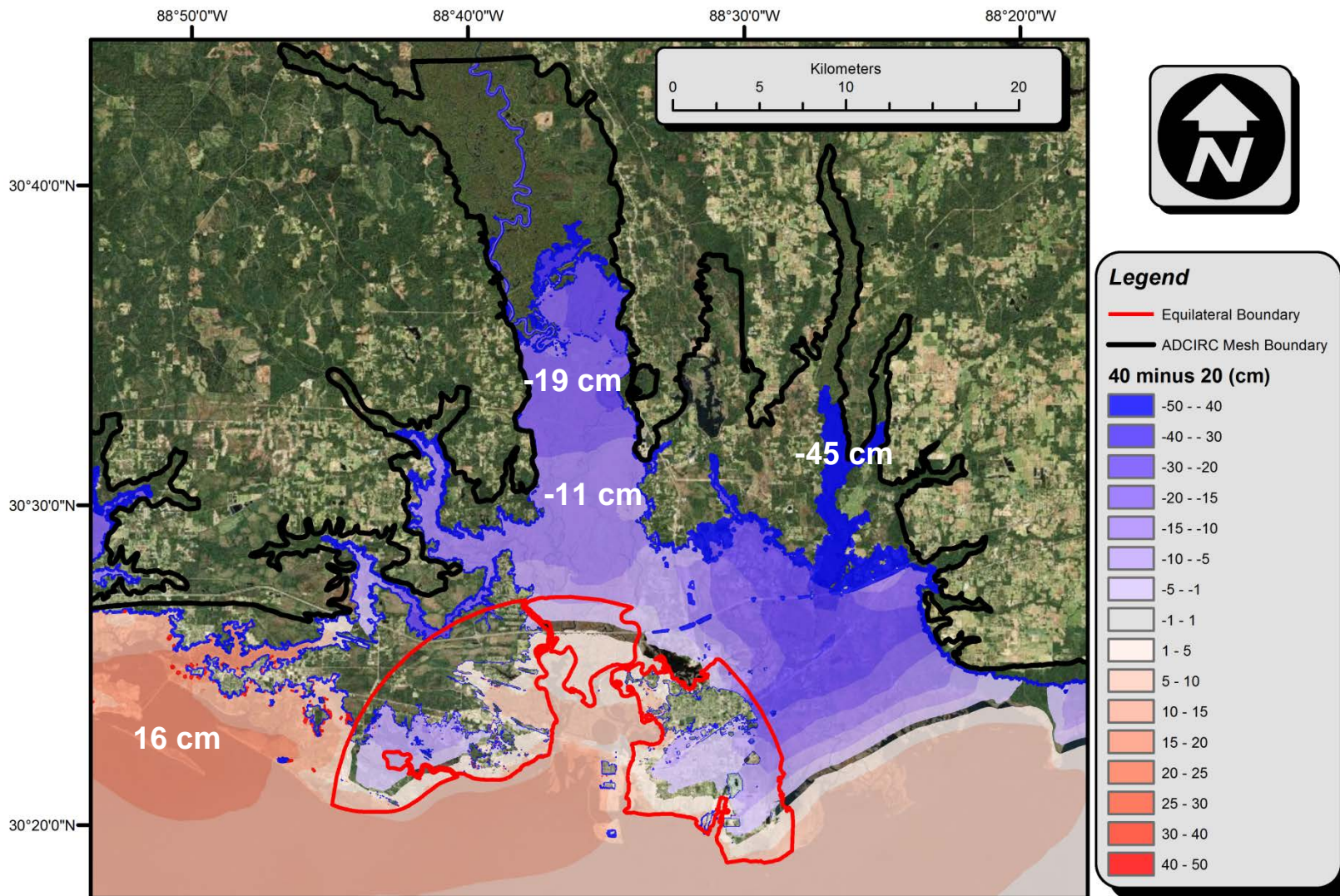


Figure 114 Difference in maximum water levels between the 40-m and 20-m equilateral mesh simulations. Hot colors represent higher water levels for the 40-m mesh and cool colors are higher water levels for the 20-m mesh.

CHAPTER 13: CONCLUSIONS AND FUTURE WORK

This thesis presents a method for determining topographic elevation error in DEMs and overland unstructured FEMs derived from bare earth LiDAR and its influence on simulated astronomic tides and hurricane storm surge. Also, an accurate interpolation method based on element size to minimize errors in vertical elevations was investigated.

First, a method for assessing topographic elevation error was developed in southern Mississippi and further verified in southeastern Louisiana. Second, two in-bank FEMs of the Pascagoula River were developed and incorporated into the WNAT model domain such that astronomic tides could be accurately modeled. Third, the methodology developed to test topographic error was applied to three large regions in coastal Pascagoula, Mississippi. Fourth, a high-resolution DEM was created for coastal Mississippi based on minimal topographic error and data efficiency. Fifth, a large-domain, high-resolution, FEM was constructed up to the 15-m contour to study regional topographic elevation error and the effect topographic representation has on simulated storm tide. Four variations were made to the FEM by changing the element resolution using equilateral elements of 160-m, 80-m, 40-m, and 20-m in three areas surrounding the overland region of the East and West Pascagoula inlets. Lastly, astronomic tides, winds and pressures from Hurricane Katrina were simulated on all four FEMs using the ADCIRC-2DDI code to determine topographic influence on inundation extent and total water levels.

Five major conclusions were drawn from this study (not listed in order of importance):

1) DEM/FEM topographic elevation error is not normally distributed; 2) significantly increasing

element resolution (more than three elements spanning the river bank) in the Pascagoula River did not produce more accurate results when simulating astronomic tides; 3) the 5-m raster DEM interpolated to the FEMs performed with the most accuracy and efficiency compared to other bare earth derived-source elevation datasets; 4) a set of equations to interpolate a 5-m raster DEM to a FEM was established based on minimizing topographic elevation error:

$$CA = \begin{cases} 1 & \text{for } \mathbb{N} < 1 \\ [2(\mathbb{N}) + 1]^2 & \text{for } \mathbb{N} \geq 1 \end{cases} \quad 13.1$$

5) changes in topographic representation affect inundation extent and maximum water levels from simulated storm tide both locally and non-locally.

It is also noted how the Shannon-Nyquist theorem from digital signal processing served well in determining the minimum limit of grid size in a bare earth LiDAR-derived DEM.

Topographic elevation error was found to be highly dependent on interpolation error and element size. This was shown with RMSE and it changed was changed drastically with adjustment of either the interpolation method, element size, or both. Additionally, since storm surge response was found to be non-local to changes in topography, it is important to consider the description of the ground surface in all regions and not just in the area of interest. A final product of this thesis is a methodology to examine topographic error that is based on an efficient interpolating scheme to acquire elevation values from high-density bare earth LiDAR to mesh nodes with minimal elevation error.

The following are subjects to future work. First, an analysis should be conducted to better assess topographic elevation error for non-normal distributions. The non-normality of the errors eliminate the use of RMSE in computing the 95th percentile, as required by both FEMA

and ASPRS (FEMA, 2003; ASPRS, 2004). Additionally, transforming the error dataset to a normal distribution to compute the standard deviation (equal to the RMSE of the differences) may allow a better assessment of topographic accuracy.

Second, a topographic error assessment including vertical features could benefit the methodology. Since larger errors of elevation were found around high gradients in slope (i.e. roadbed, creek, etc.), placing mesh nodes along these features should drastically increase the accuracy of the FEM. An algorithm is needed to efficiently automate unstructured triangular element paving of the overland region by incorporating significant raised features while minimizing topographic error and generating numerically stable elements.

Finally, a hydrodynamic assessment including wind driven waves would enable assessment of how the topographic representation affects waves and their momentum transfer to the water column.

Results of physically based numerical models improve when inputs mimic those of the real world, provided the applicability of the governing equations. This thesis provides a foundation for quantitatively assessing the uncertainty in the discrete topographic surface representation of bare earth LiDAR. Such quantitative assessment of mesh quality, as related to capture of the underlying source data, can serve a useful component to an overall scheme of assessing model uncertainty for a tide and storm surge model.

REFERENCES

- Aguilar, F. J., Aguera, F., Aguilar, M. A., & Carvajal, F. (2005). Effects of terrain morphology, sampling density, and interpolation methods on grid DEM accuracy. *Photogrammetric Engineering & Remote Sensing*, 71(7), 805-816.
- Aguilar, F. J., & Mills, J. P. (2008). Accuracy Assessment of LiDAR-Derived Digital Elevation Models. *The Photogrammetric Record*, 23(122), 148-169.
- Ali, T. (2004). *On the selection of an interpolation method for creating a terrain model (TM) from LIDAR data*. Paper presented at the American Congress on Surveying and Mapping (ACSM) Conference 2004, Nashville, TN, U.S.A.
- Anderson, E. S., Thompson, J. A., & Austin, R. E. (2005). LIDAR data density and linear interpolator effects on elevation estimates. *International Journal of Remote Sensing*, 26(18), 3889-3900.
- Anderson, E. S., Thompson, J. A., Crouse, D. A., & Austin, R. E. (2006). Horizontal resolution and data density effects on remotely sensed LIDAR-based DEM. *Geoderma*, 132(3-4), 406-415.
- Aquaveo. (2007a). SMS: Inverse Distance Weighted Interpolation, from http://www.xmswiki.com/xms/SMS:Inverse_Distance_Weighted_Interpolation
- Aquaveo. (2007b). SMS: Linear Interpolation, from http://www.xmswiki.com/xms/SMS:Linear_Interpolation
- Aquaveo LLC. (2010). Surface-water Modeling System (Version 10.1). Provo, Utah. Retrieved from <http://xmswiki.com/xms/SMS:SMS>,
- Aquaveo LLC. (2011). GMS: Triangulation, from <http://www.xmswiki.com/xms/GMS:Triangulation>

- ASPRS. (2004). ASPRS Guidelines, *Vertical Accuracy Reporting for LiDAR Data*: American Society for Photogrammetry and Remote Sensing.
- Atkinson, J. (2007). *Representation of vegetation on the wind boundary layer and surface bottom friction*. Paper presented at the 10th International Workshop on Wave Hindcasting and Forecasting and Coastal Hazard Symposium, Oahu, Hawaii.
- Atkinson, J. H., Roberts, H. J., Hagen, S. C., Zou, S., Bacopoulos, P., Medeiros, S., . . . Cobell, Z. (2011). Deriving frictional parameters and performing historical validation for an ADCIRC storm surge model of the Florida Gulf Coast. *Florida Watershed Journal*, 4(2), 22-27.
- Axelsson, P. (1999). Processing of laser scanner data - algorithms and applications. *ISPRS - Journal of Photogrammetry and Remote Sensing*, 54(2-3), 138-147.
- Bacopoulos, P. (2009). *Estuarine Influence on Tidally Driven Circulation in the South Atlantic Bight*. Ph.D., University of Central Florida, Orlando, FL.
- Bater, C. W., & Coops, N. C. (2009). Evaluating error associated with lidar-derived DEM interpolation. *Journal of Computers and Geosciences*, 35(2), 289-300.
- Bates, P. D., Marks, K. J., & Horritt, M. S. (2003). Optimal Use of High-Resolution Topographic Data in Flood Inundation Models. *Hydrological Processes*, 17, 537-557. doi: 10.1002/hyp.1113
- Bilskie, M. V., Hagen, S. C., Salisbury, M., & Coggin, D. (2011). *Low- Versus High-Resolution Finite Element Modeling of the Yellow River, FL*. Paper presented at the Solutions to Coastal Disasters 2011, Anchorage, AL.
- Blain, C. A., Westerink, J. J., & Luetich, R. A. (1994). The influence of domain size on the response characteristics of a hurricane storm surge. *Journal of Geophysical Research*, 99(C9), 18,467-418,479.
- Blain, C. A., Westerink, J. J., & Luetich, R. A. (1998). Grid convergence studies for the prediction of hurricane storm surge. *International Journal of Numerical Methods in Fluids*, 26, 369-401.

- Blanton, J. O., Werner, F. E., Seim, H. E., Luettich, R. A. J., Lynch, D. R., Smith, K. W., . . . Way, F. (2004). Barotropic tides in the South Atlantic Bight. *Journal of Geophysical Research*, 109(C12024), 1-17.
- Blue Marble Geographics. (2011). Global Mapper (Version 12.02). Retrieved from <http://www.globalmapper.com/>
- Bunya, S., Dietrich, J. C., Westerink, J. J., Ebersole, B. A., Smith, J. M., Atkinson, J. H., . . . Roberts, H. J. (2010). A high-resolution coupled riverine flow, tide, wind, wind wave, and storm surge model for southeastern Louisiana and Mississippi. Part I: Model development and validation. *Monthly Weather Review*, 128(345-377).
- Burrough, P., & McDonnell, R. A. (1998). *Principles of geographical information systems*: Oxford University Press.
- Carter, R. W. G. (1988). *Coastal Environments* London: Academic Press Limited.
- Chaplot, V., Darboux, F., Bourenane, H., Leguedois, S., Silvera, N., & Phachomphon, K. (2006). Accuracy of interpolation techniques for the derivation of digital elevation models in relation to landform types and data density. *Journal of Geomorphology*, 77, 126-141.
- Coggin, D. (2008). *LIDAR in coastal storm surge modeling: modeling linear raised features*. M.S., University of Central Florida, Orlando, FL.
- Coggin, D. (2011). A digital elevation model for Franklin, Wakulla, and Jefferson Counties. *Florida Watershed Journal*, 4(2), 5-10.
- Darboux, F., Gascuel-Oudou, C., & Davy, P. (2002). Effects of surface water storage by soil roughness on overland-flow generation. *Earth Surface Processes and Landforms*, 27, 223-233.
- Dean, R. G., & Dalrymple, R. A. (2002). *Coastal Processes with Engineering Applications*. Cambridge: Cambridge University Press.

- Department of Atmospheric Sciences at University of Illinois at Urbana-Champaign. (2010). Pressure and Winds Retrieved 09-24, 2011, from [http://ww2010.atmos.uiuc.edu/\(Gh\)/guides/mtr/hurr/stages/cane/pswd.rxml](http://ww2010.atmos.uiuc.edu/(Gh)/guides/mtr/hurr/stages/cane/pswd.rxml)
- Desmet, P. J. J. (1997). Effects of interpolation errors on the analysis of DEMs. *Earth Surface Processes and Landforms*, 22, 563-580.
- Dietrich, J. C., Tanaka, S., Westerink, J. J., Dawson, C. N., Luettich, R. A., Zijlema, M., . . . Westerink, H. J. (2012). Performance of the Unstructured-Mesh, SWAN+ADCIRC Model in Computing Hurricane Waves and Surge. *Journal of Scientific Computing, In Press*.
- Dietrich, J. C., Westerink, J. J., & Kennedy, A. B. (2011). Hurricane Gustav (2008) Waves and Storm Surge: Hindcast, Synoptic Analysis, and Validation in Southern Louisiana. *Monthly Weather Review*, 139(8), 2488-2522.
- Dietsche, D., Hagen, S. C., & Bacopoulos, P. (2007). Storm surge simulations for Hurricane Hugo (1989): On the significance of inundation areas. *Journal of Waterway, Port, Coastal, and Ocean Engineering*, 133(3), 183-191.
- EarthData International. (2005a). Elevation Mapping Jackson and Hancock Counties, MS LiDAR Final Project Report. Frederick, MD.
- EarthData International. (2005b). Harrison County, Mississippi LiDAR Acquisition Report. Frederick, MD.
- EarthData International. (2005c). Harrison County, Mississippi LiDAR Processing Report. Frederick, MD.
- Eckstein, W., & Munkelt, O. (1995). *Extracting objects from digital terrain models*. Paper presented at the SPIE.
- ESRI. (2008). ArcGIS: The complete enterprise GIS Retrieved 04-25-2011, 2011, from <http://www.esri.com/software/arcgis/>

- ESRI. (2011a). ArcGIS Desktop: Release 10. Redlands, CA: Environmental Systems Research Institute.
- ESRI. (2011b). ArcGIS Resource Center, from <http://resources.arcgis.com/>
- FEMA. (2003). Appendix A, Guidance for aerial mapping and surveying, *Guidelines and Specifications for Flood Hazard Mapping Partners*: Federal Emergency Management Agency.
- Fisher, P. F., & Tate, N. J. (2006). Causes and Consequences of Error in Digital Elevation Models. *Progress in Physical Geography*, 22(1), 33-60.
- Florinsky, I. V. (1998). Combined analysis of digital terrain models and remotely sensed data in landscape investigations. *Progress in Physical Geography*, 22(1), 33-60.
- Florinsky, I. V. (2002). Errors of signal processing in digital terrain modelling. *International Journal of Geographical Information Science*, 16(5), 475-501.
- Franke, R., & Nielson, G. (1980). Smooth interpolation of large sets of scattered data. *International Journal for Numerical Methods in Engineering*, 15(11), 1691-1704.
- Fritsch, D., & Kilian, J. (1994). Filtering and calibration of laser scanner measurements. *International Archives of Photogrammetry and Remote Sensing*, 30(3/1), 227-234.
- Gao, J. (1997). Resolution and accuracy of terrain representation by grid DEMs at a micro-scale. *International Journal of Geographical Information Science*, 11(2), 199-212.
- Garratt, J. R. (1977). Review of drag coefficients over oceans and continents. *Monthly Weather Review*, 105(7), 915-929.
- Gesch, D., Oimoen, M., Greenlee, S., Nelson, C., Steuck, M., & Tyler, D. (2002). The National Elevation Dataset. *Photogrammetric Engineering and Remote Sensing*, 68(1), 5-11.
- Gesch, D. B. (2007). The National Elevation Dataset. In D. F. Maune (Ed.), *Digital Elevation Model Technologies and Applications: The DEM Users Manual* (Second Edition ed., pp.

- 99-118). Bethesda, Maryland: American Society for Photogrammetry and Remote Sensing.
- Gong, J., Li, Z., Zhu, Q., Zhou, S., & Zhou, Y. (2000). Effects of Various Factors On the Accuracy of DEMs: An Intensive Experimental Investigation. *Photogrammetric Engineering & Remote Sensing*, 66(9), 1113-1117.
- Goslee, S. C. (2011). Analyzing remote sensing data in R: The landsat package. *Journal of Statistical Software*, 43(4), 1-25.
- Greenwalt, C. R., & Shultz, M. E. (1962). Principles of error theory and cartographic applications *ACIC Technical Report No. 96* (pp. 89). St. Louis, Missouri.
- Hagen, S., Bacopoulos, P., Medeiros, S., Coggin, D., Salisbury, M., Atkinson, J. H., & Roberts, H. J. (2009). Storm surge modeling for FEMA map modernization for Franklin, Wakulla, and Jefferson Counties, Florida: University of Central Florida.
- Hagen, S. C. (2001). Estimation of the Truncation Error for the Linearized, Shallow Water Momentum Equations. *Engineering with Computers*, 17, 354-362.
- Hagen, S. C., Bacopoulos, P., Cox, A. T., & Cardone, V. J. (2011). Hydrodynamics of the 2004 Florida Hurricanes. *Journal of Coastal Research*, *In Press*. doi: 10.2112/JCOASTRES-D-10-00170.1.
- Hagen, S. C., & Parrish, M. (2004). Meshing Requirements for Tidal Modeling in the Western North Atlantic. *International Journal of Computational Fluid Dynamics*, 18(7), 585-595.
- Hagen, S. C., Westerink, J. J., & Kolar, R. L. (2000). One-dimensional finite element grids based on a localized truncation error analysis. *International Journal for Numerical Methods in Fluids*, 32, 241-261.
- Hagen, S. C., Westerink, J. J., Kolar, R. L., & Horstmann, O. (2001). Two-dimensional, unstructured mesh generation for tidal models. *International Journal for Numerical Methods in Fluids*, 35, 669-686.

- Hagen, S. C., Zundel, A. K., & Kojima, S. (2006). Automatic, unstructured mesh generation for tidal calculations in a large domain. *International Journal of Computational Fluid Dynamics*, 20(8), 593-608.
- Harris, D. L. (1963). Characteristics of the Hurricane storm surge *Technical Paper No. 48*: U.S. Weather Bureau.
- Hasan, A., Pilesjo, P., & Persson, A. (2011). The use of LiDAR as a data source for digital elevation models - a study of the relationship between the accuracy of digital elevation models and topographical attributes in northern peatlands. *Hydrology and Earth System Sciences Discussion*, 8, 5497-5522.
- Hengl, T. (2006). Finding the right pixel size. *Computers & Geosciences*, 32(9), 1283-1298. doi: DOI 10.1016/j.cageo.2005.11.008
- Hjelle, O., & Dæhlen, M. (2006). *Triangulations and Applications* (1 ed.): Springer.
- Homer, Huang, C. C., Yang, L., Wylie, B. K., & Coan, M. (2004). Development of a 2001 National Land Cover Database for the United States. *Photogrammetric Engineering and Remote Sensing*, 70(7), 829-840.
- Horrit, M. S., & Bates, P. D. (2001). Predicting floodplain inundation: raster-based modelling versus the finite-element approach. *Hydrological Processes*, 15, 825-842.
- Kennedy, A. B., Gravois, U., Zachry, B. C., Westerink, J. J., Hope, M. E., Luettich, R. A., & Dean, R. G. (2011). Origin of the Hurricane Ike forerunner surge. *Geophysical Research Letters*, 38(L08608).
- Kenward, T., Lettenmaier, D. P., Wood, E. F., & Fielding, E. (2000). Effects of digital elevation model accuracy on hydrological processes. *Remote Sensing of Environment*, 74, 432-444.
- Kienzle, S. (2004). The Effect of DEM Raster Resolution on First Order, Second Order and Compound Terrain Derivatives. *Transactions in GIS*, 8(1), 83-111.
- Kinnmark, I. (1985). The shallow water wave equations: formulation, analysis, and application *Lecture Notes in Engineering*. New York, New York: Springer-Verlag.

- Kojima, S. (2005). *Optimization of an unstructured finite element mesh for tide and storm surge modeling applications in the western north Atlantic Ocean*. M.S., University of Central Florida, Orlando, FL.
- Kolar, R. L., Grey, W., Westerink, J. J., & Luetlich, R. A. (1994). Shallow water modeling in spherical coordinates: Equation formulation, numerical implementation, and application. *Journal of Hydraulic Research*, 32(1), 3-24.
- Kubik, K., & Botman, A. G. (1976). Interpolation accuracy for topographic and geological surfaces. *ITC Journal*, 2(236-274).
- Le Provost, C., Lyard, F., Molines, J. M., Genco, M. L., & Rabilloud, F. (1998). A hydrodynamic ocean tide model improved by assimilating a satellite altimeter-derived data set. *Journal of Geophysical Research*, 103(C3), 5513-5529.
- Lefsky, M. A., Cohen, W. B., Parker, C. G., & Harding, D. J. (2002). LiDAR remote sensing for ecosystem studies. *Bioscience*, 52, 19-30.
- Lennon, G. W. (1963). *A frequency investigation of abnormally high tidal levels at certain west coast ports*. Paper presented at the Institution Civil Engineers.
- Li, Z., Zhu, Q., & Gold, C. (2005). *Digital Terrain Modeling: Principles and Methodology*. London, New York, and Washington, D.C.: CRC Press.
- Lilliefors, H. (1967). On the Kolmogorov-Smirnov test for normality with mean and variance unknown. *Journal of the American Statistical Association*, 62, 399-402.
- Liu, X. (2008). Airborne LiDAR for DEM generation: some critical issues. *Progress in Physical Geography*, 32(1), 31-49.
- Liu, X., Zhang, Z., Peterson, J., & Chandra, S. (2007a). *The effect of lidar data density on DEM accuracy*. Paper presented at the International Congress on Modelling and Simulation (MODSIM07), Christchurch, New Zealand.
- Liu, X., Zhang, Z., Peterson, J., & Chandra, S. (2007b). LiDAR-derived high quality ground control information and DEM for image orthorectification. *GeoInformatica*, 11(1), 37-53.

- Liu, X., Zhang, Z., Peterson, J., & Chandra, S. (2008, June 25-27). *Large area DEM generation using airborne LiDAR data and quality control*. Paper presented at the 8th International Symposium on Spatial Accuracy Assessment in Natural Resources and Environmental Sciences, Shanghai, P.R. China.
- Lloyd, C. D., & Atkinson, P. M. (2002). Deriving DSMs from LiDAR data with kriging. *International Journal of Remote Sensing*, 23(12), 2519-2524.
- Lloyd, C. D., & Atkinson, P. M. (2006). Deriving ground surface digital elevation models from LiDAR data with geostatistics. *International Journal of Geographical Information Science*, 20(5), 535-563.
- Lohmann, P., & Hug, C. (1998). Topographic mapping using the scanning laser altitude and reflectance Sensor (ScaLARS). *Proc. ISPRS Joint Workshop "Sensors and Mapping from Space", University of Hanover, Institute for Photogrammetry and Engineering Surveys, WG I/1 & IV/4*, 83-96.
- Lohr, U. (1998). Digital elevation models by laser scanning. *Photogrammetric Record*, 16(9), 105-109.
- Longley, P., Goodchild, P. F., Maguire, D. J., & Rhind, D. W. (1999). *Spatial Interpolation Geographical Informational Systems: Principles, Techniques, Management and Applications*. New York: Wiley.
- Louisiana State University. (2009). Louisiana LiDAR, from <http://atlas.lsu.edu/lidar/>
- Luetlich, R. A., & Westerink, J. J. (2006). ADCIRC User's Manual - v46, from http://www.adcirc.org/documentv46/fort_15.html
- Luetlich, R. A., Westerink, J. J., & Scheffner, N. W. (1992). ADCIRC: An Advanced Three-Dimensional Circulation Model For Shelves, Coasts, and Estuaries, I: Theory and Methodology of ADCIRC-2DDI and ADCIRC-3DL: U.S. Army Corps of Engineers.
- Maune, D. F. (2007). *Digital Elevation Model Technologies and Applications: The DEM Users Manual* (2 ed.). Bethesda, Maryland: American Society for Photogrammetry and Remote Sensing.

- McCullagh, M. J. (1988). Terrain and surface modelling systems: theory and practice. *Photogrammetric Record*, 12(72), 747-779.
- Medeiros, S., & Hagen, S. C. (2011). Review of wetting and drying algorithms for numerical tidal flow models. *International Journal for Numerical Methods in Fluids*, Under Review.
- Medeiros, S. C., Ali, T., & Hagen, S. C. (2011). Development of a seamless topographic/bathymetric digital terrain model for Tampa Bay, Florida. *Photogrammetric Engineering & Remote Sensing*, In Press.
- Mendenhall, W., & Sincich, T. (2007). *Statistics for Engineering and the Sciences* (Fifth ed.). Upper Saddle River, NJ: Pearson Prentice Hall.
- Mississippi Department of Environmental Quality. (2001). Pascagoula River Basin Status Report 2001.
- Mossa, J., Walker, F., Hermansen, G., Coley, D., & Ogbugwo, M. (2003). Geomorphic assessment of channel changes along a modified floodplain, Pascagoula River, Mississippi: Year 1 Interim Report. Gainesville: University of Florida.
- Mukai, A., Westerink, J. J., Luettich, R. A., & Mark, D. (2002). Eastcoast 2011: A tidal constituent database for the Western North Atlantic, Gulf of Mexico, and Caribbean Sea. Tech. Rep. ERDC/CHL TR-02-24, U.S. Army Corps of Engineers (pp. 201).
- National Oceanic and Atmospheric Administration (NOAA). (1998). Population: Distribution, Density, and Growth *NOAA's State of the Coast Report*. Silver Springs, MD: NOAA.
- National Weather Service. (2009). Glossary of NHC Terms. *National Hurricane Center*, from <http://www.nhc.noaa.gov/aboutgloss.shtml>
- NDEP. (2004). Guidelines for Digital Elevation Data Version 1.0. Reston, VA: National Digital Elevation Program.
- NOAA. (2010). Storm Surge Overview Retrieved 09-22, 2011, from <http://www.nhc.noaa.gov/surge/>

- Northwest Florida Water Management District. (2011). Flood Insurance Study: Florida Panhandle and Alabama: In Review.
- Oksanen, J., & Sarjakoski, T. (2006). Uncovering the statistical and spatial characteristics of fine topographic DEM error. *International Journal of Geographic Information Science*, 20, 345-369.
- Oldham, M. B. J., & Rushing, J. W. (1970). Water Resources Planning for Pascagoula Basin. *Journal of Waterways and Harbors Division, Proceedings of the American Society of Civil Engineers*, 96(WWI), 65-85.
- Parrish, M. (2007). *Target Element Sizes For Finite Element Tidal Models From A Domain-Wide, Localized Truncation Error Analysis Incorporating Bottom Stress and Coriolis Force*. Ph.D., University of Central Florida, Orlando, FL.
- Pawlowicz, R. B., Beardsley, B., & Lentz, S. (2002). Classical tidal harmonic analysis including error estimates in MATLAB using T_TIDE. *Computers and Geosciences*, 28, 929-937.
- Pearson, F. (1990). *Map Projections: Theory and applications*. Boca Raton, Florida: CRC Press.
- Perrott, C. (2007). Pascagoula River Basin Retrieved 08/10/2011, 2011, from http://www.deq.state.ms.us/mdeq.nsf/page/WMB_Pascagoula_River_Basin?OpenDocument
- Pielke, R. A. (1990). *The Hurricane*. London: Routledge.
- Pore, A. N. (1965). Chesapeake bay extratropical storm surges. *Chesapeake Science*, 6(3), 172-182.
- Powell, M. D., Vickery, P. J., & Reinhold, T. A. (2003). Reduced drag coefficient for high wind speeds in tropical cyclones. *Nature*, 422, 279-283.
- Pugh, D. (2004). *Changing Sea Levels*. United Kingdom: Cambridge University Press.
- Rappaport, J. (2003). The United States as a Coastal Nation. *Journal of Economic Growth*, 8, 5-46.

- Reid, R. O. (1990). *Waterlevel changes, tides and storm surges*. Houston, Texas.
- Roberts, H. J. (2004). *Grid Generation Methods for High Resolution Finite Element Models Used For Hurricane Storm Surge Prediction*. Master of Science in Civil Engineering, Notre Dame, South Bend.
- Salisbury, M. B., Hagen, S. C., Coggin, D., Bacopoulos, P., Atkinson, J. H., & Roberts, H. J. (2011). Unstructured mesh development for the Big Bend Region (Florida). *Florida Watershed Journal*, 4(2), 11-14.
- Samburg, A. (1997). What laser scanning can do today: current techniques. *Advances in Remote Sensing*, 5(Yearbook 1997), 114-119.
- Schoorl, J. M., Sonneveld, M. P. W., & Veldkamp, A. (2000). Three-dimensional landscape process modelling: The effect of DEM resolution. *Earth Surface Processes and Landforms*, 25, 1025-1034.
- Shannon, C. E. (1949). *Communication in the presence of noise*. Paper presented at the Institute of Radio Engineers.
- Shapiro, S. S., & Wilk, M. B. (1965). An analysis of variance test for normality (complete samples). *Biometrika*, 52, 591-599.
- Shepard, D. (1968). *A two-dimensional interpolation function for irregularly-spaced data*. Paper presented at the ACM National Conference.
- Shi, W. (2010). *Principles of Modeling Uncertainties in Spatial Data and Spatial Analysis*. Boca Raton, FL: CRC Press.
- Sibson, R. (1981). A brief description of natural neighbor interpolation *Interpreting Multivariate Data* (pp. 21-36). Chichester: John Wiley.
- Slack, L. J. (1991). Mississippi Stream Water Quality: National Water Summary 1990-91 *United States Geological Survey Water Supply Paper 2400* (pp. 343-350).

- Smith, J. M., Sherlock, A. R., & Resio, D. T. (2002). STWAVE: Steady-State Spectral Wave Model User's Manual for STWAVE, Version 3.0 *Technical Report ERDC/CHL SR-01-1, Coastal Hydraulic Laboratory, U.S. Army Corps of Engineers, Engineer Research and Development Center*. Vicksburg, MS.
- Southeast Digital Mapping, L. (2003). Standards and Specifications for Mobile County LiDAR Products. Theodore, AL.
- Strom, E. W. (1998). The Pascagoula River Basin. *The Rivers of Mississippi* Retrieved 08/11/2011, 2011, from http://ms.water.usgs.gov/ms_proj/eric/pasca.html
- Su, J., & Borke, E. (2006). Influence of vegetation, slope and lidar sampling angle on DEM accuracy. *Photogrammetric Engineering & Remote Sensing*, 72(11), 1265-1274.
- Takahashi, N. (2008). *A high-resolution storm surge model for the Pascagoula region, Mississippi*. University of Central Florida, Orlando, FL.
- Turnipseed, D. P., & Storm, J. B. (1995). *Streamflow characteristics of the Lower Pascagoula River, Mississippi*. Paper presented at the Twenty-Fifth Mississippi Water Resources Conference, Jackson, MS.
- Vogelmann, J. E., Howard, S. M., Yang, L., Larson, C. R., Wylie, B. K., & DVan Driel, N. (2001). Completion of the 1990s National Land Cover Data Set for the conterminous United States from Landsat thematic mapper data and ancillary data sources. *Photogrammetric Engineering and Remote Sensing*, 67, 650-652.
- Wang, Q. (2008). *Finite element modeling of tides and currents of the Pascagoula River*. M.S., University of Central Florida, Orlando.
- Watershed Concepts. (2004). Quality Control Evaluation of LiDAR Data For Louisiana FEMA Region VI Task Area 5 *Louisiana Phase 1 LiDAR Project: Final Lidar Evaluation* (pp. 139).
- Weber, D., & Englund, E. (1994). Evaluation and comparison os spatial interpolators II. *Mathematical Geology*, 26, 589-603.

- Wehr, A., & Lohr, U. (1999). Airborne laser scanning - an introduction and overview. *Journal of Photogrammetry and Remote Sensing*, 54, 68-82.
- Westerink, J. J., Blain, C. A., Luettich, R. A., & Scheffner, N. W. (1994a). ADCIRC: An advanced three-dimensional circulation model for shelves, coasts, and estuaries: Report 2 (pp. 168). Vicksburg, Mississippi: U.S. Army Corps of Engineers.
- Westerink, J. J., Feyen, J. C., Atkinson, J. H., Luettich, R. A., Dawson, C. N., Powell, M. D., . . . Pourtaheri, H. (2004). A New Generation Hurricane Storm Surge Model for Southern Louisiana ADCIRC Development Group Publications.
- Westerink, J. J., Luettich, R. A., Feyen, J. C., Atkinson, J. H., Dawson, C., Roberts, H. J., . . . Pourtaheri, H. (2008). A basin- to channel-scale unstructured grid hurricane storm surge model applied to Southern Louisiana. *Monthly Weather Review*, 136, 833-864.
- Westerink, J. J., Luettich, R. A., & Muccino, J. C. (1994b). Modeling tides in the western North Atlantic using unstructured graded grids. *Tellus*, 46A, 178-199.
- Zandbergen, P. A. (2008). Positional accuracy of spatial data: non-normal distributions and a critique of the National Standard for Spatial Data Accuracy. *Transactions in GIS*, 12(1), 103-130.
- Zandbergen, P. A. (2011). Characterizing the error distribution of LiDAR elevation data. *International Journal of Remote Sensing*, 32(2), 409-430.
- Zhu, C., Shi, W., Li, Q., Wang, G., Cheung, T. C. K., Dai, E., & Shea, G. Y. K. (2005). Estimation of average DEM accuracy under linear interpolation considering random error at the nodes of a TIN model. *International Journal of Remote Sensing*, 26(24), 5509-5523.
- Zimmerman, D., Pavlik, C., Ruggles, A., & Armstrong, M. (1999). An experimental comparison of ordinary and universal kriging and inverse distance weighting. *Mathematical Geology*, 31, 375-390.